A method for quantifying the absolute accuracy and precision of dynamic contrast enhanced MRI acquisition techniques

Submitted in accordance with the requirements for the degree of
Doctor in Philosophy
in School of Medicine, Clinical Medicine

April 2018

by

Silvin Paul Knight

Trinity College Dublin
Coláiste na Tríonóide, Baile Átha Cliath
The University of Dublin

Declaration

I declare that this thesis has not been submitted as an exercise for a degree at this or any other university and it is entirely my own work.

I agree to deposit this thesis in the University's open access institutional repository or allow the library to do so on my behalf, subject to Irish Copyright Legislation and Trinity College Library conditions of use and acknowledgement.

_____

Silvin Paul Knight

25th April 2018

Summary

To data a method has been lacking which allows for the quantitative evaluation of the accuracy and precision of dynamic contrast-enhanced (DCE) MRI techniques, as implemented at the MR scanner, with results calculated against precisely-known 'ground truth' values. In this thesis a novel anthropomorphic dynamic phantom test device is presented which mimicked the male pelvic-region (in terms of size and complexity) within which ground truth contrast agent concentration time-intensity curves (CTCs) were generated and presented to the MRI scanner for measurement, thereby allowing for an assessment of a particular DCE-MRI protocol's ability to repeatedly and accurately measure a given physiologically-relevant curve-shape. The device comprised of a 4-pump flow system, wherein CTCs derived from prior patient prostate data were produced for measurement at chambers placed within the imaged volume. The ground truth was determined using a highly-precise, MRI-independent, custom-built optical imaging system. Initial experiments performed using this system measuring prostate-tissue-mimicking CTCs (with a model population-averaged arterial input function (AIF)) at various temporal resolutions (T_{res}: the temporal spacing between successive DCE measurements) and revealed significant errors in MRI-measured pharmacokinetic (PK) modelling outputs, amounting to values of up to 42%, 31%, and 50% for K^{trans} (*volume transfer coefficient*), v_e (*extravascular-extracellular space volume fraction*), and k_{ep} (*rate constant*) respectively. Further DCE-MRI experiments were performed wherein the T_{res} was varied in the range [2 - 24.4 s] and the acquisition duration (AD: the length of time that the CTCs were sampled for) in the range [30 - 600 s]. The phenomenological parameter '*wash-in'* derived from the CTCs gave underestimation errors up to 40% when using T_{res} values $\geq$ 16.3 s; however, the measured '*wash-out'* rate did not vary greatly across all T_{res} values tested. Errors in all derived PK parameter values were <14% for acquisitions with $T_{res} \leq$8.1s, AD $\geq$360s, but increased dramatically outside of this range.

The phantom test device was further used to investigate the effects of T_{res}, as well as B_1^+-field non-uniformities, on the accuracy and precision of simultaneously-measured AIF and prostate-tissue-mimicking CTCs, and derived PK parameters. A population-average AIF was established from the mean of 32 prostate patient dataset measurements (T_{res} = 3.1 s), and this formed the basis for the ground truth AIF used. The phantom device was modified to allow for a 'thin slab' 3D-volume to be acquired with a T_{res} approaching 1 s using a standard spoiled gradient echo sequence. Five repeat intra-session and five inter-session AIF measurements were made simultaneously with either prostate 'healthy' or 'tumour' CTCs, with T_{res} varied in the

range [1.2 – 30.6 s], providing a total of 450 full DCE-MRI datasets for analysis. Flip angle errors deriving from B_1^+-field non-uniformities of -29% to -33% were measured. Performing voxel-wise flip-angle correction (VFAC) on the data to correct for this effect increased the PK parameter estimation accuracy by 12.9%, 9.2% and 20.2% for K^{trans}, v_e and k_{ep} respectively, and increased intra-session precision by up to 11.2%. It was also demonstrated that the use of a linear implementation of the standard Tofts PK model, rather than the more traditionally-used non-linear form, almost doubled the accuracy of K^{trans} estimates, caused an increase in K^{trans} and k_{ep} precision of ~4%, and relaxed the dependence of the parameter accuracy on the T_{res} used.

A final set of experiments using the phantom system investigated the effect of under-sampling the data on the accuracy and precision of the measured CTCs and AIF, and the derived PK parameters. The data was acquired using a continuous golden-angle (GA) radial *k*-space trajectory and subsequently reconstructed using three approaches: (i) no parallel imaging (PI) or compressed sensing (CS) (i.e. coil-by-coil (CbC) inverse gridding), (ii) PI only, and (iii) PI combined with CS (PICS). Overall, the PICS reconstruction approach was shown to provide the highest accuracy for PK parameter estimation, with all errors in K^{trans}, v_e, and k_{ep} parameter values less than 12%, 6.6%, and 12%, respectively, for data reconstructed with as little as 3% of the data required to fulfil the Nyquist criterion. This corresponds to a twenty-one-fold gain in acquisition speed, compared to a standard fully-sampled Cartesian approach with the same acquisition spatial resolution and geometries. PICS reconstruction was shown to provide a gain in accuracy in PK parameter estimations of up to 34% and 42% compared with the PI and CbC approaches, respectively.

Across the breadth of this thesis various factor which influence the absolute accuracy and precision on PK parameter estimations have been systematically and quantitatively investigated, refining the methodologies used, and ultimately arriving at an acquisition and data processing protocol which provided PK parameter estimations with mean errors all $\leq$ 2%, and with intra- and inter-session precision of $\leq$ 4% . This protocol comprises of a continuous GA radial acquisition with 100% radial sampling density, VFAC applied, and with linear fitting of the standard Tofts model to the measured data. However, the phantom device presented in this thesis allows for the quantitative assessment of any DCE-MRI protocols (both existing and emerging), and could be used to refine these techniques, for example to maintain errors below a certain level deemed to be acceptable for the specific anatomy under investigation. The quantitative results presented herein demonstrate the strong reliance of the PK modelling accuracy and precision on the DCE-MRI methodologies used.

Acknowledgments

I would like to acknowledge and express my sincere gratitude to the following people:

My PhD supervisor, Prof Andrew Fagan, National Centre for Advanced Medical Imaging (CAMI), St James Hospital / Trinity College, University of Dublin (Dublin, Ireland), who provided me with the guidance, tools, and freedom to pursue my research directions that were necessary in order to complete this research. Thank you Andrew for your unfaltering day-to-day support and dedication to the project; I could not have hoped for a better mentor.

The Irish Cancer Society (Dublin, Ireland), this work was funded by an Irish Cancer Society Research Scholarship, supported by The Movember Foundation [grant number CRS13KNI].

Prof Jacinta Browne, Dublin Institute of Technology (Dublin, Ireland), for her assistance with the production of the tissue-mimicking-materials used in the construction of the phantom, as well as her invaluable advice and expertise when designing the phantom system.

Prof David Smith, Vanderbilt University (Nashville, TN, USA), for his partial-supervision of my work during a 3-month period spent conducting part of this research at Vanderbilt University, as well as his mentorship with regards implementing various DCE-MRI reconstruction methods and pharmacokinetic analysis technique. I would also like to thank Prof Thomas Yankeelov for hosting me at Vanderbilt, and Prof Brian Welch for his advice and assistance.

Dr Matthew Clemence, Philips Healthcare (UK), for his assistance with implementing the continuous golden-angle radial acquisition protocol on the scanner.

Dr Sean Cournane, St James's Hospital (Dublin, Ireland), for his assistance with initial attempts to measure the ground truths for the phantom system using X-ray.

Prof Martin Hegner, Trinity College, University of Dublin (Dublin, Ireland), for his assistance with the 3D printing of the prostate structure.

My colleagues in the Imaging Physics Group, Trinity College, University of Dublin (Dublin, Ireland), for their feedback on the project at our monthly group-meetings, as well as moral and experimental support during the course of this project.

The Irish Association of Physicist in Medicine (IAPM; Dublin, Ireland), for their support of the project in the form of a “Young Investigator Grant”, awarded to help partially-fund the construction of the phantom test device.

The staff at the National Centre for Advanced Medical Imaging (CAMI), St James’s Hospital (Dublin Ireland) and Vanderbilt University Institute of Imaging Science (VUIIS; Nashville, TN, USA) MRI centres for assistance with scanner access.

The staff in the Medical Physics and Bioengineering department at St James’s Hospital (Dublin, Ireland) who supported this project by generously provided the highly-stable light source used in the optical imaging system.

To my family and friends who supported me during this project.

Table of Contents

List of Figures

Abbreviations

Abbreviation	Definition
AD	Acquisition Duration
ADC	Apparent Diffusion Coefficient
AFI	Actual Flip angle Imaging
AIF	Arterial Input Function
CA	Contrast Agent
CCC	Concordance Correlation Coefficient
CS	Compressed Sensing
CTC	Concentration-Time Curve
DCE	Dynamic Contrast Enhanced
DTI	Diffusion Tensor Imaging
DWI	Diffusion Weighted Imaging
EBRT	External Beam Radiotherapy Treatment
EES	Extravascular-Extracellular Space
FID	Free-induction decay
FOV	Field Of View
GA	Golden Angle
Gd	Gadolinium
GS	Gleason Score
ICC	Intraclass Correlation Coefficient
LLS	Linear Least Squares
MP	Multi Parametric
MRI	Magnetic Resonance Imaging
MRSI	Magnetic Resonance Spectroscopic Imaging
NLS	Non-linear Least Squares
NMR	Nuclear Magnetic Resonance
NSA	Number of Signal Averages
PCa	Prostate Cancer
PD	Proton Density
PI	Parallel Imaging
PICS	Parallel Imaging and Compressed Sensing
PK	Pharmacokinetic
PSA	Prostate Specific Antigen
PSD	Pulse Sequence Diagram
RF	Radiofrequency
RMSE	Root Mean Square Error
ROI	Region Of Interest
SNR	Signal-to-Noise Ratio
STC	Signal-Time curve
TE	Echo Time
TMM	Tissue Mimicking Material
TR	Repetition Time
T_{res}	Temporal Resolution
TRUS	Transrectal Ultrasound
VFAC	Voxel-wise Flip-Angle Correction

List of Symbols

Quantity	Definition	Unit
α	Flip angle	°
α_{act}	Actual flip angle	°
α_{set}	Set flip angle	°
α_{set}	Set flip angle	°
AIF	Arterial Input Function: Concentration entering the capillary bed on the arterial side	mM*
B_1	Rotating radiofrequency magnetic field	T
C_c	Concentration in the capillary plasma volume	mM
C_e	Concentration in the extravascular-extracellular space volume	mM
C_t	Tissue bulk concentration	mM
F	Perfusion (or flow) of the whole blood per unit mass of tissue	ml g^{-1} min^{-1} #
k_{ep}	Rate constant	min^{-1}
K_{PS}	Capillary transfer coefficient	min^{-1}
K^{trans}	Volume transfer coefficient	min^{-1}
M_o	Equilibrium magnetisation	T
M_{xy}	Transverse magnetisation	T
M_z	Longitudinal magnetisation	T
ρ	Tissue density	g ml_{-1}
P	Total permeability of the vessel wall	cm min^{-1}
PS	Permeability surface area product per unit mass of tissue	ml min^{-1} g^{-1}
r_1	Relaxivity of the contrast agent	mM^{-1} s^{-1}
S	Surface area product per unit mass of tissue	cm g^{-1}
T_1	Longitudinal magnetisation relaxation time	ms
T_2	Transverse magnetisation relaxation time	ms
T_2^*	Effective transverse magnetisation relaxation rate	ms
TE	Echo Time	ms
TR	Repetition Time	ms
V_c	Total capillary plasma volume	ml
V_e	Total extravascular-extracellular space volume	ml
V_p	Total plasma volume	ml
V_t	Total tissue volume	ml
v_c	Capillary plasma volume fraction	
v_e	Extravascular-extracellular space volume fraction	
v_p	Plasma volume fraction	

*1 mM = 1 mmole L^{-1}
1 ml = 1 cm^{-3}

List of Tables

Chapter 1: Introduction

1.1. Context and Motivation

As men age, benign or malignant changes commonly occur in the prostate tissue, with prostate cancer (PCa) being one such a malignant disease. PCa is the second most frequently diagnosed cancer among males worldwide [1] and the second leading cause of cancer death in men [2]. As with most diseases, the early and accurate diagnosis of PCa greatly enhances treatment prognosis. Currently the main method for PCa screening is prostate specific antigen (PSA) testing, with patients who present with elevated PSA results generally sent for an invasive transrectal ultrasound (TRUS) guided biopsy. TRUS biopsies are known to be inaccurate , with data suggesting that up to 30% of tumours are not detected [3], and repeat random biopsies failing to improve tumour detection rates [4-6]. There is thus a need for more accurate and precise, preferably non-invasive, technique for the detection and characterisation of PCa.

The use of dynamic contrast enhanced (DCE) MRI in the study of PCa began over 20 years ago. Although early work indicated no additional benefit in using contrast enhanced over conventional T_2-weighted imaging techniques in the assessment of

PCa [7, 8], studies conducted in 1995 found an improvement in tumour localisation when imaged early after contrast administration [9], as well as an improvement in the detection of minimal seminal vesicle invasion by tumour tissue [10]. Since then, studies have repeatable shown the potential of DCE-MRI as a possible non-invasive gold standard imaging technique for PCa detection [11], localisation [12, 13], and grading [14, 15].

However, although numerous patient studies over the past twenty-plus years have shown the effectiveness of DCE-MRI for PCa imaging, to data no method has been proposed which allows for a comprehensive validation and quantification of DCE-MRI acquisition, reconstruction, pre-processing, and analysis techniques. This has hindered this potentially-diagnostically-useful technique's full adoption for routine clinical use.

In this thesis a phantom test device is presented that essentially provided a 'model patient', wherein concentration-time curves (CTCs) were precisely known and controlled, and could be repeatedly produced and measured using DCE-MRI. The device addressed two key limitations of patient-based attempts to quantify the accuracy and precision of DCE-MRI, namely: knowledge of the ground truth contrast agent (CA) CTCs (both tissue and arterial), and repeatability. The device allowed for the absolute accuracy and precision of various DCE methodologies to be quantitatively accessed for the first time

1.2. Dynamic Contrast Enhanced (DCE) MRI for Prostate Cancer Imaging

Briefly, in DCE-MRI an MRI CA is intravenously administered to the subject, and subsequently a series of consecutive MR-images are acquired over time as the CA arrives at and perfuses through the tissue of interest, from which CA CTCs can be derived at each imaging voxel. Since the shape of these CTCs is governed by physiological factors related to the perfusion conditions of the tissue being imaged, pharmacokinetic (PK) modelling can be applied to the data in order to estimate physiologically-relevant parameters, such as the volume transfer coefficient (K^{trans}) [min^{-1}], rate constant (k_{ep}), and extravascular-extracellular volume fraction (v_e), which are known to vary significantly between heathy and tumorous prostate tissue. (This is further discussed at length in the Chapter 2).

1.2.1. Tumour Detection

In a 2005 study on men with elevated PSA levels (PSA > 2.5 ng/ml), Hara *et al.* imaged 90 patients prior to TRUS-biopsy. Of the 90 patients, 57 patients presented with PSA < 10.0 ng ml^{-1}, of which the initial TRUS-biopsy had a detection rate of 36.8% and DCE-MRI was reported as being successful in detecting 92.9% of the clinically significant PCa for the first biopsy session, with a specificity of 96.2%. This study used qualitative analysis of the results; a radiologist manually inspected the DCE data and considered a lesion with an early enhanced peak and immediate wash-out to be PCa [13]. A 2011 study by Tamada *et al.* on 50 men with PSA values between 4 and 10 ng ml^{-1} reported sensitivity and specificity of 74% and 80% respectively, backing up the conclusion put forward by Hara *et al*. that DCE-MRI alone is equivalent or occasionally superior to 6 or 8 core biopsy protocols in the detection of PCa, even with PSA levels less than 10 ng ml^{-1} [16].

In a clinical setting, DCE-MRI is usually performed as part of a multi parametric (MP) MRI imaging protocol, combining various MRI techniques, such as: T_2-weighted imaging, DCE, diffusion weighted imaging (DWI), diffusion tensor imaging (DTI), and MR spectroscopic imaging (MRSI), into a single protocol. The inclusion of DCE in this MP approach has shown great promise for PCa imaging, as discussed in a brief review of the literature below.

Kozlowski *et al.,* in a 2006 study on 14 patients, correlated multiple DCE-MRI parameters with histology and found that K^{trans}*, onset time, mean gradient* and *maximum enhancement* of the contrast time-intensity curve (CTC) showed significant differences between tumour and normal tissue, with overall sensitivity of 59% and specificity of 74% when using DCE-MRI alone. In cancerous prostate tissue the normal glandular architecture is replaced by aggregated cancer cells and fibrotic stroma, which inhibits the movement of water macromolecules, resulting in restricted diffusion and a reduction in the apparent diffusion coefficient (ADC) values, which can be measured using DWI-MRI. Kozlowski also investigated the use of DCE in combination with DWI-MRI, and found that when the average values of the ADC and DCE parameters were combined there was an increase in sensitivity of 28% over DCE alone, to 87% [17]. A study by Tanimoto *et al.* on 83 patients reported an improvement in sensitivity from 73% to 95%, and specificity from 54% to 74% in the detection of PCa, when comparing a T_2-weighted protocol to a protocol containing T_2-weighted, DWI, and DCE [18]. In a 2014 study, Li *et al.* investigated the effectiveness of

combining DCE with DTI for the detection of PCa in the peripheral zone. The study compared the MR images to sextant biopsy results by drawing regions of interest according to the biopsy zones. They found significant difference in the *ADC,* K^{trans}*,* and k_{ep} values between tumorous and non-tumorous sextants. The area under the curve for the combination of DCE and DTI-MRI was also found to be greater than for either DCE (0.93 vs. 0.84) or DTI (0.93 vs. 0.86) alone, suggesting better diagnostic performance when these techniques are used conjointly [19].

Several other studies [4, 20, 21] have also investigated the additional diagnostic value of combining MRSI and DCE-MRI, with reported sensitivities of 29-100%, specificities of 48-96%, and accuracies of 67-91%. MRSI detects abnormal metabolism rather than abnormal anatomy, differentiating tumorous from healthy prostate tissue by differences in the choline-creatine-to-citrate ratio [21]. In a 2010 study on 68 patients, Portalez *et al.* compared T_2-weighted, DCE, MRSI, and DWI techniques in guided repeat biopsies. They reported that out of the four techniques, DCE had the lowest sensitivity for PCa detection of 29%, it did however have high specificity (93%) and accuracy (86%). As noted by the authors, their DCE protocol had too low a temporal resolution (T_{res} = 13 s) to accurately apply quantitative pharmacokinetic (PK) modelling to the data [22], instead a qualitative approach was employed, which looked at *maximum enhancement*, *wash-in rate*, *time-to-peak*, and *wash-out* information, which may have led to such low sensitivity [20]. The importance of adequate T_{res} is well demonstrated by another larger study performed the same year by Panebianco *et al.* on 150 patients. This study was conducted in a similar manor to the Portalez study, but with the DCE data being acquired at a higher temporal resolution of 3s. The Panebianco study reported a sensitivity of 76.5%, and specificity of 89.5% for DCE alone, and sensitivity of 93.5% and specificity of 90.7% for MRSI and DCE combined, with a reported accuracy of 90.9% in detecting prostate carcinoma [21]. A 2013 study by Perdonā *et al.* on 106 patients reported diagnostic accuracy for DCE combined with MRSI of 85%, with sensitivity of 71% and specificity of 48% for PCa detection [23].

1.2.2. Accessing Tumour Aggressiveness

DCE has also shown some promise in assessing the aggressiveness of PCa. Chen *et al.*, in a study on 43 patients using DCE in combination with DTI found good correlation between the *wash-out gradient* and Gleason score (GS), demonstrating the potential use of the *wash-out gradient* as a marker of GS [15]. A study by Vos *et al.* used

phenomenological and PK analysis of high T_{res} (3 s) DCE data to access the aggressiveness of PCa in the peripheral zone, with *wash-in*, K^{trans}, and k_{ep} offering the best possibility to discriminate low-grade, intermediate-grade, and high-grade PCa [14]. Conversely, studies by Padhani *et al.* [24] and Ota *et al.* [25] found no significant correlation between DCE parameters and GS. Padhani did however report weak correlation between local tumour stage and both *tumour vascular permeability*, and *maximum tumour Gd concentration* [24], and Ota found that both mean blood vessel count, and mean vessel area fraction, had significant correlation with k_{ep} [25].

1.2.3. Treatment Monitoring and Detection of Recurrence

Approximately 30% of patients diagnosed with PCa will undergo external beam radiotherapy treatment (EBRT) as their initial treatment [26]. It has been reported that 15% of low-risk and 67% of high-risk patients will experience an increase in PSA levels within 5 years of EBRT [27]. An increase in PSA level post-treatment (over a threshold of 0.2 ng ml^{-1} [28]) can indicate a relapse of PCa, however PSA levels may fluctuate after therapy, and an increase in PSA level does not necessarily indicate recurrence [29, 30]. In a 2013 meta-analysis of nine previous studies of PCa recurrence detection after EBRT, Wu *et al.* reported pooled sensitivity of 82% and specificity of 74% using DCE alone [31]. The addition of DCE-MRI has also been shown to significantly increase sensitivity for the detection of recurrent PCa after EBRT, compared with T_2-weighted imaging alone; with one study reporting increases in sensitivity from 38% to 72%, and specificities from 80% to 85% [32]. Kara *et al.* reported greater sensitivity, specificity, and accuracy using DCE (93%, 100%, and 95% respectively), when compared to TRUS biopsy (53.3%, 60% and 55% respectively), concluding that TRUS biopsy without the use of additional imaging or biochemical modalities was not sufficient for the detection of PCa recurrence [33]. A study by Moman *et al*. also highlighted the potential use DCE in the planning of focal salvage treatment, which could reduce the adverse effects of radiotherapy [34].

The detection of recurrence after radical prostatectomy can be difficult, mainly because of the postsurgical deformity at the site of the vesicourethral anastomosis. However, DCE-MRI has shown great promise in this regard also. The same meta-analysis study by Wu *et al.* analysed seven studies which looked at the effectiveness of MRI in detecting recurrence of PCa after radical prostatectomy, reporting pooled sensitivity of 85% and specificity of 95% for the use of DCE [31]. A 2012 study by Boonsirikamchai *et*

al. on 47 patients highlighted the potential use of DCE in the detection of recurrence of PCa after radical prostatectomy, reporting a high degree of accuracy in the detection of sub-centimetre local recurrences within the post-prostatectomy bed. They used a spatial resolution of 3mm and reported good sensitivity in detecting local recurrences greater than 5mm [35]. Similarly, a study by Cirillo *et al.* demonstrated an increase in sensitivity from 61% to 84% and specificity from 82% to 89%, with the inclusion of DCE, compared with T_2-weighted imaging alone, in the detection of PCa recurrence post-prostatectomy [36].

Another method used in the treatment of PCa is high-intensity focused ultrasound ablation (HIFU), which causes coagulation necrosis in the targeted tissue by converting mechanical energy into heat and generating a cavitation effect. In a 2008 study, Kim *et al.* compared DCE-MRI to T_2-weighted combined with DWI and found higher average sensitivity for DCE (84%) compared to T_2-weighted with DTI (67%), but higher specificity and accuracy using T_2-weighted with DTI (76% and 73% respectively), compared to DCE (66% and 72% respectively) [37]. Rouviēre *et al*. investigated the use of T_2-weighted and DCE-MRI in guiding targeted biopsies after HIFU treatment. They found that targeted biopsies detected more cancers than routine biopsies (36 vs. 27 patients), implying that MRI combining T_2-weighted and DCE images could be a promising method for post-HIFU guided biopsy [38].

.

1.3. Aims and Objectives of the Thesis

The main aim of this thesis was to develop a model system capable of producing highly-repeatable, precisely-known, physiologically-relevant CTCs and arterial input function (AIF) curves within an anthropomorphic environment for repeated measurement using DCE-MRI. This degree of DCE-MRI measurement quantification has simply not been possible to date for either patient or phantom studies, due to a lack of accurate and precise knowledge of the ground-truth conditions within the subject / device being imaged, as well as the fact that DCE-MRI, by its very nature, intrinsically precludes repeated patient-measurements from being made (since this would require repeated injection of Gd-based CA). Once the device was developed, another objective of the current study was to demonstrate its operation in several experiments designed to quantify the effects of various DCE-MRI methodologies on the absolute accuracy and intra- / inter-session precision of CTC and AIF measurements, as well as derived pharmacokinetic (PK) parameters, comparing DCE-MRI-measured

values against precisely-known ground truths. This was all done with the overall goal of informing future phantom and patient studies, ultimately with the intention of improving the PCa diagnostic capabilities of DCE-MRI, and potentially leading to a wider acceptance of the technique for use in routine clinical examinations.

The specific objectives of the thesis can be summarised as follows:

1. Design and build a physical dynamic phantom test device for the validation and development of DCE-MRI techniques. The device must be:
    - able to reproducibly generate arbitrarily-shaped (programmable) and precisely-known CTCs which mimic those observed in healthy and tumorous prostate tissue, as well as other physiological curve shapes, such as the arterial input function (AIF)
    - anthropomorphic in nature, mimicking the male pelvic-region in terms of size, image complexity, and sparsity; to allow for comprehensive testing of DCE-MRI techniques, provide patient-relevant results, and allow for easy clinical translation of protocols developed on the device
    - capable of producing MR-measurable CTCs, i.e. produced in a region large enough to accommodate several imaging voxels, while avoiding any partial-volume issues
    - capable of producing CTCs at low flow rates, to avoid flow related artefacts and minimise CA usage
    - able to produce two distinct curves simultaneously, to allow for different tissue CTCs (‘healthy’ and ‘tumour’) and an AIF to be measured simultaneously (for the purposes of performing PK modelling on the data)

2. Fully validate the phantom test device, as well as accurately and precisely establish ground truth values for the system using a modality other than MRI. This validation approach had to provide:
    - highly-precise, temporally-stable, high-spatiotemporal resolution measurements of the exact CA concentration-change over time
    - measurements which were directly comparable with the DCE-MRI results

3. Use the phantom system to quantitatively investigate the effects of various

parameters and methodologies related to the acquisition, reconstruction, pre-processing, and analysis, on the accuracy and precision of DCE measurements, namely:

- temporal resolution (T_{res}): the temporal spacing between successive DCE images
- acquisition duration (AD): the length of time that the CTCs and AIF are sampled for
- voxel-wise flip-angle correction (VFAC): in order to compensate for non-uniformity in the B_1^+-field
- PK model fitting regime: non-linear verses linear fitting approaches
- *k*-space acquisition trajectory: the order and manner in which the MR frequency-encoded data are sampled
- under-sampling *k*-space: in order to achieve faster imaging times
- reconstruction methodologies: using coil-by-coil (CbC) inverse gridding, parallel imaging (PI), and PI combined with compressed sensing (PICS) approaches

1.4. Thesis Overview

This thesis is divided into seven main chapters, with each chapter thematically related, and subsequent chapters being informed by the results of the preceding ones. The outline of the thesis reads as follows:

Chapter 2: Background

Background knowledge that is required in order to understand all subsequent chapters is provided in Chapter 2. Firstly, a classical description of MR theory is concisely outlined, as well as an overview of the main components of an MR-imaging system, and how such a system forms MR images. This is followed by a more specific description of DCE-MRI, how using this technique relates to the actual prostate physiology, as well as various qualitative and quantitative techniques used in the analysis of the data. Finally, some of the confounding factors related to the use of DCE-MRI for pelvic imaging are outlined. Detailed literature reviews are integrated into the introductions to later chapters, specific to the contents of each respective chapter.

The subject matter of this chapter formed the basis of the following:

Conference Proceeding

Knight, S.P., Meaney J.F., Fagan A.J., *A review of dynamic contrast enhanced MRI for the diagnosis of prostate cancer.* [poster] Irish Association of Physicists in Medicine (IAPM) annual scientific conference, 22nd February, 2014, Dublin, Ireland. Phys Medica 30(6): 721 (2014) DOI: 10.1016/j.ejmp.2014.06.024

Chapter 3: Design, fabrications, and validation of a novel anthropomorphic DCE-MRI prostate phantom test device

As previously stated, one of the main factors currently limiting the implementation of DCE-MRI as a truly quantitative technique is the lack of a comprehensive validation method, stemming from a lack of knowledge of the ground-truth conditions within the patient or object being scanned. In this initial phase of the project a novel anthropomorphic phantom test device was designed and built. The device allowed for precisely and accurately known ground truth CTCs to be repeatedly generated within an environment with mimicked that of a patient, and presented to the MRI scanner for measurement, thereby allowing for a quantitative assessment of the accuracy and precision of a particular DCE-MRI approach. CTC derived from prior patient prostate data were produced by means of a custom-built 4-pump flow system. The ground truths for the system was determined using an MRI-independent, highly-precise, custom-built optical imaging system. Preliminary DCE-MRI data for the phantom device is also presented in this chapter, demonstrating the operation of the device.

The subject matter of this chapter formed the basis of the following:

Journal Publication

Knight, S.P., Browne, J. E., Meaney J.F., Smith, D.S., Fagan A.J., *A novel anthropomorphic flow phantom for the quantitative evaluation of prostate DCE-MRI acquisition techniques.* Phys Med Biol, 2016. **61**(2): p. 7468-7483 (2016) DOI: 10.1088/0031-9155/61/20/7466

Conference Proceedings

Knight, S.P., Browne, J. E., Meaney J.F., Smith, D.S., Fagan A.J. *A Novel Prostate DCE-MRI Flow Phantom for the Quantitative Evaluation of Pharmacokinetic Parameters.* [oral] International Society for Magnetic Resonance in Medicine (ISMRM) 24th Annual Scientific Meeting and Exhibition, 7th – 13th May 2016, Singapore. Proc. Intl. Soc. Mag. Reson. Med. **24**: 0655, (2016)

Knight, S.P., Browne, J. E., Meaney J.F., Smith, D.S., Fagan A.J., *Error quantification in pharmacokinetic parameters derived from DCE-MRI data using a novel anthropomorphic dynamic prostate phantom.* [oral] Irish Association of Physicists in Medicine (IAPM) annual scientific conference, 2nd April, 2016, Waterford, Ireland. Phys Medica **32**(7): 949 (2016) DOI: 10.1016/j.ejmp.2016.05.012

Knight, S.P., Browne, J. E., Meaney J.F., Fagan A.J. *A novel flow phantom for the quantitative evaluation of prostate DCE-MRI techniques*. [oral] European Society for Magnetic Resonance in Medicine and Biology (ESMRMB) annual scientific conference, 1st – 3rd October, 2015, Edinburgh, Scotland. Magn Reson Mater Phy **28**(Suppl 1): p. S383-384. (2015) DOI: 10.1007/s10334-015-0489-0

Knight, S.P., Meaney J.F., Fagan A.J., *A flow phantom for the quantitative validation of DCE-MRI techniques.* [oral] Irish Association of Physicists in Medicine (IAPM) annual scientific conference, 27th February 2015, Dublin, Ireland. Phys Medica **32**(2): 417 (2016) DOI: 10.1016/j.ejmp.2015.07.016

Knight, S.P., Meaney J.F., Fagan A.J., *Rapid prototyping: Offering new opportunities in phantom design and construction*. [poster] Irish Association of Physicists in Medicine (IAPM) annual scientific conference, 27th February 2015, Dublin, Ireland. Phys Medica **32**(2): 427 (2016) DOI: 10.1016/j.ejmp.2015.07.053

Chapter 4: Effects of acquisition duration and temporal resolution on the accuracy of prostate tissue concentration-time curve measurement and derived phenomenological and pharmacokinetic parameter values

This chapter utilises the phantom test device presented in Chapter 3 to investigate the effect of the T_{res} and AD on the measurement accuracy of tissue CTCs, and derived phenomenological and pharmacokinetic parameter values. The T_{res} and AD values tested were representative of the wide-range of values reported in the literature to date for DCE studies in the prostate (T_{res} = 2 - 24.4 s and AD = 30 – 600 s), and the effects on the measurement accuracy of the *wash-in, wash-out,* K^{trans}, and v_e parameters were quantified. The hypothesis under investigation was whether measurement inaccuracies in tissue CTCs deriving from features of the DCE imaging pulse sequence itself, namely two of the most widely-varied acquisition parameters: T_{res} and AD, may contribute significantly to the wide divergence in DCE PK modelling results published in the literature to date.

The subject matter of this chapter formed the basis of the following:

Journal Publication

Knight, S.P., Browne, J. E., Meaney J.F., Fagan A.J., *Quantitative effects of acquisition duration and temporal resolution on the measurement accuracy of prostate dynamic contrast enhanced MRI data.* Magn Reson Mater Phy,. **30**(5): p. 461-471 (2017) DOI: 10.1007/s10334-017-0619-y

Conference Proceedings

Knight, S.P., Browne, J. E., Meaney J.F., Fagan A.J. *Quantitative evaluation of the effect of temporal resolution and acquisition duration on the accuracy of DCE-MRI measurements in a prostate phantom.* [poster] International Society for Magnetic Resonance in Medicine (ISMRM) 25th Annual Scientific Meeting and Exhibition, 22nd – 27th April, 2017, Honolulu, Hawaii, USA. Proc. Intl. Soc. Mag. Reson. Med. **25**: 2890, (2017)

Knight, S.P., Browne, J. E., Meaney J.F., Fagan A.J. *Effects of sampling frequency on the accuracy of phenomenological and pharmacokinetic parameters derived from dynamic contrast enhanced MRI data.* [oral] Irish Association of Physicists in Medicine (IAPM) Annual Scientific Conference, 25th March, 2017, Dublin, Ireland

Knight, S.P., Browne, J. E., Meaney J.F., Fagan A.J. *Quantitative evaluation of the effects of dynamic contrast enhance MRI acquisition parameters on the accuracy of derived prostate cancer biomarkers.* [poster] Irish Association for Cancer Research (IACR) annual scientific conference, 23rd – 24th February, 2017, Kilkenny, Ireland

Knight, S.P., Browne, J. E., Meaney J.F., Fagan A.J. *A novel anthropomorphic phantom test device for the validation and development of dynamic contrast enhanced MRI protocols.* [oral] Bioengineering in Ireland[23], 20th – 21st January, 2017, Belfast, Northern Ireland

Knight, S.P., Browne, J. E., Meaney J.F., Fagan A.J. *A novel anthropomorphic test device for the assessment of dynamic contrast enhanced MRI of prostate cancer.* [poster] The 10th International Cancer Conference, 17th – 18th October, 2016, Dublin, Ireland

Knight, S.P., Browne, J. E., Meaney J.F., Fagan A.J. *Effect of temporal resolution and sampling duration on pharmacokinetic parameters derived from prostate DCE-MRI data: a quantitative phantom study.* [oral] European Society for Magnetic Resonance in Medicine and Biology (ESMRMB) annual scientific conference, 29th September – 1st October, 2016, Vienna, Austria. Magn Reson Mater Phy **29**(Suppl 1): p. S261 (2016). DOI:10.1007/s10334-016-0570-3

Chapter 5: Effects of temporal resolution, voxel-wise flip-angle correction, and model-fitting regime on the accuracy and precision of arterial and prostate-tissue contrast-time curve measurements and derived pharmacokinetic

parameter values

Accurate and precise measurement of the AIF is essential for PK modelling to be accurately performed using certain PK models, such as the widely-used standard Tofts model. Although a number of population-average formations of the AIF have been proposed, acquiring a patient-specific AIF remains the only method that allows for truly quantitative patient-specific PK parameters to be derived. However the measurement of the AIF has proved challenging due to several confounding factors, such as the use of an inappropriately-long T_{res} in the acquisition sequence and non-uniformities in the B_1^+-field. The aim of this phase of the project was to use the anthropomorphic phantom test device presented in Chapter 3 to perform a quantitative investigation into the effects of T_{res} and B_1^+-field non-uniformities on the accuracy of AIF (and tissue CTC) measurements. The protocol under investigation used a full-sampled, standard Cartesian *k*-space acquisition trajectory. The ground truth AIF used in this chapter was based on a population-average derived from 32 high-T_{res} prostate patient datasets, the data from which is also presented. MR-measured tissue CTCs, AIFs, and derived PK parameters, taken from five intra-session and five inter-session phantom experiments (each measuring a 'healthy' and 'tumour' CTC simultaneously with the ground truth AIF), were compared with precisely-known ground truth values and measurement errors were calculated. Additionally, the data was fit using both non-linear, and more recently proposed linear interpretations of the standard Tofts model, and the performance of both modelling approaches was accessed.

Chapter 6: Effect of golden-angle radial k-space under-sampling and image reconstruction methodology on DCE-MRI accuracy and precision

Rapid imaging techniques, such as PI and CS, offer the prospect of greatly reducing imaging times with MRI, thereby vastly improving the T_{res} for DCE-MRI, and possibly leading to more accurate characterisation of tissue CTCs and AIF, and by extension the derived quantitative PK parameters. However, as was the case for DCE-MRI in general, the lack of a quantitative method for testing and validating these techniques *in vivo* has meant that the actual effect of using PI and CS on the absolute accuracy and precision of DCE measurements has remained unknown to date.

In this chapter, again the phantom device presented in Chapter 3 was utilised, this time to quantitatively investigate the effects of a continuous golden-angle radial *k*-space

sampling trajectory, with data reconstructed using three approaches, namely: CbC inverse gridding, PI, and PICS. The fidelity of tissue CTC and AIF curve-shape measurements, as well as the accuracy and precision of the derived PK parameters, were quantified for each reconstruction approach, at a range of different under-sampling factors from 5% to fully-sampled, with all results compared against the precisely-known ground-truth values. As with the preceding chapter, MR-measurements were taken from five intra-session and five inter-session phantom experiments (each measuring a 'healthy' and 'tumour' CTC simultaneously with the ground truth AIF). The results from this chapter were also compared with the results of the preceding chapter, which was performed using similar methodologies, but using a fully-sampled Cartesian *k*-space sampling trajectory.

Chapter 7: Conclusions

Finally, the most important conclusions discussed in the thesis are summarised in Chapter 7, and closing remarks are given, as well as possible directions for future related work.

Chapter 2: Background

2.1. Magnetic Resonance Imaging

MRI is a non-ionizing medical imaging technique which is used to non-invasively investigate the structure and function of living tissues. The concept was first proposed 1972 by Lauterbur, and the following year the first two-dimensional (2D) images were published [39, 40]. In 1976 and 1977 Mansfield introduced two new techniques which allowed for faster imaging [41, 42], and in 1980 Edelstein and Hutchison introduced the first practical implementation of 2D Fourier transformed MR imaging, dubbed 'spin warp' at the time [43]. Since then, the field of MRI has grown exponentially, with multiple different MR imaging techniques proposed for use in many different physiological locations, each designed to measure different specific tissue properties or functional information. These developments allow currently for the production of high-quality diagnostic images using MRI, for interpretation by a trained eye. However more recently there has been a drive towards developing imaging techniques which provide quantitative information about patient-specific physiology, which should allow for more rapid, accurate, and specific diagnosis, as well as easier comparison between datasets.

2.1.1. Nuclear Magnetic Resonance Physics

Magnetisation and Precession

The nuclear magnetic resonance (NMR) phenomenon is quantum mechanical in nature, however at the macro scale it can be practically described using classical mechanics. In this Chapter a classical interpretation is presented.

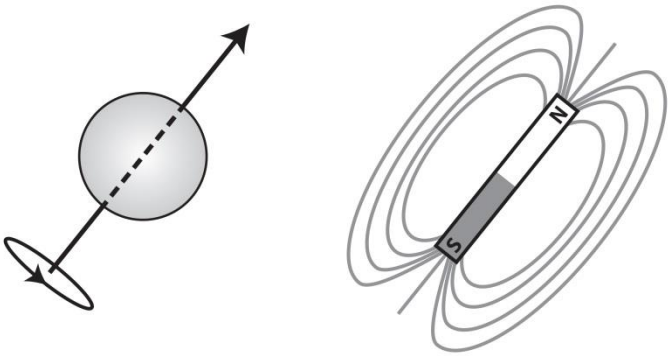

Figure 2.1: Schematic representation showing the rotation of the magnetic moment at the nucleus in a non-ferromagnetic material, along with a bar magnet illustrating magnetic-field line.

NMR can be conceptualised by thinking of each nucleus in a non-ferromagnetic material as a small independent bar-magnet, rotating around an axis located between its magnetic poles, as illustrated in Figure 2.1. In the absence of an external magnetic field the orientations of each nucleus's magnetic moment is random with respect to one another, as shown in Figure 2.2 (a). If an external magnetic field is applied, B_0, a portion of the nuclei magnetic moments will align parallel with the field, others will align antiparallel, while some will remain misaligned due to Brownian motion, as shown in Figure 2.2 (b); producing a small net magnetic moment across the sample, M_z (the longitudinal direction of the B_0 field is conventionally designated as the z-axis).

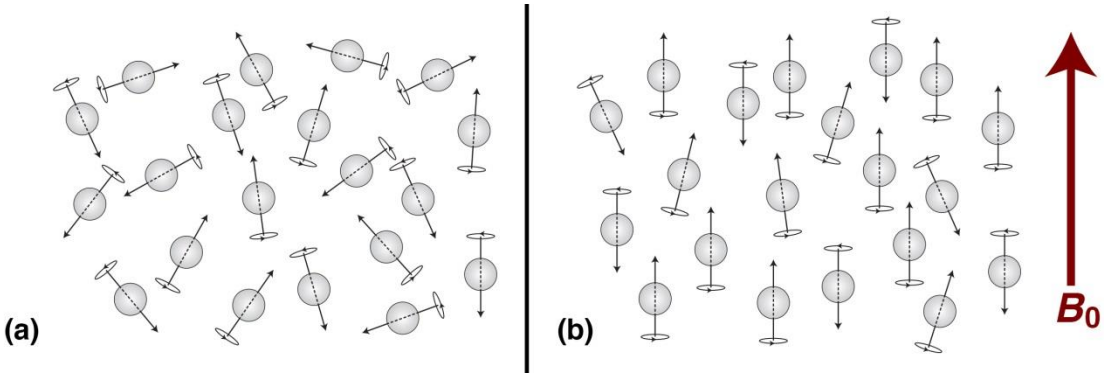

Figure 2.2: (a) Schematic representation of the random orientation of magnetic moments of a group of nuclei in the absence of an externally-applied magnetic field; the vector sum of these magnetic moments will be practically zero. (b) Effect of applying a strong magnetic field, B_0, on the magnetic moments of a group of nuclei; some of the magnetic moments will be aligned parallel or antiparallel with the applied magnetic field, with a bias toward aligning parallel with the applied field causing a non-zero net magnetic moment for the sample. (Generally speaking the majority of alignments in a sample are due to Brownian motion, in the figure alignments with the B_0-field are exaggerated for illustrative purposes)

In 1946 the NMR phenomenon was mathematically described by Felix Bloch, in what is now commonly referred to as the *Bloch equation* [44], given as:

$$\frac{\partial \vec{M}}{\partial t} = \vec{M} \text{ x } \omega_0 - \frac{M_x \hat{\imath} + M_y \hat{\jmath}}{T_2} - \frac{(M_z - M_0)\hat{k}}{T_1}, \qquad [2.1]$$

where: $\vec{M}$ is the magnetic moment of a volume, with $\vec{M}$ = (M_x, M_y, M_x)^T; M_0 is the magnitude of the longitudinal net magnetisation at thermal equilibrium; T_1 and T_2 are time constants specific to the material being imaged (discussed later in this section); $\hat{\imath}$, $\hat{\jmath}$, and $\hat{k}$ are unit vectors in the *x*, *y*, and *z* direction respectively; and ω_0 is the angular frequency of procession, known as the *Larmor frequency* (first described by the Irish physicist, Joseph Larmor), and given as:

$$\omega_0 = \gamma \vec{B}, \qquad [2.2]$$

where γ is the gyromagnetic ratio (in MHz T^{-1}) and $\vec{B}$ is the strength of the applied magnetic field (in T).

Magnetic resonance

Magnetic resonance (MR) occurs when a radiofrequency (RF) pulse, B_1, is applied orthogonal to the B_0 field at the Larmor frequency. If we visualise this using a frame of reference rotating at the Larmor frequency [45], this causes M_0 to tilt away from B_0, and it forms a magnetisation component on the transverse plane (M_{xy}), as illustrated in Figure 2.3. The precession of the M_{xy} component induces a current, which when amplified can be detected, and this is called the NMR signal or free-induction decay (FID). If a B_1 pulse is applied in the presence of a uniform B_0 field then a signal is induced inside everything that receives the RF power, this is called non-selective excitation.

Selective Excitation

Since the frequency at which the nuclei spin (the Larmor frequency, ω_0) is directly related to the strength of the applied *B*-field, $\vec{B}$, if a magnetic gradient, *G*, is applied along one of the axes, producing a spatially-varying *B*-field, this causes the nuclei to process at different rates depending on their spatial location along that axis, as shown in Figure 2.4 Using a RF pulse (B_1) of a particular frequency will only excite nuclei

processing at that frequency, and hence a volume, or 'slice', can be selected in the subject. The thickness of the volume is dictated by the RF bandwidth and strength of the applied magnetic gradients used, also illustrated in Figure 2.4 Selective excitation allows for the imaging field of view to be reduced, and thereby the acquisition time to also be reduced.

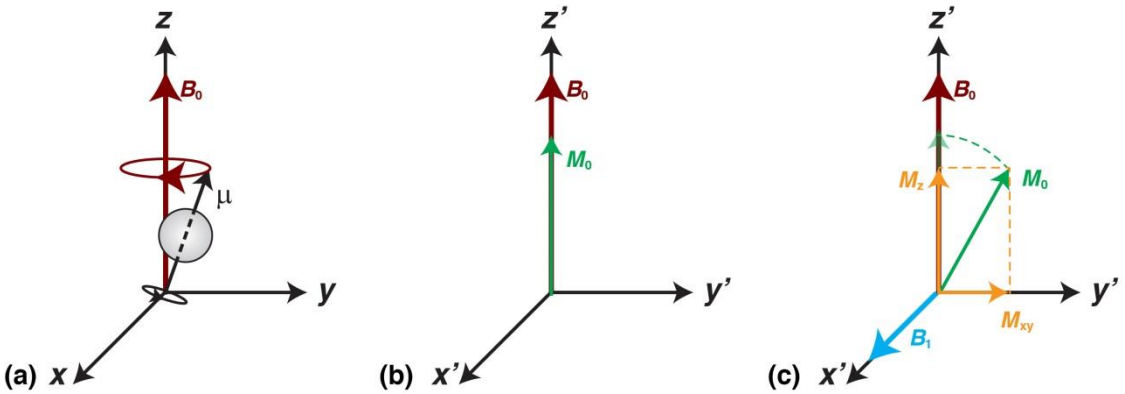

Figure 2.3: (a) Schematic representation of the precession of an isolated magnetic moment, μ, in a static magnetic field B_0 (static frame of reference). (b) The net magnetisation, M_0, in the equilibrium state, and (b) in the presence of an RF pulse (B_1) where the spins are tipped toward the xy-plane, producing magnetisation components, M_z and M_{xy} (frame of reference rotating at the Larmor frequency)

Relaxation

During the applied RF pulse the system is in an excited state, however once the RF is stopped the spin system return back to an equilibrium state, through a process called relaxation. There are two mechanisms by which it does this: longitudinal relaxation of the M_z component and transverse relaxation of the M_{xy} component.

Longitudinal relaxation is related to how quickly the net magnetisation returns to thermal equilibrium by means of the nuclear spins exchanging energy with their surroundings (known as the lattice). It is described by the $-(M_z - M_0)\,\hat{k} / T_1$ term in Equation [2.1]. Assuming $\vec{B}$ is entirely in the *z* direction, Equation [2.1] simplifies to:

$$\frac{\partial M_z}{\partial t} = -\frac{(M_z - M_0)\hat{k}}{T_1}, \qquad [2.3]$$

the solution to which is:

$$M_z(t) = M_0 + \left(M_z^i - M_0\right)\exp\left(-\frac{t}{T_1}\right), \qquad [2.4]$$

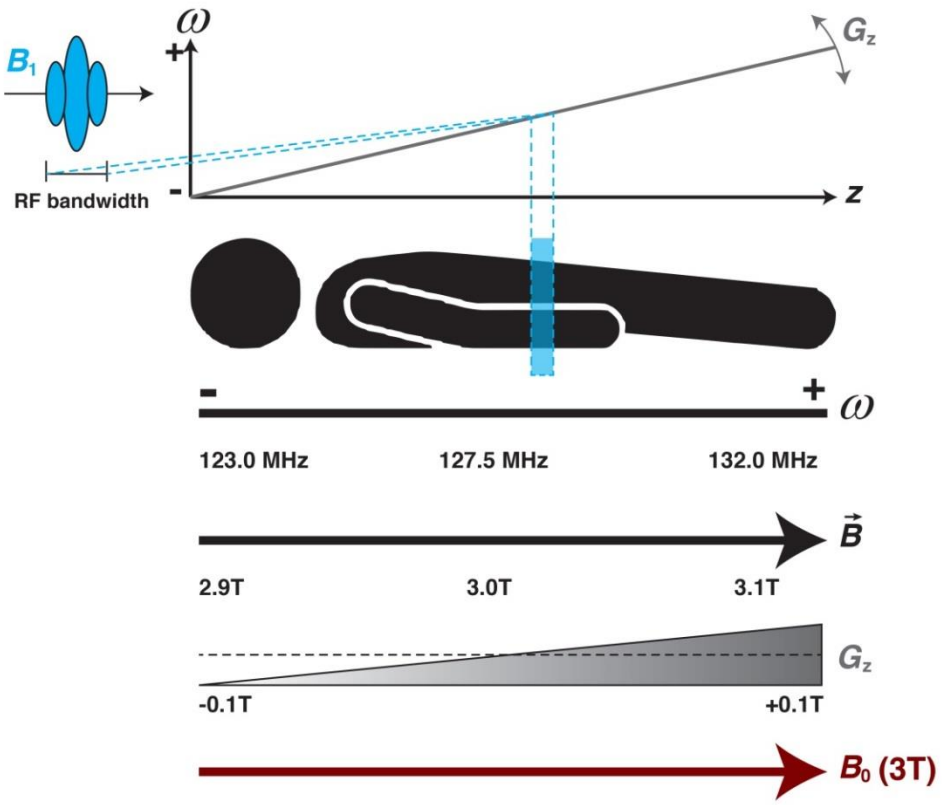

Figure 2.4: Illustration of selective excitation, showing: the static B_0 field (shown at 3T); the applied spatially-varying magnetic gradient, G_z; the combined magnetic fields, $\vec{B}$; and the effects on the procession frequency, ω. The diagram also illustrates the dependence of the thickness of the excited 'slice' on the B_1 RF bandwidth and the strength of the applied magnetic gradient, G_z.

where t is the time relative to the initial magnetisation and M_z^i is the initial longitudinal magnetisation. This longitudinal relaxation of the M_z component (spin-lattice relaxation) is characterised by the time constant T_1.

The second mechanism, transverse relaxation (spin-spin relaxation), does not involve an exchange of energy with the lattice, but rather relates to a loss of phase coherence between spins in the transverse plane. It is characterised by the time constant T_2, and is described by the term $-(M_x\hat{\imath} - M_y\hat{\jmath}) / T_2$ term in Equation [2.1]. Only considering this term, the Bloch equation (Equation [2.1]) becomes:

$$\frac{\partial \vec{M}}{\partial t} = -\frac{M_x\hat{\imath} + M_y\hat{\jmath}}{T_2}, \qquad [2.5]$$

the solution to which is a simple exponential decay, give as:

$$\vec{M}_{xy}(t) = \vec{M}^{i}_{xy}\exp\left(-\frac{t}{T_2}\right), \qquad [2.6]$$

where $\vec{M}_{xy} = M_x\hat{\imath} + M_y\hat{\jmath}$, and $\vec{M}^{i}_{xy}$ is the initial magnetisation in the transverse plane at $t = 0$. In practice the T_2^* time constant is often reported, and this takes into account the both the effects of T_2 decay and magnetic-field non-uniformity.

2.1.2. Hardware

In this section the main hardware components of an MR imaging system will be introduced. The scanner manipulates the magnetisation of a sample though the use of three types of magnetic fields, namely the static B_0 field, the RF B_1 field, and the linear magnetic field gradients, G_x, G_y, and G_z. as illustrated in Figure 2.5.

The Static Magnetic Field (B_0)

Generally the static longitudinal magnetic B_0 field is generated in a clinical scanner using a superconducting solenoid electromagnet, which allows for a homogenous field to be produced along the axis of the scanner bore. The field strength of clinical scanners typically ranges from 0.3T to 7T (as of 2017); the stronger the magnetic field, the larger the partial alignment of nuclei along the direction of B, and hence the larger the longitudinal magnetisation in the sample with correspondingly higher signal to noise ratio (SNR).

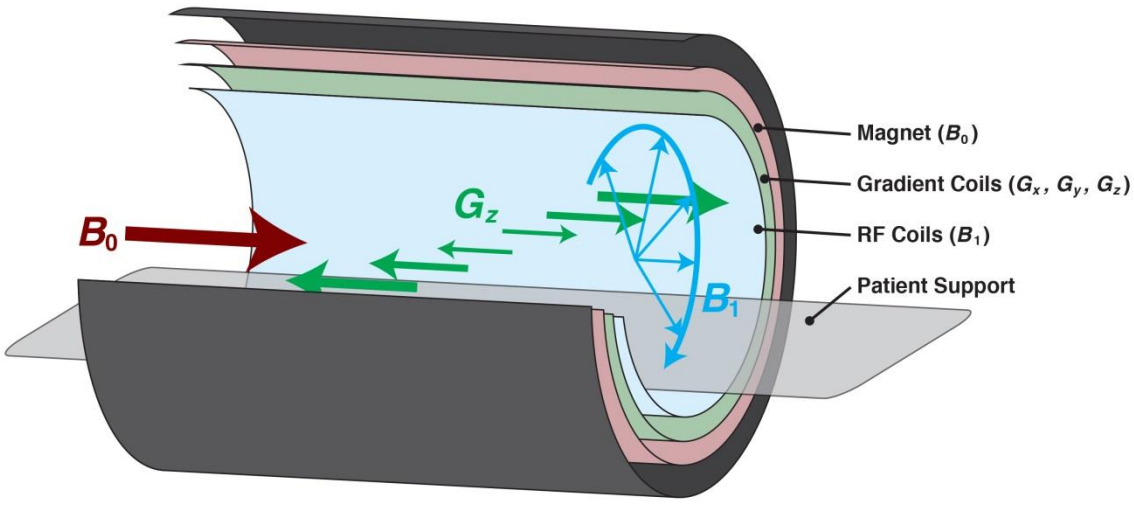

Figure 2.5: Schematic representation of the MR scanner hardware (section removed) showing the locations of the shielding and respective Magnet, gradient, and RF coils, as well as the three types of magnetic fields that these coils produces.

The Radio Frequency Field (B_1)

The transverse RF B_1 field is produced using a specialised coil that is tuned to the Larmor frequency, with a typically body coil produces a field strength ~ 1.6 x 10^{-5} T. The B_1-transmit field, generally given as B_1^+, is used to excite the magnetisation from an equilibrium state by perturbing, or tipping, the magnetisation from a longitudinal direction to the transverse plane, as previously described. The amount by which the magnetisation is perturbed is given as the *flip angle*, and is dictated by the amount of RF energy supplied to the subject.

The Linear Magnetic Field Gradients (G_x, G_y, and G_z)

Spatial information, which is used in image formation, is generated through the application of three additional spatially-varying magnetic fields. Three gradient coils are used, G_x, G_y and G_z, to create three linear gradients oriented orthogonal to each other, producing variations in the longitudinal magnetic field strength as a function of spatial position. This causes the resonance frequency of the magnetisation to likewise vary proportionally with the gradient fields, and this variation is used to resolve the resonance signal spatial distribution.

2.1.3. MR Image Formation

k-Space Trajectory

The spatial information that the magnetic gradients of an MR system provides is acquired encoded in the time-domain, and this time-domain is known as *k*-space (sometimes also referred to as Fourier space). The order in which the *k*-space data is acquired is known as the trajectory. One way to acquire *k*-space is to scan it line-by-line in a Cartesian fashion. Data sampled this way can be reconstructed into an image fast and reliably using the inverse fast Fourier transform (iFFT). Its fast and simple implementation, coupled with the fact that this method of acquisition and reconstruction has proven robust to systemic errors, with remaining artefacts being well documented and understood, has meant that Cartesian *k*-space sampling is currently the mostly widely used approach for clinical imaging.

Various other 2D and 3D *k*-space trajectories have also been proposed however, such as radial 2D multi-slice ‘stack-of-stars’, radial 3D ‘koosh-ball’, and 2D multi-slice ‘stack-of-spirals’. These trajectories have some advantages over a Cartesian approach, for example radial acquisitions have been shown to be less susceptible to motion artefacts

than Cartesian trajectories [46], while spiral trajectories make very efficient use of the gradient coils, and have been shown effective for rapid and real-time imaging applications [47, 48]. Radial trajectories also lend themselves well to certain rapid under-sampled imaging techniques, such as compressed sensing [49]; this will be discussed at length in Chapter 6. Reconstruction of data acquired using these non-Cartesian trajectories is more complex, requiring the use of *k*-space interpolation schemes, such as Cartesian gridding, where the data samples are weighted for sampling density and convolved with a finite kernel, before being combined into a Cartesian grid, and the iFFT used to complete the reconstruction [50].

In-plane localisation: Frequency Encoding (1D)

Frequency encoding is one method of deriving the strength of signal being produced at a particular spatial position. It works by applying a constant and continuous magnetic gradient during the readout that causes a variation in magnetic field strength across the subject being imaged. If we take the case of a magnetic gradient being applied along the *z*-axis, G_z, then the magnetic field will vary spatially along that axis, and by extension the angular frequencies of procession will also vary as follows:

$$\omega(z) = \gamma(|B_0| + G_z z), \qquad [2.7]$$

where $\omega(z)$ is the angular frequency at spatial position *z*. Due to this linear variation in processional frequancy with respect to spatial position, a spectral decompostion can be applied to the data in order to derive the spatial magnetisation distribution. As mentioned previously, the most widely-used method for converting this raw *k*-space data into spatially-encoded information is by using the Fourier transform. The Fourier transform works by decomposing the various spatially-varying signal frequencies into their constituent parts, and providing a measure of the magnetisation magnitude (signal) at a particular spatial position. However, this process only allows for spatial information to be acquired in one dimension; the following section describes how phase encoding is used to spatially resolve the other one or two orthogonal dimensions.

In-plane Localisation: Phase Encoding (2D and 3D)

Phase encoding works on a similar principle to frequency encoding, however here the gradients are applied before the acquisition at a fixed amplitude and duration, instead of continuously during the acquisition. Since a magnetic field gradient causes the

nuclei to process at different frequencies depending on locations along the axis it is applied, the processions of the nuclei increasingly go out of phase with one another while the gradient is applied. By precisely controlling the timing and amplitude of the applied gradient field, different spatial frequencies can be encoded prior to acquisition. Iterating this process at different gradient amplitudes and / or durations, allows for the spatial frequency information to be calculated in that dimension. Phase encoding is applied in one dimension for 2D imaging, and in two dimensions for 3D imaging.

We can investigate the Fourier relationship mathematically by taking the general case of a gradient-induced variation in the normal frequency of procession causing the development of a location (**r**) dependant phase dispersion. The additional frequency contributions from the gradient field can be adapted from Equation [2.7] as:

$$f(\mathbf{r}) = \frac{\gamma}{2\pi} G(t) \cdot \mathbf{r}, \qquad [2.8]$$

where *G*(*t*) is a vector giving the gradient fields' amplitudes. The phase of magnetisation can be formulated as a intergral of the frequencies starting at $t = 0$, given as:

$$\emptyset(\mathbf{r}, t) = 2\pi \int_0^t \frac{\gamma}{2\pi} G(s) \cdot \mathbf{r}\, ds = 2\pi \cdot k(t), \qquad [2.9]$$

where:

$$k(t) = \frac{\gamma}{2\pi} \int_0^t G(s)\, ds, \qquad [2.10]$$

where *k*(*t*) is the spatial frequency at time t. Since the receiver coil integrates over the entire imaging volume, a spatially-dependant signal equation can be formulated as:

$$S(t) = \int_R M(\mathbf{r}) \exp(-i 2\pi k(t) \cdot \mathbf{r}) d\mathbf{r}, \qquad [2.11]$$

that is, the signal at time *t*, *S*(*t*), is the Fourier transform of the transverse magnetisation at position **r**, *M*(**r**), sampled at the spatial frequency *k*(*t*).

Resolution and Field-of-View (FOV)

Image resolution is proportional to the size of the sampling region of *k*-space, with a

larger region giving higher resolutions, and the field-of-view (FOV) is determined by the *k*-space sampling density, traditionally such that the Nyquist criterion is met. With traditional acquisition and reconstruction techniques, breaking the Nyquist criterion leads to artefacts in the reconstructed images, however some emerging under-sampling techniques propose methods to negate this constraint [49].

Spin and Gradient Echo Sequences

The time between successive phase-encode steps is known as the repetition time (*TR*). The NMR signal is not generally measured directly in MR-imaging, instead 'echoes' are created and measured, and the time between the excitation pulse and the peak of the echo is known as the echo time (*TE*). Two types of echoes are used; *spin echoes* (SE) and *gradient echoes* (GE). In a SE sequence the spins are left to dephase naturally after the application of the initial 90° excitation pulse, after a period of time a second pulse 180° is then used to flip all the spins through 180°, this reverses the spins phase angles but does not modify the processional frequencies. After the same period of time has passed as was left between the 90° and 180° pulses the spins come back into phase and form the *spin echo*.

A pulse sequence diagram (PSD) is a useful way to visualise the timing of the pulses, applied gradient fields, and acquisition window used in MRI. A PSD for the basic SE sequence is shown in Figure 2.6.

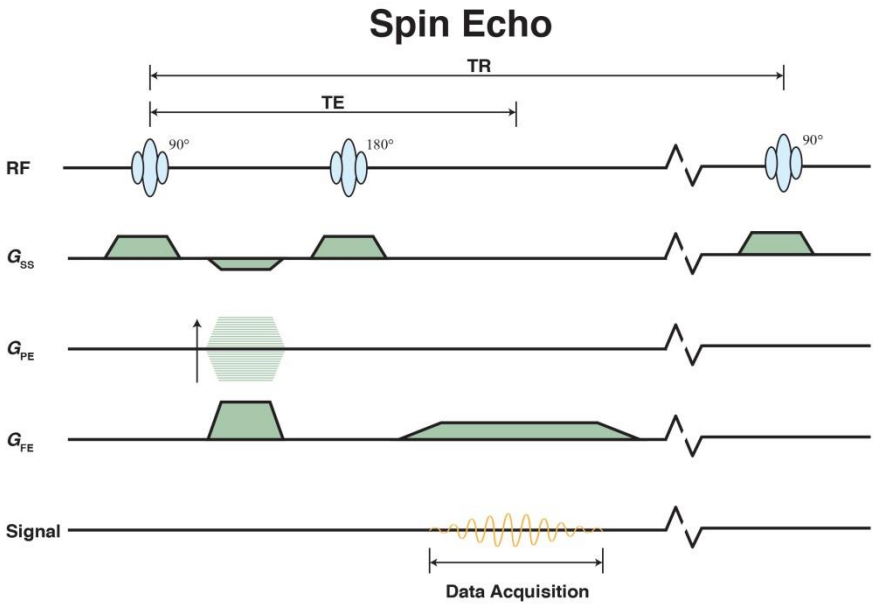

Figure 2.6: Pulse sequence diagram (PSD) for the basic spin echo sequence. Figure illustrates the timing of the B_1 radiofrequency (RF) transmit field, as well as the gradients used for slice selection (G_{SS}), phase encoding (G_{PE}), and frequency encoding (G_{FE}).

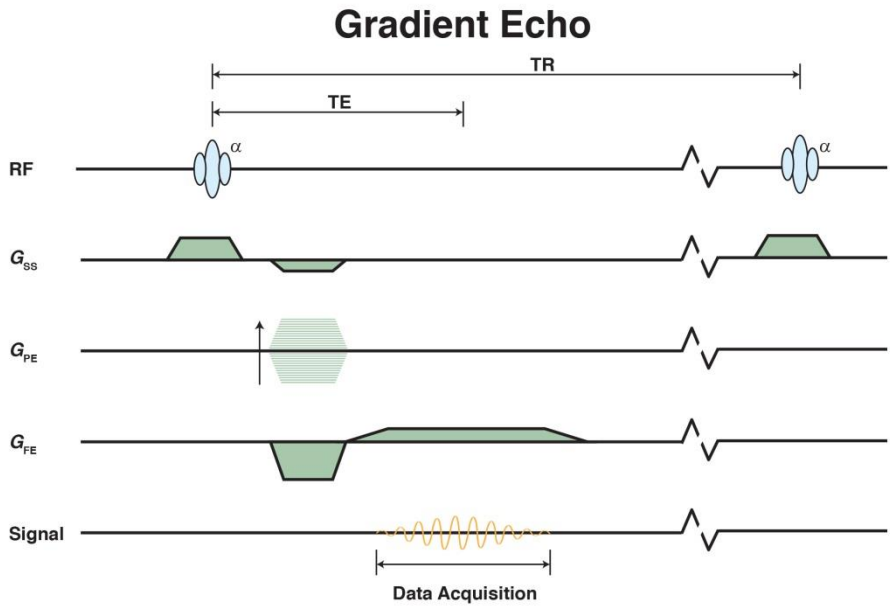

Figure 2.7: Pulse sequence diagram (PSD) for the basic gradient echo sequence. Figure illustrates the timing of the B_1 radiofrequency (RF) transmit field, as well as the gradients used for slice selection (G_{SS}), phase encoding (G_{PE}), and frequency encoding (G_{FE}).

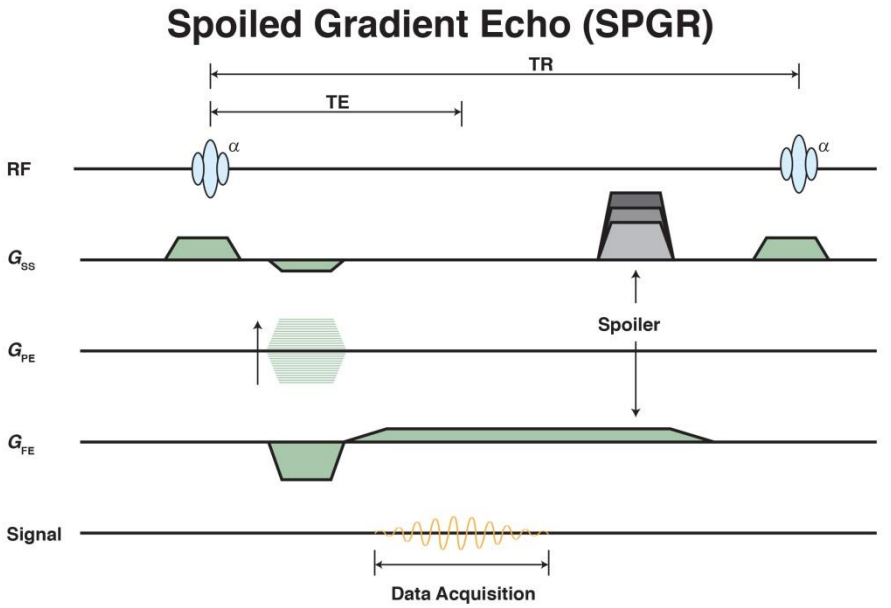

Figure 2.8: Pulse sequence diagram (PSD) for the basic spoiled gradient echo sequence. Figure illustrates the timing of the B_1 radiofrequency (RF) transmit field, as well as the gradients used for slice selection (G_{SS}), phase encoding (G_{PE}), and frequency encoding (G_{FE}).

GEs are created using the gradient fields. After the application of the excitation pulse a negative gradient lobe is immediately applied, causing rapid dephasing of the transverse magnetisation. Subsequently a positive magnetic gradient is applied, causing spins which were previously dephasing to rephase, and after a certain time all spins come back into phase along the axis the gradient was applied along, forming the

gradient echo. One limitation with this method of echo formation is that the positive gradient only compensates for dephasing caused by the negative gradient lobe, and does not take into account dephasing caused by non-uniformities in the B_0 field or T_2 spin-spin relaxation. As such, we must define the height of the echo (S_{GE}) is terms of T_2^*, which is a composite relaxation time which includes contributions from T_2 relaxation, non-uniformities in the B_0 field / tissue susceptibility, and protons diffusion. A PSD for the basic GE sequence is shown in Figure 2.7.

When a regularly-spaced train of pulses are used with a GE sequence, the TR can be less than T_2, leading to a portion of the transverse magnetisation supplied by one RF pulse remaining when the next RF pulse is applied. This results in additional signal components from previous excitations (known as 'Hahn' or partial echoes) in addition to the FID signal generated by the current excitation. There are three main ways that these partial echoes are dealt with, namely by: (i) 'spoiling' to remove the transverse coherence, ideally measuring signal from the FID only; (ii) 'rewinding', which utilises the signal from both the partial echoes and FID; and (iii) 'time-reversed', which utilises the signal from the partial echoes only. Each of these techniques affects the contrast of the resulting images differently.

The spoiled gradient echo (SPGR) pulse sequence is the most common sequence used for DCE-MRI [51]; a PSD for this sequence is shown in Figure 2.8. Since a short TR is used with SPGR sequences, a number of repetitions are required before a steady state is reached. If we assume that the spoiling is perfect, Equation [2.4] can be modified to give the longitudinal magnetisation just before an RF pulse is applied, given as [52]:

$$M_z\big((n+1)TR\big) = M_0\left(1-\exp\left(-\frac{TR}{T_1}\right)\right) + M_z(nTR)\cos(\alpha)\exp\left(-\frac{TR}{T_1}\right), \qquad [2.12]$$

with all data acquisition taking place once a longitudinal magnetisation steady state ($M_{z,ss}$) has been established, defined as:

$$M_{z,ss} = M_z\big((n+1)TR\big) = M_z(nTR). \qquad [2.13]$$

$M_{z,ss}$ is related to the measured signal (S) by:

$$S \propto M_{z,ss}\sin(\alpha)\exp\left(-\frac{TE}{T_2^*}\right), \qquad [2.14]$$

where the exponential term derives from the signal decay which occurs between the excitation and the echo (*TE*). Combining Equations [2.12] and [2.14], and assuming that a steady state has been reached, gives us the signal equation for the SPGR pulse sequence:

$$S \propto M_0\sin\alpha\exp\left(-\frac{TE}{T_2^*}\right)\left(\frac{1-\exp\left(-\frac{TR}{T_1}\right)}{1-\cos(\alpha)\exp\left(-\frac{TR}{T_1}\right)}\right). \qquad [2.15]$$

Contrast Mechanisms

The choice of TE and TR (and flip angle (α) in the case of GE sequences) affects the contrast in the acquired image, and MR pulse sequences are generally stratified into 3 groups: proton-density-weighted, T_1-weighted, and T_2^*-weighted images, so-named because the image contrasts are respectively dominated by three parameters: proton density (PD), T_1 relaxation, and T_2 relaxation. MRI has proved to be a very powerful diagnostic tool, since many diseases cause changes in tissue which affect at least one of these three parameters. PD-weighted images, as the name suggests, give signal magnitudes correlated to the density of protons in that region, and are acquired with long TRs and short TEs (though a short TR can also be used to image more rapidly, but only if a small enough flip angle is used). For T_1-weighted contrast, images are acquired with short TR and short TE, with the subject T_1 values inversely proportional to the measured signal. T_2^*-contrast weighting is achieved using with long TR and long TE, with the subject T_2^* values proportional to the measured signal.

MRI Contrast Agents (CAs)

From very early in NMRs conception, it was realised that the NMR signal of water can be modified by the addition of a small quantity of a paramagnetic material [44], with such substances commonly referred to as contrast agents (CAs). By far the most commonly used CAs today are gadolinium (Gd) based [53], however numerous other materials have been proposed for use as MRI CAs, such as Iron oxide [54], manganese chloride [55], and nanoparticles [56]. In 1988 Gd-DTPA (gadopentetate; *Magnevist*; Berlin, Germany) [57] was the first gadolinium-based MR CA to receive clinical approval and since then several other Gd-based molecules have been approved for use in patients

as CAs. All of these Gd-based CAs have a similar effect, namely reducing the T_1 and T_2 relaxation times of adjacent nuclei. However the magnitude of this effect varies from CA to CA, and is quantified as the relaxivities, r_1 and r_2, of that particular CA, as defined in a particular environment. This linear relationship can be described simply as:

$$R_1 = R_{10} + r_1 C, \quad [2.16]$$

and:

$$R_2 = R_{20} + r_2 C, \quad [2.17]$$

where R_1 and R_2 are the relaxation rates ($1/T_1$ and $1/T_2$, respectivly), R_{10} and R_{20} are the initial relaxation rates of the target prior to the addition of the CA, and C is the CA molar concentration used.

2.2. Dynamic Contrast Enhanced (DCE) MRI

In DCE-MRI a series of consecutive T_1-weighted MR images are acquired after the administration of a bolus of CA. As the CA arrives at the tissue of interest it modifies the inherent relaxation rates of the of the hydrogen nuclei in that region, resulting in a change in the measured signal intensity, as discussed previously. By collecting a series of images over time a signal-time curve (STC) is produced at each imaging voxel, from which the effective longitudinal relaxation rate ($R_1 = 1/T_1$) can be derived by means of the signal equation for SPGR sequence (Equation [2.15]), which can be written as:

$$S(t) = S(0)\sin\alpha \frac{1 - \exp[-R_1(t)TR]}{1 - \cos(\alpha)\exp[-R_1(t)TR]} \quad [2.18]$$

where $S(t)$ is the signal, and $R_1(t)$ the effective longitudinal relaxation rate, both as a function of time, t. R_2^* decay is generally ignored for T_1-weghted DCE-MRI, on the assumption that the TE used is much shorter than T_2^*. The concentration of CA in the tissue (C_t) can then be calculated at each imaging voxel from the effective relaxation rate using Equation [2.16], which can be rewritten as:

$$C_t(,t) = \frac{R_1(t) - R_1(0)}{r_1} \quad [2.19]$$

where $C_t(t)$ is the tissue CA concentration as a function of time, $R_1(0)$ is the longitudinal relaxation rate at $t = 0$, and r_1 is the relaxivity of the CA used. Since the shape of the resultant CTCs is related to the perfusion conditions of the tissue being imaged; pharmacokinetic (PK) modelling can be used to estimate physiological parameters, such as the volume transfer coefficient (K^{trans}) [min^{-1}], extravascular-extracellular volume fraction (v_e), and rate constant (k_{ep}) [min^{-1}], providing quantitative information about the vascular properties of the tissue being imaged.

2.2.1. Contrast Enhancement Prostate Physiology

The prostate gland is a component of the male reproductive system located just below the bladder, in front of the rectum. Its main function is to excrete prostatic fluid, one of the three components of semen. The prostate is generally divided into four histologic zones, namely: (i) the peripheral zone (PZ), (ii) the central zone (CZ), (iii) the transition zone (TZ), and (iv) the anterior fibromuscular stroma; the PZ, CZ, and TZ zones are illustrated in Figure 2.9.

Benign or malignant changes commonly occur in the prostate tissue as a man ages, with PCa being one such a malignant disease and the most frequently diagnosed cancer type in men from North and South America; Northern, Western, and Southern Europe; and Oceania [58]. Generally, when a tumour in the prostate grows to a diameter of 200 μm or greater, it induces angiogenesis (the formation of new blood vessels) through the sprouting of capillaries from pre-existing micro-vessels [59], which causes an increase in microvasculature [60]. This microvasculature tends to be more heterogeneously distributed and have higher permeability when compared to the microvasculature of healthy tissue [61]. Since the small molecular weight of certain commonly used Gd-based MR CAs allows them to permeate in and out of the blood vessels into the tissue, the signal measured over time at a particular location provides a measure of the rate at which materials within the blood are absorbed and distributed, which differs between healthy and tumorous tissue. One major challenge however that is faced when using DCE-MRI to investigate this microvasculature is relates to the relatively low spatial resolution (millimetre scale) at which MR images are acquired, whereas micro-vessels in the capillary bed have an average internal diameter of approximately 8 μm [62]. This discrepancy in scale means that the signal measured from a single voxel, the bulk concentration, is actually a measure of the contribution

from several ‘compartments’, as illustrated in Figure 2.9, which shows micro-vessels, cells, and extravascular extracellular space (EES), all of which are usually contained within a single voxel.

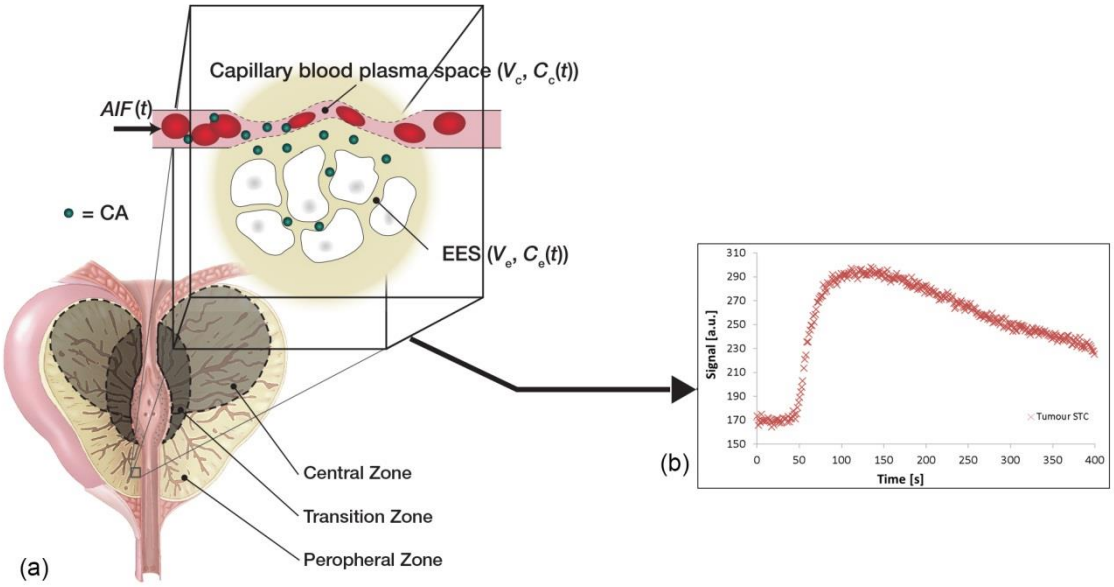

Figure 2.9: (a) Illustration of the prostate gland, showing the peripheral zone (PZ), central zone (CZ), and transition zone (TZ) as well as a schematic representation of the contrast agent exchange process, taking place on the micro-vessel scale. (b) An example bulk signal-time curve (STC).

2.3. Image Analysis

Various different qualitative and quantitative methods have been proposed for use in the analysis of STCs and CTCs derived from DCE-MRI data of the prostate; in this section some of the more commonly used techniques are outlined.

2.3.1. Phenomenological Modelling

Phenomenological parameters can be extracted directly from the STC data, such as; *wash-in*, *wash-out*, and *time to peak*, or more advanced model-free parameters such as the *integral area under the curve after 60 seconds* (*IAUC60*), as illustrated in Figure 2.10. The use of this type of analysis has shown promising result in PCa detection, with reported sensitivities of 29%-96% and specificities of 82%-96.2% [13, 20, 63-66]. For example, a 2005 study by Kim *et al.* on 53 patients reported an increase in sensitivity and specificity using the *wash-in* rate from 65% to 96% and 60% to 82% respectively in the detection and localisation of PCa, compared to T_2-weighted images alone [64].

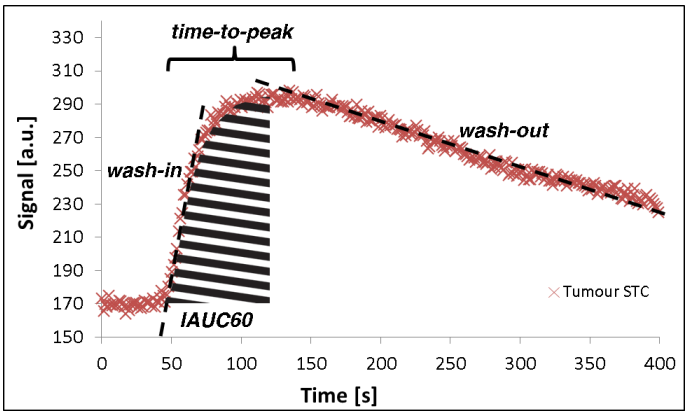

Figure 2.10: Signal-time curve (STC) time curve showing examples of phenomenological parameters, namely: *wash-in, wash-out, time-to-peak*, and *integral area under the curve after 60 seconds* (*IAUC60*).

Although this type of model-free analysis has been shown to be useful in differentiating normal from tumour prostate tissue, the functional information it provides about the tissue is limited, since the enhancement curve is dependent on multiple factors, such as; contrast dosage, micro-vessel density, flow in vessels, vessel wall permeability, structure of the extracellular space, and venous outflow, which are all considered together in this type of semi-quantitative analysis.

2.3.2. Quantitative Pharmacokinetic (PK) Modelling

Pharmacokinetics describes the behaviour of substances, such as CAs, after they have been introduced into a living organism, including the mechanisms by which they are absorbed and distributed. The factors governing these mechanisms are physiological (as discussed in section 2.2.1), and therefore modelling these parameters can provide quantitative, sub-voxel information on physiological parameters, such as tumour perfusion, microvascular vessel wall permeability, and extravascular–extracellular volume fraction, allowing for a more accurate and complete description of tissue behaviour [67].

Various pharmacokinetic (PK) models have been used for the analysis of prostate DCE data, most commonly conventional compartmental (CC) models such as, the Tofts [68-72], Extended Tofts [73, 74], and Brix [14, 75, 76] models, as well as combinations of these [11, 15]. Other more complex models have also been used with prostate DCE data, such as the Shutter Speed model [77, 78] and the Adiabatic Approximation of Tissue Homogeneity model [79-82].

Most CC PK models used in DCE-MRI are extensions of the general open two-compartment model, in which the first compartment serves as input to the second compartment, as proposed by Brix *et al.* [83] (as schematically-illustrated in Figure 2.11 (a)). The majority of these models are considered 'open' because the main blood circulation is not modelled as a third compartment, but as an input and output to and from the system, governed by the apparent plasma flow (*F*). The exchange between compartment one, the capillary blood plasma compartment, and the second compartment, the extravascular-extracellular space (EES), is governed by K_{PS}, the permeability surface area product (*PS*). From the general open two-compartment model one can derive the following mass balance equations:

$$V_c \frac{dC_c(t)}{dt} = F\big(AIF(t) - C_c(t)\big) - K_{PS}\big(C_c(t) - C_e(t)\big) \quad [2.20]$$

and

$$V_e \frac{dC_e(t)}{dt} = K_{PS}\big(C_c(t) - C_e(t)\big), \quad [2.21]$$

where $C_c(t)$ is the CA concentration in the capillary plasma volume (V_c); C_e is the concentration in the EES volume (V_e); and $AIF(t)$ is concentration entering the capillary bed on the arterial side, otherwise known as the arterial input function (AIF); all as a function of time, *t*. Adapting this model to meet the convention as proposed by Tofts *et al*. [84], we introduce a new parameter, K^{trans}, the volume transfer coefficient, where:

$$K^{trans} = FE\rho, \quad [2.22]$$

where ρ = tissue density and *E* is the extraction fraction, given as:

$$E = \frac{PS}{F + PS}. \quad [2.23]$$

Using this convention, we can derive the following mass balance equations:

$$v_e \frac{dC_e(t)}{dt} = K^{trans}\left(AIF(t) - \frac{C_t(t)}{v_e}\right), \quad [2.24]$$

and

$$C_{\mathrm{t}}(t) \approx v_{\mathrm{e}} C_{\mathrm{e}}(t), \qquad [2.25]$$

where $C_t(t)$ is the measured tissue bulk CA concentration and v_e is the extravascular-extracellular volume fraction ($v_e = V_c / V_t$). Combining Equations [2.24] and [2.25] we arrive at the following differential equation describing the kinetic behaviour of the CA in the tissue of interest:

$$\frac{dC_t(t)}{dt} = K^{\mathrm{trans}} AIF(t) - \frac{K^{\mathrm{trans}}}{v_{\mathrm{e}}} C_{\mathrm{t}}(t). \qquad [2.26]$$

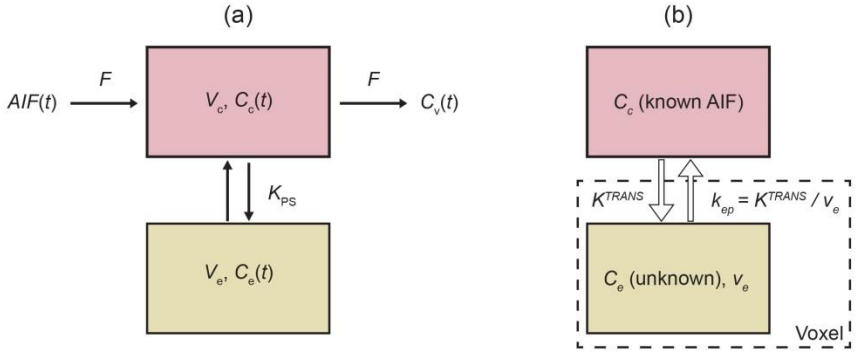

Figure 2.11: Schematic diagrams showing: (a) the general open two-compartment model and (b) the standard Tofts model.

Similar implementations of this type of adapted model have been suggested by Larsson *et al.* [85] and Tofts *et al*. [68, 73, 84], with the differences between these models being mainly due to their respective measurement schemes. Since the conventions proposed by Tofts *et al*. are the most widely used, this type of model is generally known as the *standard Tofts model*, illustrated in Figure 2.11 (b). For this model the solution to Equation [2.26] becomes a convolution of the AIF with the impulse response function (IRF) [73], where:

$$\mathrm{IRF} = K^{\mathrm{trans}} \exp\left(-\frac{K^{\mathrm{trans}}}{v_{\mathrm{e}}} t\right). \qquad [2.27]$$

Solving Equation [2.26], with the assumption that the initial conditions are zero, the total tissue concentration thus becomes:

$$C_{\mathrm{t}}(t) = K^{\mathrm{trans}} \int_0^t AIF(\tau) \exp\left[-\left(\frac{K^{\mathrm{trans}}}{v_{\mathrm{e}}}\right)(\tau - t)\right] d\tau. \qquad [2.28]$$

The ratio of K^{trans} and v_e is sometimes reported as k_{ep}, the rate constant between the EES and the capillary plasma fraction [84], such that:

$$k_{ep} = \frac{K^{trans}}{v_e}. \quad [2.29]$$

By fitting Equation [2.28] to CTCs derived from DCE-MRI data, one can estimate values for K^{trans}, v_e, and k_{ep}. This is generally performed using a non-linear fitting approach, such as using the non-linear least-squares (NLS) method [86], however using a linear least-squares (LLS) method has been shown to have several advantages over an the NLS approach, which include: faster computational time, better model fitting under low SNR conditions, and less sensitivity to temporal resolution (T_{res}; the rate at which the data is sampled) [87, 88], as well as not requiring initial estimates of the parameters to be provided prior to the fitting [86]. The use of LLS for PK modelling of DCE data is investigated in Chapter 5. In 2004, Murase *et al*. introduced a linear interpretation of the Tofts model, [88], as outlined below.

Integrating both sides of Equation [2.26] with the assumption that the initial conditions are zero [89] and giving the result in a discrete form we have:

$$C_t(t_k) = \left(K^{trans} + k_{ep}\right) \cdot \int_0^{t_k} AIF(\tau) - k_{ep}\, d\tau \cdot \int_0^{t_k} C_t(\tau)\, d\tau \quad [2.30]$$
$$(k = 1, 2, \cdots, n),$$

which can be written in matrix form as:

$$\vec{C} = \vec{A} \cdot \vec{B}, \quad [2.31]$$

where:

$$\vec{A} = \begin{bmatrix} \int_0^{t_1} AIF(\tau)\, d\tau & -\int_0^{t_1} C_t(\tau)\, d\tau \\ \int_0^{t_2} AIF(\tau)\, d\tau & -\int_0^{t_2} C_t(\tau)\, d\tau \\ \vdots & \vdots \\ \int_0^{t_n} AIF(\tau)\, d\tau & -\int_0^{t_n} C_t(\tau)\, d\tau \end{bmatrix}, \quad [2.32]$$

$$\vec{B} = \begin{bmatrix} K^{\text{trans}} + k_{\text{ep}} \\ k_{\text{ep}} \end{bmatrix}, \qquad [2.33]$$

And

$$\vec{C} = \begin{bmatrix} C_{\text{t}}(t_1) \\ C_{\text{t}}(t_2) \\ \vdots \\ C_{\text{t}}(t_n) \end{bmatrix}. \qquad [2.34]$$

When C_t and the AIF are known, Equation [2.32] can easily be solved for $\vec{B}$ using the LLS approach, and PK parameter values obtained from the resulting matrix elements.

2.3.3. The Arterial Input Function (AIF)

The AIF is a measure of the intra-arterial contrast medium over time feeding the tissue of interest, and is a critical component for PK modelling of DCE-MRI data [77, 84, 90]. However, measurement or estimation of the AIF to date has proven challenging, making it a major source of error in PK parameter estimates [91-93].

The AIF curve-shape profile differs from that of the tissue CTCs, as it is characterised by an initial sharp uptake, followed by a short-lived second peak, and subsequently a longer wash-out period, as illustrated in Figure 2.12. Current methods to quantify the AIF can be stratified into four main approaches: (i) subject-specific direct blood sampling; (ii) subject-specific MR-measurement; (iii) estimation from a population average; and (iv) indirect calculation / estimation, for example using a reference-tissue-based method; these four methods are outlined below.

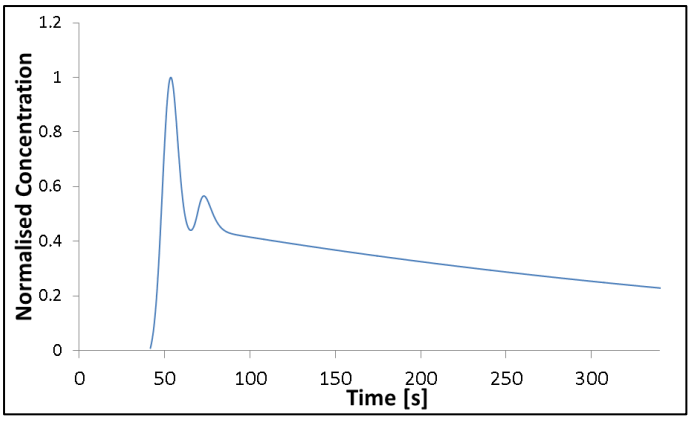

Figure 2.12: Example of an arterial input function (AIF).

Direct Blood Sampling

The most direct way to measure the AIF, and considered by some the 'gold standard' method [94], is by directly collect blood samples during the DCE-MRI acquisition from an arterial catheter inserted into the subject, and subsequently analysing the samples to extract a CA concentration at each time point [57, 85, 95]. The main advantage of this technique is the high accuracy by which the CA concentration can be determined from the blood samples, providing excellent characterisation of the actual patient-specific AIF. However, this is an invasive and inconvenient method, and is still reliant on the T_{res} at which the blood samples are collected, as well as where in the patient the samples are acquired from.

Subject-Specific MR-Measurement

The arterial supply to the prostate is primarily from the inferior vesical artery, originating from the iliac artery [96], which is generally contained within the imaging volume for prostate DCE-MRI, thus the patient-specific AIF can be determined by measuring the time-dependent contrast concentration within this aortic region. This approach is non-invasive and is expected to closely approximate the true AIF at the prostate. However, accurate measurement of the AIF *in vivo* has proved challenging to date, due in part to the high T_{res} [22, 97, 98] and signal-to-noise ratio (SNR) [99] requirements, as well as other effects such as inflow, partial volume, and non-uniformity of the B_1-field across the volume of interest [99-102]. Investigating the accuracy and precision with which a patient-specific AIF can be measured using a standard Cartesian DCE MR protocol is the subject of Chapter 5, and using a novel golden-angle continuous radial protocol with compressed sensing and parallel imaging, the subject of Chapter 6.

Population Averaged

Due to the confounding factors influencing patient-specific AIF measurement, various parametrised forms of the AIF have been proposed which are based on average patient measurements [57, 103-107]. The most widely-used AIF models are the biexponential function proposed by Weinmann *et al*. in 1984 [57] and the more complex 10-paramater function outlined by Parker *et al*. in 2006 [105]. In the Weinmann study the population-based AIF was derived from low temporal resolution arterial blood samples [57], with the parametrised form given as:

$$AIF(t) = D[a_1 \exp(-m_1 t) + a_2 \exp(-m_2 t)], \qquad [2.35]$$

where D is the CA dose in mM kg^{-1} of body mass, a_1 and a_2 are amplitudes of the exponentials, and m_1 and m_2 are their rate constants. Parker's parameterised form of the AIF was derived from data measured with a T_{res} of 5 s from patients' aortas or iliac arteries following a standard bolus administration of a Gd-based CA (dose = 0.1 mM kg^{-1}) [105], and is given as:

$$AIF(t) = \sum_{n=1}^{2} \frac{A_n}{\sigma_n \sqrt{2\pi}} \exp\left[-\frac{(t-T_n)^2}{2{\sigma_n}^2}\right] + \frac{\alpha \exp[-\beta t]}{1+\exp[-s(t-\tau]}, \qquad [2.36]$$

where: A_1 and A_2 are the scaling constants; T_1 / T_2, and σ_1 / σ_2 are the centres and widths of the 1st and 2nd Gaussians respectively; α and β are the amplitude and decay constants of the exponential respectively; and s and τ are the width and centre of the sigmoid, respectively.

Population-based AIFs are widely used in DCE-MRI, and their use has been shown effective with low T_{res} data sets [98, 108], however, due to inter- and intra-patient variations in cardiac output, organ function, contrast injection rate, body fat, etc., and their influence on the AIF profile [107, 109], the use of a general population average AIF is known to adversely affect the accuracy of patient-derived PK parameters and weaken patient-specific physiological assessment [103, 104]. As such, the measurement of a patient-specific AIF during the DCE-MRI acquisition is desirable.

Indirect AIF Derivation

Several other novel approaches have been suggested to overcome the limitation associated with the measurement of the AIF, including the use of either a reference tissues to obtain the AIF [67, 91, 110], and techniques which remove the need to estimate the AIF altogether, such as through the use of independent component analysis [111].

Extracting a reference tissue-based AIF overcomes some of the limitations of the direct subject-specific AIF measurement, as well as inaccuracies deriving from using a population-based AIF approach. Instead of measuring the MRI signal in a feeding artery, or assuming a particular form of the AIF, the reference-region model presumes prior knowledge of the PK parameter values for a well-characterised healthy reference tissue (e.g., muscle), and uses these values in conjunction with the reference tissue CTC to inversely derive the AIF [110]. This model makes a number of assumptions

which affect the accuracy and reproducibility of the derived AIF [112], most notably: no inter-patient variation for the set 'known' reference tissue PK parameters values, and that the AIF is the same for the reference tissue and the tissue of interest.

2.4. Sources of Error in Quantitative DCE-MRI

Many factors influence or limit the accuracy and precision of measurements made using DCE-MRI; in this section some of the main sources of these errors are outlined.

2.4.1. Sampling Limitations

The speed at which MR images are acquired is fundamentally limited by physical (e.g. gradient amplitude and slew-rate) and physiological (e.g. peripheral nerve stimulation) constraints. Additionally, when *k*-space is greatly under-sampled and the Nyquist criterion violated, this leads to aliasing artefacts in images reconstructed using the Fourier transform. In an effort to negate some of the temporal limitations intrinsic to MRI, as well as provide a means to reconstruct high-quality images from limited data, various different rapid imaging methods have been proposed. These can be stratified into three main groups: (i) techniques which generate less-visible, incoherent artefacts, at the expense the SNR [48, 113]; (ii) techniques which exploit redundancies in *k*-space, such as parallel imaging (PI) [114, 115]; and (iii) techniques which exploit redundancies in either the temporal or spatial domain (or both) [116, 117]. Other more recently proposed methods combine these approaches such as compressed sensing (CS) [49] or methods which use both CS and PI techniques in combination [118]. These rapid imaging methods potentially allow for more accurate modelling of the DCE-MRI data, however further validation work is needed in order to access how these techniques affects the accuracy and precision of the quantitative PK parameters extracted from the data.

2.4.2. Temporal Resolution (T_{res}) and Acquisition Duration (AD)

In DCE-MRI the time-spacing between subsequent image volumes is known as the temporal resolution (T_{res}) and the length of time that the curves are sampled for from the start of the CA enhancement is known as the acquisition duration (AD). Whether phenomenological or PK analysis is performed, it has been shown that the

T_{res} at which the data are sampled affects the accuracy and precision of the derived parameter values, since rapid sampling is required in order to properly characterise the high-frequency components of the curves (such as the wash-in phase) [119, 120]. Additionally, the use of a MR-measured AIF for use in PK analysis of the data requires even faster sampling of the data [22, 121], as discussed in section 2.3.3. However, even when the Nyquist criterion is met, high sampling rates usually result in compromised image quality, as with current clinical protocols there is a trade-off between T_{res}, spatial resolution, SNR, and / or imaging field of view [122].

Adequate AD is also required for accurate PK model fitting, as too short an AD may not accurately measure the low-frequency features of the curves (such as the wash-out phase of certain tissue CTCs). Long ADs can also introduce motion artefacts when imaging patients, which can be an addition source of measurement errors, as discussed below [120], while conversely, inadequate ADs can lead to underestimation of PK parameters [119].

2.4.3. B_1-Transmit Field Non-Uniformity

Spatially selective excitation pulses are typically used in MRI to limit the field of view and reduce scan times [123], as discussed in section 2.1.1. However, variations in the actual flip angle across the excitation volume due to non-uniformities in the B_1 transmit field (B_1^+) will inevitably lead to variations in signal intensity, and by extension errors in the measured AIF and tissue CTCs, as well as the derived parameters. In fact, B_1^+ non-uniformity is probably the largest source of systematic error in T_1 measurements, and therefore CA concentration measurements which are essential for accurate DCE-MRI [121, 124]. This effect is particularly pronounced with abdominal and pelvic imaging, due to the large dielectric load imposed on the scanner producing a non-uniform RF distribution across the FOV caused by variations in the RF wave deriving from the formation of standing waves in the tissue [125].

Voxel-wise flip-angle correction (VFAC) can be performed by acquiring a B_1^+ map of the subject at the same geometry as used for the DCE acquisition, and subsequently using this data to correct the flip angles used in the voxel-wise T_1 calculations for the DCE data. In this thesis the term "B_1^+ mapping" refers to both techniques which estimate the B_1^+ field strength directly, or indirectly by estimating the flip angle, which is a function of the transmit B_1 field. The general idea behind B_1^+ mapping is to acquire data using a

pulse sequence that varies with respect to the B_1^+ only. To this end, at least two images are usually acquired, and a mathematical operation is used to cancel out all other undesired features in the image.

There are two general categories of B_1^+-mapping techniques: magnitude-based, such as the dual-angle method proposed by Insko and Bollinger in 1993 [126] and the actual flip-angle imaging method Yarnykh introduced in 2007 [127]; and phase-based, such as the spin echo phase-sensitive technique introduced by Oh *et al*. in 1990 [128], and Morrell's phase-sensitive method [129].

In Chapter 5 of this thesis the actual flip-angle imaging (AFI) B_1^+-mapping method proposed by Yarnykh *et al*. is used to investigate the effects of flip angle correction on the measured CTCs and AIF, as well as the derived PK parameters.

2.4.4. Partial Volume

Due to the relatively low spatial resolution of MRI (typically millimetre scale), and the structural-complexity of the human body, imaging voxels often contain more than one tissue type. This can negatively affect measurements, since affected voxels will contain signal-components deriving from tissues other than the tissue-of-interest [130]. Fortunately it is not too difficult to minimise this partial volume effect, or remove it altogether by using a high enough spatial resolution to resolve the tissue-of-interest from any surrounding tissue, as well as ensuring that any ROIs defined in the data only contain the tissue-of-interest.

One example where careful consideration needs to be taken to avoid partial volume effects is in the measurement of the AIF using DCE-MRI. As outlined previously in section 2.3.3, the AIF is measured in an artery feeding the tissue-of-interest, with the objective of measuring the signal change in the blood plasma only, deriving from the arrival and passage of the bolus of CA. If too low a spatial resolution is used and / or too large an ROI defined in the artery, this can cause the signal from voxels at the edge of the ROI to be contaminated with signal deriving from the vessel wall, thereby reducing the accuracy of the measured AIF [100, 131].

2.4.5. Inflow

Another factor that can have an effect on the accuracy of DCE-MRI measurements, specifically in the measurement of the AIF, is the inflow effect [100, 102]. This effect is caused by fresh blood flowing into the imaging volume with fully-relaxed spins, falsely increasing the signal and resulting in an apparent shortening of the measured T_1 values, leading to over-estimation errors in the derived CA concentrations.

One way to compensate for this effect is by using a nonselective inversion pulse to drive the longitudinal magnetisation of the inflowing blood toward an equilibrium level prior performing the measurements; however this correction method is limited to a single slice acquisition [132]. Several other simple considerations can be taken into account to minimise this effect, such as assuming a literature value for the T_{10} of the blood (this initial T_1 value for the blood plasma prior to the arrival of the CA bolus), ignoring errors due to variations in hematocrit, temperature, and blood oxygen, and removing / minimising potential error in the T_{10} measurement deriving from the inflow effects [100]. Additionally, the ROI where the AIF is measured can be defined in a central slice, so that the inflowing blood will have received a sufficient number of RF pulses prior to measurement to drive the magnetisation to an equilibrium state [102].

2.4.6. Motion

Motion artefacts are a particular issue with DCE-MRI, since a complete DCE scan may take up to ten minutes, during which time any patient motion will cause the tissue at a particular imaging voxel to shift spatially at that time point, replaced with tissue from a different spatial location in the patient. This causes errors in the measured CTCs since the signal measured at each time-point does not necessarily originate from the same tissue source. Gross patient motion is one of the most common causes of artefacts in MRI, producing a range of ghosting effects in the images. Unfortunately there's no way to completely remove this source of error, however careful preparation before the scan to ensure the patient discomfort is minimised can help with reduce this effect. Motion artefacts may also derive from patient organ motion, however this can be minimised by administering a muscle relaxant prior to the DCE scan, such as butylscopolamine bromide (*Buscopan*; Boehringer-Ingelheim, Ingelheim, Germany) [133].

2.5. Conclusions

As highlighted in this chapter, DCE-MRI is overall a very complex technique to implement correctly, with a whole plethora of possible confounding factors influencing the accuracy and precision of tissue / arterial DCE-MRI-measurements, and by extension the derived PK parameter values. The following chapter outlines new phantom-based methodologies designed to allow for the absolute quantification of the accuracy and precision of DCE-MRI measurements, with subsequent chapters demonstrating the phantoms use, presenting quantitative results which will be of great use informing current and emerging clinical DCE-MRI protocols, as well as future DCE studies.

Chapter 3: Design, fabrication, and validation of a novel anthropomorphic DCE-MRI prostate phantom test device

3.1. Introduction

As discussed in the previous chapter, the technique of DCE-MRI with pharmacokinetic (PK) modelling of the contrast agent uptake curves has been shown effective for prostate cancer (PCa) detection, monitoring PCa therapy, as well as shown considerable potential as a quantitative marker of tumour malignancy. However, its adoption into routine clinical practice has been hindered by uncertainties surrounding the most appropriate or optimum acquisition protocol to use to measure the contrast agent (CA) uptake curves. Although DCE-MRI has been qualitatively validated by various studies, that show good correlation between modelled parameters derived from the DCE data and histologically measured parameters, such as microvascular density [134], a gold-standard DCE-MRI quantitative validation technique is still lacking. This is mainly to do with difficulties associated with determining the accuracy of measured parameters in a validation study, since the actual parameter values are generally not precisely known in the patient or object being scanned. This has resulted in the reported use of a plethora of *in vivo* DCE protocols and processing methodologies in

the published literature, with a commensurate wide divergence in published data, such as K^{trans}, v_e, and k_{ep} values, which has diminished the discriminative potential of the technique.

The temporal resolution (T_{res}) used for the data acquisition has been shown to affect the accuracy of derived PK parameters [135, 136]; however, in previous DCE studies of the prostate that used PK modelling, temporal resolutions varied widely from 2 to 30 s [137]. Advances in phased array detector technology, which implement various forms of accelerated imaging, such as k-t SENSitivity Encoding (SENSE) [114], SiMultaneous Acquisition of Spatial Harmonics (SMASH) [115], and GeneRalized Autocalibrating Partially Parallel Acquisitions (GRAPPA) [138], faster gradient coils, coupled with novel acquisition techniques, such as compressed sensing [49], show potential to greatly improve T_{res} without sacrificing image quality, allowing for more accurate modelling of the data. However, as discussed previously in section 2.4.2, there is always a trade-off between acquisition speed and image quality, and to date a gold standard method to quantitatively evaluate this 'trade-off' is lacking. There is thus a need for a physical device to quantitatively and prospectively test these new DCE techniques *in situ* in the scanner, and various phantom designs have been proposed to this end.

One such design type utilises the hollow fibres found commonly in commercial haemodialysis cartridges to produce 'leaky' phantom devices, which physically mimic permeable microvasculature. Heilmann *et al.* demonstrated the usefulness of this type of phantom design in the classification of the permeability characteristics for CAs with different molecular weights [139]. In a study by Mehrabian *et al.*, a similar phantom design was used to test an independent component analysis technique for separating the AIF and extravascular space signals using the signal that is measured in the target tissue [140]. However, since these phantom designs physically mimic the behaviour of blood vessels, the CA concentration-time curves (CTCs) produced are dependent on the porosity and perfusion conditions of the system and hence it is not possible to theoretically calculate actual parameter values against which to check the accuracy of the PK modelling results. Furthermore, the inevitable retention of CA in the gel space surrounding the hollow fibres limits the use of such devices for multiple experiments, further limiting their usefulness in, for example, determining reproducibility. Other designs include 'lesion' phantoms, which produce an enhancement curve within single or multiple compartmentalised spaces. In a study by Freed *et al.*, a single 10 mm spherical measurement chamber was mounted into a breast phantom, and the phantom's ability to produce measurable CTCs was demonstrated [141]. The behaviour

of the system was characterised using a high spatial resolution X-ray system, although its T_{res} was poor (2.6 – 24.7 s). Additionally, the MR data was acquired at a very low temporal resolution (79 s), making it difficult to access the CTCs measured using MRI. Ledger *et al.* presented a phantom which consisted of a 40 mm spherical object divided into four inter-linking compartments, for use in quality assurance and the development of DCE-MRI breast protocols [142]. Good repeatability was reported for MR measurements made in the phantom, however the curves produced by the system were not independently verified or characterised by a modality other than MRI, meaning that the system's utility was limited to the relative comparison between MR measurements. A further limitation of the above-described studies was that none allowed for measurements to be made in an environment which realistically challenges prostate DCE-MR imaging by closely emulating conditions observed *in vivo,* in terms of physical size, image complexity, and sparsity.

The aim of this initial phase of the project was to develop a novel anthropomorphic phantom device in which precisely and accurately known 'ground truth' CTCs were generated and thus could be presented to the MRI scanner for measurement, thereby allowing for a quantitative assessment of the scanner's ability to accurately measure the CA wash-in and wash-out curve-shapes. The hypothesis under investigation was that measurement inaccuracies in these 'tissue' curves-shapes, whether slowly or rapidly-varying, deriving from features of the DCE imaging pulse sequence themselves, contribute significantly to the wide divergence in DCE PK modelling output parameter values in the published literature.

3.2. Materials and Methods

3.2.1. Phantom Device Design

The phantom contained two measurement chambers, the geometry of which (illustrated in Figure 3.1(a)) was optimised in a previous study using computational fluid dynamical modelling to allow for optimal uniform distribution of liquids at low flow rates [143]. Measurement chambers with a wall thickness of 0.3 mm were produced using an *Eden 250* 3D-printing system (Stratasys, USA) and *VeroClear* polymer (*FullCure-GD810*; Stratasys, USA): for further information see Appendix A, section A 1.1. The 12 mm

diameter of these chambers was selected specifically so that several DCE imaging voxels, of a size typically used in prostate DCE, could be positioned within, minimising any partial volume effects due to the chamber walls. These two measurement chambers were set within a larger prostate-sized object (manufactured using a rapid prototyping system) containing a further arrangement of chambers, as shown in Figure 3.1(b). Liquid containing the Gd-DTPA CA (*Multihance*; Bracco, USA) was pumped into each measurement chamber through the two inputs and subsequently flowed out through the central output (illustrated in Figure 3.1 (a)) and then through the larger prostate 'volume', before leaving via a single waste output, as shown in Figure 3.1(b). This larger volume was designed to mimic the enhancement profile typical of the entire prostate, imitating the reduction in sparsity in the temporal domain observed in *in vivo* scans.

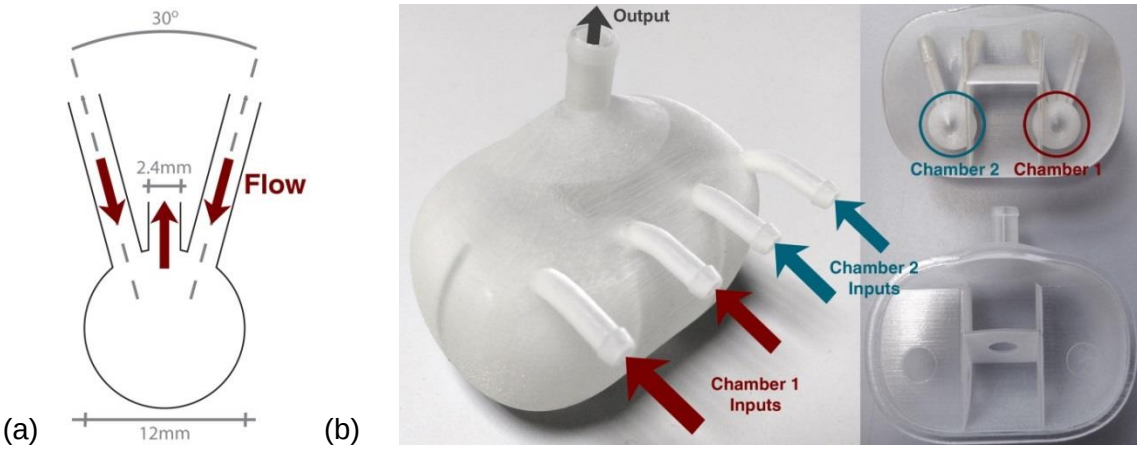

Figure 3.1: (a) Schematic representation of the geometry of the one measurement chamber's input/output configuration, and (b) photographs of the final prostate-mimicking object (left: complete, and right: sectioned) containing the two measurement chambers, with inputs into chambers 1 (red) and 2 (blue) highlighted.

Table 3.1: Composition of tissue mimic materials (TMMs) used in construction of anthropomorphic phantom

	Agar [wt. %]	Gd-DTPA [mM]	$MnCl_2$ [mM]	NaCl [wt. %]	Benzalkonium Chloride [wt. %]
Bone	2.5	-	0.085	0.5	0.046
Muscle	4.0	-	0.026	0.5	0.046
Fat	2.7	0.35	-	0.5	0.046
Bladder	3.0	-	-	0.5	0.046

This prostate was set into a large custom-built anthropomorphic phantom device (shown in various stages of construction in Figure 3.2, and completed in Figure 3.3; phantom size = 280(w) x 390(l) x 200(h) mm^3). Agar-based tissue mimic materials

(TMMs) were developed and used to mimic the T_1 and T_2 properties of bone, muscle, fat, and bladder tissue [144] (details of TMM composition are presented in Table 3.1). Latex moulds were produced and used to shape certain components, such as the femur bones and bladder.

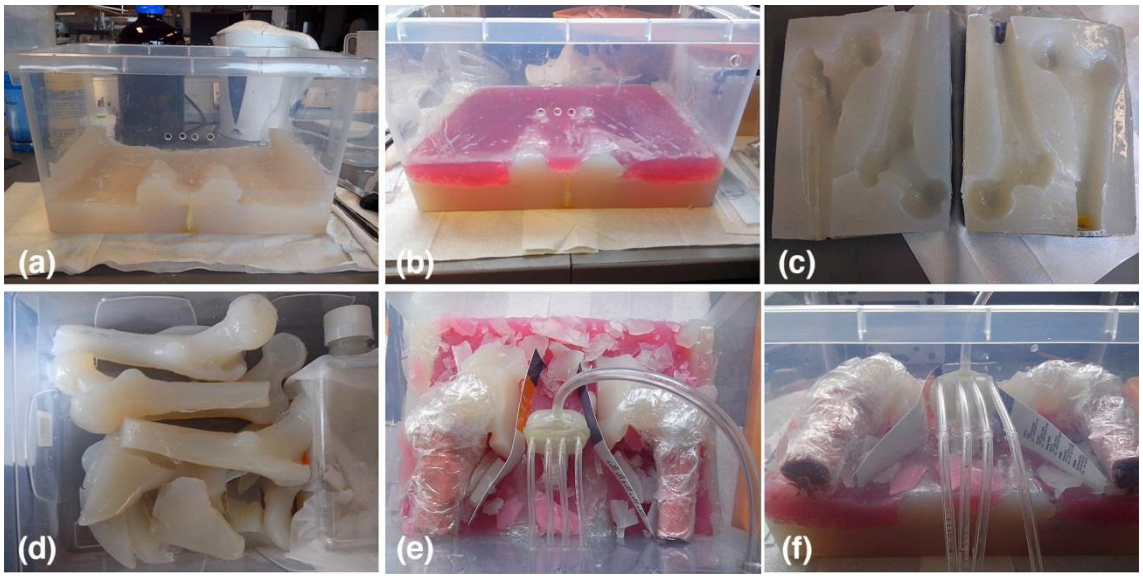

Figure 3.2: (a–f) Photographs showing various stages during construction of the large anthropomorphic phantom, with: (a) an initial layer of fat TMM; (b) a layer of muscle TMM (red dye used to differentiate from other TMMs); (c) latex moulds used to cast the 'femur bones'; (d) cast physiologically-shaped components for the phantom, composed of various different TMM materials; (e, f) the prostate mimicking object *in situ* prior to surrounding TMM being deposited, as well as two 'femur bones' composed of bone TMM, and deposition of a heterogeneously distributed fat / muscle layer.

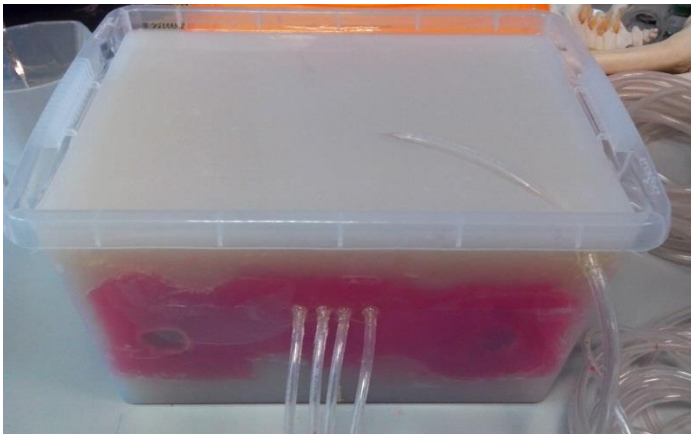

Figure 3.3: Photograph of the final phantom device. Dimensions: 280(w) x 390(l) x 200(h) mm^3.

3.2.2. Fluid Pump System Design and Operation

A computer-controlled multi-pump system was designed to produce two simultaneous CTCs within the two separate measurement chambers. The pump system consisted of

four gear pumps (*Reglo-Z*; Ismatec, Switzerland), and was designed to produce CTCs by varying the relative flow rates of two pumps feeding a given measurement chamber in parallel over time, one pumping a lower concentration, the other a higher concentration of the CA (pumps 1 and 2 feeding measurement chamber 1, and pumps 3 and 4 feeding measurement chamber 2, as illustrated in Figure 3.4 and shown in Figure 3.5). This configuration ensured a constant volumetric flow rate so that any potential flow-related artefacts would be constant across the concentration range. The inlet tubing placement within the phantom was designed such that, for imaging fields of view typical of DCE protocols, the inflowing liquid was driven to a steady-state prior to entering the measurement chambers, thereby eliminating inflow artefacts. Concentrations of CA (0.15mM and 1.5mM) were selected to give a similar relative peak enhancement to that observed *in vivo*. The flow rate produced by the pumps was controlled by a time-varying voltage signal produced via a 12-bit analog output module (*USB-DA12-8A*; ACCES, USA), controlled using code custom-written in the *Delphi* programming language (Embarcadero Technologies, USA): for further information see Appendix A, sections A 1.2 and A 1.3. The fluid from both pumps flowed through 8 m of 6.4 mm internal diameter (ID) tubing (*Tygon-R*; Saint-Gobain, France) before mixing together via a 'Y' connection, following which the fluid travelled a further 1.2 m down a single 6.4 mm ID tube before bifurcating to two 3.2 mm ID tubes and traveling into the phantom. After passing through the mixing chambers and prostate object the liquid was output to a waste container through a single 6.4 mm ID tube (for further details related to the tubing configuration used see Appendix A, section A 1.4). The phantom device and various system components are shown *in situ* in Figure 3.5.

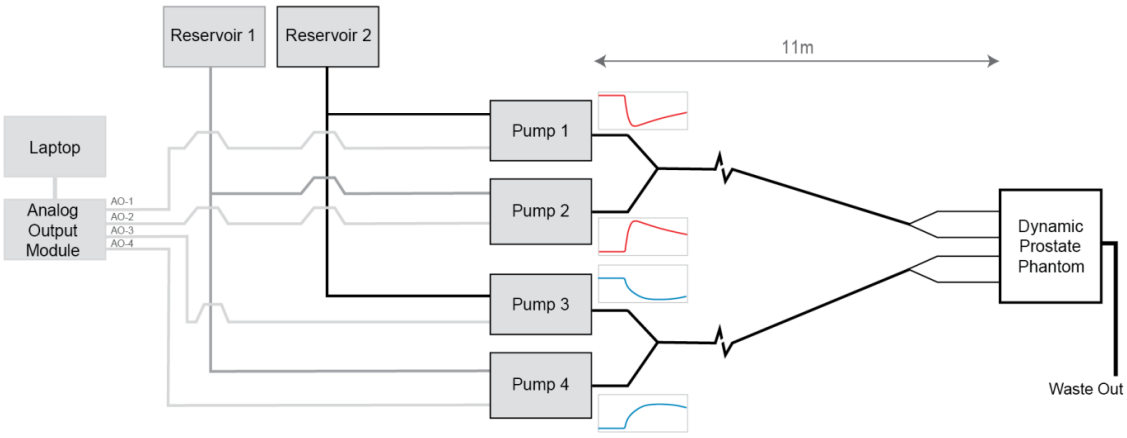

Figure 3.4: Schematic diagram of complete pump system (red and blue traces are representative of the change in flow rate at each pump over time, with the overall flow-rate kept constant)

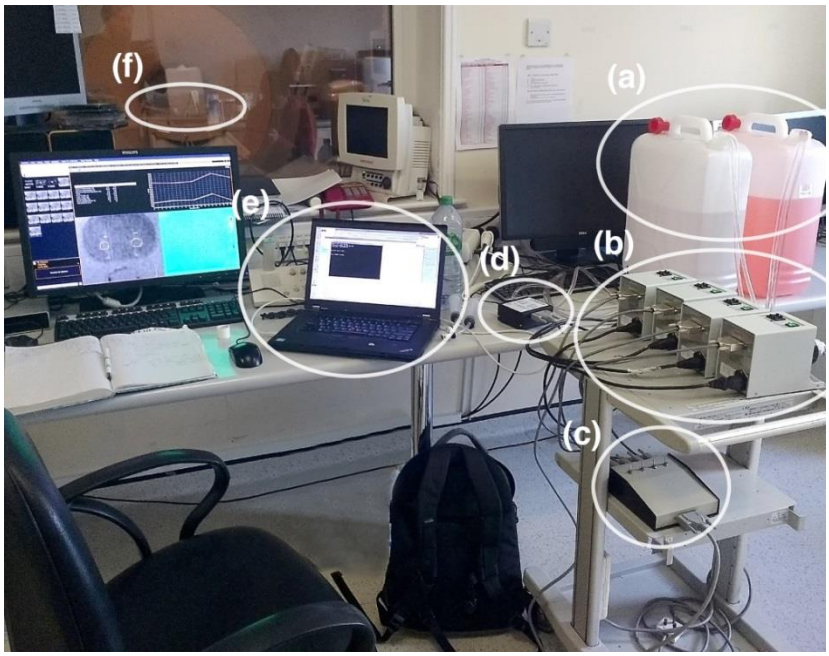

Figure 3.5: Photograph of the phantom system set up *in situ* in the MR centre. Shown are the (a) the contrast agent reservoirs, (b) the 4-pump system, (c) a custom built control box connecting (d) the analog output module to the pumps, (e) the laptop used to control the phantom system, and (f) the phantom test device *in situ* at the MR scanner bore.

3.2.3. Tissue Concentration-Time Curves (CTCs)

Realistic 'physiological' curves mimicking both healthy and tumour tissues were artificially generated via an inversion of the standard Tofts model using specific PK parameter values taken from a representative patient data published in an earlier work [145]. This was performed using code developed in *Matlab* (*R2015b*; MathWorks, USA). The values used were:

- K^{trans} = 0.126 min^{-1} (healthy) and 0.273 min^{-1} (tumour),
- v_e = 0.292 (healthy) and 0.412 (tumour)

A model AIF was also artificially generated using the method and model parameter values reported by Parker *et al.*[105]. These curves were used to control the output of the pumps in order to produce the desired CTCs within the measurement chambers within the phantom in the magnet. For each experiment, the CTCs thus generated consisted of 120 s of baseline flow and a 300 s physiological curve (representing either tumour or healthy tissue).

3.2.4. Characterising CTCs and Establishing the Optimal Flow Rates

In order to characterise the response of the phantom system, and hence the actual shape of the CTCs produced in the measurement chamber (the 'ground truth') after the fluid has been pumped through 11 m of tubing and several tubing connectors, an optical imaging system was designed and set-up as shown in Figure 3.6. This optical imaging system was also used to establish a threshold minimum flow rate, above which CTC curve-shape distortions were minimised and uniform distribution of dye within the measurement chambers was achieved.

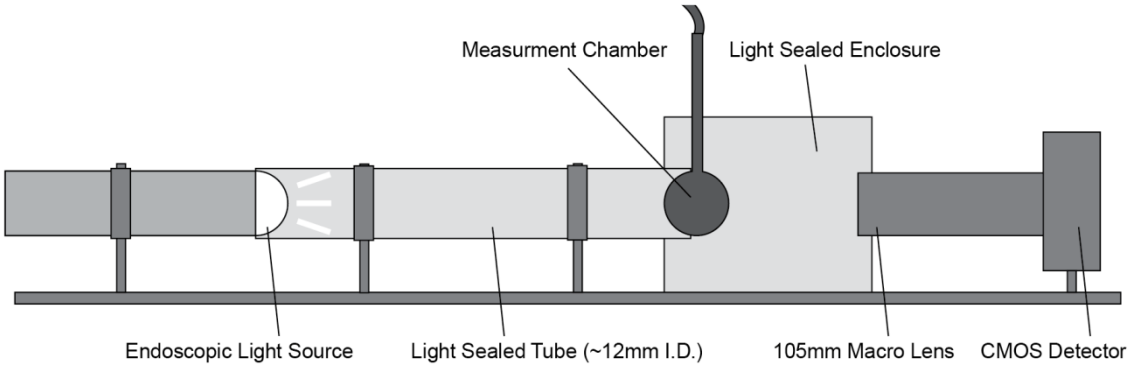

Figure 3.6: Schematic diagram of optical imaging system setup used to establish minimum flow rates and ground truth measurements for the CTCs produced by the system.

In this system, a single measurement chamber was connected to two pumps, with the same tubing configuration and lengths as for the main phantom device, and set within a custom-built light-sealed enclosure. An endoscopic light source (*Fujinon Eve Σ400*; Fujifilm Corp, Japan) was used in conjunction with a high resolution CMOS camera (*Canon EOS 50D*; Canon Inc, Japan) with a 4752 x 3168 array for detection, giving 4 x 4 μm^2 pixels, and a T_{res} of 1 s. A region of interest (ROI) was defined across approximately the same spherical region of the measurement chamber as used in the ROI analysis of the MR data. The temporal stability of measurements made using the optical scanner was measured over a thirty-minute period by imaging the chamber without liquid flow every second and calculating the variation in mean signal over that period. Black dye was used as a CA surrogate in the system, which caused a change in the measured intensity at different concentrations due to the attenuation of incident photons. Imaging known concentrations of dye in the chamber across a range of concentrations used for the CTC runs produced a calibration curve. The calibration curve was fitted using a non-linear least squares method with a model adapted from

the Beer-Lambert equation [146], given as:

$$C(t) = ae^{bS(t)} + c, \quad [3.1]$$

where: $C(t)$ is the dye concentration, and $S(t)$ in the average intensity measured at a region of interest (ROI), at time-point t; and a, b , and c are constants derived from fitting the model to the calibration curve data. Very good agreement was observed between the model and the calibration data (R^2 = 0.998). An example calibration curve, as used for the optical measurements, is shown in Figure 3.7.

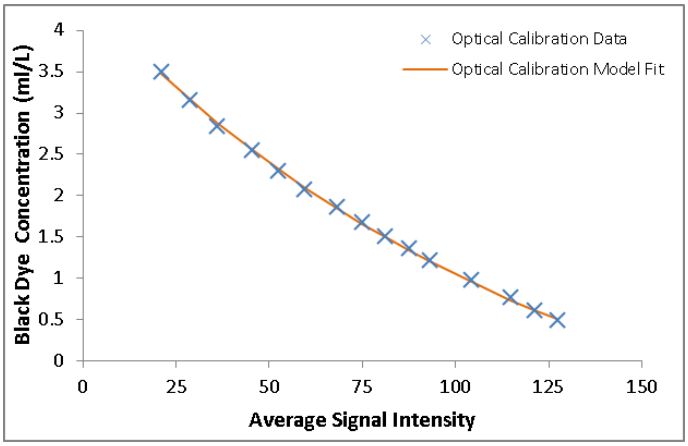

Figure 3.7: Example optical calibration curve with the calibration model fit to the data.

The calibration curve was used to derive the black dye CTCs from the optical signal-time curves (STCs), which were subsequently converted to Gd CTCs (for comparison against the DCE-MRI data). Since the concentration of dye in the chamber is controlled by varying the relative flow rates of two pumps in parallel, one pumping the higher concentration of CA, the other the lower, we can model the contribution from each pump to the overall concentration of CA in the chamber using the following:

$$C_{\mathrm{dye}}(t) = C_{\mathrm{Hdye}}F_1(t) + C_{\mathrm{Ldye}}F_2(t), \quad [3.2]$$

and

$$C_{\mathrm{Gd}}(t) = C_{\mathrm{HGd}}F_1(t) + C_{\mathrm{LGd}}F_2(t), \quad [3.3]$$

where $C_{dye}(t)$ is the concentration of dye in the measurement chamber, and $C_{Gd}(t)$ is the concentration of Gd in measurement chamber, at time t. C_{Hdye} and C_{HGd} are respectively the concentrations of dye and Gd used in reservoir one, the higher CA concentrations; and C_{Ldye} and C_{LGd} are respectively the concentrations of dye and Gd

used in reservoir two, the lower CA concentrations. $F_1(t)$ and $F_2(t)$ give the normalised instantaneous flow rate for pumps one and two respectively at time t. Since $F_1(t)$ and $F_2(t)$ are varied relative to one another across the full dynamic range of the pumps, we have:

$$F_1(t) + F_2(t) = 1. \quad [3.4]$$

Substituting Equation [3.4] into Equations [3.2] and [3.3] and rearranging yields:

$$C_{\mathrm{dye}}(t) = (C_{\mathrm{Hdye}} - C_{\mathrm{Ldye}})F_1(t) + C_{\mathrm{Ldye}}, \quad [3.5]$$

and

$$C_{\mathrm{Gd}}(t) = (C_{\mathrm{HGd}} - C_{\mathrm{LGd}})F_1(t) + C_{\mathrm{LGd}}. \quad [3.6]$$

Combining Equations [3.5] and [3.6], one can then easily derive the following linear relationship:

$$C_{\mathrm{Gd}}(t) = \frac{C_{\mathrm{HGd}} - C_{\mathrm{LGd}}}{C_{\mathrm{Hdye}} - C_{\mathrm{Ldye}}} C_{\mathrm{dye}}(t) + \frac{C_{\mathrm{LGd}}C_{\mathrm{Hdye}} - C_{\mathrm{HGd}}C_{\mathrm{Ldye}}}{C_{\mathrm{Hdye}} - C_{\mathrm{Ldye}}}. \quad [3.7]$$

Equation [3.7] provides a general model for the conversion of measured dye concentration to Gd concentration, which is only dependent on the reservoir concentrations used, which were constant.

In order to establish the minimum flow rate for the system, full CTC runs of the tumour curve were measured at flow rates from 0.5 to 3.5 ml s^{-1}, in 0.5 ml s^{-1} increments. Two criteria were accessed when selecting the minimum threshold flow rate, namely:

(i) how well the measured curves fit those expected based on the pump voltage input (programmed), assessed by calculating the percentage root mean square error (%RMSE) between the programmed and measured CTCs (RMSE reported as a percentage of the overall enhancement of the tumour CTC);
(ii) the uniformity of CA distribution measured within the chamber, calculated by subtracting a static image with no-flow from several images with flow, taken from different experimental runs during the most rapidly changing portion of the CTC (i.e. ‘wash-in’ region on tumour curve), with percentage uniformity across the resultant images calculated.

Once a minimum flow rate had been established, five full CTC runs were measured for each curve (tumour and healthy). Intraclass correlation coefficient (ICC) analysis was performed on the data to access the repeatability of CTCs produced by the system, and the mean CTCs values taken as the measured ground truth, for comparison with the MR data.

3.2.5. MRI Measurements

To demonstrate the operation of the phantom, DCE-MRI data were acquired using a 3T multi-transmit scanner (*Achieva*; Philips, Netherlands) using a 32-channel detector coil. A 3D spoiled gradient echo imaging sequence was used, with the following scan parameters: TR = 3.8 ms, TE = 1.4 ms, flip angle (α) = 10°, FOV = 224 x 224 x 80 mm^3, spatial resolution = 1 x 1 x 4 mm^3, and number of slices = 20. The parallel imaging factor (SENSE) and number of signal averages (NSA) were varied to give T_{res} values from 1.9 s to 21.4 s, as shown in Table 3.2. Two manually-selected ROIs were used in the analysis of the data, each containing 24 voxels and set within the respective measurement chamber. The relaxivity (r_1) of the CA in aqueous solution was calculated using a multi-flip-angle approach (α = 2° to 20° in increments of 2°) by imaging a phantom containing vials with known concentrations of CA. This phantom was deliberately kept small (60 x 60 x 120 mm^3), and positioned at the centre of the bore in order to minimise any effects of B_1 non-uniformity on the measurements.

Table 3.2: MRI scan parameters, adjusted to achieve temporal resolutions (T_{res}) from 1.9 s to 21.4 s.

Scan Number	*R*-factor (AP / FH)	NSA	T_{res} [s]
1	1.8 / 2	1	1.9
2	1.4 / 1.6	1	3.4
3	1.2 / 1.4	1	5
4	1	1	7.1
5	1	2	14.3
6	1	3	21.4

3.2.6. Data Analysis

The AIF was generated using the method proposed by Parker *et al.* [105] with code developed in *Matlab* at T_{res} values matching those used in the optical and MR studies,

to simulate measurement of the AIF, and was then subsequently used in the analysis of all optical and MR data. All PK modelling was performed using the *DCEMRI.jl* toolkit [147]. The standard Tofts model was used to derive K^{trans}, v_e, and k_{ep} values for the ground truth CTCs (i.e. as measured in the optical experiments) and the MR-measured CTCs, and the percentage differences calculated. The optical data were analysed using a ROI approach (i.e. PK parameters were derived from single mean CTCs, averaged from multiple pixel measurements), and the MR data using both ROI and voxel-wise methods (i.e. PK parameters calculated for multiple CTCs taken from each voxel within the ROI, and mean PK parameter values and standard deviations calculated). The flow diagram presented in Figure 3.8 visually illustrates the steps that were implemented in the acquisition and analysis of the data.

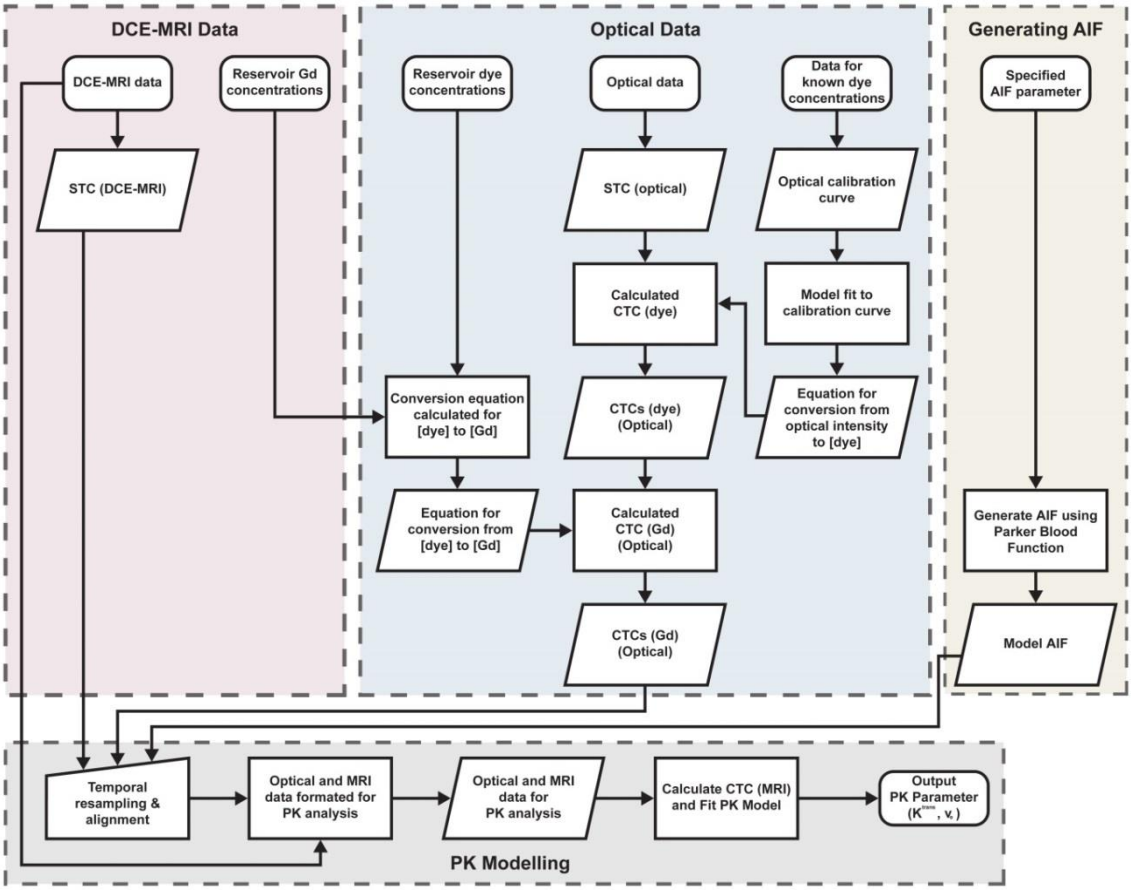

Figure 3.8: Flow diagram illustrating the steps implemented in the analysis of the DCE-MRI and optical data.

3.3. Results

3.3.1. Optical Experiments

The system was demonstrated to be stable, with signal-variation measured to be ≤ 0.4% over a 30-minute period. The %RMSE values between the optically-measured and programmed CTCs were lowest (< 4%) with flow rates ≥ 1.5 ml s^{-1}, with no further decrease in the %RMSE values observed at flow rates greater than 1.5 ml s^{-1}, as shown in Figure 3.9. At a flow rate of 1.5 ml s^{-1} the uniformity of CA distribution across the chambers was measured to be 96%, with uniformity decreasing at lower flow rates, and not changing significantly at flow rates higher than this. This analysis revealed a clear threshold minimum flow rate for the phantom setup of 1.5 ml s^{-1}, and as such this flow rate was used for all subsequent experiments. Excellent reproducibility was demonstrated by the very good correlation measured between the five consecutively-measured CTCs for both curve shapes (tumour and healthy) as illustrated in Figure 3.10, with high ICC values of 0.996 and 0.998 for healthy and tumour CTCs respectively. Average values from each of the five measured CTCs were converted to Gd concentration (using Equation [3.7]), and used as the measured ground truth CTCs in subsequent MRI experiments. PK parameters values were also calculated from each of the optically-measured CTCs, with the mean values taken as the ground truths. Ground truth K^{trans} values were measured to be 0.123 ± 0.001 min^{-1} and 0.233 ± 0.002 min^{-1}, and v_e 0.355 ± 0.001 and 0.461 ± 0.002, for healthy and tumour CTCs respectively (errors are given by the standard deviation across repeated optical-measurements).

(a) 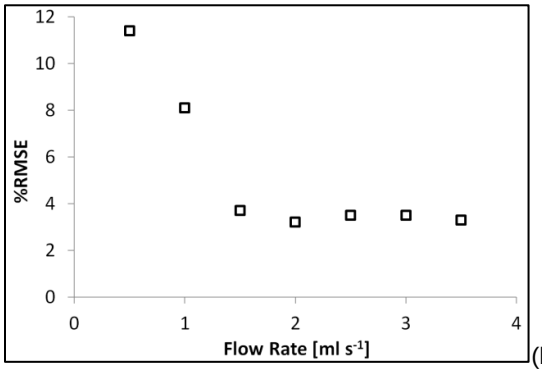

(b) 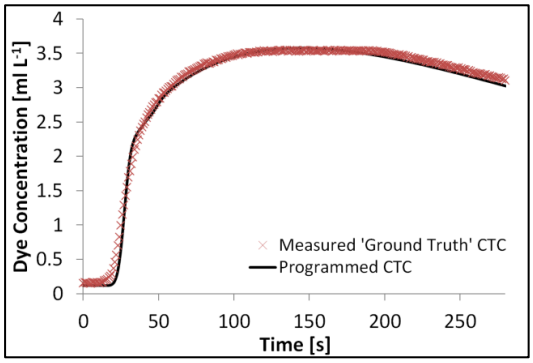

Figure 3.9: Graphs showing: (a) the % root mean square error (%RMSE) values calculated between the programmed and optically-measured CTCs at different flow rates (presented as a percentage of the overall programmed CTCs amplitude); and (b) the programmed and optically-measured ground truth tumour CTCs (measured with 1.5 ml s^{-1} flow rate).

(a) 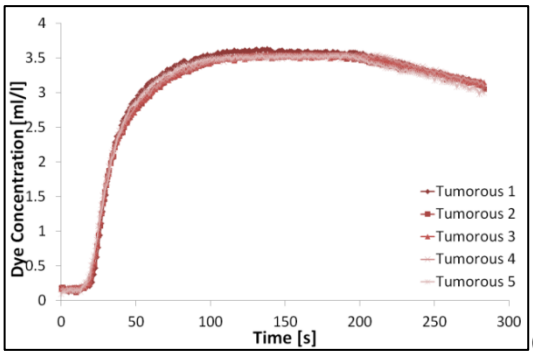

(b) 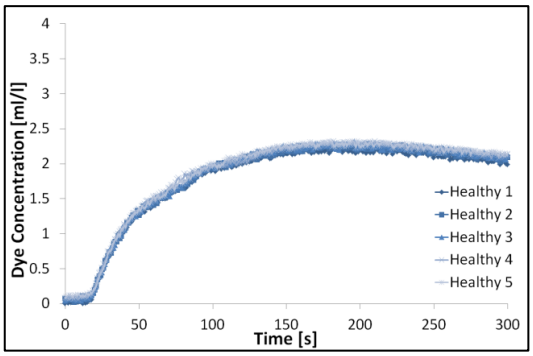

Figure 3.10: Graphs showing five repeated measurements of the (a) tumour and (b) healthy CTCs used in this study, using the optical imaging system at 1.5 ml s^{-1} flow rate.

3.3.2. MRI Experiments

Initial scans of the large anthropomorphic phantom show similar visual appearance to *in vivo* patient prostate scans, as shown in Figure 3.11. Figure 3.12 shows preliminary data comparing the CTCs derived from the MR data with those from the ground truths. All protocols (except for the 5 s T_{res} protocol) measured the healthy-shaped CTC with $R^2 > 0.95$, however only two protocols measured the tumour-shaped CTC with an $R^2 > 0.95$ (T_{res} of 7.1 and 14.3 s).

Given the ability to generate and characterise any arbitrary CTC-shape, it was possible to quantify errors in PK output parameter estimation deriving exclusively from the DCE acquisition protocol. Using specific K^{trans} and v_e values (taken from prior prostate patient studies) to generate CTCs, using the optical imaging system to determine the actual CTCs arriving in the phantom, and finally performing a PK analysis on the optically-measured CTCs (and hence re-deriving the actual 'ground truth' K^{trans} and v_e values that would give rise to this curve-shape); differences between the ground truth PK parameter values and those derived from the MR-measured CTCs could be used to quantify errors in the DCE acquisition protocol. K^{trans}, v_e and k_{ep} values derived from the MR data were found to differ from the ground truths by up to 42%, 31%, and 50% respectively; details of the specific PK parameter errors as a function of the T_{res} used for the DCE acquisitions are presented in Figure 3.13, for both a voxel-wise and ROI analysis of the data. PK parameters derived using these two different methods (voxel-wise versus ROI) differed by < 4%, with all PK parameter values derived using the ROI method within the standard deviations of those derived using the voxel-wise approach. The lowest errors in the measurement of both tumour and healthy K^{trans}, v_e and k_{ep} values occurred using the 7.1-, 21.4-, and 1.9-second T_{res} protocols respectively.

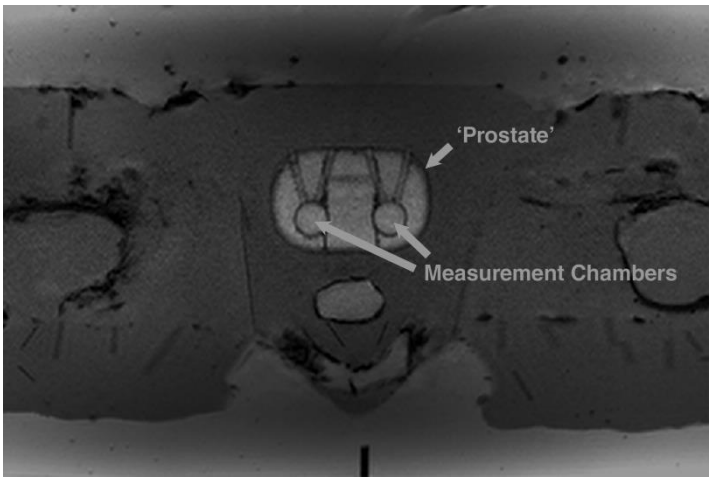

Figure 3.11: Axial T_1-weighted image of the anthropomorphic phantom with the 'prostate' and measurement chambers highlighted. Regions mimicking subcutaneous fat, muscle, and bone are also visable.

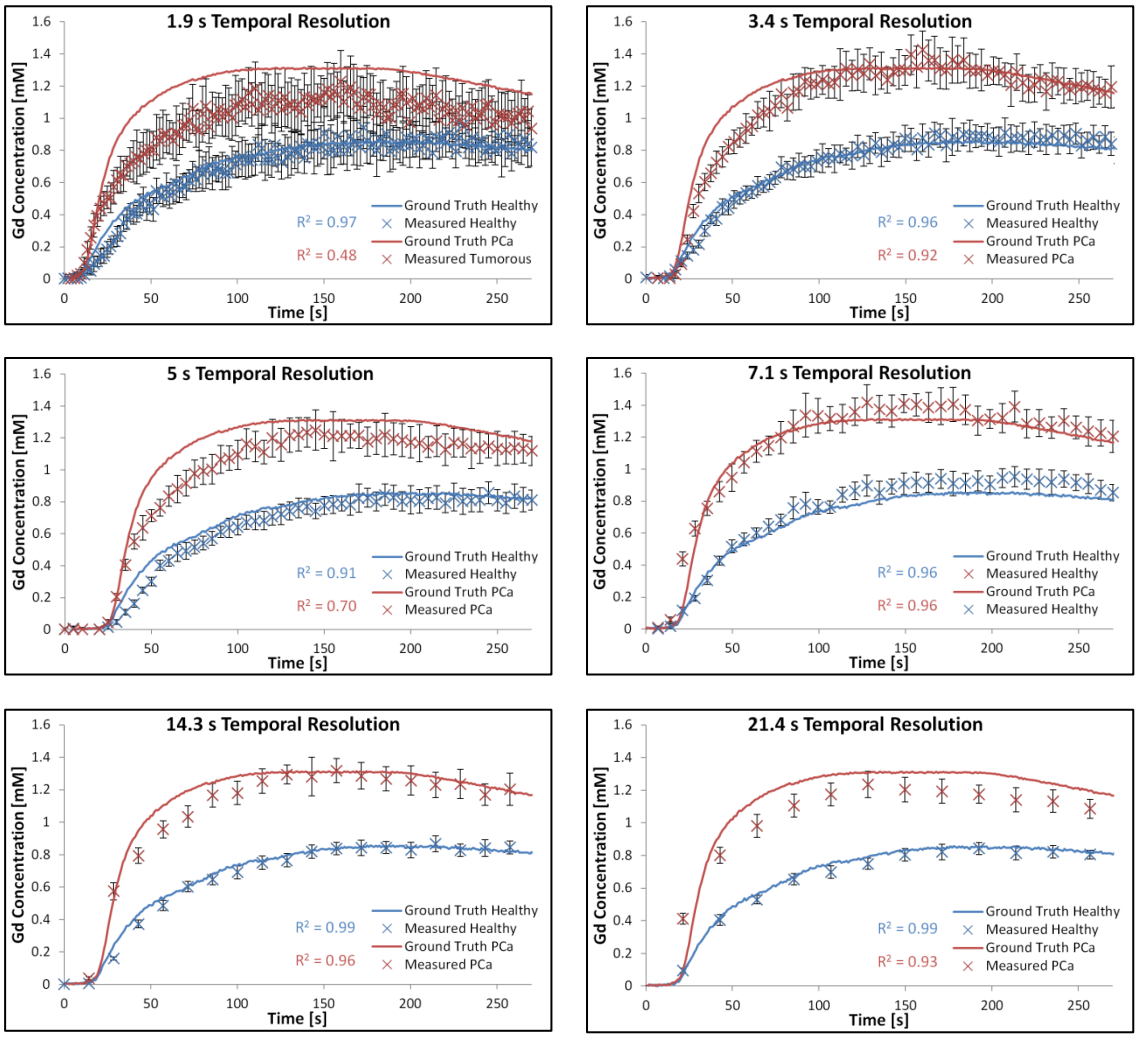

Figure 3.12: Plots presenting tumour and healthy CTCs derived from DCE-MRI data at 1.9 to 21.4 s temporal resolutions, compared with the ground truths derived from optical scanner data.

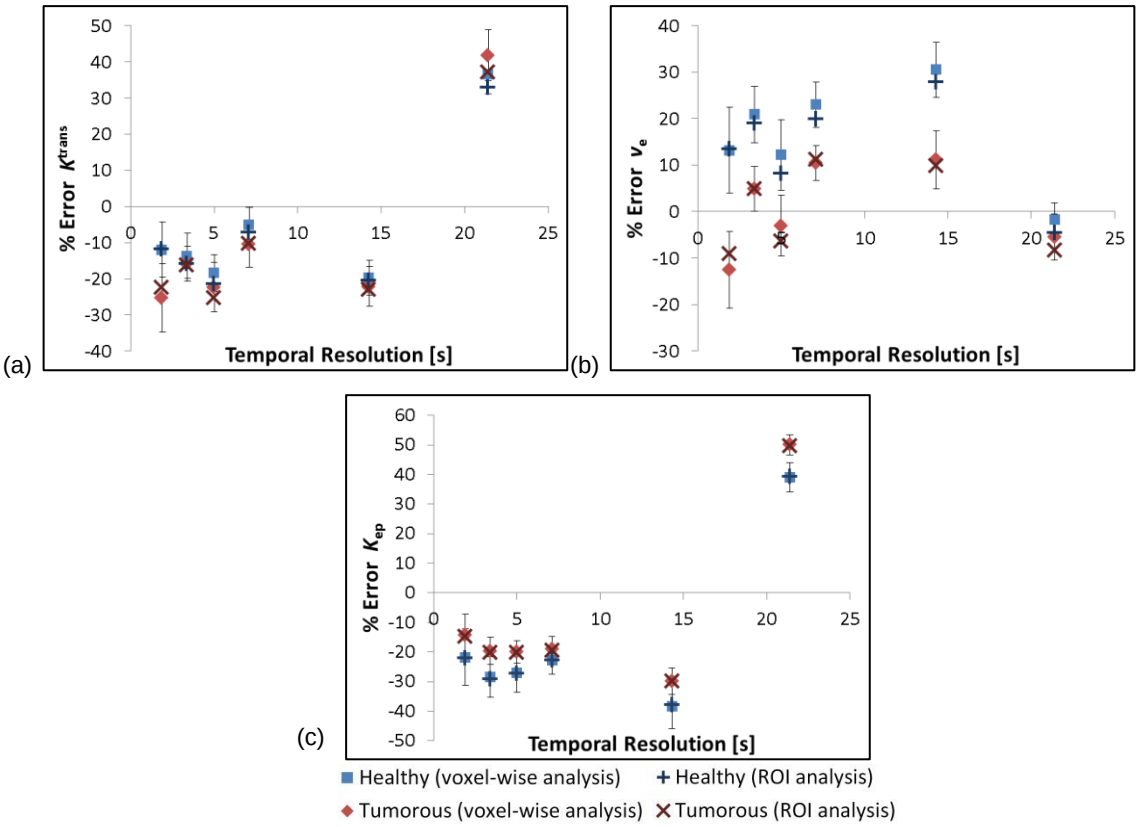

Figure 3.13: Percentage errors in (a) K^{trans}, (b) v_e, and (c) k_{ep} values derived from the DCE-MRI data using the standard Tofts model. Values shown for both a voxel-wise and ROI analysis of the data. Error bars shown for voxel-wise results taken from the standard deviation in the data.

3.4. Discussion

There is currently a lack of standardisation of clinical prostate DCE-MRI image acquisition protocols, particularly in relation to the trade-off which must be made between spatial and temporal resolution, with studies in the prostate tending to give preference to either spatial resolution [148, 149] or temporal resolution [14, 15]. The European Society of Urogenital Radiology presented guidelines which recommend a T_{res} of ≤ 15 s and spatial resolution of ≤ 0.7 x 0.7 x 4 mm^3 [135]; however, there is growing consensus that T_{res} values much lower than 15 s are required when PK models are used to analyse the data [22]. The effect on measurement accuracy of pushing the temporal resolution to these values remains unclear, and to date it has not been possible to quantitatively assess measurement errors deriving from acquisition protocol-related factors. It has rather been assumed that such protocols accurately measure slowly-changing CTCs, such as those in healthy tissue and most tumours, whereas only rapidly-changing tumour CTCs, and AIFs in particular, pose a problem for MRI measurement. However, the results presented herein using the novel quantitative

phantom system demonstrate the significant influence the acquisition protocol has on the measured shape of even slowly-changing CTCs.

Key to this determination of accuracy was a precise and accurate knowledge of the ground truth CTC presented to the MRI scanner for measurement. In attempts to characterise the CTCs produced by their phantom systems, previous studies have used repeated MR measurements [150], prediction models [151, 152], and X-ray measurements [141]; however, these system designs do not allow for a true determination of the ground truth against which DCE-MRI measurements can be compared. In the current study the ground truth CTCs were independently determined using a high spatial and temporal resolution, calibrated optical imaging system. The use of a 'ground truth' descriptor for the CTCs in this context was considered reasonable due to the low measurement error associated with the optical imaging system (±0.4% measurement accuracy; ICC > 0.996 for consecutive runs, both tumour and healthy CTCs). Concentration values were derived via a calibration curve, the data for which was acquired by imaging known concentrations of black dye with no flow; however, the same known concentrations were also imaged with flow of 1.5ml s^{-1}, with no measurable differences observed between the two datasets. Differences between the programmed and optically-measured CTCs translated to an 18% maximum difference between the programmed and optically-measured ground truth PK parameters values, for the CTCs used in the study. However, the resultant ground truth PK parameters values were still well within the range of patient-derived values for tumour and healthy prostate tissue reported in the literature [145]. Furthermore, repeat optical experiments demonstrated the ability of the phantom system to precisely reproduce contrast curves with these PK parameter values, with low standard deviations of <1.2% recorded for all optically-measured ground truth PK parameter values.

The choice of flow rate used in the phantom device struck a balance between minimising discrepancies between the programmed and optically-measured CTCs (which imposed a lower limit on the flow rate that could be used) and reducing the potential for flow artefacts in the MR images (which mitigated against using very high flow rates). Discrepancies between the programmed and measured CTCs occur at lower flow rates due to two principal factors: (i) excessive longitudinal mixing along the length of the tubing caused by diffusional and turbulent flow effects which adversely affected the shape of the CTCs produced; and (ii) an incomplete flushing of the solution within the entire volume of the measurement chamber at each time-point within

a DCE run, resulting in undesired dye (and hence MR contrast agent) concentration variations within the chambers. This latter effect was noted in an earlier study involving computational fluid dynamics of flow profiles in measurement chambers of similar design to that used herein [143]. In the current study, a flow rate of 1.5 ml s^{-1} was found to be sufficient to eliminate this effect, as determined by the highly-uniform (> 96%) dye distribution measured within the measurement chambers. This flow rate also marked the threshold at which the %RMSE between the programmed and measured CTCs was minimised (< 4%).

There were minor differences between the two modalities (optical and MRI) in where and how the signal was measured; for example, the ROI used for the optical experiments encompassed data from approximately 90% of the measurement chamber's volume, whereas with the MRI experiments the ROI analysis was performed on voxels measured in a 4 mm slice taken through the centre of the chambers. However, since the phantom system provided highly-uniform distribution of CA within the measurement chambers at the flow rate used, one may assume that the concentration measured at a particular voxel in the MR data is representative of the overall concentration within the chamber, and since the optical experiments also provide a measure of the overall CA concentration within the measurement chamber, direct comparison between the two modalities was possible.

The anthropomorphic phantom design that was developed had an internal complexity and physical dimensions sufficient to present a clinically-realistic challenge to the image acquisition protocols under test, with a specific emphasis herein on prostate imaging although the principal is valid for other body areas. Thus, protocols developed and validated using the phantom can be easily translated to patient studies in the clinic. A visual comparison of the CTCs presented in Figure 3.12 shows discrepancies between the measured and ground truth curve-shapes, and this is reflected in the calculated R^2 values. An apparent bias was observed in the MR-measured curves in the form of an underestimation of the concentration values in the ~ 20 – 100 s time range (see Figure 3.12). This was possibly caused by differences between the 'set' and 'actual' flip angle used for the spoiled gradient echo sequence, deriving from non-uniformities in the B_1-transmit field, this is further investigated in Chapters 5 of this thesis. Of the acquisition protocols tested, it was found that K^{trans} was most accurately measured using a protocol with a T_{res} of 7.1 s. As the parallel-imaging factor was increased with resultant improvement in temporal resolution, the accuracy of K^{trans} measurements decreased by up to 15%, which may be related to

decreased SNR in the images, although other parallel imaging-related factors may also have contributed to these increased errors. Furthermore, as the NSA was increased in subsequent experiments, causing a deterioration in temporal resolution, the accuracy of the measured K^{trans} values also decreased by up to 31%, as one would expect due to the reduced number of sampling points leading to a loss of fidelity in the shape of the measured CTCs, particularly in rapidly changing portions of the curves such as the initial wash-in (on which K^{trans} is strongly dependant), as well as the resampled AIF used for the PK modelling. v_e was measured with the lowest error at T_{res} = 21.4 s, possibly due to more accurate measurement of the CTCs' wash-out section for which v_e is most sensitive. Errors in measured k_{ep} were lowest using T_{res} = 1.9 s, and increased at T_{res} > 1.9 s. These preliminary data highlight the need to further refine acquisition protocols to identify the source of and hence to reduce these errors. These data also demonstrate the critical dependence of the accuracy of PK output parameter values on the quality of the data inputted to the models, whether that be adequate temporal sampling of the uptake curves, or adequate data quality to ensure faithful fitting of the model.

In the preliminary data presented in this chapter, no B_1 corrections to the measured data were performed; however, as previously mentioned, it is likely that any inhomogeneity present may have contributed to errors. Other factors, such as inadequate acquisition duration, inaccuracies in the AIF measurement, and the choice of model fitting regime, may also have contributed to the errors in the MR-measurements. The anthropomorphic nature of the phantom facilitated further investigation of these deviations in ideal performance of the spoiled gradient echo imaging sequence, and is the focus of the work presented in Chapters 4 and 5 of this thesis. The phantom device developed herein was also used in chapter 6 to investigate further potential errors which may arise specifically from the use of rapidly-accelerated techniques such as parallel imaging and compressed sensing. These initial results nevertheless serve to demonstrate the difficulties in performing quantitative measurements using what is substantially a qualitative instrument, that is, a clinical MRI scanner. Precise and accurate knowledge of the ground truth CTC values in the phantom design presented herein, absent in other phantom designs, facilitated a more quantitative approach to DCE-MRI by providing a test-bed on which new and existing acquisition protocols can be quantitatively assessed.

Chapter 4: Effects of acquisition duration and temporal resolution on the accuracy of prostate tissue concentration-time curve measurements and derived phenomenological and pharmacokinetic parameter values

4.1. Introduction

Tissue properties are known to vary significantly between malignant and benign prostate tissues [134], and as such phenomenological curve-shape analysis and pharmacokinetic (PK) modelling of DCE-MRI data shows great promise as a potential non-invasive gold standard imaging technique for prostate cancer (PCa) detection [11], localisation [12, 13], and grading [14, 15]. However, the widespread acceptance of DCE-MRI has been hindered by discrepancies in the published results, mainly as a result of methodological differences between studies. The quality of MR-derived parameters is known to be influenced by the experimental settings governing the data acquisition and hence the measurements [153], with adequate acquisition duration (AD) and temporal resolution (T_{res}) being required for accurate PK model fitting [119, 120] (described in further detail in section 2.4.2). Considering the range of DCE-MRI acquisition and analysis

protocols reported in the literature, and the large variability in data deriving from these varied approaches, it is apparent that a reliable 'gold standard' method is required for determining the measurement accuracy of the contrast agent (CA) concentration-time curves (CTCs), as well as derived parameters, with errors calculated against known ground truth values [119, 154, 155].

As discussed in the preceding chapter, there have been previous attempts to investigate DCE-MRI measurements using model phantom systems [140, 156], however, in none of these systems were the 'ground truth' values known, additionally none of these previous designs have allowed for MR-measurements to be made in an environment which realistically challenges the prostate DCE-MR imaging protocol by closely mimicking conditions observed *in vivo*. Theoretical approaches have also been used to investigate the effects of T_{res} and AD on PK parameters measurement [22, 119]; however, although beneficial in the planning of MRI protocols, a purely theoretical approach does not allow for the full assessment the MR scanner's ability to accurately measure known reference CTCs using a particular protocol. Other studies have used retrospectively resampled patient prostate data to investigate the effects of reduced AD and T_{res} [154, 157, 158], but again the ground truth values are not known and hence the measurement accuracy of the resampled data (or even the fully-sampled data) cannot be assessed. Previous DCE-MRI studies have reported using a wide range of both T_{res} [2 – 30 s] and AD [90 – 760 s] values for the acquisition of data in the prostate [74, 137, 159, 160]. The aim of the work presented in this chapter was to use the novel DCE-MRI prostate phantom test device described in Chapter 3 to quantitatively investigate the effects of T_{res} and AD on the accuracy of MR-measured prostate tissue CTCs (which mimic those observed in patient prostate data), and on the phenomenological and PK parameters derived from these CTCs, across a range of T_{res} and AD values used in previously published prostate DCE-MRI studies.

4.2. Materials and Methods

4.2.1. MRI Measurements

DCE-MRI data were acquired using a 3T multi-transmit scanner (*Achieva*; Philips, Netherlands) using a 32-channel detector coil. A 3D spoiled gradient echo imaging sequence was used, with the following scan parameters: TR = 4.3 ms; TE = 1.4 ms; flip angle (α) = 10°; FOV = 224 x 224 x 80 mm^3; spatial resolution = 1 x 1 x 4 mm^3; no

parallel imaging (*R*-factor); and number of signal averages (NSA) = 1; resulting in a T_{res} of 8.1 s. This protocol was then modified by applying parallel imaging (PI; SENSE) to produce protocols with T_{res} values of 2, 3.8, and 5.3 s (*R*-factor (AP / FH) = 2 / 2, 1.8 / 1.3, and 1.3 / 1.3 respectively). Additionally, the NSA was increased to produce protocols with T_{res} = 16.3 and 24.4 s (NSA = 2 and 3 respectively). This resulted in six scanning protocols, with T_{res} values across a range which was in line with those used in previously published prostate DCE-MRI studies. Each 720-second experimental run consisted of at least five dynamic scans measured at the baseline CA concentration and with the remaining dynamics measured for a further 600 s (i.e. AD = 600 s). The fully-sampled MR data thus acquired was then retrospectively truncated to produce sub-sets of data at AD = 480, 360, 240, 180, 120, 60, and 30 s.

4.2.2. Concentration-Time Curves (CTCs)

'Healthy' and 'tumour' tissue-mimicking CTCs were generated using an inversion of the standard Tofts model [84], a population-average AIF as proposed by Parker *et al*. [105], and input PK parameters taken from representative published patient data (K^{trans} = 0.14 ('healthy) and 0.36 ('tumour'); v_e = 0.47 ('healthy) and 0.55 ('tumour')) [74, 161]. The CTCs consisted of 120 seconds of baseline data, followed by a 600-second physiological CTC shape mimicking those typically observed in healthy or tumour tissue. Ground truth CTCs were established from repeated measurements made using the highly precise, high spatiotemporal-resolution optical imaging system described in Chapter 3. Concordance correlation coefficient (CCC) analysis was performed on the repeat optical measurements, using *SPSS* (*v. 22.0*, IBM Corp, USA), with high reproducibility calculated between repeat optical experimental CTC runs (CCC = 0.992, 95% confidence intervals = 0.990, 0.993).

4.2.3. Data Analysis

A population average AIF [105] was used in this chapter for the analysis of all optical and MR data, which was generated using code developed in *Matlab* (*R2015b*, MathWorks, USA) at temporal resolutions matching those used in the optical and MR studies. CCC values were calculated between the MR-measured and ground truth CTCs (AD = 600 s); the CTCs were temporally-aligned (MR-measured and ground truth), and ground truth CTC temporally-resampled to match the MR data-points prior to analysis. CCC

values were used as a metric for both the precision (ρ, the Pearson correlation coefficient, a measure of the degree of scatter) and accuracy (C_b, a bias correction factor, the degree of systematic location and scale shifts) of the full CTC measurements [162]. The *wash-in* (the maximum slope between the time of onset of contrast inflow and the time of peak intensity) and *wash-out* (the maximum slope of the late-wash phase of the curve) rates [14] were calculated from the CTCs at two manually-selected regions of interest (ROI), each containing 26 voxels and set within the respective measurement chamber (voxel-wise analysis), as illustrated in Figure 4.1. Voxel-wise PK modelling using the standard Tofts model was also performed at the same ROIs using the *DCEMRI.jl* toolkit [147]. *Wash-in*, *wash-out*, K^{trans}, and v_e values were derived from the MR-measured CTCs and compared with the ground truth values (derived from the optically-measured CTCs), with the percentage differences calculated.

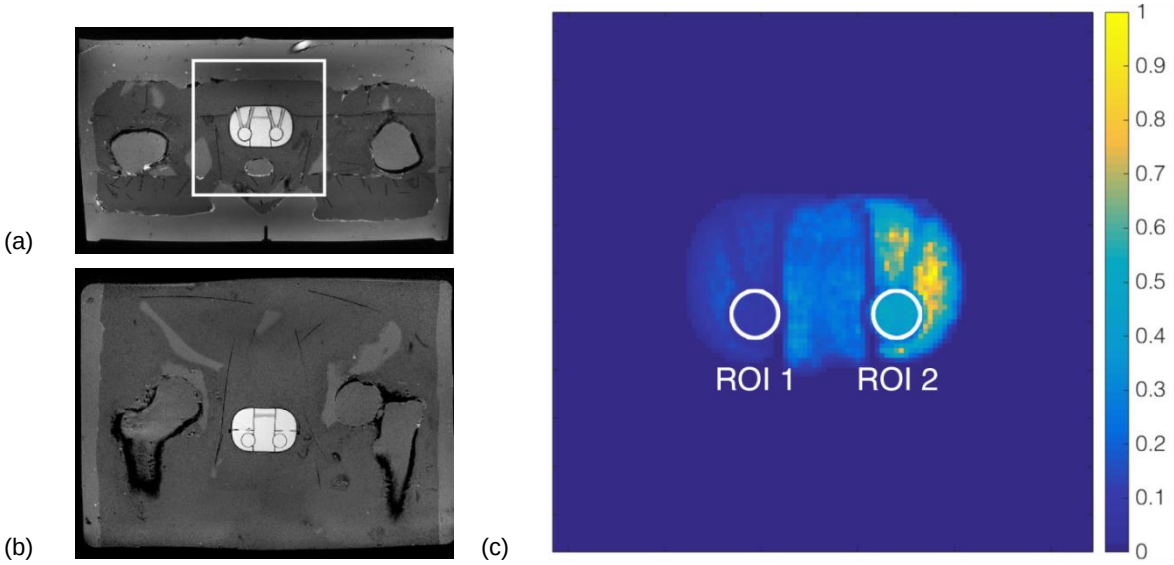

Figure 4.1: Representative T_1-weighted (a) axial and (b) coronal scans of the phantom during peak enhancement within the 'prostate' region. The white box in (a) outlines the region shown in (c). (c) Example pharmacokinetic parameter map (K^{trans}) showing the ROIs placed within the measurement chambers which were used to measure the 'healthy' (ROI 1) and 'tumour' (ROI 2) parameter values

SNR values were calculated in the same ROIs used for the CTC analysis using a 'difference method' [163], based on the evaluation of a difference between two repeated acquisitions at baseline concentration, given as:

$$\mathrm{SNR}_{\mathrm{diff}}(b_1, b_2) = \frac{\frac{1}{2}\bar{S}_{\mathbf{r}\in\mathrm{ROI}}(S_{\mathrm{N}}(\mathbf{r}, b_1) + S_{\mathrm{N}}(\mathbf{r}, b_2))}{\frac{1}{\sqrt{2}}\sigma_{\mathbf{r}\in\mathrm{ROI}}(S_{\mathrm{N}}(\mathbf{r}, b_1) - S_{\mathrm{N}}(\mathbf{r}, b_2))}, \qquad [4.1]$$

where $\bar{S}_{\mathbf{r}\in\mathrm{ROI}}$ is the mean signal value and $\sigma_{\mathbf{r}\in\mathrm{ROI}}$ is the standard deviation, for calculations performed at each imaging voxel ($\mathbf{r}$) in the ROI, and $S_N(\mathbf{r},b_n)$ is the signal

at each imaging voxel in the ROI for each respective baseline measurement (b_1 and b_2). A difference method was chosen for the SNR calculations, instead of one of the more commonly used '2-region' approaches, since parallel imaging (PI) was employed in this study which is known to influences the spatial noise distribution, and as such only methods of SNR measurement remain valid that determine the noise at the same spatial position as the signal [163].

4.3. Results

Figure 4.2 shows representative images from approximately the same time-point within the dynamic series at the 'tumour' CTC peak at each of the T_{res} values tested. The measured SNR values derived from the DCE-MRI data are indicated in each image, showing how the SNR increased as the T_{res} was decreased.

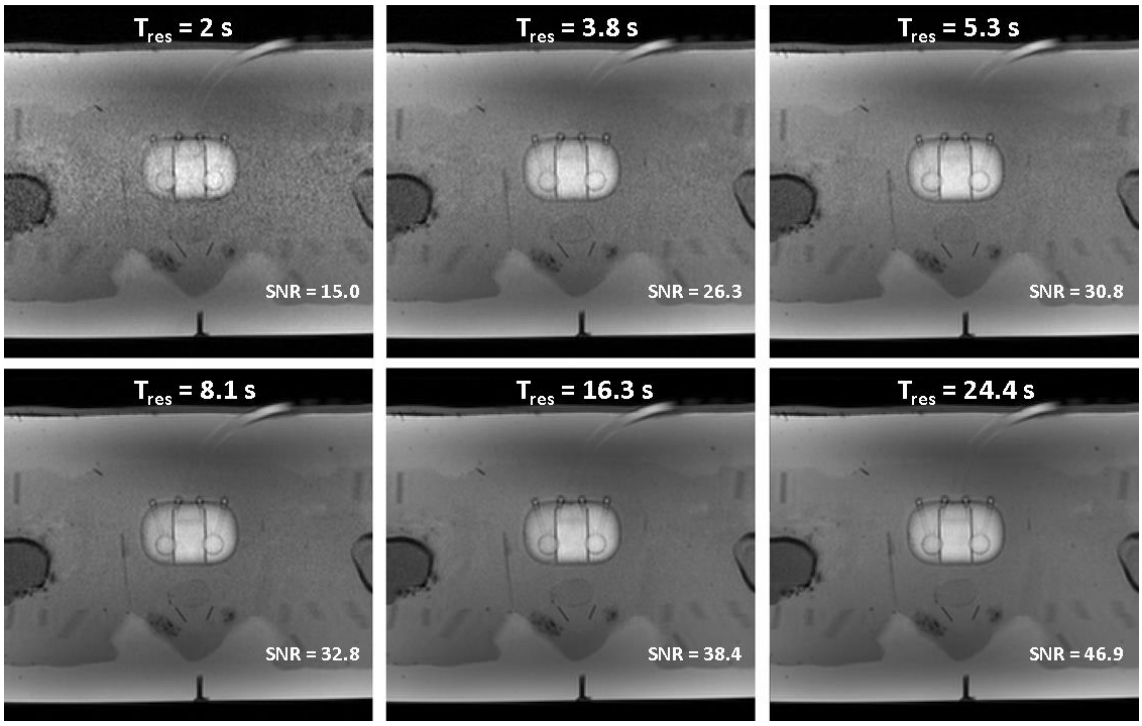

Figure 4.2: Representative images from approximately the same time-point within the dynamic series at the CTC peak (tumour) at each of the temporal resolution (T_{res}) values tested. SNR values derived from the DCE-MRI data are also presented. (SNR results presented herein should be treated as relative, for the purpose of highlighting relative behavioural trends in the data)

Furthermore, this increase in SNR was evident in the MR-measured CTCs as a decrease in signal variation across the ROIs, resulting in a reduction in the calculated uncertainties, as shown in Figure 4.3. Figure 4.3 also shows an underestimation in the measurement of the 'tumour' CTC peak using protocols with T_{res} < 8.1 s, as well as an

overestimation of the wash-out phase of the tumour CTC for all protocols tested. Ground truth CTCs are shown in this figure as solid red ('tumour') and blue ('healthy') lines.

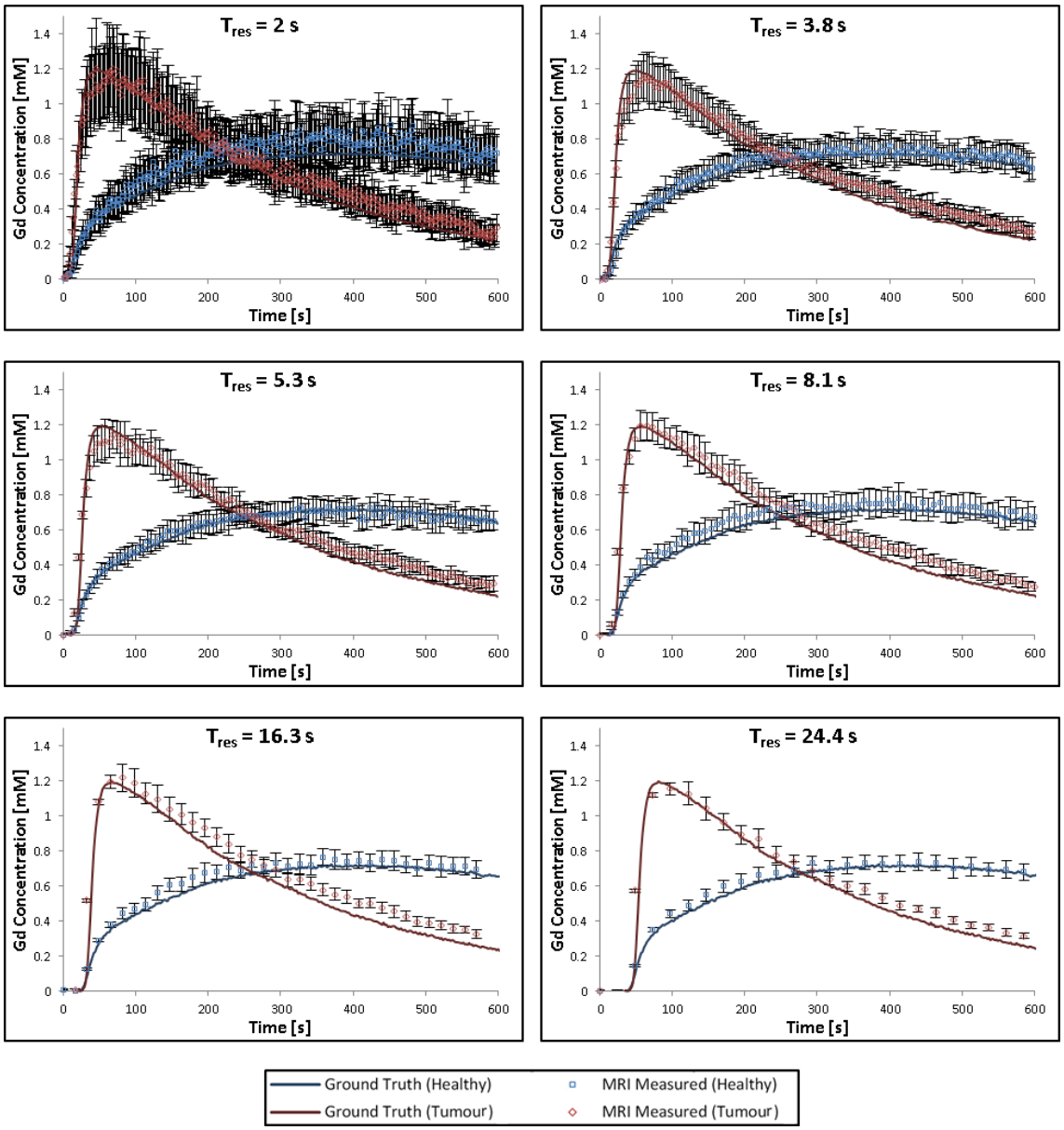

Figure 4.3: Graphs showing the MR-measured CTCs at different temporal resolution (T_{res}) values, with error bars derived from the standard deviation across the ROI. The larger error bars for shorter T_{res} times reflect the decreased SNR in these datasets. Ground truth CTCs are also shown as solid lines.

Figure 4.4 shows the correlation plots comparing the MR-measured and ground truth CTCs, as well as the CCC values with 95% confidence intervals. Inaccuracies in the measurement of the wash-in phase of the 'tumour' CTC were evident as outlying data points, when using T_{res} values $\leq$ 8.1s. Using the fastest protocol (T_{res} = 2 s), there was an overestimation of the MR-measured healthy CTC at higher concentration (> 0.3

mM), and these measurement inaccuracies were also apparent in the relatively low CCC value of 0.906 (95% C.I = 0.889, 0.920). There was a general trend for higher CCC values for the lower-T_{res} data.

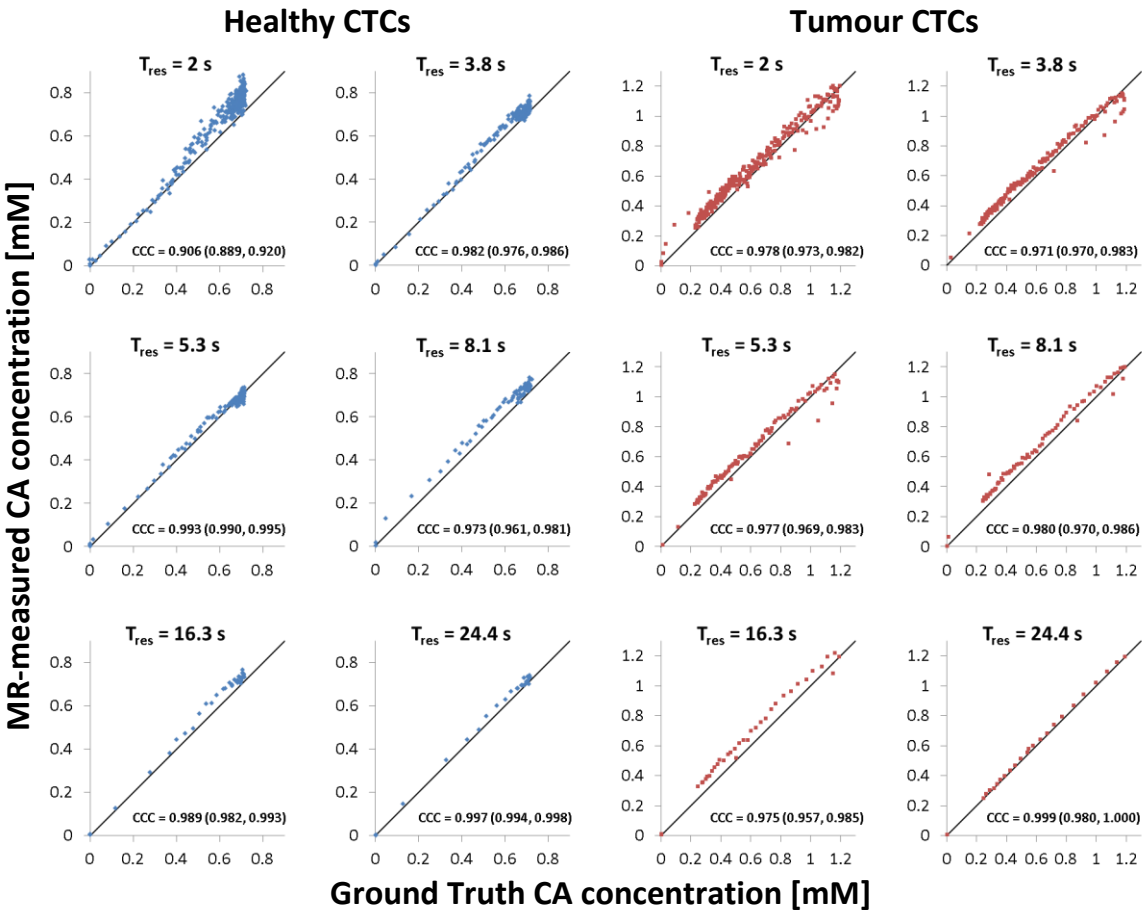

Figure 4.4: Correlation plots of the MR-measured versus ground truth CTCs for full 600-second CTC measurements. The diagonal line indicates equality, with divergence from this line indicating discrepancies between the MR-measured and ground truth values. The CCC values are also shown, along with their 95% confidence intervals.

Errors in the measured *wash-in* and *wash-out* parameter values are presented in Figure 4.5. For the measurement of the *wash-in*, despite the fact that the standard deviation across the ROI was reduced with increased T_{res} (as evident by a reduction in the size of the error bars), large underestimation errors of up to 40% were measured using protocols with T_{res} values $\geq$ 16.3 s. Errors in the measurement of the tumour CTC *wash-out* did not vary greatly across all T_{res} values tested, with all errors < 15%; however there was large variation in the *wash-out* values calculated across the ROI for the 'healthy' CTCs (as evident by the large uncertainties of up to ±65%, see Figure 4.5), indicating that all protocols struggled to measure this portion of the 'healthy' CTC accurately.

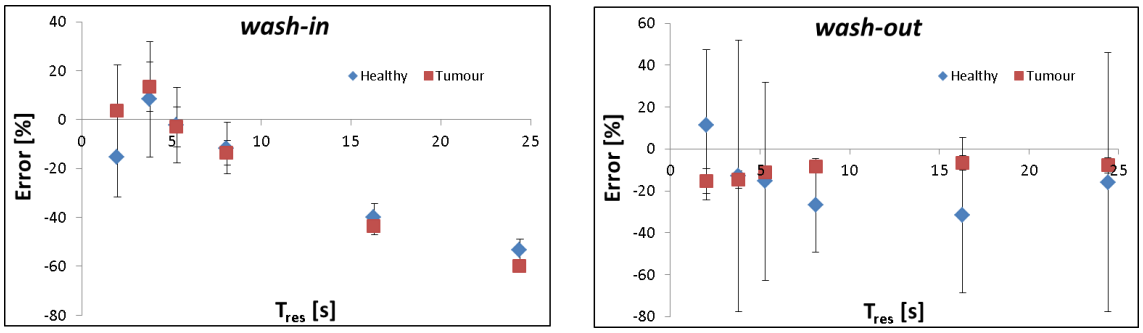

Figure 4.5: Percentage errors in *wash-in* and *wash-out* parameter values derived from the DCE-MRI data at different temporal resolutions (T_{res}) using the standard Tofts model. Error bars derived from the standard deviation of the data.

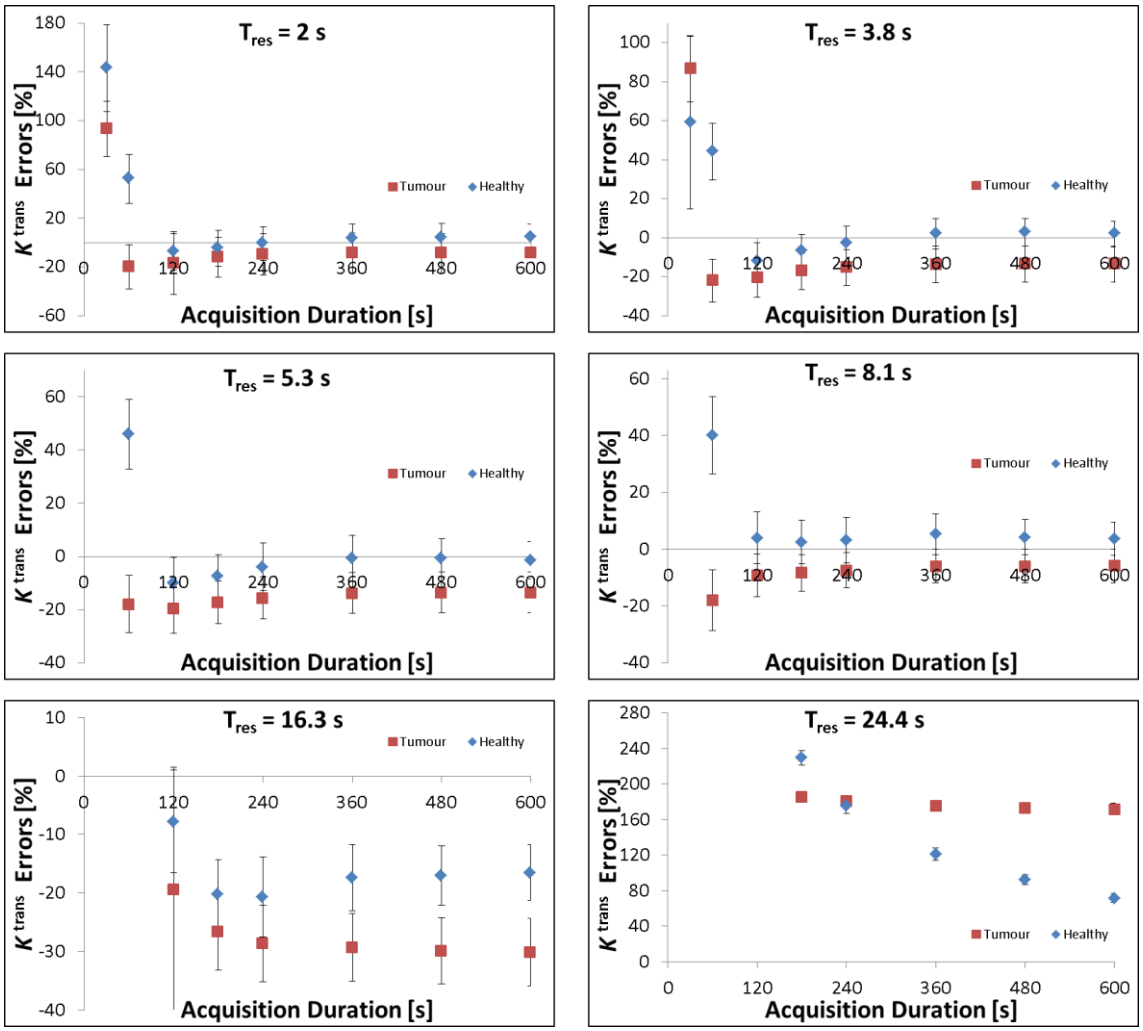

Figure 4.6: Percentage errors in K^{trans} values derived from the DCE-MRI data at different temporal resolutions (T_{res}) and acquisition durations using the standard Tofts model. Error bars were derived from the standard deviation of the data.

Figures 4.6 and 4.7 present the percentage errors in the PK parameter values derived from the DCE-MRI data at different T_{res} and AD values using the standard Tofts model.

K^{trans} and v_e values derived from the MR data differed from the ground truth values by up to 230% and 98% respectively. Errors of < 14% were found for all MR-measurements of K^{trans} made at AD ≥ 360 s and T_{res} ≤ 8.1 s. The 24.4-second protocol was the least accurate in the measurement of K^{trans}, with errors of up to 172% using the full 600-second acquisition: these errors increased as the AD was reduced, as shown in Figure 4.6 (bottom-right graph). For the measurement of v_e, errors of < 12% were measured at T_{res} ≤ 16.3 s, with AD ≥ 360 s. As with the measurement of K^{trans}, the greatest errors in the measurement of v_e were observed in data measured at T_{res} = 24.4 s. The lowest overall errors (< 10%) in the measurement of both 'tumour' and 'healthy' K^{trans} and v_e values occurred using: T_{res} = 2 s, with AD ≥ 360 s.

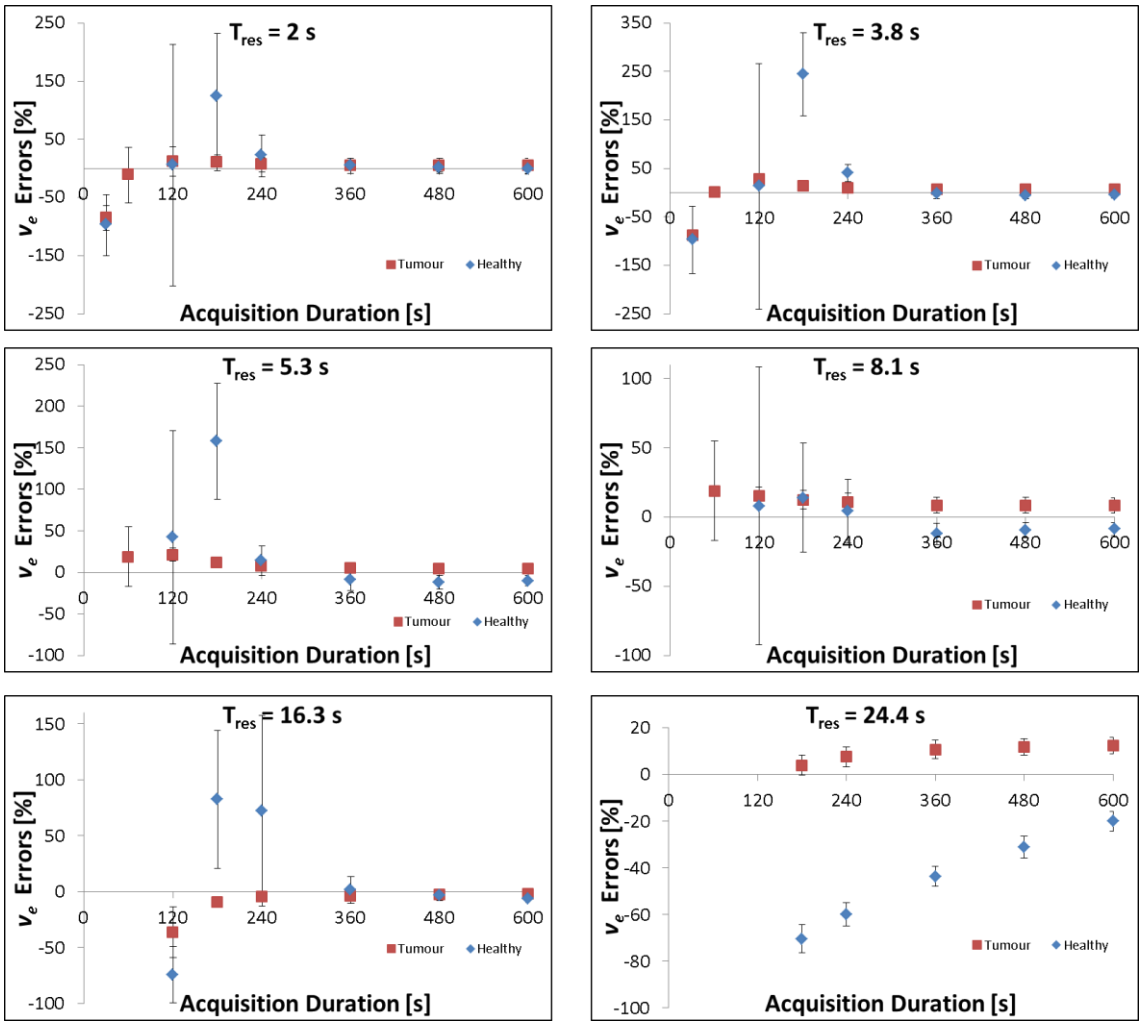

Figure 4.7: Percentage errors in v_e values derived from the DCE-MRI data at different temporal resolutions (T_{res}) and acquisition durations using the standard Tofts model. Error bars derived from the standard deviation of the data

4.4. Discussion

The results of this chapter demonstrate the trade-offs which arise from modifications of a prostate DCE acquisition protocol involving two of the most widely varied acquisition parameters: temporal resolution and acquisition duration. This was possible through the use of a novel phantom device wherein precisely-known ground truth CTCs could be repeatedly produced and presented to the MRI scanner for measurement, and hence the accuracy of the measured CTCs, as well as phenomenological and PK parameter values derived from these CTCs, could be determined.

The data presented herein for a standard 3D SPGR DCE imaging sequence (with a T_{res} of 8.1 s) demonstrates that non-negligible errors in *wash-in*, *wash-out*, K^{trans} and v_e parameters occur for both tumour and healthy tissue-like regions. The measured CCC values increased with decreasing T_{res}, indicating greater precision and accuracy in the point-by-point measurement of the CTCs; however, further parametric analysis of the CTCs showed that the reduced number of data points, resulting from larger T_{res} values, hindered the accurate measurement of certain important curve-shape features. Prior studies have reported that model-free phenomenological parameters, such as the *wash-in* and *wash-out* rates, increase the specificity and sensitivity for prostate cancer detection compared with other diagnostic techniques, even when using T_{res} values as high as 30 s [13, 64]. However, the actual *wash-in* and *wash-out* rates were not known in these studies, but rather a relative comparison of the measured rate values across the prostate area was performed. The current work demonstrates that a T_{res} value $\leq$ 8.1 s is, in fact, required for accurate measurement of the absolute *wash-in* rate.

Conflicting data has been published in the literature regarding the effect of T_{res} on PK parameter measurements. For example, in a theoretical simulation study, Aerts *et al*. reported that the T_{res} requirements were strongly related to the actual PK parameter values being measured, with higher T_{res} required for the precise measurement of larger K^{trans} values [119]. The physical data from the current study corroborates these theoretical findings, with up to 50% greater precision in the measurement of the lower (healthy) versus higher (tumour) K^{trans} values observed, as well as twice to ten-times higher accuracy in the measured K^{trans} values (using T_{res} of $\leq$ 8.1 s). At lower T_{res} K^{trans} accuracy decreased significantly due to inadequate sampling of the wash-in portion of the curves. T_{res} had less effect on the accuracy of v_e measurements, with errors found to be fairly consistent at up to approximately 10% for T_{res} values $\leq$ 16.3 s (AD = 600 s),

increasing moderately to approximately 20% using T_{res} = 24.4 s; in this case, a variation in the number of sampling points due to modified T_{res} did not cause a major hindrance in the measurement of the final peak value of the CTCs, a key component for the accurate measurement of v_e. This is in line with the recent findings of Ginsburg *et al*., where it was reported that the effect of temporal resolution was significantly different for estimates of K^{trans} than for v_e [154]. Another recent study reported no significant effect of varying T_{res} on PK parameter values [158]; however, T_{res} values of 5 - 30 s in this study were obtained by a retrospective resampling of the original T_{res} = 5 s data set, with a relative comparison among datasets used to explore any PK parameter changes, without knowledge of the absolute ground truth values.

Reported acquisition duration (AD) values have also varied widely in published DCE-MRI studies, again with conflicting results presented. In one theoretical study, AD values greater than 420 s were found to offer no improvement in PK parameter estimation for T_{res} values of less than 10 s, whereas below 420 s the precision in the measurement of higher K^{trans} values was found to decrease [119]. Conversely, another study investigated the effect of retrospectively reducing the AD of patient prostate DCE data on the measured K^{trans} and v_e values reported no statistical difference using acquisition lengths as short as 150 s for the former and 50 s for the latter [157]. However, these results were based on a 'full-acquisition' length of only 250 s, against which the PK parameter values measured from retrospectively-reduced data sets (AD = 50, 100, 150, and 200 s) were compared in a relative sense, and hence any potential CTC truncation effects (particularly on v_e measurements) are unknown. In the current study, large errors in 'healthy' v_e values were measured for AD values ≤ 240 s, which may be attributed to the appearance of the peak in the 'healthy' CTC at approximately 345 s: the v_e parameter estimation from PK model fitting is critically dependent on the CTC reaching a clearly-identifiable peak, with some degree of subsequent wash-out, in order for the model fit to produce an accurate v_e value. For instance, this explains why, in the current study for the 'tumour' CTC used (where the peak of the CTC appeared at approximately 35 s), a reasonably good v_e measurement accuracy was maintained to AD values as low as 180 s (< 13% error using all T_{res} values tested). Thus the findings in reference [157] that ADs as low as 50 s did not significantly change the measured v_e values may only be valid for certain CTC shapes with peaks occurring at early time points (for example, as found typically in malignant tumours with fast wash-in / wash-out profiles) and hence cannot be generalised.

Indeed, this critical dependence on an adequate AD for the accurate measurement of

v_e for different tissue / tumour types may explain the wide discrepancy in published v_e values and the consequent perceived lack of diagnostic sensitivity and specificity to prostate cancer detection. One such example is provided by a study by Chen *et al.*, which reported no significant difference for v_e values measured in tumour verses healthy prostate tissue which, in the light of the present study's results, may have been strongly influenced by the short 120 s AD used for the measurements [15]. On the other hand, the authors did report that the measured K^{trans} values were significantly higher in tumour tissue compared with healthy tissue, even at the short 120 s AD [15], and this was also seen in the present work where the AD was not found to exert a strong influence on the accuracy of K^{trans} measurements for AD values $\geq$ 120 s and for $T_{res} \leq$ 8.1 s. Considering the critical dependence of the accuracy of the K^{trans} parameter estimation on the initial wash-in slope of the CTC, this result is perhaps not surprising. Indeed, the results presented herein, along with those of certain previous patient studies, suggest that acquisition times as low as 120 s could be justified if K^{trans} is the sole object of any PK modelling exercise. On the other hand, if v_e is also to be measured, longer acquisition durations are required. In establishing an optimum AD, clinical studies will also need to consider the potential detrimental effect of patient movement with longer dynamic scan times [120]. However, various image registration techniques, specific to DCE, are being developed which may go some way to mitigating these effects [164, 165]. Such effects could be investigated using the current phantom system, using techniques similar to previous phantom studies where motion was simulated [166].

The phantom used in the present study was designed to be anthropomorphic in both size and complexity, mimicking the conditions associated with abdominal patient imaging; as such, the protocols tested herein faced the same challenges, such as B_1 and B_0 inhomogeneity, and potential inadequate spoiling and off-resonance effects, all of which may have contributed to the errors in the MR-measurements. Although some of these homogeneity issues were compensated for in the data presented in this chapter, further work using this quantitative phantom-based approach (presented in the following chapters) probed these effects in more detail.

Chapter 5: Effects of temporal resolution, voxel-wise flip-angle correction, and model-fitting regime on the accuracy and precision of arterial and prostate-tissue contrast-time curve measurements and derived pharmacokinetic parameter values

5.1. Introduction

5.1.1. AIF Measurement

The arterial input function (AIF) is a measure of changes of the contrast agent (CA) concentration over time in a blood vessel feeding the tissue of interest before, during, and after intravenous bolus injection of a CA, and is critical to retrieve pharmacokinetic (PK) perfusion parameters using certain models in quantitative DCE-MRI [77, 84, 88, 90], with the choice of AIF affecting the accuracy of derived PK parameters [92, 93, 167]. Various methods have been proposed for estimating the AIF which include: direct measurement in each individual patients [57, 85, 95]; indirectly deriving the AIF for each individual patient from a well characterised reference tissue, such as muscle [67, 91,

[110]; or mathematically-formulating a population-average AIF [57, 103-107], as discussed previously in Section 2.3.3.

Although various population-averaged parameterised forms of the AIF have been proposed and are widely used, both in scientific studies and clinically, these do not take into account inter-patient physiological variability, and as such derived PK parameter values may not be accurate to the actual patient-specific values. Furthermore, the use of a population average AIF has also been shown to greatly increase sensitivity to B_1-transmit (B_1^+) field non-uniformity, since the AIF and tissue concentration-time curves (CTCs) are not affected by the same B_1^+ errors, considering that the AIF is not measured from the acquired DCE-MRI data in this case [168, 169]. Additionally, the manner in which the original data were acquired, on which these population average AIF are based, has an impact on the physiological relevance of these AIFs for use in prostate DCE-MRI data analysis. For example, the popular biexponential Weinmann plasma curve (Equation [2.35]) [57], which has been utilised in a number of prostate DCE-MRI studies [103, 170, 171], was derived from blood samples acquired at low temporal resolution, which impeded the ability to correctly measure the intrinsic features of the AIF curve, such as the bolus first pass and recirculation; in fact, these features are not even represented in this model, as shown in Figure 5.1. Further, the blood samples were collected from the right cubital vein (a superficial vein located in the arm), and as such this AIF is not representative of the actual CA concentration input function feeding the prostate, and hence it is not an appropriate model to use for PK analysis in the prostate.

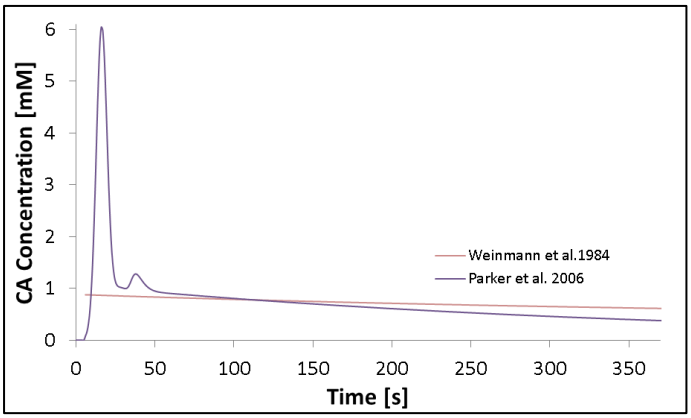

Figure 5.1: Graph showing the empirical mathematical formulations for the arterial input function (AIF) as proposed by Weinmann *et al*. and Parker *et al*.

Another widely used mathematical formulation of the AIF is the 10 parameter model proposed by Parker *et al*. (given previously as Equation [2.36]) [105]. This more complex

model of the AIF was derived from relatively higher temporal resolution DCE-MRI datasets (temporal resolution (T_{res}) = 5 s), and in this case the AIFs were measured in either the descending aorta or iliac arteries (the data was taken from patients with either abdominal or pelvic tumours). Although this model may be a reasonable approximation of the AIF as measured in the iliac artery that feed the prostate, the fact that this model is a derived from data taken from various sites in the patients means that it is not possible to affirm that this is indeed the case. Further, as with any population averaged AIF proposed in the literature, the AIF profile proposed by Parker was strongly influenced by the methodologies employed in its formulation, such as the CA dose and injection rate [107, 109], and as such only holds relevant when the same methodologies are employed in the study it is applied to. Additionally, other patient-specific physiological factors such as cardiac output, organ function, and body fat also influence the AIF profile, further limiting the usefulness of a population averaged formation with regards extracting truly patient-specific information from the data.

Other methods for indirectly deriving the AIF, such as variations of the reference region model, have been proposed as a possible alternative to direct measurement in an artery, as these methods relax the requirements on the T_{res} and signal-to-noise ratio (SNR) of the acquisition sequence [67, 91, 110]. However, the patient-specific accuracy of this method is heavily influenced by the choice of 'known' PK parameter values for the reference tissue, usually taken from the literature. Due to this assumption, i.e. that the perfusion conditions for the reference tissue, usually muscle, are the same for all patients, this method cannot provide a true patient specific AIF.

Certain considerations need to be taken into account when designing DCE-MRI protocols, such as choosing an appropriate T_{res} for the anatomical region of interest, correcting for differences between the set and actual flip angle due to non-uniformities in the B_1^+ field, and choosing an appropriate technique for analysing the data. To date a method has been lacking which allows for repeated acquisitions of a known 'ground truth', physiologically-relevant AIF in an anthropomorphic environment which replicates the challenges faced in patient abdominal / pelvic imaging. This has hampered a comprehensive investigation into the absolute accuracy and precision of various DCE-MRI approaches, as implemented at the scanner. There have been previous attempts to investigate the measurement of the AIF using phantom devices, probing effects such as: in-flow, RF spoiling and field non-uniformity, as well as magnitude verses phase derived measurements [102, 172, 173]. However, none of the devices proposed to date were able to produce a physiologically relevant AIF containing all the features observed

in patient-measured curves, with precisely known ground truths established using a modality other than MRI, and in an anthropomorphic environment which mimics the patient's physiology: the phantom device presented in Chapter 3 of this thesis allowed for this.

As discussed in the preceding chapters, the T_{res} values reported in previous prostate DCE-MRI studies vary widely, from ~2 - 30 s [137]. The optimal value to use is unknown and likely to depend on several factors. Even recommendations from simulation studies differ, with some studies reporting that a $T_{res} \leq 1$s is required to accurately capture the rapid changes during the initial bolus passage, and thus was felt to be essential for reliable DCE-MRI quantification of the AIF [22, 174], while another study recommends a T_{res} of 2 – 3 s as adequate to characterise the AIF [121], with further published guidelines specifying that a $T_{res} \leq 15$ s is sufficient for performing PK analysis in the prostate [135, 136]. As with the measurement of the tissue CTCs, which was the subject of Chapter 4, to date a method has been lacking to quantitatively investigate the sampling requirements for the accurate and precise measurement of the AIF *in vivo*. With this in mind, in this chapter methodologies were further developed for use with the phantom device presented in Chapter 3 to allow for the production of a precisely-known, physiologically-relevant AIF with a high level of repeatability. Further, phantom modifications also allowed for the field of view (FOV) to be reduced in the *z*-direction, while still negating any inflow effects by ensuring that an appropriate length of the input tubing was contained within the imaging slab [102]. This allowed for rapid 3D imaging to be performed (T_{res} ~1 s) without the need to use of any accelerated imaging techniques, such as parallel imaging, as was used in the preceding chapter. This AIF could then be measured across a range of T_{res} values from ~1 – 30 s, and the effects of T_{res} on the accuracy, as well as intra- and inter-session precision, quantified.

Advances in MR hardware, acquisition and analysis techniques, as well as computational processing power over the last decade or so, and the subsequent gain in T_{res} and SNR this has provided to DCE-MRI, mean that measurement of an accurate patient-specific AIF *in vivo* is now feasible. One of the aims of the work presented in this chapter was to use a modified version of the phantom test device presented in Chapter 3 to quantitatively investigate the accuracy and intra- / inter-session precision of MR-measured AIFs, as well as to investigate their effects on the derived PK parameter values

5.1.2. Effects of B_1^+ Non-uniformity

Despite the fact that B_1^+-field non-uniformity is thought to be one of the main sources of systematic error in CA concentration measurements [121, 124], and it being known that the B_1^+-field homogeneity can vary by ~30 % for abdominal imaging at 3T [168, 175], the reported use of B_1^+ correction for DCE-MRI studies in the prostate is rare, with a few exceptions [176, 177], although none of these provided a comprehensive evaluation for how the flip angle correction affected the accuracy of DCE-MRI measurements *in vivo*. However several studies have investigated the use of such correction strategies for DCE in other anatomical regions, such as in the breast, reporting large discrepancies between the set flip angle (α_{set}) and actual flip angle (α_{act}) of up to ~55% [178-180]. It is known that these differences between the set and actual flip angles have a strong effect on the accuracy of the PK parameters derived from the data [168]; for example in a simulation study by Buckley and Parker, which was based on patient prostate DCE-MRI data, it was reported that a -30% deviation in flip angle resulted in PK parameter estimation errors of up to 40% [168]. Another recent simulation study by Park *et al*. estimated B_1^+-inhomogeneity-induced flip angle variation using a water phantom and images taken from the brains of three healthy volunteers using a head coil. This data was subsequently used to simulate the effects of B_1^+ non-uniformities on derived PK parameters, reporting that a -23 to +5% fluctuation in flip angle resulted in errors of up to 49% in the derived PK parameter values [181]. In this chapter, the Actual Flip-angle Imaging (AFI) method, as proposed by Yarnykh *et al*., was used to estimate the α_{act} at each imaging voxel [127]. The AFI method allows for a rapid 3D implementation, with minimal post-processing requirements facilitating fast computational time, and providing accurate α_{act} measurements that are highly insensitive to off-resonance and physiological effects, as well as T_1 [127, 182]. This technique is based on a T_1-weighted fast-field echo (FFE) sequence with an arbitrarily set flip angle, α, and two alternating repetition times, where $TR_1 < TR_2$. Here two assumptions are made, namely: (i) that the relaxation effect is non-negligible, and a fast repetition rate of the sequence results in establishing a pulsed steady state of magnetisation; and (ii) that the sequence is ideally spoiled. Below the mathematical formulation used in the AFI method to estimate the α_{act} is derived, as first outlined in reference [127].

In the pulsed steady state, a consecutive solution of the Bloch equation (Equation [2.1]) for the AFI sequence results in the following expression for the longitudinal magnetisations, M_{z1} and M_{z2}, before each excitation pulse:

$$M_{z1} = M_0 \frac{1 - \mathrm{E}_2 + (1 - \mathrm{E}_1)\mathrm{E}_2 \cos\alpha}{1 - \mathrm{E}_1\mathrm{E}_2\cos^2\alpha}, \quad [5.1]$$

and

$$M_{z2} = M_0 \frac{1 - \mathrm{E}_1 + (1 - \mathrm{E}_2)\mathrm{E}_1 \cos\alpha}{1 - \mathrm{E}_1\mathrm{E}_2\cos^2\alpha}, \quad [5.2]$$

where M_0 is the equilibrium magnetisation,

$$\mathrm{E}_1 = \exp\left(-\frac{TR_1}{T_1}\right), \quad [5.3]$$

and

$$\mathrm{E}_2 = \exp\left(-\frac{TR_2}{T_1}\right). \quad [5.4]$$

The observed signals, S_1 and S_2, are proportional to the above magnetisations, M_{z1} and M_{z2}, and the ratio, r, of the measured signals can be expressed as a function of α, TR_1, TR_2, and T_1, given as:

$$r = \frac{S_2}{S_1} = \frac{1 - \mathrm{E}_1 + (1 - \mathrm{E}_2)\mathrm{E}_1 \cos\alpha}{1 - \mathrm{E}_2 + (1 - \mathrm{E}_1)\mathrm{E}_2 \cos\alpha}. \quad [5.5]$$

For short TR_1 and TR_2, the first-order approximation can be applied to the exponential terms, such that:

$$\exp\left(-\frac{TR_\mathrm{n}}{T_1}\right) \approx 1 - \frac{TR_\mathrm{n}}{T_1}, \quad (\mathrm{n} = 1, 2) \quad [5.6]$$

and thus Equation [5.5] can be simplified to:

$$r \approx \frac{1 + n\cos(\alpha)}{n + \cos(\alpha)}, \quad [5.7]$$

where

$$n = \frac{TR_2}{TR_1}. \quad [5.8]$$

Therefore, we can use the signal ratio, r, to approximate the α_{act} independent of T_1 as:

$$\alpha_{act} \approx \arccos\left(\frac{rn-1}{n-r}\right), \quad [5.9]$$

allowing for the α_{act} to be estimated at each imaging voxel. This information can then be used to correct the DCE data for the effects caused by non-uniformity in the transmit B_1 field.

5.1.3. Linear Versus Non-Linear Least-Squares Model Fitting

In the majority of DCE-MRI studies reported in the literature, kinetic parameters were estimated by fitting the PK model using a non-linear least-squares (NLS) approach [86]. However, using a linear least-squares (LLS) method has several advantages, which include: faster computational time, better model fitting under low SNR conditions, and less sensitivity to T_{res} [87, 88]. For both the NLS and LLS approaches, finding the 'best fit' of a model to the data involves the minimisation of a merit function, which in the case of this study is the sum of the squares of the differences between the measured data points and the model estimated points. However, results from NLS fittings of the Tofts model are highly dependent on the initial estimates of the constants to be calculated [86], which is not the case for LLS fitting, as this method does not require any initial parameter estimation. In 2004, Murase *et al*. introduced a linear version of the Tofts model and used simulations to demonstrate its advantages over a NLS approach [88]. Since then this linear interpretation of the Tofts model has been used in many DCE-MRI studies of several anatomies, including the prostate [183, 184], breast [185, 186], liver [187], and brain [188]. However, to date no study has been able to properly quantify the performance of this PK modelling approach, owing to a lack of knowledge of the ground truth curves; in this chapter data from the DCE-MRI phantom device was used to this end.

There were three main aims to the work presented in this chapter, namely to use a modified version of the phantom device presented in Chapter 3 to quantify the effects of (i) T_{res}, (ii) voxel-wise flip-angle correction (VFAC), and (iii) the use of a linear verses non-linear version of the standard Tofts model, on the accuracy and intra- / inter-session precision of the MR-measured AIFs and CTCs, as well as the derived PK parameters.

5.2. Materials and Methods

5.2.1. Phantom

One limitation of the phantom described in Chapter 3 was that it did not allow for the use of an imaging protocol with a FOV smaller than the width of the prostate section without artefacts corrupting the data, due to the inflowing spins not reaching a steady-state by the time they entered the measurement chamber (see Section 2.4.5). In order to facilitate the use of an ultra-fast 3D protocol the phantom was modified to include an additional measurement section. These modifications, shown at various stages of construction in Figure 5.2 (b) and (c), allowed for a thin FOV to be placed through the phantom in the axial plane, as illustrated in Figure 5.2 (a), which encompassed enough of the feeding tubing (150mm) to ensure the spins reached a steady-state before entering the measurement chamber. This was informed by a simple set of experiments performed using the unmodified phantom, wherein the phantom was imaged several times using the same protocol used for the phantom DCE experiments in this chapter, but with varying imaging volume widths in the *z*-direction (i.e. with different lengths of the feeding tubing encompassed by the imaging volume [across the range: 20 - 100 mm]), while pumping baseline CA concentration at the flow rate used in all experiments (1.5 ml s^{-1}). This revealed that > 50 mm of both of the 3.2mm internal diameter tubes (which feed each measurement chamber) were required to be contained within the imaging volume in order to negate any inflow effects

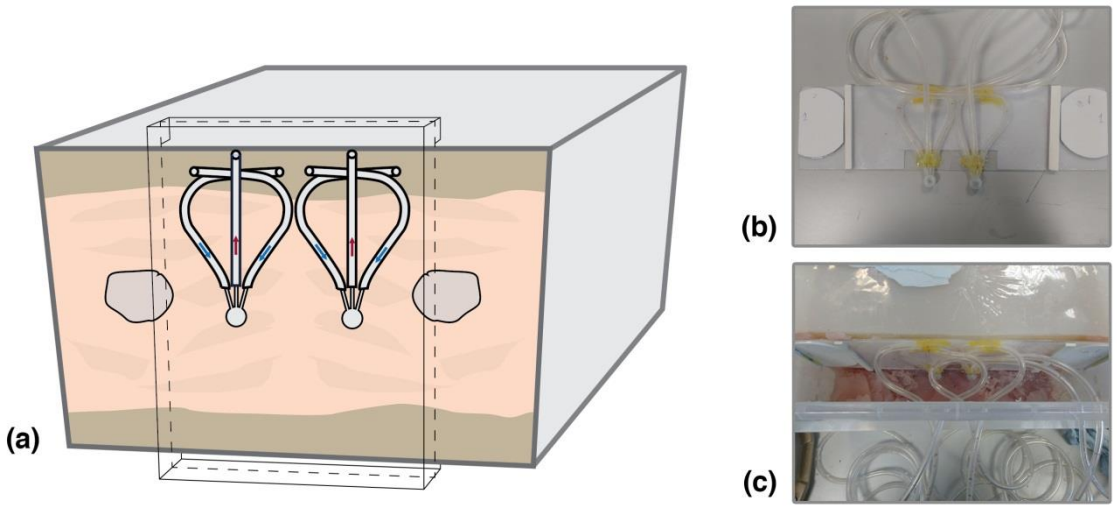

Figure 5.2: (a) Diagram of modified section of the phantom, showing the input tubing set within the imaging volume, with direction of flow indicated. Photographs showing (b) the additional 2 chambers added into the phantom device and (c) the two chambers and tubing *in situ* in the phantom.

The modified phantom device allowed for the simultaneous production of two distinct CTCs, each produced within a separate measurement chamber, the geometry of which was the same as the measurement chambers previously described in Chapter 3 for use in the 'prostate' section. The chambers were surrounded with heterogeneously distributed tissue-mimicking materials with T_1 and T_2 properties similar to that of the tissue found in the abdomen, as described in Chapter 3. The CTCs were produced using the same computer-controlled four-pump system previously described, pumping liquid containing the Gd-DTPA CA (*Multihance*; Bracco, USA), and at the same low flow rate previously used (1.5 ml s^{-1}).

5.2.2. Extraction of in vivo AIF Data

In order to establish an appropriate, physiologically-relevant curve-shape for the AIF used in this phantom study, prostate DCE data from an earlier *in vivo* patient study was used, acquired with T_{res} = 3 s, and with AIFs measured close to the prostate gland in the feeding artery (the internal iliac artery). In this retrospective study, DCE data from 81 patients with clinical suspicion of PCa (abnormal results from prostate specific antigen (PSA) screening and / or digital rectal exam) who were recruited onto a clinical research study were analysed. These research subjects underwent a multi-parametric prostate examination prior to a 12-core biopsy. The MR protocol included: including high-resolution T_1-weighted and T_2-weighted imaging, diffusion-weighted imaging, spectroscopic imaging, and DCE imaging using a Philips 3T MR imaging system (*Achieva*; Philips, Netherlands) with an 8-channel phased array detector coil coupled with an endorectal coil. Inclusion criteria included the patient's ability to undergo endorectal coil prostate MRI and exclusion criteria included any contraindication to MRI using Gd-based CAs.

Of the 81 research subjects recruited onto this study, it was only possible to accurately extract AIF data from 32 of these for the following reasons:

- 41 patients were excluded due to gross motion during the DCE scan; the lack of use of a muscle relaxant such as butylscopolamine bromide (*Buscopan*; Boehringer-Ingelheim, Ingelheim, Germany) [133] in the study was likely the reason for this high degree of motion artefacts encountered
- 8 patients were excluded due to the size/orientation of the vessel, i.e could not place an ROI with voxels ≥ 4 and completely avoid signal contamination from the vessel walls (see Section 2.4.4)

The presence or absence of PCa in each of these 32 patient datasets ultimately used was irrelevant for this retrospective study, since only the AIF data measured in the internal iliac artery was used from the DCE data, which was assumed to not be influenced by the presence or absence of cancer in the prostate.

The *in vivo* patient DCE data were acquired using a 3D spoiled gradient echo imaging sequence with the following scan parameters: TR = 5.5 ms, TE = 2.0 ms, α = 15°, FOV = 256 x 265 x 60 mm^3, spatial resolution = 1 x 1 x 6 mm^3, number of signal averages (NSA) = 2, and number of slices = 10. A SENSE parallel imaging factor (*R*-factor) of 2 was used, which gave a T_{res} of 3.1 s, with 116 dynamics being acquired giving an acquisition duration ~360 s. 0.1 mM kg^{-1} of Gd-based CA (*Gadovist*; Bayer, Germany) was administered in an antecubital vein using a syringe pump (rate 4 ml s^{-1}), followed by 20 ml saline flush. The protocol included a minimum of 5 baseline scans prior to contrast injection for estimation of baseline signal intensities. An ROI (4-8 voxels) was manually defined at a central slice in the internal iliac artery and AIFs derived from the measured STCs using Equation [2.18]. Care was taken when defining the ROIs to avoid the vessel walls, ensuring that the measured signal originated from the blood plasma only, thereby avoiding any partial volume effects. All 32 MR-measured AIFs were then temporally aligned and the mean taken as the representative patient population-average AIF (AIF_{PA}) for use in this study.

5.2.3. Ground Truth AIF

Firstly, the AIF_{PA} was converted from Gd to black dye concentration using an inverted form of Equation [3.7]. The pumps used in the phantom system were intrinsically limited with regards how rapidly they could effect a change in concentration at the phantom. As such, in order to produce the smooth, rapidly-changing curve-shape of the patient-data-derived AIF_{PA}, the natural slew rates of the pumps used in the system was exploited. First a string of square wave pulses at the maximum voltage for the required flowrate, and at widths of 5, 10 , 15, 20, 25, and 30 s, were programmed and the change in black dye concentration over time was measured using the optical imaging system (as described in section 3.2.2). A pulse width of 10 s was chosen as a starting point for the 1st peak of the AIF, with a shorter, lower-amplitude pulse chosen for the 2nd peak, and the 'wash-out' phase of the AIF was programmed using the data from this section of the patient derived data. Though a set of iterative, empirical experiments, where the programmed voltage-time profile was slightly modified between

consecutive runs and the black dye concentration measured, a programmed voltage-time profile was developed which produced an AIF curve-shape which closely correlated with the MR-measured population average (concordance correlation coefficient (CCC) $\geq$ 0.99). The 'ground truth' AIF, AIF_{GT}, was then established from 9 repeat-optical measurements: five measured consecutively on the same day, and a further four measured on separate days, with CCC and root mean square error (RMSE) values also calculated in order to establish the accuracy and intra- / inter-session precision of the phantom system. All statistical data analyses were performed using *SPSS* (*v.22.0*, IBM Corp, USA).

5.2.4. Ground Truth Tissue CTCs

As with the work presented in Chapters 3 and 4, 'healthy' and 'tumour' tissue-mimicking CTCs were generated using the standard Tofts model [84], and in the case of this study, the optically-measured AIF_{GT}, and input PK parameters representative of those observed in patient data (K^{trans} = 0.13 ('healthy) and 0.70 ('tumour'); v_e = 0.29 ('healthy) and 0.34 ('tumour')) [145, 189]. CTCs consisted of 120 seconds at baseline concentration, followed by a 360-second physiological CTC. Ground truth tissue CTCs were again established from nine repeated optical measurements (five intra-session, five inter-session), as outlined previously.

5.2.5. MRI Phantom Data Acquisition

DCE-MRI phantom data were acquired using a 3T multi-transmit scanner (*Achieva*; Philips, Netherlands) using a 32-channel detector coil. A 'thin-slab' 3D spoiled gradient echo imaging sequence was used, with the following scan parameters: TR = 3.5 ms, TE = 1.6 ms, α = 23°, FOV = 224 x 224 x 18 mm^3, spatial resolution = 1.75 x 1.75 x 6 mm^3, and number of slices = 3. 450 consecutive MR images were acquired at a T_{res} of 1.2 s. A flip angle of 23° was chosen in order to ensure that every concentration in the range used in this study was measured with the lowest possible uncertainty, by optimising the SNR of the measurements while providing a good dynamic range to the measurement based on the TR and concentration ranges used, calculated using the method outlined by Da Naeyer *et al*. [190]. Each experiment consisted of two measurements of the AIF and either the 'tumour' or 'healthy' CTC, each repeated on 5 separate days, and 5-times within the same scanning session, in order to measure the

inter- and intra-session precision of measurements. Each dataset was then retrospectively averaged with using a number of signal averages (NSA) ranging from 2 to 25 (in increments of 1) to give a range of T_{res} values, from the original starting value of 1.2 s, to 30.5 s: this provided a total of 450 DCE-MRI dataset. B_1^+ maps were also acquired using a dual-steady-state sequence with the same geometry and spatial resolution as above and with: TR_1 / TR_2 / TE = 30 ms / 150 ms / 2 ms, flip angle = 60°.

5.2.6. Voxel-wise Flip-Angle Correction (VFAC)

Actual flip angles were calculated at each voxel using the B_1^+ mapping data and Equation [5.9]. CA concentrations were then derived from the data using both the programmed and corrected flip angles, for comparison.

5.2.7. Data Analysis

RMSE and CCC values were calculated between the MR-measured and ground truth AIFs and CTCs; curves were aligned, and ground truths temporally-resampled to match MR data prior to analysis. CCC and RMSE values were calculated for the entire CTC and AIF, and the RMSE is reported as a percentage of the maximum CA concentration change (%RMSE). SNR values were calculated as per the same method outlined in section 4.2.4.

PK analysis was performed by fitting the data with standard Tofts model using both linear least squared (LLS; implemented in *Matlab*) and non-linear least squared approaches (NLS; using *DCEMRI.jl* toolkit [147], as previously used in Chapters 3 and 4) on two manually-selected regions of interest, each containing 12 voxels and set within the respective measurement chamber. K^{trans}, v_e, and k_{ep} values were derived from the MRI-measured CTCs and AIFs, compared with the ground truth values (derived from the optically-measured data), and the percentage differences calculated. PK analysis was performed on all datasets, i.e. T_{res} values from 1.2 s to 30.6 s, with and without flip angle correction, for each of the five intra- and five inter-session datasets.

5.3. Results

5.3.1. Patient Population Average AIF

Figure 5.3 shows the MR-measured AIFs taken from the 32 patients, and Figure 5.4 the mean AIF, taken as the AIF_{PA}, with the standard deviation across all 32 patients represented by the error bars. The AIF_{PA} was fit with the Parker model using a NLS fitting approach (R^2 = 0.98), as also shown in Figure 2.4, with the fit parameters given in Table 5.2.

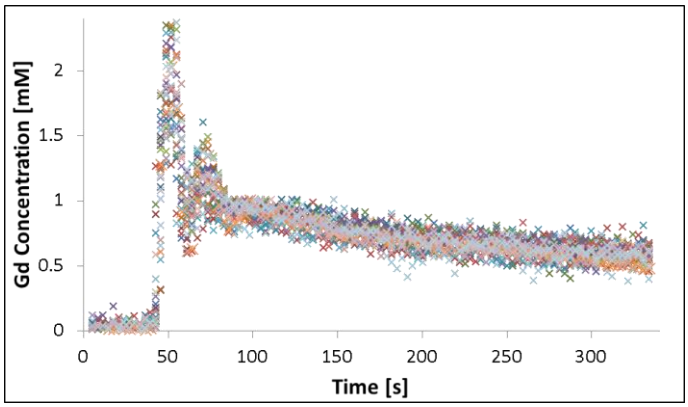

Figure 5.3: Graph showing the arterial input functions (AIFs) derived from 32 patient DCE-MRI datasets.

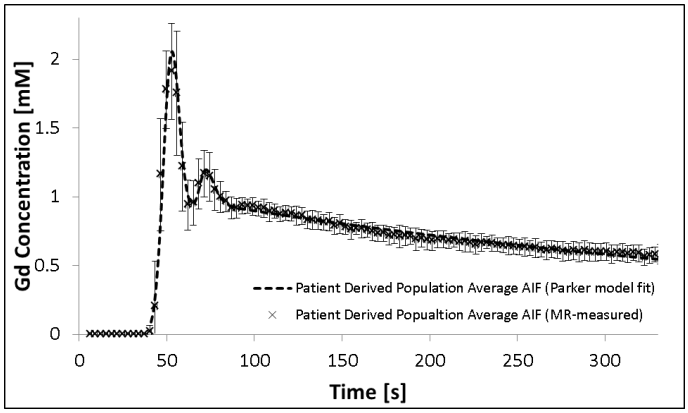

Figure 5.4: Graph showing the population-average arterial input function (AIF), taken as mean of the 32 measured AIFs, with error bars showing standard deviation from the mean, with the Parker model fit also shown.

5.3.2. Ground Truth AIF

The range of CA concentration-time waveforms produced by the phantom pump system at 5 to 35 second square-wave voltage input widths are shown in Figures 5.5 and 5.6.

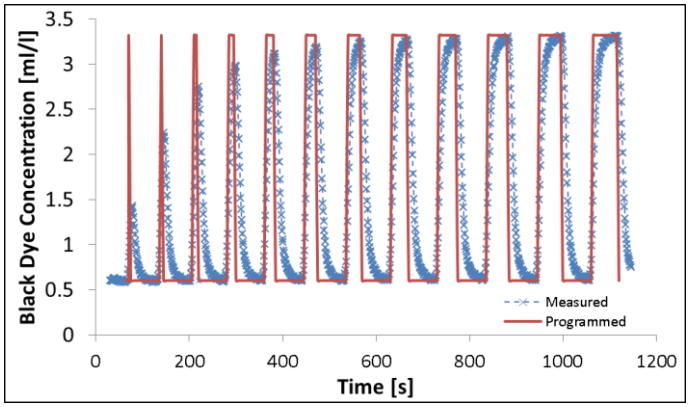

Figure 5.5: Graph showing the intrinsic pump response to square wave voltage inputs of varying widths from 5 to 60 s in increments of 5 s.

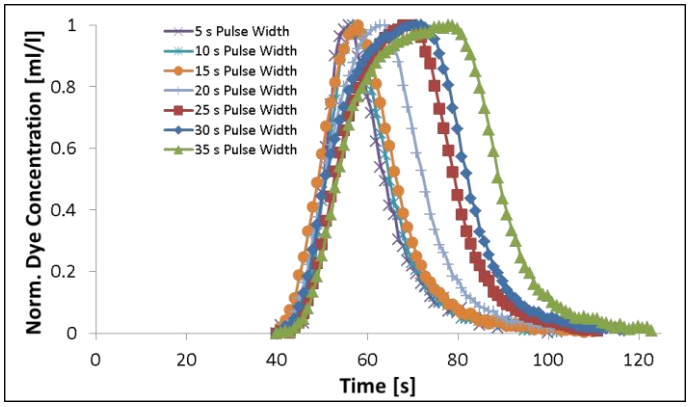

Figure 5.6: Graph the normalised pump response curves all transposed to the same temporal starting position.

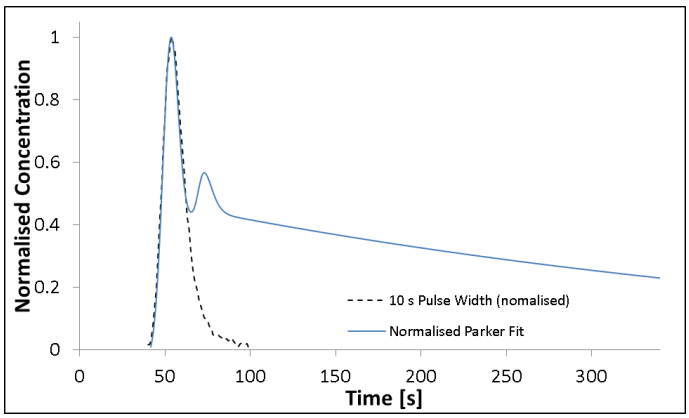

Figure 5.7: Graph showing the patient derived population average AIF (blue plot) and the intrinsic pump response to 10 s square wave input (dashed black plot).

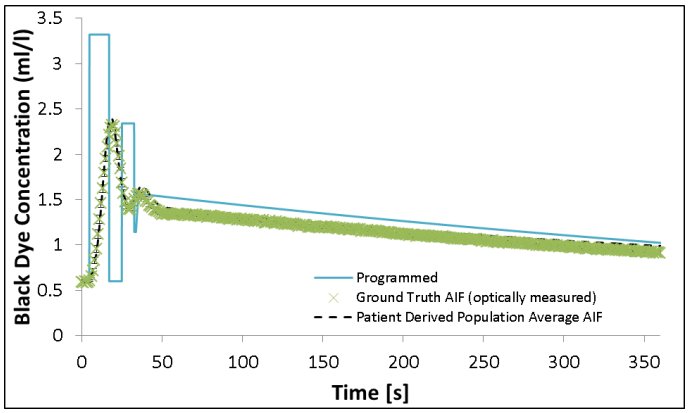

Figure 5.8: Graph showing the patient derived population average AIF (AIF_{PA}; dashed black plot), the empirically-derived input curve required to produce the desired AIF shape (light blue plot), and the resultant optically measured 'ground truth' AIF (AIF_{GT}; green data points).

A 10 s square wave was selected as a starting point when empirically deriving a voltage waveform to produce the AIF, as this waveform produced a response which closely approximated the initial rapidly-changing portion of the AIF curve, as shown in Figure 5.7. The empirically derived 'programmed' waveform used to produce the required AIF shape is shown in Figure 5.8 (cyan plot), along with the AIF_{PA}, which was the target AIF waveform of this experiment, and the resulting optically measured AIF_{GT}.

The AIF_{GT} was taken as the average of nine optical experiments, five from within the same experimental session, and a further four measured on different days. Each individually-optically-measured AIF was then compared with the mean (AIF_{GT}), with all nine measurements having a CCC > 0.995 and %RMSE ≤ 1.1%, as shown in Table 5.1. The AIF_{GT} was then also fit with the Parker model (R^2 = 1.00), with the resulting parameters given in Table 5.2.

Table 5.1: The concordance correlation coefficient (CCC) and pecentage root mean square error (%RMSE) results from repeat intra- and inter-session optical experiements.

	Optical Measurements	
	CCC (95% CI)	**%RMSE**
Session 1	0.997 (0.997, 0.998)	0.8
Session 2	0.995 (0.993, 0.996)	0.6
Session 3	0.996 (0.995, 0.997)	0.9
Session 4	0.998 (0.998, 0.999)	1.1
Session 5A	0.998 (0.997, 0.998)	0.9
Session 5B	0.999 (0.999, 0.999)	0.7
Session 5C	0.997 (0.996, 0.998)	1.1
Session 5D	0.995 (0.992, 0.996)	0.9
Session 5E	0.998 (0.997, 0.998)	0.6

Table 5.2: Parker AIF function parameter values for the MR-measured population average AIF (AIF_{PA}) and the optically-measured ground truth AIF (AIF_{GT}) used in this study.

	A_1	A_2	T_1	T_2	s_1	s_2	a	b	s	t
AIF_{PA}	0.329	0.262	0.188	0.370	0.075	0.128	1.020	0.130	29.239	0.468
AIF_{GT}	0.454	0.132	0.194	0.467	0.092	0.091	1.065	0.166	9.788	0.446

5.3.3. Ground Truth Tissue CTCs

The final AIF_{GT} used in this study is shown in Figure 5.9, given as Gd concentration, with the AIF_{GT} Parker model fit also shown, along with the Parker model fit of the AIF_{PA}. The tissue CTCs generated using the PK parameter values given previously are shown in Figure 5.10 as the respective 'programmed' plots, along with the optically-measured 'ground truth' tissue CTCs for both 'healthy' and 'tumour' tissue. Ground truth PK parameter values were derived by fitting the standard Tofts model using both the LLS and NLS approaches, and the resulting values are presented in Table 5.3.

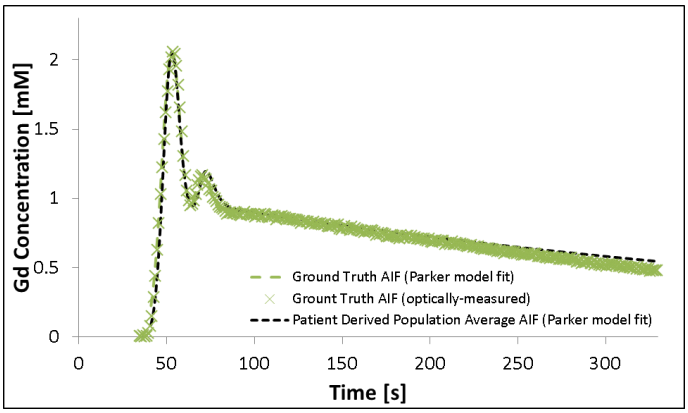

Figure 5.9: Graph showing the mean patient-data derived AIF, the established ground truth AIF, with the Parker AIF model fit also shown

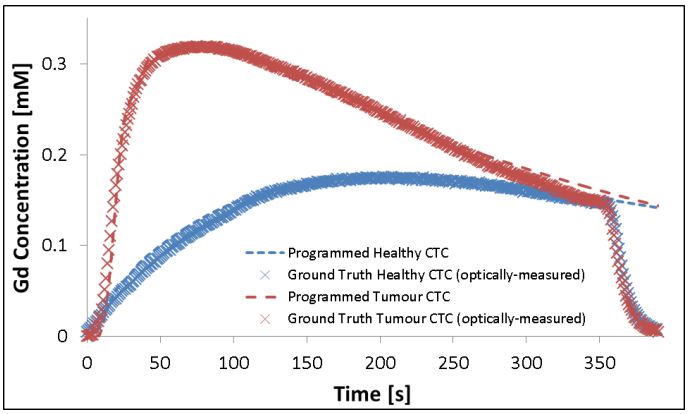

Figure 5.10: Graph showing the programmed and ground truth (optically-measured) tissue CTCs (generated using the standard Tofts model with the ground truth AIF and PK parameters representative of reported patient values).

Table 5.3: Programmed and optically-established ground truth PK parameter, derived by fitting the standard Tofts model using LLS and NLS approaches (± the standard deviation across all 9 experiments)

	K^{trans} [min^{-1}]	v_e	k_{ep} [min^{-1}]
Programmed			
Healthy	0.13	0.29	0.45
Tumour	0.70	0.34	2.06
LLS fit Tofts model			
Healthy	0.112 ± 0.001	0.293 ± 0.001	0.379 ± 0.001
Tumour	0.711 ± 0.001	0.350 ± 0.001	2.028 ± 0.002
NLS fit Tofts model			
Healthy	0.118 ± 0.001	0.291 ± 0.001	0.388 ± 0.001
Tumour	0.719 ± 0.002	0.358 ± 0.001	2.021 ± 0.002

5.3.4. MRI Phantom Experiments

The α_{act} at the ROIs where the AIF and tissue CTCs were measured differed from the set value by between -29% and -33% for all experiments, with inter-session standard deviation in α_{act} calculations of ~2% at any particular voxel, and a maximum recorded standard deviation in α_{act} across any individual ROI (used for the measurement of either the AIF or tissue CTC) of ~3%. AIFs and tissue CTCs derived from the MR-measured STCs with no flip angle correction applied to the data showed large underestimations in the derived Gd concentrations, as shown in Figure 5.11, with correspondingly low CCC values of > 0.42, and %RMSE of up to 14% for the measurement of the AIF (see Table 5.4). These errors were greatly reduced when a VFAC map was calculated and applied to the data, as illustrated in Figure 5.12, with a corresponding gain in the CCC (> 0.83) and %RMSE (< 8%) values, for both intra- and inter-session measurements (see Table 5.4).

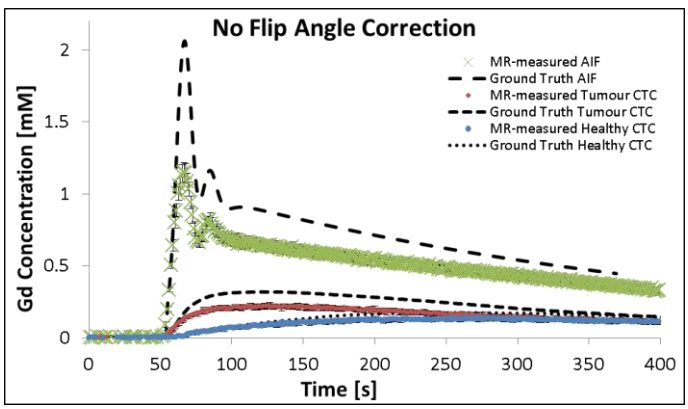

Figure 5.11: Graph showing the MR-measured AIF and tissue contrast contrast-time curves (CTCs) for the non-flip-angle corrected MR data for a single experimental run, with error bars showing the standard deviation across the ROIs.

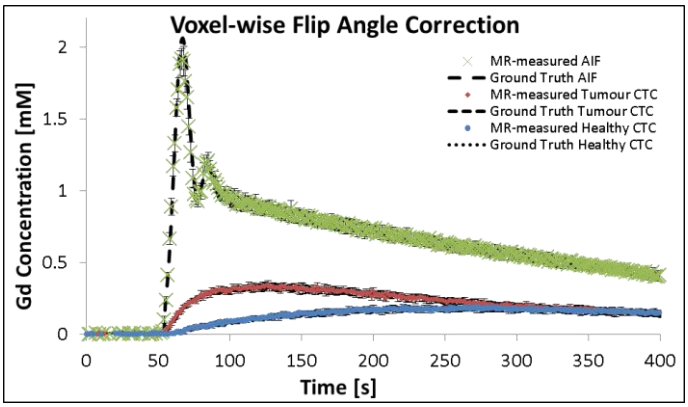

Figure 5.12: Graph showing the MR-measured AIF and tissue contrast contrast-time curves (CTCs) for the voxel-wise flip angle corrected data for a single experimental run, with error bars showing the standard deviation across the ROIs.

Table 5.4: The concordance correlation coefficient (CCC) with 95% confidence intervals (CI) and percentage root mean square error (%RMSE) results from repeat intra- and inter-session DCE-MRI experiments (given with and without voxel-wise flip-angle correction (VFAC).

	MRI Measurements			
	Without VFAC		**With VFAC**	
	CCC (95% CI)	**%RMSE**	**CCC (95% CI)**	**%RMSE**
Session 1	0.528 (0.480, 0.573)	12.1	0.882 (0.855, 0.904)	6.2
Session 2	0.505 (0.457, 0.549)	11.8	0.893 (0.868, 0.914)	5.8
Session 3	0.518 (0.472, 0.561)	12.3	0.920 (0.901, 0.935)	5.2
Session 4	0.464 (0.416, 0.509)	12.6	0.867 (0.837, 0.892)	6.5
Session 5A	0.429 (0.383, 0.473)	14.1	0.839 (0.805, 0.868)	7.4
Session 5B	0.431 (0.382, 0.477)	13.8	0.829 (0.791, 0.860)	7.6
Session 5C	0.449 (0.403, 0.494)	13.6	0.861 (0.830, 0.887)	6.8
Session 5D	0.438 (0.391, 0.483)	13.7	0.847 (0.813, 0.875)	7.2
Session 5E	0.420 (0.373, 0.465)	14.1	0.826 (0.788, 0.857)	7.7

Table 5.5: Measured signal-to-noise ratio (SNR) values across the range of temporal resolution (T_{res}) values used in this study.

NSA	**T_{res}**	**SNR**	**NSA**	**T_{res}**	**SNR**	**NSA**	**T_{res}**	**SNR**	**NSA**	**T_{res}**	**SNR**
1	1.2	30.9	**8**	9.8	73.7	**15**	18.4	116.8	**22**	26.9	143.9
2	2.4	52.0	**9**	11.0	81.1	**16**	19.6	128.4	**23**	28.2	173.5
3	3.7	59.5	**10**	12.2	89.6	**17**	20.8	111.5	**24**	29.4	195.2
4	4.9	59.2	**11**	13.5	115.2	**18**	22.0	131.0	**25**	30.6	224.7
5	6.1	71.0	**12**	14.7	126.4	**19**	23.3	153.2			
6	7.3	77.7	**13**	15.9	138.1	**20**	24.5	157.7			
7	8.6	67.6	**14**	17.1	133.3	**21**	25.7	152.2			

Table 5.5 shows that, overall, SNR values increased from 20.9 up to 224.7 as the T_{res} values were reduced by averaging the data in the temporal dimension. Figure 5.13 show the absolute PK parameter values derived from the non-flip-angle corrected MR data, along with known ground truth values (shown as dashed lines). The error bars in these graphs show the intra- (black error bars) and inter-session variation (red / blue error bars). Figure 5.14 shows the VFAC MR-data similarly presented. Both Figures show a drop in accuracy in the measurement of K^{trans} and k_{ep} when using T_{res} values > ~15 s; in this T_{res} region, both parameter values were overestimated using the LLS fitting approach and underestimated using NLS fitting. v_e values did not vary greatly across the range of T_{res} values tested.

Performing VFAC on the data increased the accuracy of the derived PK parameters by up to 12.9%, 9.2% and 20.2% for K^{trans}, v_e and k_{ep} respectively using the base 1.2 s protocol, as well as an increase in inter-session precision of up to 11.2%, as shown in Table 5.6, and illustrated by the error bars in Figures 5.13 and 5.14. With the VFAC data, the LLS fitting approach almost doubled the accuracy of the K^{trans} estimates, and affected an increase in the precision of K^{trans} (intra-session) and k_{ep} (intra- and inter-session) of ~4%. These trends were seen across the range of T_{res} values tested in this study, the results of which are presented in Appendix B.

Table 5.7 presents the T_{res} values which resulted in derived PK parameter values with errors ≤ 5, 10, 15, and 20% for both the LLS and NLS approaches, based on the results from 9 experimental runs (five intra-session and five inter-session, VFAC applied to all data). k_{ep} was estimated with errors ≤ 5% using both the LLS and NLS methods at T_{res} ≤ 11.5 s and 9.8 s respectively, and only the LLS method provided estimates of K^{trans} with errors ≤ 5%, at a T_{res} ≤ 7.3 s. Neither fitting approach could estimate v_e with errors ≤ 5%. To achieve PK parameter errors of ≤ 10% the NLS approach required a T_{res} ≤ 8.6 s and the LLS method a T_{res} ≤ 11 s. Both approaches had similar T_{res} requirements in order to achieve PK parameter errors ≤ 15%. For rough PK parameter estimated with errors ≤ 20% the LLS and NLS fitting regimes required T_{res} ≤ 17.1 s and 23.3 s respectively. As previously mentioned, v_e values were not strongly affected by the T_{res}, with ≤ 7% and ≤ 11% errors in PK parameter estimations at all T_{res} values tested, using the LLS and NLS fitting approaches respectively.

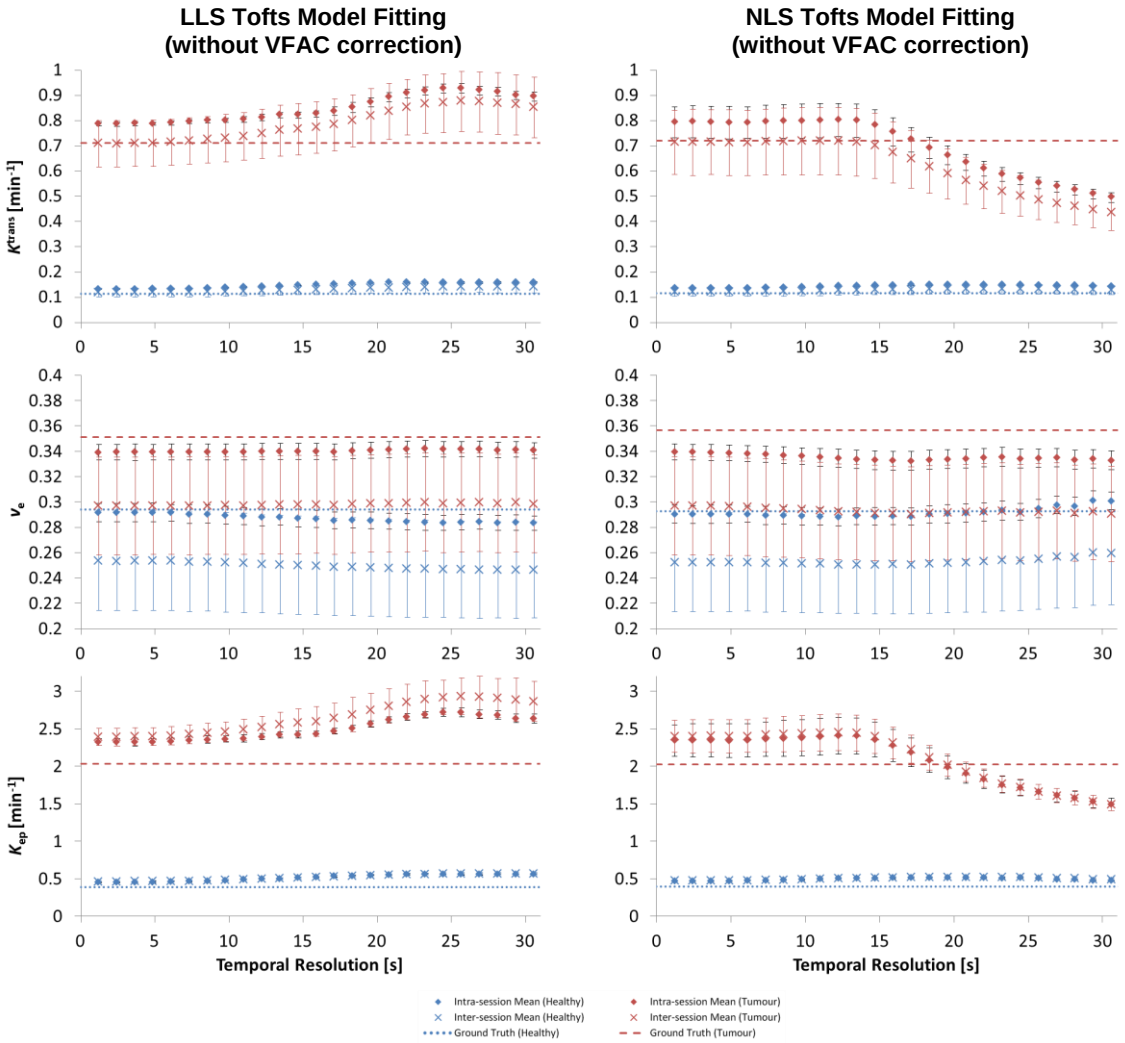

Figure 5.13: Graphs showing the mean absolute pharmacokinetic parameter values derived from both the intra- and inter-session datasets without voxel-wise flip-angle correction (VFAC) applied to the data. Black error bars show the intra-session standard deviation from the mean, and the red / blue error bars show the inter-session standard deviation from the mean.

Table 5.6: Absolute maximum % error and % standard deviation (S.D.) in the measurement of pharmacokinetic parameters using the base 1.2 s temporal resolution (T_{res}) acquisition protocol, with and without voxel-wise flip-angle correction (VFAC).

	Accuracy		**Intra-session Precision**		**Inter-session Precision**	
	NLS Fitting Max %Error	**LLS Fitting Max %Error**	**NLS Fitting Max %S.D.**	**LLS Fitting Max %S.D.**	**NLS Fitting Max %S.D.**	**LLS Fitting Max %S.D.**
			Without VFAC			
K^{trans}	18.9	15.9	7.6	0.9	17.9	13.6
v_e	15.4	15.5	2.4	2.5	15.4	15.5
k_{ep}	23.1	19.9	9.1	2.2	8.9	4.9
			With VFAC			
K^{trans}	6.0	3.3	5.1	0.8	6.7	6.2
v_e	6.2	6.9	2.8	2.9	7.6	7.6
k_{ep}	2.9	3.3	6.7	2.1	6.3	2.8
	LLS Tofts Model Fitting			**NLS Tofts Model Fitting**		

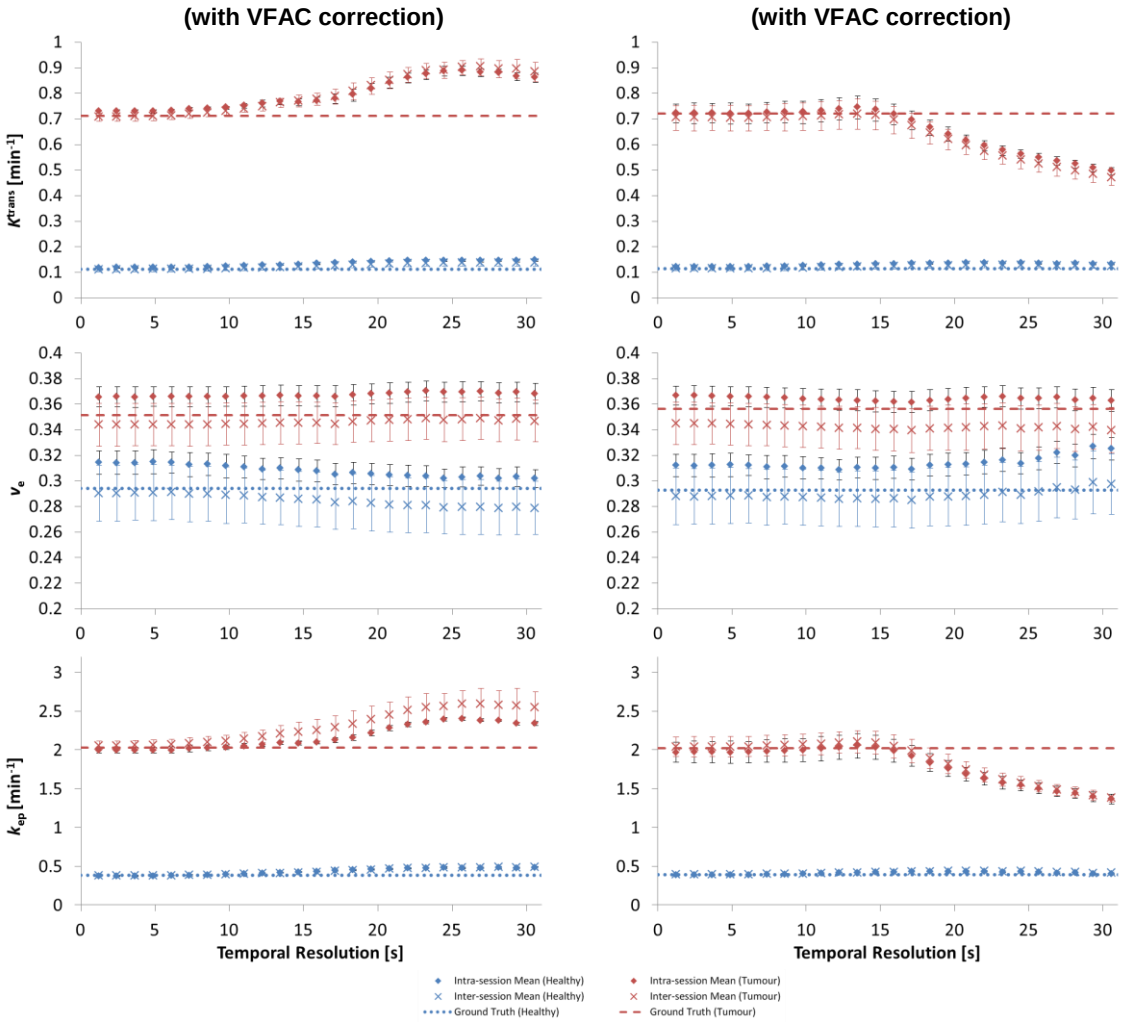

Figure 5.14: Graphs showing the mean absolute pharmacokinetic parameter values derived from both the intra- and inter-session datasets with voxel-wise flip-angle correction (VFAC) applied to the data. Black error bars show the intra-session standard deviation from the mean, and the red / blue error bars show the inter-session standard deviation from the mean.

Table 5.7: Temporal resolution (T_{res}) requirements in order to achieve errors ≤ 5%, 10%, 15%, and 20% in pharmacokinetic parameter estimates. Data taken from all 9 experimental runs (five intra-session and five inter-session), with voxel-wise flip-angle correction (VFAC) applied.

	LLS Tofts Model Fitting (with VFAC correction)				**NLS Tofts Model Fitting (with VFAC correction)**			
	All	**K^{trans}**	**v_e**	**k_{ep}**	**All**	**K^{trans}**	**v_e**	**k_{ep}**
Errors	**T_{res}**				**T_{res}**			
≤ 5%	-	≤ 7.3 s	-	≤ 11 s	-	-	-	≤ 9.8 s
≤ 10%	≤ 11 s	≤ 11 s	≤ 30.6 s	≤ 14.7 s	≤ 8.6 s	≤ 8.6 s	≤ 28.2 s	≤ 14.7 s
≤ 15%	≤ 14.7 s	≤ 14.7 s	≤ 30.6 s	≤ 15.9 s	≤ 14.7 s	≤ 14.7 s	≤ 30.6 s	≤ 19.6 s
≤ 20%	≤ 17.1 s	≤ 17.1 s	≤ 30.6 s	≤ 19.6 s	≤ 22 s	≤ 23.3 s	≤ 30.6 s	≤ 22 s

5.4. Discussion

In this chapter MR-data derived PK parameter values were compared with precisely known ground truth values and errors of up to 47% were found in parameter estimations, when an inappropriate T_{res} was used and no flip angle correction was performed on the data. By optimising the T_{res} these errors reduced to ~20%, and further, by applying VFAC to the data the maximum error in PK parameter estimations dropped further to $\leq$ 7%. The data presented in this chapter demonstrate the strong dependence of PK modelling accuracy and precision on both the DCE-MRI acquisition and analysis methodologies used, and further emphasises the need for quantitative studies such as that described herein to inform appropriate DCE-MRI protocols. Improved reproducibility and standardisation for how DCE-MRI is performed at the prostate, along with how PK analysis is performed on the data, should lead to greater acceptance into a clinical setting of this potentially powerful diagnostic tool.

Simulation studies can be very informative, particularly when based on patient datasets, however they are limited as they cannot fully simulate the plethora of factors which influence the implementation of a particular protocol at the scanner, such as scanner-specific features (e.g. B_1^+-field non-uniformities), inter-session variation deriving from patient positioning, inter-session scanner performance, to name but a few. The phantom device used in the present study allowed, for the first time, for a physiologically-relevant, known AIF to be precisely reproduced and repeatedly measured using DCE-MRI in an environment which mimics that of an actual patient. This type of phantom-driven approach allows for a level of protocol quantitative validation which is simply not achievable in patient studies, and is essential for accurate PK modelling of the data. A recent multi-centre study illustrates this well: in the study, the same set of patient prostate DCE-MRI data was analysed by nine separate MR centres, each using their respective AIF calculation strategy, and with each yielding significantly different PK parameter estimates from the same data sets [167]. Although this study illustrated the dependence of the accuracy of the derived PK parameters on the input AIF, because the ground truth AIF for each patient dataset was unknown, it is not possible to conclude from the data presented which analysis method was the most appropriate or accurate, but rather that the analysis method used has a large impact on the final results, i.e. causing a relative variation in derived PK parameter values.

In the present study, differences between the α_{set} and α_{act} of up to -33% were calculated at the ROI where the AIF was measured. This is in line the previous simulation study by Buckley and Parker, which was based on patient prostate data, where a measured flip angle difference as large as -30% was reported [168]. Studies in the breast have reported larger underestimation errors of 33 – 55 % [178-180]. Although a substantial difference was calculated between the α_{set} and α_{act}, this difference remained relatively consistent across the entire ROI where the AIF was measured, only deviating by a maximum of 3%, with the mean ROI flip-angle-differences fluctuating by <2% across all intra- and inter-session DCE-MRI experiments. Applying VFAC to the data resulted in a substantial gain in both the precision and accuracy of the AIF measurements, with the range of CCC values increasing from 0.42 – 0.53 to 0.83 – 0.92, and %RMSE values decreasing from 12% – 14% to 6% - 8%, for both intra- and inter-session measurements. As would be expected, this gain in precision and accuracy was also apparent in the PK parameters values calculated from the data.

The ~30% difference in flip angle calculated in the present work reduced PK parameter estimation accuracy by up to 12.9%, 9.2% and 20.2% for K^{trans}, v_e and k_{ep} respectively, and also resulted in a decrease in inter-session precision of up to 11.2% (using the base 1.2 s protocol). This reflects the results from the previously mentioned prostate-data-based simulation study by Buckley and Parker, where a -30% deviation in flip angle was found to produce PK parameter errors of ~10% when the AIF was measured simultaneously with the tissue CTCs (reported errors increased up to 40% when the AIF was not measured simultaneously with the tissue CTCs) [168], as was the case with this present study. In another simulation study, which this time used B_1^+-field non-uniformity data taken from breast DCE datasets, Di Gionni *et al* reported that a difference between the α_{set} and α_{act} of ~30% resulted in discrepancies in the derived PK parameters values of ~30 - 40% [178], further highlighting the potentially large errors that B_1^+-field non-uniformities can introduce into the analysis results. Variations in flip angles are likely due to variety of effects, including hardware imperfections, errors in the calculated RF pulse reference voltage values, and dielectric effects / wavelength-related RF interference effects within patients particularly at field strengths ≥ 3T. Performing a truly-quantitative measurement is strongly dependent on *actual* acquisition parameters achieved in the sample (i.e. not just the values *set* in the protocol, but those actually achieved in the patient / sample by the scanner hardware), and this is particularly the case for the flip angle, since correct knowledge of the actual flip angle directly affects the accuracy of the contrast-agent concentration value

calculated from the signal intensity using Equation [2.18].

Published guidelines recommend a $T_{res} \leq 10$ for performing PK analysis in the prostate [135, 136], whereas simulation studies reported that a T_{res} of 1 – 3 s is required for accurate measurement of the AIF [22, 121]. One of the aims of this study was to investigate the influence of T_{res} on the measurement of the AIF, across a range of T_{res} values from 1 s to 30 s, similar to the range previously reported for DCE-MRI studies in the prostate [137]. This was achieved without using any acceleration techniques, such as parallel imaging (as was used in the preceding two Chapters) or compressed sensing, but rather by reducing the FOV in the second phase-encoded dimension, resulting in a 'thin-slab' 3D protocol with a T_{res} of 1.2 s. This was done in order to comprehensively investigate the effects of T_{res} when using a standard SPGR protocol, without the compounding effects that rapid-imaging techniques may introduce (for example a reduction in the SNR); an investigation into the use of some of these rapid-imaging techniques is the subject of Chapter 6. In the present study it was found that errors in PK parameters were ≤ 10% at a $T_{res} \leq 8.6$ s using the NLS approach, however the LLS method was shown to acheive the same accuracy levels with $T_{res} \leq 11$ s. K^{trans} and k_{ep} values were both strongly affected by the T_{res}, particularly at T_{res} values > ~15 s, however, v_e values did not vary greatly across the range of T_{res} values tested, and this is in line with the results presented in Chapter 4, as well as other published works [154, 178], with errors in $v_e \leq 7\%$ errors at all T_{res} values tested using the LLS fitting approach, and ≤ 11% using the NLS fitting.

The use of a LLS regime to fit the standard Tofts model, rather than the more traditionally-used NLS approach, was found to almost double the accuracy of K^{trans} estimates, as well as providing an increase in K^{trans} (intra-session) and k_{ep} (intra- and inter-session) precision of ~4%. The accuracy of the LLS approach also showed lower dependence on the T_{res} used, with all PK parameter errors ≤ 10% at a $T_{res} \leq 11$ s using the LLS approach, with the NLS method requiring $T_{res} \leq 8.6$ s to achieve the same accuracy. This may be due to high SNR in the data (SNR range: [31 – 225]; see Table 5.3.5), since the LLS approach has been previously reported to outperform the NLS fitting method when applied to high SNR datasets [88, 191, 192].

Due to its acquisition-time efficiency and low sensitivity to off-resonance and physiological effects, the AFI method of VFAC has potential for use in quantitative *in vivo* clinical imaging applications [182, 193], and the results presented herein clearly

demonstrate the substantial increase in accuracy and precision that this would provide. Overall, the best balance between accuracy, precision, and current clinically-achievable T_{res} values for prostate imaging was achieved through the use of a T_{res} value $\leq$ 8.6 s, with VFAC performed, and the resulting CTC data fit using the LLS fitting approach; using this acquisition / analysis regime all PK parameters were measured with $\leq$ 7% errors, $\leq$ 3% intra-session standard deviation, and $\leq$ 8% inter-session standard deviation. Within these T_{res} constraints, of the three PK parameters derived, k_{ep} provided the highest accuracy and precision overall, with $\leq$ 3% error and standard deviation across all intra- and inter-session measurements; this is in line with the results of Huang *et al*., where it was suggested that k_{ep} might provide a more robust imaging biomarker of prostate microvasculature than K^{trans}, due to lower sensitivity to AIF variation [167].

Limitations with the pump system used in this study meant that had the AIFs been produced by simply programming the desired curve shape directly (as was used to produce the slower-changing tissue CTCs) it would have resulted in noise being introduced during the initial rapidly-changing portion of the AIF curves. The source of the potential noise is the pump system's intrinsic voltage stepping constraints, i.e. the voltage resolution (the smallest voltage change that would cause a change in the flow-rate) and the flow-system's temporal response (how quickly a change in the flow rate at the pumps produced a change in CA concentration at the phantom device). However, by exploiting this intrinsic response of the pumps by using square-wave voltage inputs, the desired AIF shape could be produced. One downside to this approach was that it required the desired curve-shape to empirically derived through a time-consuming iterative experimental process. However, once established, the AIF curves produced by this method gave the same high repeatability as was measured for the tissue CTCs, with CCC values of >0.99 and low %RMSE of <1.2% between all nine optical experiments, conducted over five days (five intra- and five inter-session measurements), providing an accurate and precise 'ground truth' AIF for the system.

There were some further limitations of this study. For example, a population average AIF was derived from 32 prostate patient DCE-MRI datasets, and although the data was acquired at a T_{res} of 3.1 s, which according to the results of this present study gave adequate T_{res} for the measurement of the AIF curve-shape, no flip angle correction was applied to the data. However, for the purpose that this data was used for in this study, namely to establish a physiologically-relevant shape for the AIF to be produced at the phantom, this was accepted as a reasonable limitation. The 'tissue' and 'AIF' base-line

T_1 values (T_{10}) were precisely known from the ground truth optical experiments and these values were used in all calculations. However errors in T_{10} measurements, which are particularly pronounced when flip angle correction is not applied to the data, are known to strongly affect the accuracy of the derived PK parameters [168, 169, 178], with errors in PK parameters reported to increase by to ~ 465% when T_{10} is estimated using the widely-used variable flip angle approach without flip angle correction [178]. In the present study inflow effects, caused non-steady-state spins flowing into the imaging FOV, were also avoided. However this is another factor that needs to be taken into account when measuring the AIF *in vivo*, as the use of an inflow-affected AIF in the PK modelling of the data has been shown to introduce additional errors of up to 80% in the derived PK parameters [102]. With this in mind, in patient studies it is important to carefully choose the location of the AIF measurement, such that the effects of blood inflow are avoided.

This chapter quantitatively investigated the accuracy and precision of DCE-MRI measurements made using a standard spoiled gradient echo sequence; the further effects of using rapidly-accelerated DCE acquisition strategies (using golden-angle radial *k*-space sampling trajectories and compressed sensing image reconstruction) are the subject of the next chapter.

Chapter 6: Effect of golden-angle radial *k*-space under-sampling and image reconstruction methodology on DCE-MRI accuracy and precision

6.1. Introduction

As discussed in the preceding three chapters, the temporal resolution (T_{res}) at which DCE-MRI data are acquired strongly affects the accuracy and precision of the derived phenomenological and pharmacokinetic (PK) parameter values. For example, it was shown that a T_{res} of 11 seconds was required in order to achieve errors $\leq$ 10% in the derived PK parameter values. This was demonstrated using fully-sampled data, i.e. complete *k*-space data acquisition, while high temporal resolutions were achieved by reducing the size of the imaging volume in the *z*-direction (i.e. reducing the number of slices), as well as reducing the in-plane spatial resolution. For patient prostate DCE-MRI scanning, however, a larger imaging volume size is required in order to encompass the entire prostate, with 12 to 30 slices typically being acquired [194]. Additionally, the *European Society of Urogenital Radiology* (ESUR) recommended an in-plane resolution of 0.7 x 0.7 mm^2 for patient DCE imaging [135]. By adjusting the 1.2s-T_{res} protocol used in the previous chapter to match this recommendation, one would end up with a T_{res} of ~ 30s. When *k*-space is under-sampled, and the Nyquist criterion is violated, the Fourier reconstructions exhibit aliasing artefacts. Several

acquisition and reconstruction strategies have been proposed which aim to reduce the sampling requirements for DCE-MRI, while mitigating these under-sampling artefacts, such as the well-established parallel imaging (PI) technique [114, 115], and the more recently proposed method of compressed sensing (CS) [49, 195, 196]. These rapid imaging techniques have the potential to allow for more accurate modelling of the DCE-MRI data, by providing a means to image patients with an appropriate T_{res}, while still retaining adequate spatial resolution and tissue coverage. However quantitative validation work is needed in order to access how these techniques affect the resulting data. In this chapter, the phantom device described in Chapter 3 was used to quantitatively investigate the effects of data under-sampling on the accuracy and precision of DCE-MRI measurements with data acquired using a golden-angle (GA) radial *k*-space trajectory, with reconstruction performed using: coil-by-coil (CbC) inverse gridding, PI, and a combination of PI and CS (parallel imaging with compressed sensing (PICS)).

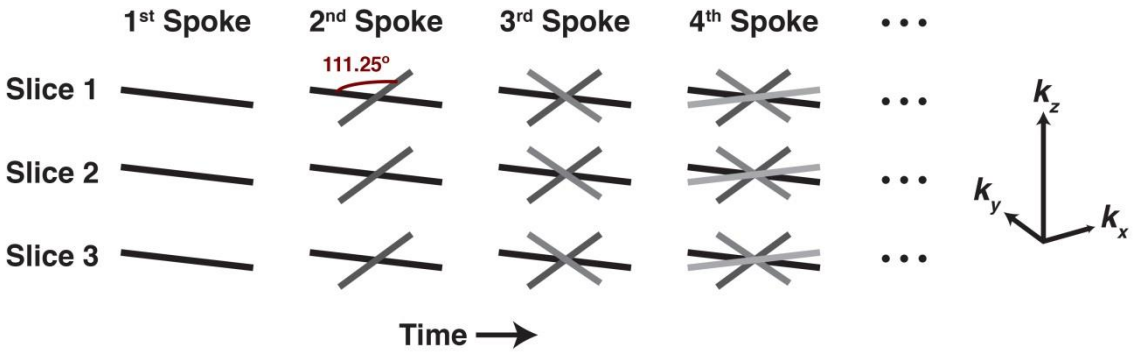

Figure 6.1: Diagram illustrating the 2D golden-angle (111.25°) radial 'stack-of-stars' *k*-space sampling scheme which employs golden angle radial sampling in-plane (k_x / k_y) and Cartesian sampling in the slice direction (k_z).

Cartesian *k*-space sampling trajectories are currently the mostly widely used approach for clinical imaging. However, the use of non-Cartesian trajectories can potentially provide more rapid coverage of *k*-space by making efficient use of MR gradient hardware, which can reduce scan times, and thereby improve the T_{res} for DCE-MRI. Furthermore, just as with standard Cartesian trajectories, these non-Cartesian trajectories can also be under-sampled to achieve even faster scan times.
Radial *k*-space trajectories offer several advantages over Cartesian trajectories, which include the inherent presence of incoherent aliasing in multiple dimensions [197], making this technique particular applicable for use with a CS reconstruction [49], as well as less susceptible to motion artefacts [46, 198]. In this chapter the use of a 2D golden-angle (GA) radial 'stack-of-stars' *k*-space sampling scheme is investigated [199], which

employs golden angle radial sampling in-plane (k_x / k_y) and Cartesian sampling in the slice direction (k_z), as illustrated in Figure 6.1. With this acquisition scheme, the radial angle of the in-plane *k*-space acquisition line is continuously increased by 111.25°, as illustrated in Figure 6.2; for comparison, a linear radial acquisition trajectory is also shown in this figure, where the angle between subsequent *k*-space lines = 360° / *N* (where *N* is typically taken as the profile resolution). One big advantage of GA radial *k*-space sampling over linear radial sampling is that it allows for a relatively uniform coverage of *k*-space with high temporal incoherence for any arbitrary number of consecutive lines [200, 201], thereby allowing for flexibility with regards the T_{res} of reconstructed datasets (as illustrated in Figure 6.2). The number of radial *k*-space profiles which are combined together to form each dynamic frame is simply defined in the reconstruction process [202]. To date continuous GA radial imaging has been used for several dynamic MRI applications, including imaging of the prostate [137, 203], liver [204], heart [205], breast [204, 206], neck [204], joints [207], and the eye [208].

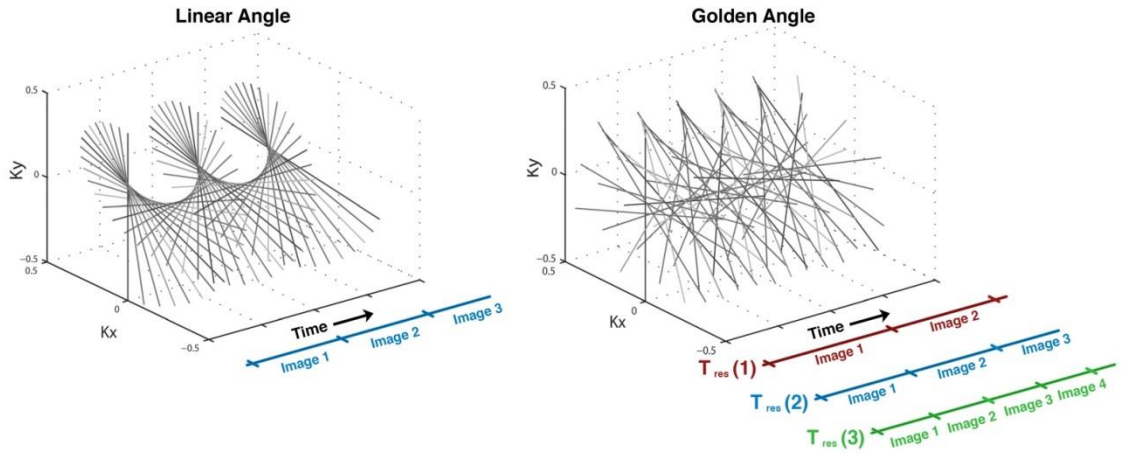

Figure 6.2: Illustration of Linear Angle and Golden Angle radial MRI data sampling trajectories (*k*-space units normalised). For linear angle, images are typically reconstructed once full radial coverage has been acquired. However, for Golden angle, an approach wherein images may be reconstructed from differing consecutive numbers of radial profiles of sampled *k*-space data, can be employed, thereby giving additional flexibility regarding the achievable temporal resolutions (T_{res}). (Image adapted from [209]).

In parallel imaging (PI), DCE-MRI data is simultaneously acquired from multiple receiver coils, with each coil exhibiting a different spatial sensitivity profile, which acts as an additional spatial encoding function. PI is a well-established technique, however, the acceleration it provides is limited by signal-to-noise (SNR) constrictions (since the image SNR reduces by square root of the acceleration factor factor) as well as limitations in the coil design, which can lead to a poorly conditioned inverse problem at high acceleration factors [204]. PI techniques, such as SENSE [114], SMASH [115], and GRAPPA [138], or combinations of these techniques, such as SPITiT [210], and ESPIRiT

[211], use the spatial information derived from the sensitivity patterns of multiple receiver coils to reconstruct images from under-sampled data, thereby allowing for faster imaging, while maintaining image quality. In this chapter the ESPIRiT approach is utilised, which combines both SENSE and GRAPPA methods by restricting the solutions from both to a subspace in order to reconstruct the missing data. SENSE realises this by combining the coil images using pre-calculated sensitivity maps, while this is achieved with GRAPPA by filtering the data with calibrated kernels in *k*-space. The dominant eigenvector of these *k*-space operators behave as sensitivity maps, and can be rapidly computed, since this algorithm uses an efficient eigenvector-based decomposition in image space, providing robust high-quality sensitivity maps, estimated directly from the DCE data [211]. Additionally, ESPIRiT combines all the advantages of SENSE (e.g. the linear scaling of the computational demand with the number of receive coils used, optimal reconstruction quality, and straightforward implementation with radial sampling) with a robustness to errors (e.g. known errors deriving from field-of-view (FOV) limitations [212]) similar to auto-calibrated methods, such as GRAPPA.

Compressed sensing (CS) was first proposed in the literature of Information Theory and Approximation Theory as an abstract mathematical idea [195, 196], and its potential application to biomedical imaging, in particular MRI, was recognised from the outset [195]. MRI is particularly compatible with CS since there is flexibility in the way in which it encodes and collects data in the spatial frequency domain. CS can be used to further accelerate the acquisition of MRI data by sampling fewer frequencies than are required to satisfy the Nyquist criterion. The technique works by exploiting spatial and temporal correlations by using (pseudo-) random under-sampling schemes to create incoherent aliasing artefacts and subsequently using a nonlinear iterative process in the reconstruction to enforce sparsity in a suitable transform domain [213-215]. Mathematically speaking, this iterative reconstruction of the missing data utilises a regularised least-squares algorithm in which the gradient of the reconstructed image typically serves as a regulariser; that is, the reconstructed image, *m*, is usually a solution to the unconstrained minimisation problem:

$$\arg_m \min \|Sm\|_1 + \lambda \|Fm - d\|_2^2, \qquad [6.1]$$

where *S* is a sparsity transform (such as a wavelet decomposition or the gradient), *F* is the partial Fourier measurement operator, *d* is the measured *k*-space data from the scanner, and λ controls the relative weighting of the l_1 and l_2 norm terms, defined as

$$|x|_1 = \sum_i |x_i|, \quad [6.2]$$

and

$$|x|_2^2 = \sum_i x_i^2, \quad [6.3]$$

respectively. During the CS reconstruction process, missing phase-encode data are selected to minimise the isotropic gradient of *m*, defined as:

$$\nabla m = \sqrt{\left(m_{i.j} - m_{i.j-1}\right)^2 + \left(m_{i.j} - m_{i-1.j}\right)^2}, \quad [6.4]$$

with boundaries treated periodically, and each slice treated independently. For quantitative DCE-MRI studies, it is worth noting that this transform does not have a simple relationship to the desired PK parameters, and as such it is not clear whether a time-independent CS MRI reconstruction will retain the necessary dynamic information to accurate and precisely retrieve DCE parameters [216].

In 2007, Lustig *et al.* published the first MRI study using CS, demonstrating experimentally several 2D and 3D Cartesian implementations of CS in MRI, with promising results; such as a 5-fold acceleration of first pass contrast enhanced MR angiography (CE-MRA) [49]. Subsequent early studies further demonstrated the potential gain in imaging speed that CS could provide, reporting up to a three-fold acceleration for dynamic cardiac MRI [213, 214] and eight-fold for ^{13}C 3D MR susceptibility imaging [217, 218], while still retaining relatively good image quality (compared with the fully-sampled data). By 2010 CS was being applied to quantitative MRI techniques, such as MR apparent diffusion coefficient mapping in the lungs [219] and T_1 and T_2 mapping in the brain [220], reporting accelerations of up to five- and six-fold respectively, while still preserving the quantitative information. Also in 2010 a study by Otazo *et al.* combined PI and CS (dubbed 'PICS') by merging *k-t* SPARSE with SENSE reconstruction, demonstrating the feasibility of an 8-fold acceleration for high resolution *in vivo* whole-heart imaging [221]. The same year saw the first application of CS to DCE-MRI; studies by Adluru *et al.* and Wang *et al.* achieved under-sampling factors of up to 5 and 10 times respectively for breast imaging, with both studies reporting good preservation of the spatiotemporal characteristics in the data, although no independent

verification was presented [222, 223]. Similarly, another study the same year, again in the breast, found that PK parameters estimated from six-times under-sampled DCE data correlated well with those derived from the fully sampled data (correlations coefficient (r) = 0.98 for $K^{trans,}$ and r = 0.85 for k_{ep}) [185]. Since then numerous studies have demonstrated the potential of CS to reduce the scan time for imaging of various anatomies, such as: brain [224, 225], spine [226, 227], breast [202, 206, 216, 228-230], muscle [231], heart [201, 232-234], liver [118, 235], lung [236], and prostate [137, 203, 237]; with further work also done to incorporate CS into various MR techniques, such as: DCE [137, 203, 206, 216, 229, 230, 238-242], spectroscopic imaging [235, 243], phase contract blood flow [244, 245], black-blood imaging [246], and water-fat imaging [247, 248]. Many of these more recent CS studies also utilise under-sampled multi-coil data, combining CS with PI, [118, 137, 201, 203, 216, 229, 239, 241, 247, 248].

The majority of DCE-MRI studies to date which utilise CS have been performed at the breast [185, 206, 216, 222, 223, 229, 230, 242], however recently this technique has also been applied to DCE in the prostate [137, 203]. In 2015, Rosenkrantz *et al*. demonstrated the feasibility of applying CS to DCE-MRI of the prostate, reporting both high spatial (3.0 x 1.1 x 1.1 mm) and temporal resolution (2.3 s) [137]. The study reported improvements in image quality, clarity of anatomical detail, and spatiotemporal resolution using the GA radial acquisition with PICS reconstruction, when compared with a standard fully-sampled Cartesian DCE acquisition. In 40% of patients, only the PICS technique was reported to have detected the tumour. However, these results were based on a qualitative analysis, i.e. radiologists observations of earlier contrast arrival in tumour compared to benign tissue. Additionally, the results derive from separate DCE examinations, performed on the same patient, but on different days. As such, the direct comparison presented is not truly valid. The same group further demonstrated the potential applicability of PICS to prostate DCE imaging in a study the following year which investigated the effectiveness of this technique for the detection of local recurrence of prostate cancer in patients with elevated prostate specific antigen (PSA) after prostatectomy [203]. This study achieved even higher spatial resolution than the previous study of 1.0 x 1.1 x 1.1 mm^3 using PICS, while still retaining the same low 2.3 s T_{res} value. Substantially better image quality and diagnostic performance was reported, when compared with standard DCE acquisition. However, in addition to the same limitations discussed for the previous Rosenkrantz study, in this study the results presented (i.e. comparing GA radial acquisition with PICS reconstruction against a standard fully-sampled Cartesian DCE acquisition) were not even taken from the same patients.

It is clear that the technique of GA radial acquisition combined with PICS reconstruction has great potential with regards improving the T_{res} for DCE-MRI, while still retaining image quality [137, 203, 206, 208]. However, in studies to date it has only been possible to investigate the effects of using this technique by comparing the under-sampled data in a relative sense, generally to the fully-sampled data from which it were retrospectively derived. However, as was the case with standard DCE-MRI, no study thus far has been able to quantify the effects of using this technique *in vivo* for the measurement of the tissue contrast agent (CA) concentration-time curves (CTCs) or the arterial input function (AIF); again deriving from a lack of knowledge of the ground truth (GT) values. *In vivo* validation is particularly important for CS in DCE-MRI, particularly considering the uncertainties such non-Cartesian under-sampling trajectories may introduce to the fidelity of the derived CTCs and AIF which, until now has been unknown. The aim of this chapter was to use the phantom test device described in Chapter 3 to quantify the effect of under-sampling the data on the accuracy and precision of measured CTCs and AIF, and the derived quantitative PK parameters, for data acquired using a GA radial *k*-space trajectory, reconstructed using three reconstruction approaches: (i) no PI or CS (CbC inverse gridding), (ii) PI only, and (iii) PICS approaches, and with MR-results compared against precisely known GT values.

6.2. Materials and Methods

The methodological choices used for the experiments described in this chapter were informed by the results of the previous chapters, such as: the acquisition duration (AD $\geq$ 360 s; see Chapter 4), the T_{res} (<11 s; see Chapter 5), the use of voxel-wise flip angle correction (VFAC; see Chapter 5), and the use of a linear version of the standard Tofts model (see Chapter 5). The same modified phantom test device described in section 5.2.1 was used in the present work, as well as the same ground truth AIF and 'healthy' and 'tumour' CTCs (see sections 5.2.2, 5.2.3, and 5.2.4 for more information).

6.2.1. MRI Phantom Data Acquisition

DCE-MRI phantom data were acquired using a 3T multi-transmit scanner (*Achieva*; Philips, Netherlands) using a 32-channel detector coil. A 2D turbo field echo (TFE) spoiled gradient echo imaging sequence was employed, with a stack-of-stars *k*-space

sampling trajectory. The following scan parameters were used: TR = 10.5 ms, TE = 1.6 ms, flip angle = 38°, FOV = 224 x 224 x 18 mm^3, spatial resolution = 1.75 x 1.75 x 6 mm^3, and number of slices = 3. A total of 97,200 (32,400 per slice) radial spokes were acquired continuously using the GA scheme with a total acquisition duration of 470 s. A single radial spoke was acquired from each of the 3 slices using the same trajectory through *k*-space, before the next 3 spokes (rotated by the GA) were acquired, again for each of the 3 slices, and so on (see Figure 6.1.1), effectively tripling the TR from 3.5 ms to 10.5 ms. As with the MR-phantom experiments presented in the previous chapter, the flip angle used herein was selected in order to ensure that every concentration in the range used in this study had the lowest possible uncertainty [136, 190]. The flip angle was adjusted in this case to account for the longer effective TR used in the GA radial acquisition. Again, as in the previous chapter, each experiment consisted of two measurements of the AIF and either the 'tumour' or 'healthy' CTC, each repeated on 5 separate days, and 5-times within the same scanning session, in order to quantify the inter-session and intra-session precision of measurements. The temporal resolutions of the reconstructed DCE datasets were defined during the reconstruction process, as outlined in the next section. B_1^+ maps were also acquired using a dual-steady-state sequence with the same geometry as above and TR_1 / TR_2 / TE = 30 ms / 150 ms / 2 ms and flip angle = 60°. The GA radial pulse sequence used herein was developed in collaboration with Dr Matthew Clemence, from *Philips Healthcare* (UK), compiled locally using the *Philips Paradise Environment* (Philips, Netherlands), and tested on simple phantom to ensure correct data acquisition ordering.

6.2.2. Image reconstruction

The amount by which the data were under-sampled was quantified by the radial sampling density (RSD), which is reported with respect to the requirement for a Cartesian acquisition to fulfil the Nyquist criterion, i.e. for an RDS of 100%, the number of radial spokes used to reconstruct each image equals the number of frequency encode steps (128 in the case of this study). This was chosen so as to allow for easy comparison with the fully-sampled Cartesian acquisition results presented in Chapter 5, and also to facilitate easier comparison with a wider range of previous works (since Cartesian trajectories are most commonly used in previous DCE-MRI studies, and radial studies often adopt the same convention [200]). It is worth noting however, that in the case of the radial acquisition scheme used in this chapter, the Nyquist sampling

requirement (NSR) is given as 128 * (π / 2) ~ 201 radial spokes per reconstructed image. Both percentage RSD and NSR values are given in Table 6.1 for the data presented in this chapter. The *Berkeley Advanced Reconstruction Toolbox* (*BART*) was used for all calibration and image reconstruction [249]. Code was developed in *Matlab* (*R2015b*; MathWorks, USA) which implemented the following step in the reconstruction process:

1. RAW radial *k*-space data (in the Philips data format) imported into *Matlab*
2. RAW data indexed and rearranged into a multidimensional array [phase encode steps (256), coil channels (32), slices (3), radial spokes (32,400)]
3. Slice selected (the central slice in the case of this study)
4. Cartesian *k*-space coordinates generated corresponding to the GA radial *k*-space trajectories, for use with Cartesian re-gridding
5. The number of radial spokes used to reconstruct each individual image in the dynamic sequence defined (i.e. the RSD), and the *k*-space radial spokes (with corresponding Cartesian *k*-space coordinates) binned together accordingly (e.g. for a RSD = 100%, the multidimensional data array outlined in Step 2 becomes: [phase encode steps (256), coil channels (32), radial spokes (128), dynamics (253)]
6. CbC inverse gridding reconstruction performed using *BART* (*k-space data,* Cartesian *k*-space trajectories, and no coil-sensitivity maps)
7. Coil sensitivity maps generated using the *ESPIRiT* calibration method [211]
8. PI and PICS reconstruction performed using *BART* (*k-space data,* Cartesian *k*-space trajectories, and *ESPIRiT* coil-calibration maps)

Step 5 – 8 were repeated at RSDs from 100% to 4.68%, giving a T_{res} range from 1.85 s to 0.09 s, as illustrated in Figure 6.3, with details given in Table 6.1, along with the corresponding image reconstruction times. A total of 7 DCE data-sets were reconstructed for each experimental run (9 'healthy' and 9 'tumour' CTCs; with 5 Intra-session and 5 intra-session experiments runs each), giving a total of 126 DCE-MRI data-sets for analysis. All calibration and reconstruction was performed using a 2.7-GHz *Intel i7* (Intel Corporation, USA) quad-core CPU laptop (*ThinkPad W530,* Lenovo*,* USA) with 32 GB of RAM.

Table 6.1: Parameters used in the reconstruction of the DCE-MRI data-sets, along with the reconstruction times.

	DCE Dataset						
	1	**2**	**3**	**4**	**5**	**6**	**7**
No. Radial Spokes	128	96	64	32	16	8	6
RSD [%]	100	75	50	25	12.5	6.25	4.68
NSR [%]	63.7	47.8	31.8	15.9	7.96	3.98	2.99
T_{res} [s]	1.85	1.39	0.93	0.46	0.23	0.12	0.09
No. of Dynamics	253	337	506	1012	2025	4050	5400
Reconstruction Times:							
CbC [s]	832	1000	1489	2880	5834	11020	15051
PI [s]	661	804	1154	2182	4451	8417	11528
PICS [s]	881	1093	1621	3077	6183	12112	16593

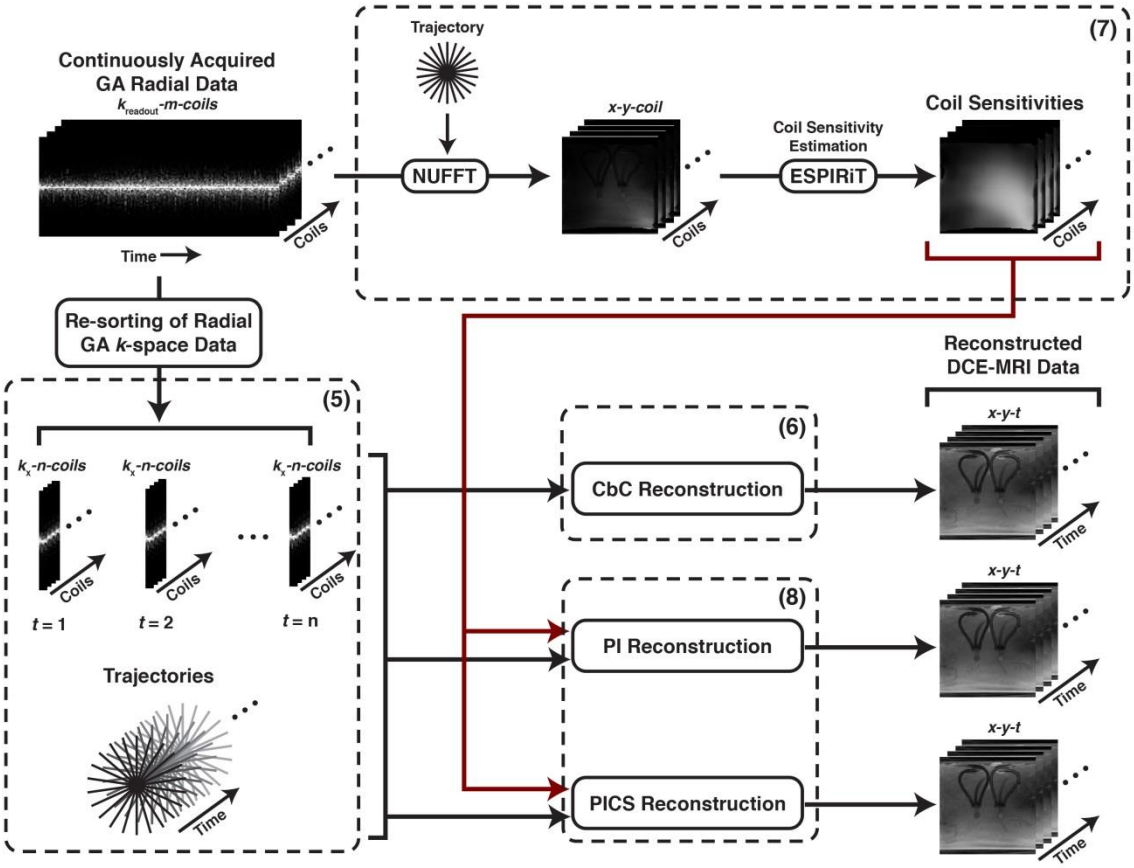

Figure 6.3: Schematic diagram showing the various steps involved in the Coil-by-Coil (CbC) inverse gridding, Parallel Imaging (PI), and PI and Compressed Sensing (PICS) DCE-MRI reconstruction. Numbering corresponds to steps outlined in section 6.2.2.

6.2.3. Voxel-wise Flip-Angle Correction (VFAC)

As was used in the previous chapter; the actual flip angles were calculated at each imaging voxel using the B_1^+ mapping data and Equation [5.9] (see section 5.1 for further details). CA concentrations were then subsequently derived from the data using the corrected flip angles.

6.2.4. Data Analysis

Root mean square error (RMSE) and concordance correlation coefficients (CCCs) [162] values were calculated between the MR-measured and ground truth AIFs and CTCs; curves were aligned, and ground truths temporally-resampled to match MR data prior to analysis. RMSE is reported as a percentage of the maximum CA concentration change (%RMSE). PK analysis was performed using the linearised form of the standard Tofts model previously described in section 2.3.2, with this model fit to the data using the same fit linear least squared (LLS; implemented in *Matlab*) approach used in Chapter 5. Two manually-selected regions of interest (ROIs) were defined at the central slice, one at each of the respective phantom measurement chambers, with each ROI containing 12 voxels. K^{trans}, v_e, and k_{ep} values were derived from the MRI-measured CTCs, compared with the ground truth values (derived from the optically-measured CTCs), and the percentage differences calculated. PK analysis was performed on all datasets, i.e. RSD values from 5% to 100%, for each of the five intra- and five inter-session datasets ('healthy' and 'tumour' CTCs, each acquired simultaneously with the AIFs).

6.3. Results

The α_{act} at the ROIs where the AIF and tissue CTCs were measured was found to differ from the set value by between -30% and -39% for all experiments, with inter-session standard deviation in α_{act} calculations of ~3% at any particular voxel, and a maximum recorded standard deviation in α_{act} across any individual ROI (used for the measurement of either the AIF or tissue CTC) of ~3%.

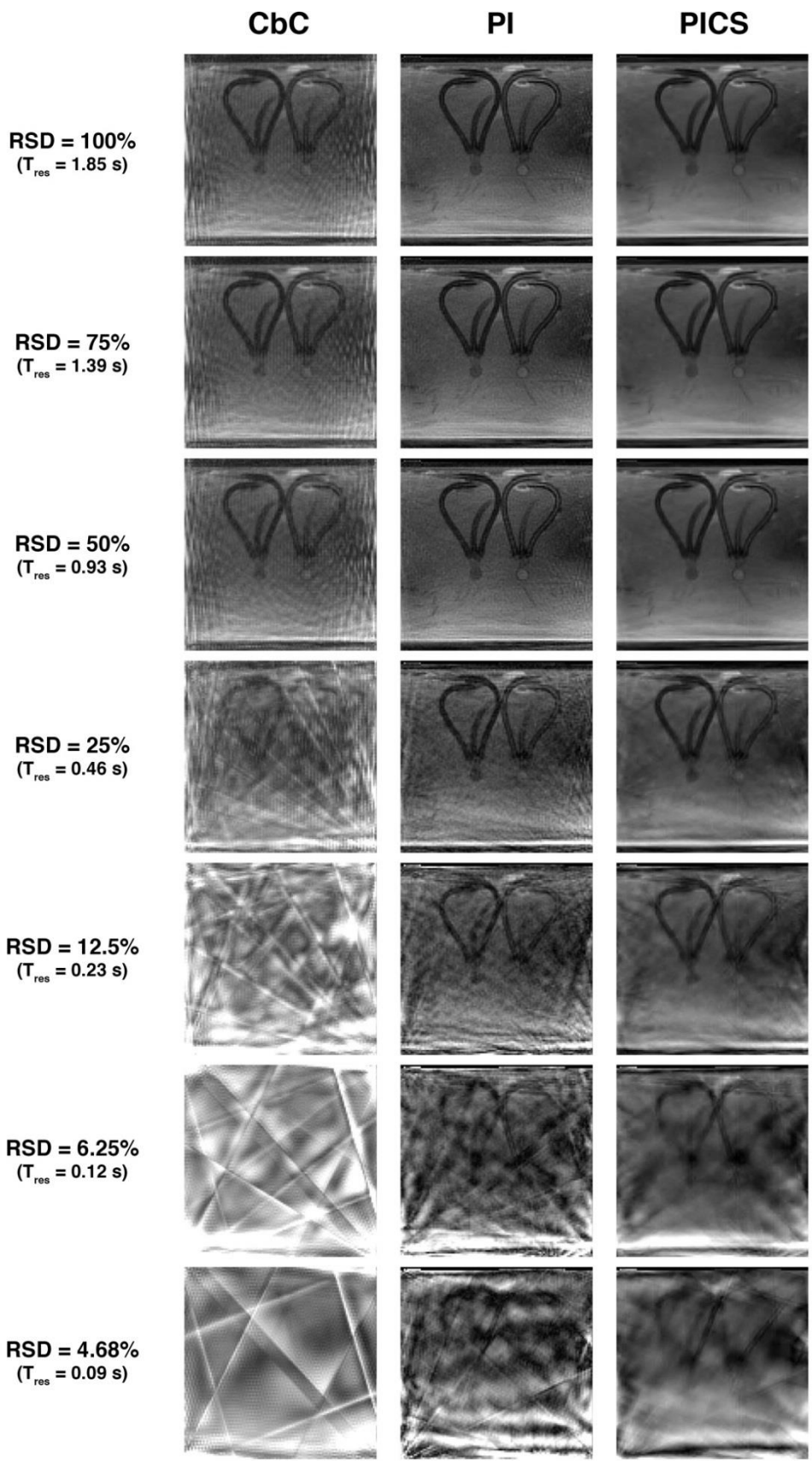

Figure 6.4 Images reconstructed with radial sampling densities (RSDs) from 100% to 4.68% using the Coil-by-Coil (CbC) inverse gridding, Parallel Imaging (PI), and PI and Compressed Sensing (PICS) reconstruction methods

Images reconstructed with RSDs across the range of 100% to 4.68% using the CbC, PI, and PICS reconstruction methods are presented in Figure 6.4. A visual comparison of the images revealed that for the CbC reconstruction approach, severe artefacts (deriving from the under-sampling of *k*-space) corrupt the entire image at RSD ≤12.5% (i.e. structures, such as the measurement chambers and tubing, are indiscernible in the images). Using the PI and PICS reconstruction approaches, artefacts were also observed in the reconstructed images, particularly with RSD ≤12.5%, however the effect was much less pronounced using these reconstruction approaches. In fact, images reconstructed with the PI approach using RSD = 6.25%, and with the PICS approach using RSD = 4.68%, have a similar visual appearance to imaging reconstructed using the CbC method with RSD = 25% (see Figure 6.4).

CCC and %RMSE values between the fully-sampled MR-measured AIFs and the ground truth values are presented in Table 6.2. Calculated CCC values were lowest for the AIFs extracted from the CbC-reconstructed MR-data (CCC range: 0.89 – 0.94), with the PI and PICS approaches both giving higher CCC ranges of 0.94 – 0.97 and 0.95 – 0.98 respectively. The highest %RMSE values in the MR-measured AIFs were also calculated in the data reconstructed using the CbC approach (4.0% - 6.0%), with the PI and PICS approaches both giving lower %RMSE ranges of 3.1% - 4.1% and 2.9% - 3.6% respectively. Overall, the AIFs derived from the data reconstructed using the PICS approach gave both the lowest %RMSE and highest CCC values.

Table 6.2 The concordance correlation coefficient (CCC) with 95% confidence intervals (CI) and percentage root mean square error (%RMSE) results from repeat intra- and inter-session DCE-MRI experiments, comparing the fully-sampled (radial sampling density (RSD) = 100%) MR-measured AIF with the ground-truth AIF. Results presented for coil-by-coil (CbC), parallel imaging (PI), and parallel imaging with compressed sensing (PICS) image reconstruction methods.

	CbC		**PI**		**PICS**	
Session	**CCC (95% CI)**	**%RMSE**	**CCC (95% CI)**	**%RMSE**	**CCC (95% CI)**	**%RMSE**
1	0.888 (0.865, 0.908)	5.8	0.947 (0.933, 0.958)	4.1	0.968 (0.959, 0.974)	3.2
2	0.892 (0.868, 0.913)	5.8	0.950 (0.937, 0.961)	4.0	0.960 (0.949, 0.969)	3.6
3	0.911 (0.887, 0.930)	5.3	0.973 (0.965, 0.980)	3.1	0.973 (0.964, 0.979)	3.1
4	0.900 (0.878, 0.918)	5.6	0.959 (0.948, 0.967)	3.6	0.975 (0.967, 0.980)	2.9
5A	0.890 (0.873, 0.905)	6.0	0.941 (0.925, 0.953)	4.3	0.954 (0.941, 0.964)	3.0
5B	0.917 (0.897, 0.933)	5.1	0.966 (0.957, 0.974)	3.3	0.968 (0.958, 0.976)	3.0
5C	0.926 (0.908, 0.941)	4.8	0.965 (0.955, 0.973)	3.4	0.968 (0.958, 0.975)	3.3
5D	0.925 (0.912, 0.936)	4.8	0.967 (0.957, 0.974)	3.3	0.968 (0.958, 0.977)	3.3
5E	0.940 (0.927, 0.951)	4.0	0.967 (0.956, 0.975)	3.4	0.957 (0.943, 0.967)	3.5

Figure 6.5 show the absolute PK parameter values (K^{trans}, v_e, and k_{ep}) derived from the data reconstructed using the CbC, PI, and PICS approaches at RSDs from 100% to 4.68%, along with known ground truth values (shown as dashed lines). The error bars in these graphs show the intra- (black error bars) and inter-session variation (red / blue error bars). No results are reported for the CbC data at RSD = 6.23% and 4.68% since artefacts in the reconstructed images meant that no discernible AIF or CTCs could be extracted from the data, and as such PK model-fitting was not possible. 'Healthy' K^{trans} values did not deviate greatly from the ground truth value, and had relatively low intra- / inter-session variability (as indicated by the small error bars) for all reconstruction approaches and at all the RSDs tested. However, the higher 'tumour' K^{trans} value showed a marked drop in both precision and accuracy when using RSD $\leq$ 25% for the CbC reconstruction approach, and RSD $\leq$ 12.5% when using the PI method. K^{trans} values derived from the data reconstructed using the PICS approach gave the lowest error and intra- / inter-session standard deviation across all the RSDs tested. For the measurement of v_e and k_{ep}, again both precision and accuracy dropped when using data reconstructed with RSD $\leq$ 25% for the CbC approach. For v_e values derived via the PI reconstruction method there was a drop in both accuracy and precision when using a RSD $\leq$ 12.5%, however k_{ep} values did not deviate greatly from the ground truth values, and had relatively low intra- / inter-session variation for all RSDs tested. Using the PICS reconstruction method, both v_e and k_{ep} values deviated relatively diminutively from the ground truth values, and had low intra- / inter-session variation, at all RSDs tested.

Table 6.3 presents the absolute maximum percentage error and percentage standard deviation in the measurement of the pharmacokinetic parameters across the RSD range from 100% to 4.68%, using for CbC, PI, and PICS image reconstruction approaches (full results for healthy and tumour CTCs are given in an Appendix C). At RSD $\geq$ 75%, all three reconstruction approaches resulted in similar accuracy, with all PK parameters measured with errors < 6%. However, as the RSD was reduced below 75%, errors in PK parameter estimations increase for all reconstruction methods. This was particularly pronounced with the CbC reconstruction, where PK parameter errors of up to 50% were calculated at RSD = 12.5%, compared with errors of 10% – 20% and 5% - 8% for the PI and PICS reconstruction approaches respectively, at the same 12.5% RSD. Overall the PICS reconstruction approach was found to provide the highest accuracy for PK parameter estimation. When compared the CbC method, PICS provided a gain in accuracy of up to 42%, 36%, and 35%, for the measurement of

K^{trans}, v_e, and k_{ep} respectively. PICS also proved a more robust reconstruction method than using PI alone, particularly at RSD ≤ 12.5% where the PICS approach provided a gain in accuracy over the PI-only reconstruction of up to 23% and 34%, for the measurement of K^{trans} and v_e respectively. The accuracy of k_{ep} measurements was similar for both PI and PICS for all RSDs tested, with < 5% variation in the measured accuracy between the two techniques.

Table 6.3: Absolute maximum % error and % standard deviation (S.D.) in the measurement of pharmacokinetic parameters at radial sampling density (RSD) from 100% to 4.68%, using for coil-by-coil (CbC), parallel imaging (PI), and parallel imaging with compressed sensing (PICS) image reconstruction approaches.

	Accuracy			**Intra-session Precision**			**Inter-session Precision**		
	CbC Max %Error	**PI Max %Error**	**PICS Max %Error**	**CbC Max %S.D.**	**PI Max %S.D.**	**PICS Max %S.D.**	**CbC Max %S.D.**	**PI Max %S.D.**	**PICS Max %S.D.**
				RSD = 100%					
K^{trans}	1.7	3.6	1.8	11.0	4.2	3.6	9.3	6.3	3.0
v_e	2.5	4.7	2.2	7.2	3.8	3.2	5.8	4.2	4.2
k_{ep}	2.7	3.0	2.2	6.4	3.3	3.7	5.8	5.9	3.7
				RSD = 75%					
K^{trans}	3.5	4.5	4.1	4.7	5.7	3.6	6.2	8.1	3.8
v_e	5.7	5.4	5.1	2.9	5.2	6.1	5.9	6.0	4.8
k_{ep}	4.4	4.5	3.0	5.0	4.3	3.2	8.2	5.9	3.4
				RSD = 50%					
K^{trans}	14.3	3.6	4.3	1.8	4.6	3.5	9.4	4.8	2.2
v_e	7.3	2.7	4.7	4.0	4.7	3.7	5.8	5.2	5.2
k_{ep}	8.2	2.0	3.0	3.9	5.3	2.7	4.6	3.6	3.4
				RSD = 25%					
K^{trans}	13.1	6.6	5.1	6.7	4.8	1.7	9.1	3.7	3.2
v_e	19.6	4.4	5.4	3.0	5.2	3.9	7.6	10.4	5.7
k_{ep}	18.0	1.9	3.6	8.7	5.7	4.5	4.9	7.4	3.9
				RSD = 12.5%					
K^{trans}	49.6	20.1	8.1	45.7	8.4	6.6	67.3	9.6	3.9
v_e	43.1	10.4	7.6	66.2	4.6	5.5	24.2	7.4	7.4
k_{ep}	40.2	10.3	5.0	50.7	5.6	3.6	60.8	5.1	4.2
				RSD = 6.25%					
K^{trans}	-	17.5	9.4	-	9.9	4.0	-	10.9	5.8
v_e	-	9.5	9.7	-	6.8	6.7	-	13.1	5.9
k_{ep}	-	7.5	10.0	-	7.1	6.1	-	5.5	6.8
				RSD = 4.68%					
K^{trans}	-	32.9	12.1	-	15.0	2.5	-	21.0	6.8
v_e	-	40.7	6.6	-	13.8	10.9	-	16.8	7.3
k_{ep}	-	14.3	11.6	-	8.0	5.2	-	15.6	3.7

Table 6.3 also shows that the PICS reconstruction method provided an increase in intra- / inter-session precision, when compared with both CbC and PI methods. Comparing the CbC to the PICS reconstruction method; intra-session precision in the measurement of K^{trans}, v_e, and k_{ep} increased by up to 39%, 61%, and 47% respectively, and inter-session accuracy by up to 63%, 17%, 57% respectively. Similarly, when comparing the PI approach to PICS; intra-session precision in the measurement of K^{trans}, v_e, and k_{ep} increased by up to 13%, 3%, and 3% respectively, and inter-session accuracy by up to 14%, 10%, 12% respectively. The increase in PK parameter measurement accuracy that PICS reconstruction provides over the CbC or PI approaches with highly-under-sampled datasets is further highlighted in Table 6.4, where the % RSD's required to limit errors below several values (5, 10, 15 and 20%) are presented for each reconstruction technique. In this table, it can be seen that the CbC and PI methods require much higher RSDs in order to achieve the same PK parameters accuracy as the PICS approach. For example, in order to achieve an overall accuracy of ≤ 10%, the CbC and PI reconstruction methods require 75% and 25% RSDs respectively, however the same accuracy can be achieved using PICS with an RSD of only 6.25%.

Table 6.4: Radial sampling density (RSD) requirements in order to achieve errors ≤ 5%, 10%, 15%, and 20% in pharmacokinetic parameter estimates. Data taken from all 9 experimental runs (five intra-session and five inter-session), using for coil-by-coil (CbC), parallel imaging (PI), and PI with compressed sensing (PICS) image reconstruction approaches.

	CbC				**PI**				**PICS**			
	All	**K^{trans}**	**v_e**	**k_{ep}**	**All**	**K^{trans}**	**v_e**	**k_{ep}**	**All**	**K^{trans}**	**v_e**	**k_{ep}**
Errors	**RSD [%]**				**RSD [%]**				**RSD [%]**			
≤ 5%	≥75	≥75	≥75	≥75	≥50	≥50	≥25	≥25	≥25	≥25	≥25	≥12.5
≤ 10%	≥75	≥75	≥50	≥50	≥25	≥25	≥6.25	≥6.25	≥6.25	≥4.68	≥6.25	≥6.25
≤ 15%	≥50	≥25	≥50	≥50	≥25	≥25	≥6.25	≥4.68	≥4.68	≥4.68	≥4.68	≥4.68
≤ 20%	≥25	≥25	≥25	≥25	≥6.25	≥6.25	≥6.25	≥4.68	≥4.68	≥4.68	≥4.68	≥4.68

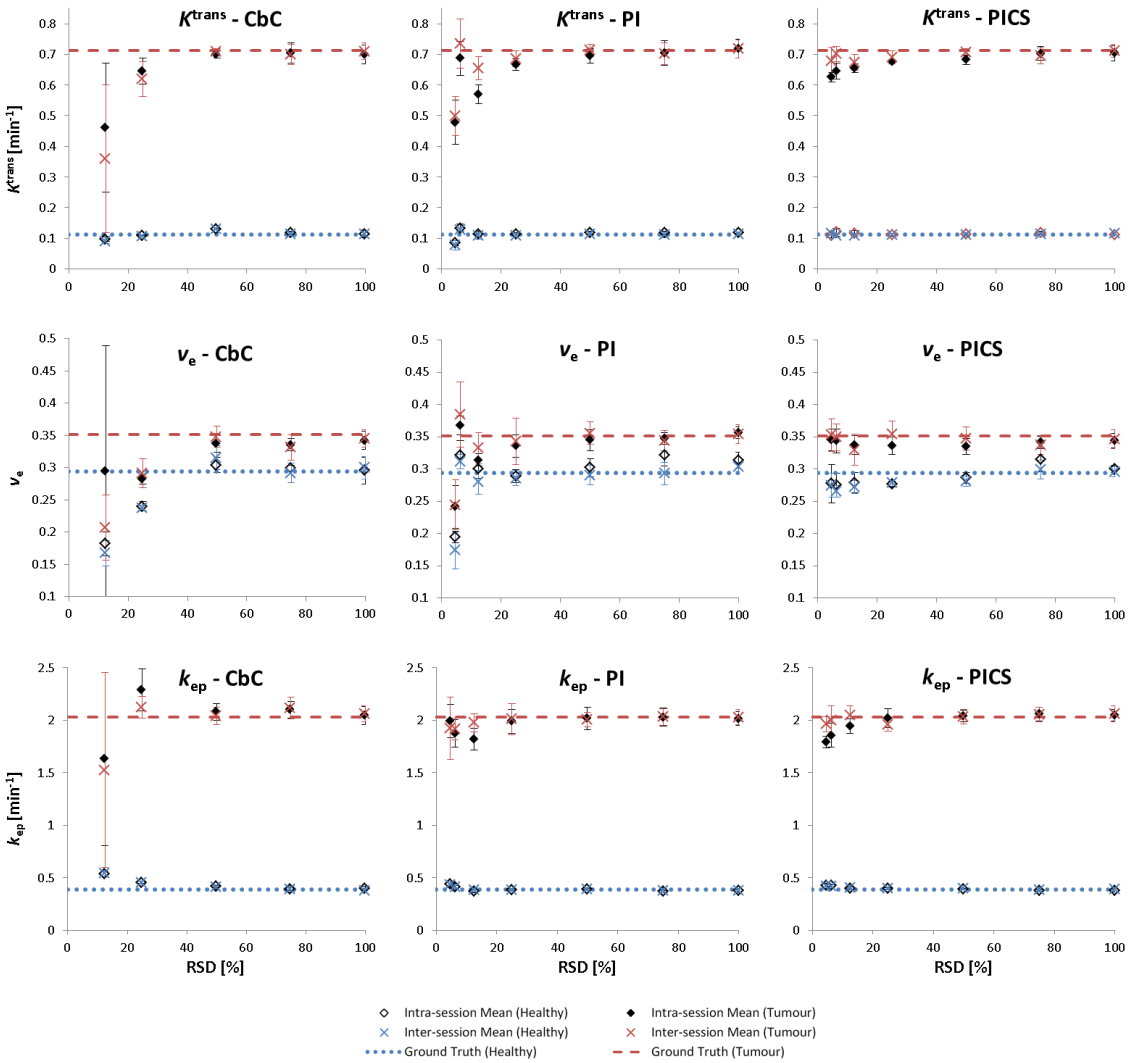

Figure 6.5: Graphs showing the mean absolute pharmacokinetic parameter values derived from both the intra- and inter-session datasets at various radial sampling densities (RSDs) for coil-by-coil (CbC), parallel imaging (PI), and PI with compressed sensing (PICS) image reconstruction methods. Black error bars show the intra-session standard deviation from the mean, and the red / blue error bars show the inter-session standard deviation from the mean. The dashed horizontal lines show the ground truth values in each case.

6.4. Discussion

The application of rapid-imaging techniques, such as PI and CS, to DCE-MRI offers the prospect of more accurate characterisation of the tissue CTCs, the AIF, and by extension the derived quantitative PK parameters, by allowing for high temporal resolution imaging while retaining the necessary tissue coverage, the clinically-appropriate spatial resolution, and good SNR in the data. These techniques can also potentially reduce / or even eliminate existing noise by reducing low-magnitude coefficients in the sparse domain during reconstruction, and can add additional true

signal if the gain in acquisition time is utilised for the acquisition of additional data [220, 237]. However, conversely, the use of any under-sampling technique can potentially lead to both loss of true signal (e.g. the loss of fine detail, or the introduction of compression artefacts) and the addition of false signal (deriving from the aliasing of the missing Fourier coefficients that do not get completely eliminated during reconstruction) [250]; as such, the addition of techniques such as PI or CS to a clinical imaging protocol can potentially introduce unpredictability to the quality of the final data and associated quantitative PK parameter values [242, 250]. As is the general case with DCE-MRI (as discussed at length in the preceding chapters), the lack of knowledge of the *in vivo* ground truth CTCs and AIF has hampered the true validation of these rapid under-sampling DCE-MRI techniques. However, as the above discussion highlights, validation studies are particularly necessary in order to quantitatively investigate the effects of using such techniques on the quality of the derived data, due to the additional possible sources of error that these techniques may introduce. The phantom test device presented in Chapter 3 was once again utilised to this end, allowing for the first time for a quantitative investigation into the effects of under-sampling and reconstruction methods, performed at the scanner in an anthropomorphic environment, with derived CTCs, AIFs, and quantitative PK parameters accessed via a comparison with precisely-known GT values.

In this study, mean CCC values of 0.91, 0.96, and 0.97 were calculated for radial data reconstructed using the CbC, PI, and PICS approaches, respectively, for RSD = 100%, showing an apparent improvement in agreement between the MR-measured and ground truth curves for all radial reconstruction methods, when compared with CCC results from the fully-sampled Cartesian data reported in Chapter 5, where a mean CCC of 0.86 was calculated. This was also reflected in the lower mean %RMSE values of 5.3%, 3.6%, and 3.2% calculated for the CbC, PI, and PICS reconstructions respectively (RSD = 100%), compared with mean %RMSE = 6.7% for the fully-sampled Cartesian acquisition (see Chapter 5). At RSD $\geq$ 75% all three reconstruction approaches gave similar results for PK parameter estimation, with all PK parameter errors $\leq$ 5%. Overall the continuous GA radial acquisition scheme used in this chapter, with RSD $\geq$ 75% (~50% Nyquist criterion fulfilled for a Cartesian acquisition, TE = 1.5ms, T_{res} = 1.4 s), outperformed the fully-sampled Cartesian acquisition approach presented in Chapter 5 (TE = 1.5ms, T_{res} = 1.2 s), both for the empirical measurement of the tissue CTCs and AIFs, and with the accuracy of the derived PK parameters, suggesting that a continuous GA radial trajectory may be a more accurate acquisition approach for use with DCE-MRI. This higher accuracy in curve-shape characterisation

may be related to the fact that radial trajectories intrinsically over-sample the centre of *k*-space, for example, at RSD = 75%, overall *k*-space is under-sampled, however, the centre of k-space is over-sampled relative to the 100% sampled Cartesian acquisition. This possibly provided more accurate measurement of the low-frequency signal components (encoded at the centre of *k*-space), and hence potentially better measurement of change in signal over time. A further advantage that a radial *k*-space sampling trajectory offers over a Cartesian trajectory is a lower susceptible to motion artefacts [46], which although not tested for in the present phantom study (since the phantom was static), is nevertheless a consideration for any *in vivo* patient scanning, particularly for a long-scan-time sequences such as DCE. Traditionally, Cartesian trajectories have been favoured over radial trajectories, since they were less susceptible to image artefacts (e.g. blurring) relating to B_0 non-uniformities, as well as gradient nonlinearities, however, advances in modern scanner hardware (i.e. magnet / gradient design) have improved these features greatly.

To date, only two preliminary patient studies have been reported in the literature which apply CS to DCE in the prostate, and although these studies both report positive results regarding tumour detection, image quality, clarity of anatomical detail, and improved spatiotemporal resolution, neither study applied quantitative PK modelling to the data, and rather only presented a qualitative analysis [137, 203]. Dikolaos *et al*. attempted to investigate the use of CS in the abdomen using a virtual simulation phantom, together with retrospectively under-sampled Cartesian DCE data, which were derived from a single prostate patient DCE-MRI dataset [251]. Although this study reports positive results with regards to the accurate recovery of kinetic parameter maps from data retrospectively under-sampled by up to a factor of eight, these result are derived either from a very simplified digital data phantom, or from a relative comparison of under-sampled patient data with a single fully-sampled MR dataset, from which the under-sampled data were derived. The present study is the first to utilise a physical dynamic phantom test device to quantitatively investigate the effects of under-sampling and CS reconstruction on the accuracy and precision of PK parameters, specifically for DCE-MRI in the prostate. In fact, this is the first truly quantitative CS DCE-MRI study, in which precise ground truth values were known *a priori*. Considering that the ground truth was not known in previous studies, direct comparisons with the current study are challenging. However, several studies which used PICS to reconstruct under-sampled DCE-MRI data in the breast have reported similar errors in derived PK parameters [206, 216, 242]. For example, Smith *et al*. reported errors of up to 6.6% and 21% for the measurement of K^{trans}, with x2 and x4 under-sampling respectively, compared with the

maximum errors of 4.3% and 8.1% in the present work at the same under-sampling factors (respectively). Similarly, for v_e parameter values, Smith *et* al. reported errors of up to 7.4% and 12%, again for x2 and x4 under-sampled data respectively, compared with maximum errors in v_e of 4.7% and 7.6% in the present study at the same under-sampling factors (respectively) [216]. The lower errors in this present study are probably a result of the VFAC pre-processing, which was lacking in the Smith study, and which was shown in Chapter 5 to have a strong detrimental effect on the accuracy of PK parameter estimation. Additionally, the Smith study was based on the retrospective under-sampling of a low temporal resolution initial dataset (T_{res} = 16.5 s), which probably also affected the results. A recent study by Kim *et al*., although not giving any exact errors in PK parameter measurements, did nevertheless report a relative difference in the accuracy of K^{trans} estimations depending on the actual K^{trans} value being measured, with higher 'tumour' K^{trans} values exhibiting a higher dependence on the amount that the data was under-sampled [206], as was also the case with the present study.

Some studies have used the qualitative interpretation of radiologists as a metric for the effects of CS on the quality of the reconstructed images, accessing image attributes such as *clarity of prostate capsule, clarity of peripheral zone / transition zone boundary, image sharpness*, and *overall image quality* [118, 137]. However the data from the present study demonstrates that when the objective of the study is the measurement of dynamic changes at a particular location over time (as is the case with DCE-MRI), although the apparent image quality may appear to be much diminished at high under-sampling factors, the quantitative temporal information (i.e. the shape of the CTC or AIF) may still be preserved, and retrieved by applying an appropriate model to the data. This is illustrated well in the present work by the data reconstructed using PICS with RSD = 4.68%, where the apparent image quality was much diminished (see Figure 6.4), however the PK parameter values were still recovered with mean errors less than 12%, 6.6%, and 12% for K^{trans}, v_e, and k_{ep} respectively, across all experimental runs.

Another possible confound with using CS in particular is the potential loss of contrast caused by omitting *k*-space data and the sparsifying constraints [227]. One common strategy in order to reduce this effect is to bias the *k*-space sampling densities toward low frequencies in order to mimic the distribution of power in *k*-space, which for anatomic images typically peaks at low spatial frequencies and reduces to a roughly constant level at higher frequencies [250]. Another advantage to using a radial sampling trajectory, such as the one used in this study, is that there is an intrinsic bias towards

the measurement of the centre of *k*-space (which corresponds to the low frequency signal components), and as such, this effects should be minimised with a such an acquisition.

Since certain methodologies are shared between this chapter and Chapter 5, with regards the phantom operation, VFAC, and PK data analysis, some of the same study limitations apply here, such as: limitations with the population patient average AIF used (i.e. derived from data acquired with T_{res} = 3.1 s, and with no VFAC applied to the original patient data); the use of a precisely known, rather than measured, base-line T_1 values (T_{10}); inflow controlled for; and patient motion not accounted for. For further details see section 5.4, where these limitations are discussed at length.

In this chapter it was demonstrated that a continuous golden angle radial *k*-space trajectory, combined with PICS reconstruction of the data, holds promise for improving the accuracy and precision of the DCE-MRI measurements, while also offering the additional benefits associated with using a continuous golden-angle radial acquisition, such as, tractability with regards the reconstructed T_{res} and a lower sensitivity to motion.

Chapter 7: Conclusions

In this thesis research was presented describing the development of a new robust phantom-based method for quantifying the absolute accuracy and precision of DCE-MRI measurements. A novel anthropomorphic phantom test device was presented, and subsequently used to perform a quantitative investigations into the effects of: temporal resolution (T_{res}), acquisition duration (AD), voxel-wise flip-angle correction (VFAC), pharmacokinetic (PK) model fitting regime, *k*-space acquisition trajectory, under-sampling *k*-space, as well as various image reconstruction methodologies.

7.1. General Conclusions

After a preliminary general introduction and theoretical background in Chapters 1 and 2, Chapter 3 describes the development of a novel dynamic anthropomorphic prostate phantom test device, and its use in quantitatively determining the measurement accuracy of several DCE-MRI acquisition protocols was demonstrated. The device was shown capable of simultaneously producing two distinct, accurate, and reproducible contrast agent concentration-time curves (CTCs), representative of those observed in DCE-MRI data of the prostate, within two separate MR-measurable

regions. The programmed shape of the CTCs produced by the system can easily be modified to simulate any shape CTC, as well as the arterial input function (AIF), as was subsequently demonstrated in Chapters 5 and 6, wherein modified methodologies also allowed for the precise and reproducible production of the rapidly-changing AIF curve-shape. The system was also optimised to allow for these curve-shapes to be precisely and repeatable produced at the lowest flow rates, thereby minimising CA use and any flow-related imaging artefact.

Of critical importance to the truly quantitative operation of the phantom device, and a step which has been lacking in previously-proposed phantom designs [139, 140, 142, 150-152], was to establish precisely-known ground truths for the CTCs and AIF produced at the device using a modality other than MR, where the signal was measured in a more direct fashion (i.e. in MRI the contrast agent (CA) concentration is indirectly derived from signal). A high spatiotemporal resolution optical imaging system was designed and built specifically for this purpose, providing highly-stable, calibrated, precisely-known measurements of the temporally-varying concentrations of CA within the measurement chambers. The calibrated manor in which the CA concentrations were derived from the optical data, as well and the design of the measurement chambers (i.e. to allow for optimal homogenous fluid distribution within the chambers at low flow rates) allowed for direct comparison between the optical and DCE-MRI data. Precise knowledge of the actual concentration of CA at a specific time-point and at a specific location within the device provided for a level of quantification simple not possible to date with patient studies alone or using other previously-proposed phantom designs.

The phantom device was constructed from agar-based tissue-mimicking materials (TMMs), which were shown to provide T_1 and T_2 values close to those of the various tissues found in the male pelvic region (muscle, fat, bone, etc.). Once fully-developed and tested, these TMMs were moulded and spatially-arranged to mimic the distribution of tissues found in the pelvic-region, providing an anthropomorphic environment wherein DCE-MRI measurements could be made which were subject to very similar confounding factors as patient measurements. This anthropomorphic design-characteristic, absent in previously proposed DCE-MRI phantom devices [139, 140, 142, 150-152], presents a clinically-relevant challenge to acquisition protocols developed and tested using the device, meaning that results from this device can directly inform patient imaging protocols.

The DCE-MRI results of Chapter 3 revealed errors in K^{trans}, v_e and k_{ep} values of up to

42%, 31%, and 50% respectively resulting from a simple variationof the T_{res}. These results demonstrated the operation of the phantom device, as well as heretofore unappreciated yet significant errors introduced by standard DCE acquisition protocols into derived PK output parameter values. The phantom device provides a system on which new and emerging DCE acquisition protocols can be accurately validated.

In Chapter 4 an in-depth study was performed investigating the effects of T_{res} and AD on the accuracy of MR-measured prostate-tissue CTCs (mimicking those typical of 'healthy' and 'tumour' prostate tissue), as well as phenomenological and PK parameters derived from these CTCs, across a range of T_{res} and AD values used in previously published prostate DCE-MRI studies. The results of this chapter demonstrated the critical dependence of the accuracy of model-free phenomenological and PK parameters derived from DCE-MRI data on the T_{res} and AD used in the acquisition. K^{trans} errors were below 14% for acquisitions with $T_{res} \leq 8.1$ s and AD ≥ 120 s, but increased dramatically for longer T_{res} and shorter AD values. v_e errors were below 12% for acquisitions with $T_{res} \leq 16.3$ s and AD ≥ 360 s, and again increased dramatically outside of this range. No major gain in K^{trans}, v_e, and *wash-in* parameters measurement accuracy was found from the use of AD ≥ 360 s, at $T_{res} \leq 8.1$ s (all measurement errors < 15%).

In Chapter 5 a physiologically-relevant AIF was established from patient prostate data, and new methodologies were developed and validated which allowed for the production of the rapidly-changing AIF curve-shape at the phantom. This AIF was then simultaneous measured with either a 'healthy' or 'tumour' CTC using a full-sampled Cartesian spoiled gradient echo sequence (five intra-session and five inter-session experiments). Similar to the previous chapters, results from this chapter gave large errors up to 47% in PK parameter estimations, when an inappropriate T_{res} was used and no flip-angle correction was performed on the data. By optimising the T_{res} these errors reduced to ~20%, and, by applying VFAC to the data the maximum error in PK parameter estimations dropped to $\leq 7\%$. These results further demonstrated the significant effect that T_{res}, as well as B_1^+-field inhomogeneity / flip angle variations, can have on the measured PK values, and thus underpins the importance of controlling these parameters by careful acquisition sequence optimisation, B_1^+-field mapping, and the use of an appropriate data pre-processing regime to correct for flip angle deviations. Further to this, the use of a linear least-squares (LLS) fitting approach was found to almost double the accuracy of K^{trans} estimates, and increased the precision of

K^{trans} (intra-session) and k_{ep} (intra- and inter-session) to ~4%, when compared with the much-more commonly used non-linear fitting method for the standard Tofts model. The LLS fitting method was also shown to be less dependent on T_{res}: for example, to measure PK parameter with errors ≤ 10%, the non-linear approach required a T_{res} ≤ 8.6 s, while the LLS method only required T_{res} ≤ 11 s. These results demonstrated that a further appreciable gain in PK modelling accuracy and precision can be achieved through the optimisation of the PK model fitting regime.

Certain methodologies used in Chapter 6 were informed by the results of the previous chapters, such as using an appropriately high T_{res}, applying VFAC to the data, and using a LLS approach to fit the PK model. The aim of this chapter was to use the phantom test device described in Chapter 3 to quantitatively investigate the effect of under-sampling the data on the accuracy and precision of measured CTCs and AIF, as well as the derived PK parameters. The data were acquired using a golden-angle (GA) radial *k*-space trajectory, reconstructed using no parallel imaging (PI) or compressed sensing (CS) (i.e. coil-by-coil (CbC) inverse gridding), PI only, and PI combined with CS (PICS) approaches; the MR-results were again compared against the precisely known ground truth values. Overall, the PICS reconstruction approach was shown to provide the highest accuracy for PK parameter estimation. Maximum mean errors in K^{trans}, v_e, and k_{ep} parameter values of less than 12%, 6.6%, and 12% respectively were calculated from five intra-session and five inter-session phantom experiments, for data reconstructed with as little as 3% of the data required to fulfil the Nyquist criterion for a radial acquisition, providing a twenty-one-fold gain in acquisition speed when compared with a standard fully-sampled Cartesian approach with the same acquisition geometries. The PICS reconstruction was shown to provide a gain in accuracy in PK parameter estimations of up to 34% and 42%, compared with the PI and CbC approaches respectively, for under-sampled data acquired with a GA radial *k*-space trajectory.

Across the breadth of this thesis the effects of various confounding factor on the absolute accuracy and precision on PK parameter estimations have systematically and quantitatively been investigated, refining the methodologies used, and ultimately arriving at a protocol which was demonstrated is capable of providing PK parameter estimations with mean errors ≤ 2%, and ≤ 4% intra- and inter-session precision (using a continuous GA radial acquisition with 100% radial sampling density, RAW data reconstructed using the PICS approach, VFAC applied, T_{res} = 1.85 s, and with LLS

fitting of the standard Tofts model).

These results may contribute towards a standardisation of DCE prostate acquisition and processing protocols, and thereby improve the consistency of data produced using this technique by avoiding known pitfalls. This could potentially lead to greater clinical confidence in the technique as a useful adjunct to existing prostate diagnostic imaging techniques, and thereby facilitate DCE's clinical adoption.

7.2. Suggestions for Future Work

Various parameters and methodologies associated with the acquisition, reconstruction, pre-processing, and analysis of DCE-MRI data have been shown in this thesis to have a strong influence on the accuracy and precision of measurements made of the tissue-mimicking CTCs and AIF. Signal-to-noise (SNR) values were presented for the data in Chapters 4 and 5, however, a more comprehensive investigation into the effects of SNR (with other confounding factors controlled for) using the phantom system (or a similar system) would be of interest. Other hardware-related limitations, such as signal linearity across different contrast agent concentration ranges, could also be investigated using quantitative, phantom-based methodologies similar to the ones outlined herein.

PK modelling shows great potential in correctly characterising prostate tissue microvascular behaviour; however, generally speaking, accurate modelling of prostate tissue is an area which requires further investigation. In this thesis PK analysis was performed via the widely-used standard Tofts model, however, more complex PK models such as the *Shutter Speed* [77] or the *Adiabatic Approximation of Tissue Homogeneity (AATH)* [79] models have also been proposed for the analysis of prostate DCE-MRI data, offering the potential for better tissue characterisation, possibly revealing additional (patho-)physiological information [78, 80-82]. However, these more complex models are thought to have an increased sensitivity to SNR [252] and T_{res} [22]; and as such, further similar phantom-based studies which focus on quantifying the requirements of these models would be useful.

In Chapter 6 of this thesis, a continuous GA radial acquisition scheme was used, exploiting the intrinsic properties of this trajectory to reconstruct multiple T_{res} datasets

from the same acquisition; a study into the effects of combining these datasets (i.e. a 'multi-T_{res}' approach) and any possible gain to temporally-varying contrast agent concentration measurements that this may provide would be of interest. Data collected with this acquisition trajectory also lends itself to a 'sliding window' reconstruction approach, where *k*-space data is shared between a specified number of temporally-adjacent image frames. A quantitative investigation in the effects of using such a reconstruction approach would also be of interest, since the sliding-window technique has shown promise in providing even higher-quality, high-spatiotemporal-resolution reconstructed datasets [185, 222, 253]. However, the effect that this *k*-space data sharing has on the dynamic temporal information remains unknown.

The use of the ESPIRiT implementation of PI was investigated in Chapter 6, however a further similar phantom-based investigation into the effects of using other PI approaches, such as SENSE [114], SMASH [115], and GRAPPA [138], would be very informative in establishing the absolute performance of each technique at various under-sampling factors. Further quantitative phantom-based studies investigating the optimal reconstruction parameters to use with CS would also be very informative. For example, a recent study by Kim *et al*. investigated the effects of the reconstruction weighting used (given as λ in Equation [6.1]) on the reconstructed data [206]. However, as the authors pointed out, the lack of any ground truth values in their study meant that a truly quantitative investigation was not possible, only a relative comparison. Likewise, the phantom-based approach outlined in Chapter 3 of this thesis (or similar approaches) could also be used to investigate the performance of other implementations of CS, such as those that also take further advantage of the sparsity that exists in the temporal domain, such as *k*-*t*-FOCUSS [214, 215], or those which estimate PK parameter directly from the under-sampled *k*-*t*-space data [251].

In a clinical setting, emphasis is placed on obtaining DCE-MRI data at high spatial resolution, since acquiring data at lower spatial resolution can lead to the possibility of missing smaller tumours or mischaracterising complex lesions [221, 254, 255]. Further work to investigate any possible effects of CS on the ability of a particular acquisition strategy to spatially resolve different sized targets would also be very beneficial, as CS can potentially loose some of the fine detail and contrast in the data during the reconstruction [250], for reasons outlined in the *Discussion* section of Chapter 6. This could be achieved by the inclusion of spatial resolution targets in possible future iteration of the dynamic phantom design proposed in this thesis (or similar design), as have been included in previously proposed static validation phantoms [256, 257].

Patient motion was not taken into account in the present study (as there was zero motion of the phantom); however this in known to effect measurements *in vivo*. For example, the abdominal aorta, where AIF measurements are generally made, can move by as much as 3 mm during a single DCE-MRI run, which approximates to ~17% of the vessels internal diameter [258], potentially leading to corruption of the data due to partial volume effects. Other phantom devices have included 'patient motion' mechanisms in their design [166], and future iterations of the phantom device presented in Chapter 3 could incorporate such mechanisms.

The methods presented in this thesis were specifically targeted at DCE MR-imaging of the prostate. However these methodologies could easily adapted for any anatomy by producing a phantom device, possibly using a similar agar-based method as outlined in Chapter 3, based on the tissue compositions and distributions at the anatomy-of-interest. In this case, the same, or similar, pump system, tubing setup, and validation methods could be used.

7.3. Outlook

The work of this thesis highlighted the critical dependence of the accuracy and precision of DCE-MRI measurements on the methodologies used, as well as demonstrated a novel phantom-based method whereby DCE protocols can be refined and optimised. Using this phantom-based method to perform a series of quantitative DCE-MRI experiments; absolute errors in PK parameter estimation were reduced from ≤50% (using a standard Cartesian acquisition) to ≤ 2% (using a continuous GA radial acquisition reconstructed using the PICS approach, with VFAC applied, and linear PK model fitting), with a similar gain in precision from ≤18% to ≤4%. Although beyond the scope of this thesis, future patient studies using highly accurate and precise protocols, developed in such a quantitative manner, would be of great interest in order to fully investigate the full diagnostic potential of DCE-MRI. The use of quantitative phantom-based approaches to access and optimise the accuracy and precision of DCE-MRI techniques, offers the prospect of standardising DCE acquisition protocols for the prostate and beyond, and ultimately a wider acceptance of the technique for use in routine clinical examinations.

References

1. Torre, L.A., Siegel, R.L., Ward, E.M., and Jemal, A., *Global Cancer Incidence and Mortality Rates and Trends—An Update.* Cancer Epidemiology Biomarkers & Prevention, 2016. **25**(1): p. 16-27.
2. Jemal, A., Siegel, R., Ward, E., Hao, Y., Xu, J., and Thun, M., *Cancer statistics.* CA Cancer J Clin, 2009. **59**: p. 225-249.
3. Hricak, H., *MR imaging and MR spectroscopic imaging in the pre-treatment evaluation of prostate cancer.* Br J Radiol, 2005. **78 Spec No 2**: p. S103-11.
4. Amsellem-Ouazana, D., Younes, P., Conquy, S., Peyromaure, M., Flam, T., Debre, B., and Zerbib, M., *Negative prostatic biopsies in patients with a high risk of prostate cancer. Is the combination of endorectal MRI and magnetic resonance spectroscopy imaging (MRSI) a useful tool? A preliminary study.* Eur Urol, 2005. **47**(5): p. 582-6.
5. Sciarra, A., Autran Gomez, A., Salciccia, S., Dattilo, C., Ciccariello, M., Gentile, V., and Di Silverio, F., *Biopsy-derived Gleason artifact and prostate volume: experience using ten samples in larger prostates.* Urol Int, 2008. **80**(2): p. 145-50.
6. Zackrisson, B., Aus, G., Bergdahl, S., Lilja, H., Lodding, P., Pihl, C.G., and Hugosson, J., *The risk of finding focal cancer (less than 3 mm) remains high on re-biopsy of patients with persistently increased prostate specific antigen but the clinical significance is questionable.* J Urol, 2004. **171**(4): p. 1500-3.
7. Mirowitz, S.A., Brown, J.J., and Heiken, J.P., *Evaluation of the prostate and prostatic carcinoma with gadolinium-enhanced endorectal coil MR imaging.* Radiology, 1993. **186**(1): p. 153-7.
8. Quinn, S.F., Franzini, D.A., Demlow, T.A., Rosencrantz, D.R., Kim, J., Hanna, R.M., and Szumowski, J., *MR imaging of prostate cancer with an endorectal surface coil technique: correlation with whole-mount specimens.* Radiology, 1994. **190**(2): p. 323-7.
9. Brown, G., Macvicar, D.A., Ayton, V., and Husband, J.E., *The role of intravenous contrast enhancement in magnetic resonance imaging of prostatic carcinoma.* Clin Radiol, 1995. **50**(9): p. 601-6.
10. Huch Boni, R.A., Boner, J.A., Lutolf, U.M., Trinkler, F., Pestalozzi, D.M., and Krestin, G.P., *Contrast-enhanced endorectal coil MRI in local staging of prostate carcinoma.* J Comput Assist Tomogr, 1995. **19**(2): p. 232-7.
11. Noworolski, S.M., Vigneron, D.B., Chen, A.P., and Kurhanewicz, J., *Dynamic contrast-enhanced MRI and MR diffusion imaging to distinguish between glandular and stromal prostatic tissues.* Magn Reson Imaging, 2008. **26**(8): p. 1071-80.
12. Futterer, J.J., Heijmink, S.W., Scheenen, T.W., Veltman, J., Huisman, H.J., Vos, P., Hulsbergen-Van de Kaa, C.A., Witjes, J.A., Krabbe, P.F., Heerschap, A., and Barentsz, J.O., *Prostate cancer localization with dynamic contrast-enhanced MR imaging and proton MR spectroscopic imaging.* Radiology, 2006. **241**(2): p. 449-58.
13. Hara, N., Okuizumi, M., Koike, H., Kawaguchi, M., and Bilim, V., *Dynamic contrast-enhanced magnetic resonance imaging (DCE-MRI) is a useful modality for the precise detection and staging of early prostate cancer.* Prostate, 2005. **62**(2): p. 140-7.
14. Vos, E.K., Litjens, G.J., Kobus, T., Hambrock, T., Hulsbergen-van de Kaa, C.A., Barentsz, J.O., Huisman, H.J., and Scheenen, T.W., *Assessment of prostate cancer aggressiveness using dynamic contrast-enhanced magnetic resonance imaging at 3 T.* Eur Urol, 2013. **64**(3): p. 448-55.
15. Chen, Y.J., Chu, W.C., Pu, Y.S., Chueh, S.C., Shun, C.T., and Tseng, W.Y., *Washout gradient in dynamic contrast-enhanced MRI is associated with tumor aggressiveness of prostate cancer.* J Magn Reson Imaging, 2012. **36**(4): p. 912-9.
16. Tamada, T., Sone, T., Higashi, H., Jo, Y., Yamamoto, A., Kanki, A., and Ito, K., *Prostate cancer detection in patients with total serum prostate-specific antigen levels of 4-10 ng/mL: diagnostic efficacy of diffusion-weighted imaging, dynamic contrast-enhanced MRI, and T2-weighted imaging.* AJR Am J Roentgenol, 2011. **197**(3): p. 664-70.
17. Kozlowski, P., Chang, S.D., Jones, E.C., Berean, K.W., Chen, H., and Goldenberg, S.L., *Combined diffusion-weighted and dynamic contrast-enhanced MRI for prostate cancer diagnosis--correlation with biopsy and histopathology.* J Magn Reson Imaging, 2006. **24**(1): p. 108-13.
18. Tanimoto, A., Nakashima, J., Kohno, H., Shinmoto, H., and Kuribayashi, S., *Prostate cancer screening: the clinical value of diffusion-weighted imaging and dynamic MR imaging in combination with T2-weighted imaging.* J Magn Reson Imaging, 2007. **25**(1): p. 146-52.
19. Li, C., Chen, M., Li, S., Zhao, X., Zhang, C., Luo, X., and Zhou, C., *Detection of prostate cancer in peripheral zone: comparison of MR diffusion tensor imaging, quantitative dynamic contrast-enhanced MRI, and the two techniques combined at 3.0 T.* Acta Radiol, 2014. **55**(2): p. 239-47.
20. Portalez, D., Rollin, G., Leandri, P., Elman, B., Mouly, P., Jonca, F., and Malavaud, B., *Prospective comparison of T2w-MRI and dynamic-contrast-enhanced MRI, 3D-MR spectroscopic imaging or diffusion-weighted MRI in repeat TRUS-guided biopsies.* Eur Radiol, 2010. **20**(12): p. 2781-90.
21. Panebianco, V., Sciarra, A., Ciccariello, M., Lisi, D., Bernardo, S., Cattarino, S., Gentile, V., and

Passariello, R., *Role of magnetic resonance spectroscopic imaging ([1H]MRSI) and dynamic contrast-enhanced MRI (DCE-MRI) in identifying prostate cancer foci in patients with negative biopsy and high levels of prostate-specific antigen (PSA).* La radiologia medica, 2010. **115**(8): p. 1314-1329.
22. Henderson, E., Rutt, B.K., and Lee, T.Y., *Temporal sampling requirements for the tracer kinetics modeling of breast disease.* Magn Reson Imaging, 1998. **16**(9): p. 1057-73.
23. Perdona, S., Di Lorenzo, G., Autorino, R., Buonerba, C., De Sio, M., Setola, S.V., Fusco, R., Ronza, F.M., Caraglia, M., Ferro, M., and Petrillo, A., *Combined magnetic resonance spectroscopy and dynamic contrast-enhanced imaging for prostate cancer detection.* Urol Oncol, 2013. **31**(6): p. 761-5.
24. Padhani, A.R., Gapinski, C.J., Macvicar, D.A., Parker, G.J., Suckling, J., Revell, P.B., Leach, M.O., Dearnaley, D.P., and Husband, J.E., *Dynamic contrast enhanced MRI of prostate cancer: correlation with morphology and tumour stage, histological grade and PSA.* Clin Radiol, 2000. **55**(2): p. 99-109.
25. Oto, A., Yang, C., Kayhan, A., Tretiakova, M., Antic, T., Schmid-Tannwald, C., Eggener, S., Karczmar, G.S., and Stadler, W.M., *Diffusion-weighted and dynamic contrast-enhanced MRI of prostate cancer: correlation of quantitative MR parameters with Gleason score and tumor angiogenesis.* AJR Am J Roentgenol, 2011. **197**(6): p. 1382-90.
26. Mettlin, C.J., Murphy, G.P., McDonald, C.J., and Menck, H.R., *The National Cancer Data base Report on increased use of brachytherapy for the treatment of patients with prostate carcinoma in the U.S.* Cancer, 1999. **86**(9): p. 1877-82.
27. Walsh, P., Retik, A., Vaughan, E., D'Amico, A., Crook, J., Beard, C., DeWeese, T., and Hurwitz, M., *Campbell's Urology; Radiation therapy for prostate cancer*. 2002, Saunders: Philadelphia. p. 3147–3170.
28. Urology, E.A.o., *Guidelines on prostate cancer*, 2009, Arnhem: European Association of Urology.
29. Caloglu, M. and Ciezki, J., *Prostate-specific antigen bounce after prostate brachytherapy: review of a confusing phenomenon.* Urology, 2009. **74**(6): p. 1183-90.
30. Horwitz, E.M., Levy, L.B., Thames, H.D., Kupelian, P.A., Martinez, A.A., Michalski, J.M., Pisansky, T.M., Sandler, H.M., Shipley, W.U., Zelefsky, M.J., Zietman, A.L., and Kuban, D.A., *Biochemical and clinical significance of the posttreatment prostate-specific antigen bounce for prostate cancer patients treated with external beam radiation therapy alone: a multiinstitutional pooled analysis.* Cancer, 2006. **107**(7): p. 1496-502.
31. Wu, L.M., Xu, J.R., Gu, H.Y., Hua, J., Zhu, J., Chen, J., Zhang, W., and Hu, J., *Role of magnetic resonance imaging in the detection of local prostate cancer recurrence after external beam radiotherapy and radical prostatectomy.* Clin Oncol (R Coll Radiol), 2013. **25**(4): p. 252-64.
32. Haider, M.A., Chung, P., Sweet, J., Toi, A., Jhaveri, K., Menard, C., Warde, P., Trachtenberg, J., Lockwood, G., and Milosevic, M., *Dynamic contrast-enhanced magnetic resonance imaging for localization of recurrent prostate cancer after external beam radiotherapy.* Int J Radiat Oncol Biol Phys, 2008. **70**(2): p. 425-30.
33. Kara, T., Akata, D., Akyol, F., Karcaaltincaba, M., and Ozmen, M., *The value of dynamic contrast-enhanced MRI in the detection of recurrent prostate cancer after external beam radiotherapy: correlation with transrectal ultrasound and pathological findings.* Diagn Interv Radiol, 2011. **17**(1): p. 38-43.
34. Moman, M.R., van den Berg, C.A., Boeken Kruger, A.E., Battermann, J.J., Moerland, M.A., van der Heide, U.A., and van Vulpen, M., *Focal salvage guided by T2-weighted and dynamic contrast-enhanced magnetic resonance imaging for prostate cancer recurrences.* Int J Radiat Oncol Biol Phys, 2010. **76**(3): p. 741-6.
35. Boonsirikamchai, P., Kaur, H., Kuban, D.A., Jackson, E., Hou, P., and Choi, H., *Use of maximum slope images generated from dynamic contrast-enhanced MRI to detect locally recurrent prostate carcinoma after prostatectomy: a practical approach.* AJR Am J Roentgenol, 2012. **198**(3): p. W228-36.
36. Cirillo, S., Petracchini, M., Scotti, L., Gallo, T., Macera, A., Bona, M.C., Ortega, C., Gabriele, P., and Regge, D., *Endorectal magnetic resonance imaging at 1.5 Tesla to assess local recurrence following radical prostatectomy using T2-weighted and contrast-enhanced imaging.* Eur Radiol, 2009. **19**(3): p. 761-9.
37. Kim, C.K., Park, B.K., Lee, H.M., Kim, S.S., and Kim, E., *MRI techniques for prediction of local tumor progression after high-intensity focused ultrasonic ablation of prostate cancer.* AJR Am J Roentgenol, 2008. **190**(5): p. 1180-6.
38. Rouviere, O., Lyonnet, D., Raudrant, A., Colin-Pangaud, C., Chapelon, J.Y., Bouvier, R., Dubernard, J.M., and Gelet, A., *MRI appearance of prostate following transrectal HIFU ablation of localized cancer.* Eur Urol, 2001. **40**(3): p. 265-74.
39. Lauterbur, P.C., *Image Formation by Induced Local Interactions: Examples Employing Nuclear Magnetic Resonance.* Nature, 1973. **242**(5394): p. 190-191.
40. Lauterbur, P.C., *Measurements of local nuclear magnetic resonance relaxation times*, in *Bull. Am. Phys. Soc., Ser. II*1972. p. 86.
41. Mansfield, P., *Multi-planar image formation using NMR spin echoes.* Journal of Physics C: Solid State Physics, 1977. **10**(3): p. L55.

42. Mansfield, P. and Maudsley, A.A., *Planar spin imaging by NMR.* Journal of Physics C: Solid State Physics, 1976. **9**(15): p. L409.
43. Edelstein, W.A., Hutchison, J.M., Johnson, G., and Redpath, T., *Spin warp NMR imaging and applications to human whole-body imaging.* Phys Med Biol, 1980. **25**(4): p. 751-6.
44. Bloch, F., Hansen, W.W., and Packard, M., *Nuclear Induction.* Physical Review, 1946. **69**(3-4): p. 127-127.
45. Rabi, I.I., Ramsey, N.F., and Schwinger, J., *Use of Rotating Coordinates in Magnetic Resonance Problems.* Reviews of Modern Physics, 1954. **26**(2): p. 167-171.
46. Glover, G.H. and Pauly, J.M., *Projection Reconstruction Techniques for Reduction of Motion Effects in MRI.* Magn Reson Med, 1992. **28**(2): p. 275-289.
47. Meyer, C.H., Hu, B.S., Nishimura, D.G., and Macovski, A., *Fast spiral coronary artery imaging.* Magn Reson Med, 1992. **28**(2): p. 202-13.
48. Scheffler, K. and Hennig, J., *Reduced circular field-of-view imaging.* Magn Reson Med, 1998. **40**(3): p. 474-480.
49. Lustig, M., Donoho, D., and Pauly, J.M., *Sparse MRI: The application of compressed sensing for rapid MR imaging.* Magn Reson Med, 2007. **58**(6): p. 1182-1195.
50. Jackson, J.I., Meyer, C.H., Nishimura, D.G., and Macovski, A., *Selection of a convolution function for Fourier inversion using gridding [computerised tomography application].* IEEE Trans Med Imaging, 1991. **10**(3): p. 473-8.
51. Schabel, M.C. and Parker, D.L., *Uncertainty and bias in contrast concentration measurements using spoiled gradient echo pulse sequences.* Phys Med Biol, 2008. **53**(9): p. 2345-73.
52. Robert W. Brown, Y.-C.N.C., E. Mark Haacke, Michael R. Thompson, Ramesh Venkatesan, *Fast Imaging in the Steady State*, in *Magnetic Resonance Imaging: Physical Principles and Sequence Design*. 2014, John Wiley & Sons Ltd. p. 447-510.
53. Caravan, P., Ellison, J.J., McMurry, T.J., and Lauffer, R.B., *Gadolinium(III) Chelates as MRI Contrast Agents: Structure, Dynamics, and Applications.* Chemical Reviews, 1999. **99**(9): p. 2293-2352.
54. Wang, Y.X.J., *Superparamagnetic iron oxide based MRI contrast agents: Current status of clinical application.* Quant Imaging Med Surg, 2011. **1**(1): p. 35-40.
55. Cory, D.A., Schwartzentruber, D.J., and Mock, B.H., *Ingested manganese chloride as a contrast agent for magnetic resonance imaging.* Magn Reson Imaging, 1987. **5**(1): p. 65-70.
56. Chapman, S., Dobrovolskaia, M., Farahani, K., Goodwin, A., Joshi, A., Lee, H., Meade, T., Pomper, M., Ptak, K., Rao, J., Singh, R., Sridhar, S., Stern, S., Wang, A., Weaver, J.B., Woloschak, G., and Yang, L., *Nanoparticles for cancer imaging: The good, the bad, and the promise.* Nano Today, 2013. **8**(5): p. 454-60.
57. Weinmann, H.J., Laniado, M., and Mutzel, W., *Pharmacokinetics of GdDTPA/dimeglumine after intravenous injection into healthy volunteers.* Physiol Chem Phys Med NMR, 1984. **16**(2): p. 167-72.
58. Ferlay, J., Soerjomataram, I., Dikshit, R., Eser, S., Mathers, C., Rebelo, M., Parkin, D.M., Forman, D., and Bray, F., *Cancer incidence and mortality worldwide: Sources, methods and major patterns in GLOBOCAN 2012.* International Journal of Cancer, 2015. **136**(5): p. E359-E386.
59. Battegay, E.J., *Angiogenesis: mechanistic insights, neovascular diseases, and therapeutic prospects.* J Mol Med, 1995. **73**(7): p. 333-346.
60. Folkman, J., *What Is the Evidence That Tumors Are Angiogenesis Dependent?* JNCI J Natl Cancer Inst, 1990. **82**(1): p. 4-6.
61. Passe, T.J., Bluemke, D.A., and Siegelman, S.S., *Tumor Angiogenesis: Tutorial on Implications for Imaging.* Radiology, 1997. **203**: p. 593-600.
62. Martini, F.H., *Fundamentals of Anatomy and Physiology*. 9th ed. 2012, Upper Saddle River, N.J, Prentice Hall: Pearson.
63. Girouin, N., Mege-Lechevallier, F., Tonina Senes, A., Bissery, A., Rabilloud, M., Marechal, J.M., Colombel, M., Lyonnet, D., and Rouviere, O., *Prostate dynamic contrast-enhanced MRI with simple visual diagnostic criteria: is it reasonable?* Eur Radiol, 2007. **17**(6): p. 1498-509.
64. Kim, J.K., Hong, S.S., Choi, Y.J., Park, S.H., Ahn, H., Kim, C.S., and Cho, K.S., *Wash-in rate on the basis of dynamic contrast-enhanced MRI: usefulness for prostate cancer detection and localization.* J Magn Reson Imaging, 2005. **22**(5): p. 639-46.
65. Noworolski, S.M., Henry, R.G., Vigneron, D.B., and Kurhanewicz, J., *Dynamic contrast-enhanced MRI in normal and abnormal prostate tissues as defined by biopsy, MRI, and 3D MRSI.* Magn Reson Med, 2005. **53**(2): p. 249-55.
66. Kim, S.H., Choi, M.S., Kim, M.J., Kim, Y.H., and Cho, S.H., *Role of semi–quantitative dynamic contrast–enhanced MR imaging in characterization and grading of prostate cancer.* European Journal of Radiology, 2017.
67. Yankeelov, T.E., Lucia, J.J., Lepage, M., Li, R., Debusk, L., Lin, P.C., Price, R.R., and Gore, J.C., *Quantitative pharmacokinetic analysis of DCE-MRI data without an arterial input function: a reference region model.* Magn Reson Imaging, 2005. **23**: p. 519–529.
68. Tofts, P.S. and Kermode, A.G., *Measurement of the blood-brain barrier permeability and leakage space using dynamic MR imaging. 1. Fundamental concepts.* Magn Reson Med, 1991(17): p.

357-367.
69. Borren, A., Groenendaal, G., van der Groep, P., Moman, M.R., Boeken Kruger, A.E., van der Heide, U.A., Jonges, T.N., van Diest, P.J., van Vulpen, M., and Philippens, M.E., *Expression of hypoxia-inducible factor-1alpha and -2alpha in whole-mount prostate histology: relation with dynamic contrast-enhanced MRI and Gleason score.* Oncol Rep, 2013. **29**(6): p. 2249-54.
70. Jackson, A.S., Reinsberg, S.A., Sohaib, S.A., Charles-Edwards, E.M., Jhavar, S., Christmas, T.J., Thompson, A.C., Bailey, M.J., Corbishley, C.M., Fisher, C., Leach, M.O., and Dearnaley, D.P., *Dynamic contrast-enhanced MRI for prostate cancer localization.* Br J Radiol, 2009. **82**(974): p. 148-56.
71. Koh, T.S., Bisdas, S., Koh, D.M., and Thng, C.H., *Fundamentals of tracer kinetics for dynamic contrast-enhanced MRI.* J Magn Reson Imaging, 2011. **34**(6): p. 1262-76.
72. Røe, K., Mikalsen, L., van der Kogel, A., Bussink, J., Lyng, H., Ree, A., Marignol, L., and Olsen, D., *Vascular responses to radiotherapy and androgen-deprivation therapy in experimental prostate cancer.* Radiation Oncology, 2012. **7**(1): p. 1-13.
73. Tofts, P.S., *Modeling tracer kinetics in dynamic Gd-DTPA MR imaging.* J Magn Reson Imaging, 1997. **7**(1): p. 91-101.
74. Barrett, T., Gill, A.B., Kataoka, M.Y., Priest, A.N., Joubert, I., McLean, M.A., Graves, M.J., Stearn, S., Lomas, D.J., Griffiths, J.R., Neal, D., Gnanapragasam, V.J., and Sala, E., *DCE and DW MRI in monitoring response to androgen deprivation therapy in patients with prostate cancer: a feasibility study.* Magn Reson Med, 2012. **67**(3): p. 778-85.
75. Brix, G., Semmler, W., Port, R., Schad, L.R., Layer, G., and Lorenz, W.J., *Pharmacokinetic parameters in CNS Gd-DTPA enhanced MR imaging.* J Comput Assist Tomogr, 1991. **15**(4): p. 621-8.
76. Heverhagen, J.T., von Tengg-Kobligk, H., Baudendistel, K.T., Jia, G., Polzer, H., Henry, H., Levine, A.L., Rosol, T.J., and Knopp, M.V., *Benign prostate hyperplasia: evaluation of treatment response with DCE MRI.* MAGMA, 2004. **17**(1): p. 5-11.
77. Li, X., Rooney, W.D., and Springer, C.S., Jr., *A unified magnetic resonance imaging pharmacokinetic theory: intravascular and extracellular contrast reagents.* Magn Reson Med, 2005. **54**(6): p. 1351-9.
78. Li, B., Du, Y., Yang, H.F., Huang, Y.Y., Meng, J., and Xiao, D.M., *Magnetic resonance imaging for prostate cancer clinical application.* Chin J Cancer Res, 2013. **25**(2): p. 240-249.
79. St Lawrence, K.S. and Lee, T.Y., *An adiabatic approximation to the tissue homogeneity model for water exchange in the brain: I. Theoretical derivation.* J Cereb Blood Flow Metab, 1998. **18**(12): p. 1365-77.
80. Buckley, D.L., Roberts, C., Parker, G.J., Logue, J.P., and Hutchinson, C.E., *Prostate cancer: evaluation of vascular characteristics with dynamic contrast-enhanced T1-weighted MR imaging--initial experience.* Radiology, 2004. **233**(3): p. 709-15.
81. Kershaw, L.E. and Buckley, D.L., *Precision in measurements of perfusion and microvascular permeability with T1-weighted dynamic contrast-enhanced MRI.* Magn Reson Med, 2006. **56**(5): p. 986-92.
82. Ludemann, L., Prochnow, D., Rohlfing, T., Franiel, T., Warmuth, C., Taupitz, M., Rehbein, H., and Beyersdorff, D., *Simultaneous quantification of perfusion and permeability in the prostate using dynamic contrast-enhanced magnetic resonance imaging with an inversion-prepared dual-contrast sequence.* Ann Biomed Eng, 2009. **37**(4): p. 749-62.
83. Brix, G., Bahner, M.L., Hoffmann, U., Horvath, A., and Schreiber, W., *Regional Blood Flow, Capillary Permeability, and Compartmental Volumes: Measurement with Dynamic CT—Initial Experience.* Radiology, 1999(January): p. 269-276.
84. Tofts, P.S., Brix, G., Buckley, D.L., Evelhoch, J.L., Henderson, E., Knopp, M.V., Larsson, H.B., Lee, T.Y., Mayr, N.A., Parker, G.J., Port, R.E., Taylor, J., and Weisskoff, R.M., *Estimating kinetic parameters from dynamic contrast-enhanced T(1)-weighted MRI of a diffusable tracer: standardized quantities and symbols.* J Magn Reson Imaging, 1999. **10**(3): p. 223-32.
85. Larsson, H.B., Stubgaard, M., Frederiksen, J.L., Jensen, M., Henriksen, O., and Paulson, O.B., *Quantitation of blood-brain barrier defect by magnetic resonance imaging and gadolinium-DTPA in patients with multiple sclerosis and brain tumors.* Magn Reson Med, 1990. **16**(1): p. 117-31.
86. Ahearn, T.S., Staff, R.T., Redpath, T.W., and Semple, S.I., *The use of the Levenberg-Marquardt curve-fitting algorithm in pharmacokinetic modelling of DCE-MRI data.* Phys Med Biol, 2005. **50**(9): p. N85-92.
87. Cardenas-Rodriguez, J., Howison, C.M., and Pagel, M.D., *A linear algorithm of the reference region model for DCE-MRI is robust and relaxes requirements for temporal resolution.* Magn Reson Imaging, 2013. **31**(4): p. 497-507.
88. Murase, K., *Efficient method for calculating kinetic parameters using T1-weighted dynamic contrast-enhanced magnetic resonance imaging.* Magn Reson Med, 2004. **51**(4): p. 858-62.
89. Blomqvist, G., *On the construction of functional maps in positron emission tomography.* J Cereb Blood Flow Metab, 1984. **4**(4): p. 629-32.
90. Yang, X., Liang, J., Heverhagen, J.T., Jia, G., Schmalbrock, P., Sammet, S., Koch, R., and Knopp, M.V., *Improving the pharmacokinetic parameter measurement in dynamic contrast-enhanced MRI by use of the arterial input function: theory and clinical application.* Magn Reson

Med, 2008. **59**(6): p. 1448-56.
91. Yang, C., Karczmar, G.S., Medved, M., and Stadler, W.M., *Estimating the arterial input function using two reference tissues in dynamic contrast-enhanced MRI studies: fundamental concepts and simulations.* Magn Reson Med, 2004. **52**(5): p. 1110-7.
92. Korporaal, J.G., van den Berg, C.A., van Osch, M.J., Groenendaal, G., van Vulpen, M., and van der Heide, U.A., *Phase-based arterial input function measurements in the femoral arteries for quantification of dynamic contrast-enhanced (DCE) MRI and comparison with DCE-CT.* Magn Reson Med, 2011. **66**(5): p. 1267-74.
93. Fennessy, F.M., Fedorov, A., Penzkofer, T., Kim, K.W., Hirsch, M.S., Vangel, M.G., Masry, P., Flood, T.A., Chang, M.C., Tempany, C.M., Mulkern, R.V., and Gupta, S.N., *Quantitative pharmacokinetic analysis of prostate cancer DCE-MRI at 3T: comparison of two arterial input functions on cancer detection with digitized whole mount histopathological validation.* Magn Reson Imaging, 2015. **33**(7): p. 886-94.
94. Khalifa, F., Soliman, A., El-Baz, A., Abou El-Ghar, M., El-Diasty, T., Gimel'farb, G., Ouseph, R., and Dwyer, A.C., *Models and methods for analyzing DCE-MRI: A review.* Med Phys, 2014. **41**(12): p. 124301-n/a.
95. Larsson, H.B. and Tofts, P.S., *Measurement of blood-brain barrier permeability using dynamic Gd-DTPA scanning--a comparison of methods.* Magn Reson Med, 1992. **24**(1): p. 174-6.
96. Bilhim, T., Pisco, J.M., Furtado, A., Casal, D., Pais, D., Pinheiro, L.C., and O'Neill, J.E., *Prostatic arterial supply: demonstration by multirow detector Angio CT and Catheter Angiography.* Eur Radiol, 2011. **21**(5): p. 1119-1126.
97. Fedorov, A., Fluckiger, J., Ayers, G.D., Li, X., Gupta, S.N., Tempany, C., Mulkern, R., Yankeelov, T.E., and Fennessy, F.M., *A comparison of two methods for estimating DCE-MRI parameters via individual and cohort based AIFs in prostate cancer: a step towards practical implementation.* Magn Reson Imaging, 2014. **32**(4): p. 321-9.
98. Meng, R., Chang, S.D., Jones, E.C., Goldenberg, S.L., and Kozlowski, P., *Comparison between population average and experimentally measured Arterial Input Function in predicting biopsy results in prostate cancer.* Acad Radiol, 2010. **17**(4): p. 520-5.
99. Cheng, H.L. and Wright, G.A., *Rapid high-resolution T(1) mapping by variable flip angles: accurate and precise measurements in the presence of radiofrequency field inhomogeneity.* Magn Reson Med, 2006. **55**(3): p. 566-74.
100. Cheng, H.L., *T1 measurement of flowing blood and arterial input function determination for quantitative 3D T1-weighted DCE-MRI.* J Magn Reson Imaging, 2007. **25**(5): p. 1073-8.
101. de Rochefort, L., Nguyen, T., Brown, R., Spincemaille, P., Choi, G., Weinsaft, J., Prince, M.R., and Wang, Y., *In vivo quantification of contrast agent concentration using the induced magnetic field for time-resolved arterial input function measurement with MRI.* Med Phys, 2008. **35**(12): p. 5328-39.
102. Roberts, C., Little, R., Watson, Y., Zhao, S., Buckley, D.L., and Parker, G.J., *The effect of blood inflow and B(1)-field inhomogeneity on measurement of the arterial input function in axial 3D spoiled gradient echo dynamic contrast-enhanced MRI.* Magn Reson Med, 2011. **65**(1): p. 108-19.
103. Azahaf, M., Haberley, M., Betrouni, N., Ernst, O., Behal, H., Duhamel, A., Ouzzane, A., and Puech, P., *Impact of arterial input function selection on the accuracy of dynamic contrast-enhanced MRI quantitative analysis for the diagnosis of clinically significant prostate cancer.* J Magn Reson Imaging, 2016. **43**(3): p. 737-49.
104. McGrath, D.M., Bradley, D.P., Tessier, J.L., Lacey, T., Taylor, C.J., and Parker, G.J., *Comparison of model-based arterial input functions for dynamic contrast-enhanced MRI in tumor bearing rats.* Magn Reson Med, 2009. **61**(5): p. 1173-84.
105. Parker, G.J., Roberts, C., Macdonald, A., Buonaccorsi, G.A., Cheung, S., Buckley, D.L., Jackson, A., Watson, Y., Davies, K., and Jayson, G.C., *Experimentally-derived functional form for a population-averaged high-temporal-resolution arterial input function for dynamic contrast-enhanced MRI.* Magn Reson Med, 2006. **56**(5): p. 993-1000.
106. Schabel, M.C., Fluckiger, J.U., and DiBella, E.V., *A model-constrained Monte Carlo method for blind arterial input function estimation in dynamic contrast-enhanced MRI: I. Simulations.* Phys Med Biol, 2010. **55**(16): p. 4783-806.
107. Wang, S., Fan, X., Medved, M., Pineda, F.D., Yousuf, A., Oto, A., and Karczmar, G.S., *Arterial input functions (AIFs) measured directly from arteries with low and standard doses of contrast agent, and AIFs derived from reference tissues.* Magn Reson Imaging, 2016. **34**(2): p. 197-203.
108. Just, N., Koh, D.M., D'Arcy, J., Collins, D.J., and Leach, M.O., *Assessment of the effect of haematocrit-dependent arterial input functions on the accuracy of pharmacokinetic parameters in dynamic contrast-enhanced MRI.* NMR Biomed, 2011. **24**(7): p. 902-15.
109. Simpson, N.E., He, Z., and Evelhoch, J.L., *Deuterium NMR tissue perfusion measurements using the tracer uptake approach: I. Optimization of methods.* Magn Reson Med, 1999. **42**(1): p. 42-52.
110. Kovar, D.A., Lewis, M., and Karczmar, G.S., *A new method for imaging perfusion and contrast extraction fraction: input functions derived from reference tissues.* J Magn Reson Imaging, 1998. **8**(5): p. 1126-34.
111. Mehrabian, H., Chopra, R., and Martel, A.L., *Calculation of intravascular signal in dynamic*

contrast enhanced-MRI using adaptive complex independent component analysis. IEEE Trans Med Imaging, 2013. **32**(4): p. 699-710.
112. Walker-Samuel, S., Parker, C.C., Leach, M.O., and Collins, D.J., *Reproducibility of reference tissue quantification of dynamic contrast-enhanced data: comparison with a fixed vascular input function.* Phys Med Biol, 2007. **52**(1): p. 75-89.
113. Marseille, G.J., de Beer, R., Fuderer, M., Mehlkopf, A.F., and van Ormondt, D., *Nonuniform Phase-Encode Distributions for MRI Scan Time Reduction.* J Magn Reson B, 1996. **111**(1): p. 70-5.
114. Pruessmann, K.P., Weiger, M., Scheidegger, M.B., and Boesiger, P., *SENSE: sensitivity encoding for fast MRI.* Magn Reson Med, 1999. **42**(5): p. 952-62.
115. Sodickson, D.K. and Manning, W.J., *Simultaneous acquisition of spatial harmonics (SMASH): fast imaging with radiofrequency coil arrays.* Magn Reson Med, 1997. **38**(4): p. 591-603.
116. Korosec, F.R., Frayne, R., Grist, T.M., and Mistretta, C.A., *Time-resolved contrast-enhanced 3D MR angiography.* Magn Reson Med, 1996. **36**(3): p. 345-51.
117. Tsao, J., Boesiger, P., and Pruessmann, K.P., *k-t BLAST and k-t SENSE: dynamic MRI with high frame rate exploiting spatiotemporal correlations.* Magn Reson Med, 2003. **50**(5): p. 1031-42.
118. Chandarana, H., Feng, L., Block, T.K., Rosenkrantz, A.B., Lim, R.P., Babb, J.S., Sodickson, D.K., and Otazo, R., *Free-breathing contrast-enhanced multiphase MRI of the liver using a combination of compressed sensing, parallel imaging, and golden-angle radial sampling.* Invest Radiol, 2013. **48**(1): p. 10-6.
119. Aerts, H.J., Jaspers, K., and Backes, W.H., *The precision of pharmacokinetic parameters in dynamic contrast-enhanced magnetic resonance imaging: the effect of sampling frequency and duration.* Phys Med Biol, 2011. **56**(17): p. 5665-78.
120. Verma, S., Turkbey, B., Muradyan, N., Rajesh, A., Cornud, F., Haider, M.A., Choyke, P.L., and Harisinghani, M., *Overview of dynamic contrast-enhanced MRI in prostate cancer diagnosis and management.* AJR Am J Roentgenol, 2012. **198**(6): p. 1277-88.
121. Leach, M.O., Morgan, B., Tofts, P.S., Buckley, D.L., Huang, W., Horsfield, M.A., Chenevert, T.L., Collins, D.J., Jackson, A., Lomas, D., Whitcher, B., Clarke, L., Plummer, R., Judson, I., Jones, R., Alonzi, R., Brunner, T., Koh, D.M., Murphy, P., Waterton, J.C., Parker, G., Graves, M.J., Scheenen, T.W.J., Redpath, T.W., Orton, M., Karczmar, G., Huisman, H., Barentsz, J., and Padhani, A., *Imaging vascular function for early stage clinical trials using dynamic contrast-enhanced magnetic resonance imaging.* Eur Radiol, 2012. **22**(7): p. 1451-1464.
122. Heisen, M., *Understanding quantitative DCE-MRI of the breast - Towards meaningful clinical application*, 2010, Universiteitsdrukkerij TU Eindhoven: Eindhoven, The Netherlands.
123. Mitsouras, D., Mulkern, R.V., and Rybicki, F.J., *Strategies for inner volume 3D fast spin echo magnetic resonance imaging using nonselective refocusing radio frequency pulses.* Med Phys, 2006. **33**(1): p. 173-86.
124. Dowell, N.G. and Tofts, P.S., *Fast, accurate, and precise mapping of the RF field in vivo using the 180 degrees signal null.* Magn Reson Med, 2007. **58**(3): p. 622-30.
125. Childs, A.S., Malik, S.J., O'Regan, D.P., and Hajnal, J.V., *Impact of number of channels on RF shimming at 3T.* MAGMA, 2013. **26**(4): p. 401-10.
126. Insko, E.K. and Bolinger, L., *Mapping of the Radiofrequency Field.* J Magn Reson Imaging, 1993. **103**(1): p. 82-85.
127. Yarnykh, V.L., *Actual flip-angle imaging in the pulsed steady state: a method for rapid three-dimensional mapping of the transmitted radiofrequency field.* Magn Reson Med, 2007. **57**(1): p. 192-200.
128. Oh, C.H., Hilal, S.K., Cho, Z.H., and Mun, I.K., *Radio frequency field intensity mapping using a composite spin-echo sequence.* Magn Reson Imaging, 1990. **8**(1): p. 21-5.
129. Morrell, G.R., *A phase-sensitive method of flip angle mapping.* Magn Reson Med, 2008. **60**(4): p. 889-94.
130. Craciunescu, O.I., Yoo, D.S., Cleland, E., Muradyan, N., Carroll, M.D., MacFall, J.R., Barboriak, D.P., and Brizel, D.M., *Dynamic contrast-enhanced MRI in head-and-neck cancer: the impact of region of interest selection on the intra- and interpatient variability of pharmacokinetic parameters.* Int J Radiat Oncol Biol Phys, 2012. **82**(3): p. e345-50.
131. Li, X., Cai, Y., Moloney, B., Chen, Y., Huang, W., Woods, M., Coakley, F.V., Rooney, W.D., Garzotto, M.G., and Springer, C.S., Jr., *Relative sensitivities of DCE-MRI pharmacokinetic parameters to arterial input function (AIF) scaling.* J Magn Reson, 2016. **269**: p. 104-112.
132. Dumoulin, C.L., Buonocore, M.H., Opsahl, L.R., Katzberg, R.W., Darrow, R.D., Morris, T.W., and Batey, C., *Noninvasive measurement of renal hemodynamic functions using gadolinium enhanced magnetic resonance imaging.* Magn Reson Med, 1994. **32**(3): p. 370-8.
133. Franiel, T., Ludemann, L., Rudolph, B., Rehbein, H., Stephan, C., Taupitz, M., and Beyersdorff, D., *Prostate MR imaging: tissue characterization with pharmacokinetic volume and blood flow parameters and correlation with histologic parameters.* Radiology, 2009. **252**(1): p. 101-8.
134. Schlemmer, H.P., Merkle, J., Grobholz, R., Jaeger, T., Michel, M.S., Werner, A., Rabe, J., and van Kaick, G., *Can pre-operative contrast-enhanced dynamic MR imaging for prostate cancer predict microvessel density in prostatectomy specimens?* Eur Radiol, 2004. **14**(2): p. 309-17.
135. Barentsz, J.O., Richenberg, J., Clements, R., Choyke, P., Verma, S., Villeirs, G., Rouviere, O.,

Logager, V., and Futterer, J.J., *ESUR prostate MR guidelines 2012.* Eur Radiol, 2012. **22**(4): p. 746-57.
136. DCE-MRI Technical Committee, *DCE-MRI Quantification Profile, Quantitative Imaging Biomarkers Alliance. Version 1.0. Publicly Reviewed Version.* QIBA, 2012.
137. Rosenkrantz, A.B., Geppert, C., Grimm, R., Block, T.K., Glielmi, C., Feng, L., Otazo, R., Ream, J.M., Romolo, M.M., Taneja, S.S., Sodickson, D.K., and Chandarana, H., *Dynamic contrast-enhanced MRI of the prostate with high spatiotemporal resolution using compressed sensing, parallel imaging, and continuous golden-angle radial sampling: Preliminary experience.* J Magn Reson Imaging, 2015. **41**: p. 1365-73.
138. Griswold, M.A., Jakob, P.M., Heidemann, R.M., Nittka, M., Jellus, V., Wang, J., Kiefer, B., and Haase, A., *Generalized autocalibrating partially parallel acquisitions (GRAPPA).* Magn Reson Med, 2002. **47**(6): p. 1202-10.
139. Heilmann, M., Vautier, J., Robert, P., and Volk, A., *In vitro setup to study permeability characteristics of contrast agents by MRI.* Contrast Media Mol Imaging, 2009. **4**(2): p. 66-72.
140. Mehrabian, H., Pang, I., Chandrana, C., Chopra, R., and Martel, A.L., *Automatic mask generation using independent component analysis in dynamic contrast enhanced-MRI.* IEEE International Symposium on Biomedical Imaging: From Nano to Macro, 2011: p. 1657-61.
141. Freed, M., de Zwart, J.A., Hariharan, P., Myers, M.R., and Badano, A., *Development and characterization of a dynamic lesion phantom for the quantitative evaluation of dynamic contrast-enhanced MRI.* Med Phys, 2011. **38**(10): p. 5601-11.
142. Ledger, A.E.W., Borri, M., Casas, H.S., Cummings, C., Schmidt1, M.A., and Leach, M.O., *A novel and affordable DCE-MRI phantom: Prospective assessment of DCE-MRI breast protocols.* Proc. Intl. Soc. Mag. Reson. Med., 2014. **2**: p. 1088.
143. Hariharan, P., Freed, M., and Myers, M.R., *Use of computational fluid dynamics in the design of dynamic contrast enhanced imaging phantoms.* Phys Med Biol, 2013. **58**(18): p. 6369-91.
144. de Bazelaire, C.M., Duhamel, G.D., Rofsky, N.M., and Alsop, D.C., *MR imaging relaxation times of abdominal and pelvic tissues measured in vivo at 3.0 T: preliminary results.* Radiology, 2004. **230**(3): p. 652-9.
145. Alonzi, R., Taylor, N.J., Stirling, J.J., d'Arcy, J.A., Collins, D.J., Saunders, M.I., Hoskin, P.J., and Padhani, A.R., *Reproducibility and correlation between quantitative and semiquantitative dynamic and intrinsic susceptibility-weighted MRI parameters in the benign and malignant human prostate.* J Magn Reson Imaging, 2010. **32**(1): p. 155-64.
146. Swinehart, D.F., *The Beer-Lambert Law.* Journal of Chemical Education, 1962. **39**(7): p. 333.
147. Smith, D.S., Li, X., Arlinghaus, L.R., Yankeelov, T.E., and Welch, E.B., *DCEMRI.jl: a fast, validated, open source toolkit for dynamic contrast enhanced MRI analysis.* PeerJ, 2015. **3**: p. e909.
148. McClure, T.D., Margolis, D.J., Reiter, R.E., Sayre, J.W., Thomas, M.A., Nagarajan, R., Gulati, M., and Raman, S.S., *Use of MR imaging to determine preservation of the neurovascular bundles at robotic-assisted laparoscopic prostatectomy.* Radiology, 2012. **262**(3): p. 874-83.
149. Costa, D.N., Bloch, B.N., Yao, D.F., Sanda, M.G., Ngo, L., Genega, E.M., Pedrosa, I., DeWolf, W.C., and Rofsky, N.M., *Diagnosis of relevant prostate cancer using supplementary cores from magnetic resonance imaging-prompted areas following multiple failed biopsies.* Magn Reson Imaging, 2013. **31**(6): p. 947-52.
150. Casas, H.S., Ledger, A.E.W., Cummings, C., Schmidt, M.A., Leach, M.O., and Borri, M., *A novel and affordable DCE-MRI phantom: experimental setup and assessment of reproducibility.* Proc. Intl. Soc. Mag. Reson. Med., 2014. **2**: p. 1145.
151. Driscoll, B., Keller, H., and Coolens, C., *Development of a dynamic flow imaging phantom for dynamic contrast-enhanced CT.* Med Phys, 2011. **38**(8): p. 4866-80.
152. Ebrahimi, B., Swanson, S.D., and Chupp, T.E., *A microfabricated phantom for quantitative MR perfusion measurements: validation of singular value decomposition deconvolution method.* IEEE Trans Biomed Eng, 2010. **57**(11): p. 2730-36.
153. Sourbron, S.P. and Buckley, D.L., *Classic models for dynamic contrast-enhanced MRI.* NMR Biomed, 2013. **26**(8): p. 1004-27.
154. Ginsburg, S.B., Taimen, P., Merisaari, H., Vainio, P., Bostrom, P.J., Aronen, H.J., Jambor, I., and Madabhushi, A., *Patient-specific pharmacokinetic parameter estimation on dynamic contrast-enhanced MRI of prostate: Preliminary evaluation of a novel AIF-free estimation method.* J Magn Reson Imaging, 2016. **44**(6): p. 1405-1414.
155. Sullivan, D.C., Obuchowski, N.A., Kessler, L.G., Raunig, D.L., Gatsonis, C., Huang, E.P., Kondratovich, M., McShane, L.M., Reeves, A.P., Barboriak, D.P., Guimaraes, A.R., and Wahl, R.L., *Metrology Standards for Quantitative Imaging Biomarkers.* Radiology, 2015. **277**(3): p. 813-25.
156. Rajan, S., Herbertson, L., Bernardo, M., and Choyke, P., *A dialyzer-based flow system for validating dynamic contrast enhanced MR image acquisition.* Magn Reson Med, 2014. **72**(1): p. 41-8.
157. Othman, A.E., Falkner, F., Martirosian, P., Schraml, C., Schwentner, C., Nickel, D., Nikolaou, K., and Notohamiprodjo, M., *Optimized Fast Dynamic Contrast-Enhanced Magnetic Resonance Imaging of the Prostate: Effect of Sampling Duration on Pharmacokinetic Parameters.* Invest

Radiol, 2016. **51**(2): p. 106-12.
158. Othman, A.E., Falkner, F., Weiss, J., Kruck, S., Grimm, R., Martirosian, P., Nikolaou, K., and Notohamiprodjo, M., *Effect of Temporal Resolution on Diagnostic Performance of Dynamic Contrast-Enhanced Magnetic Resonance Imaging of the Prostate.* Invest Radiol, 2016. **51**(5): p. 290-6.
159. Haq, N.F., Kozlowski, P., Jones, E.C., Chang, S.D., Goldenberg, S.L., and Moradi, M., *A data-driven approach to prostate cancer detection from dynamic contrast enhanced MRI.* Comput Med Imaging Graph, 2015. **41**: p. 37-45.
160. Villers, A., Puech, P., Mouton, D., Leroy, X., Ballereau, C., and Lemaitre, L., *Dynamic contrast enhanced, pelvic phased array magnetic resonance imaging of localized prostate cancer for predicting tumor volume: correlation with radical prostatectomy findings.* J Urol, 2006. **176**(6 Pt 1): p. 2432-7.
161. Sandler, K., Patel, M., Lynne, C., Parekh, D.J., Punnen, S., Jorda, M., Casillas, J., Pollack, A., and Stoyanova, R., *Multiparametric-MRI and Targeted Biopsies in the Management of Prostate Cancer Patients on Active Surveillance.* Front Oncol, 2015. **5**: p. 4.
162. Lin, L.I., *A concordance correlation coefficient to evaluate reproducibility.* Biometrics, 1989. **45**(1): p. 255-68.
163. Dietrich, O., Raya, J.G., Reeder, S.B., Reiser, M.F., and Schoenberg, S.O., *Measurement of signal-to-noise ratios in MR images: influence of multichannel coils, parallel imaging, and reconstruction filters.* J Magn Reson Imaging, 2007. **26**(2): p. 375-85.
164. Chen, X., Salerno, M., Yang, Y., and Epstein, F.H., *Motion-compensated compressed sensing for dynamic contrast-enhanced MRI using regional spatiotemporal sparsity and region tracking: block low-rank sparsity with motion-guidance (BLOSM).* Magn Reson Med, 2014. **72**(4): p. 1028-38.
165. Melbourne, A., Hipwell, J., Modat, M., Mertzanidou, T., Huisman, H., Ourselin, S., and Hawkes, D.J., *The effect of motion correction on pharmacokinetic parameter estimation in dynamic-contrast-enhanced MRI.* Phys Med Biol, 2011. **56**(24): p. 7693-708.
166. Stone, A.J., Browne, J.E., Lennon, B., Meaney, J.F., and Fagan, A.J., *Effect of motion on the ADC quantification accuracy of whole-body DWIBS.* Magn Reson Mater Phy, 2012. **25**(4): p. 263-6.
167. Huang, W., Chen, Y., Fedorov, A., Li, X., Jajamovich, G.H., Malyarenko, D.I., Aryal, M.P., LaViolette, P.S., Oborski, M.J., O'Sullivan, F., Abramson, R.G., Jafari-Khouzani, K., Afzal, A., Tudorica, A., Moloney, B., Gupta, S.N., Besa, C., Kalpathy-Cramer, J., Mountz, J.M., Laymon, C.M., Muzi, M., Schmainda, K., Cao, Y., Chenevert, T.L., Taouli, B., Yankeelov, T.E., Fennessy, F., and Li, X., *The Impact of Arterial Input Function Determination Variations on Prostate Dynamic Contrast-Enhanced Magnetic Resonance Imaging Pharmacokinetic Modeling: A Multicenter Data Analysis Challenge.* Tomography, 2016. **2**(1): p. 56-66.
168. Buckley, D. and Parker, G. *T1 estimation using variable flip angle spoiled gradient echo for dynamic contrast-enhanced MRI: Arterial input measurement improves accuracy in the presence of B1 error*. in *Proc. Intl. Soc. Mag. Reson. Med*. 2004.
169. Wang, P., Xue, Y., Zhao, X., Yu, J., Rosen, M., and Song, H.K., *Effects of Flip Angle Uncertainty and Noise on the Accuracy of DCE-MRI Metrics: Comparison Between Standard Concentration-Based and Signal Difference Methods.* Magn Reson Imaging, 2015. **33**(1): p. 166-73.
170. Delongchamps, N.B., Rouanne, M., Flam, T., Beuvon, F., Liberatore, M., Zerbib, M., and Cornud, F., *Multiparametric magnetic resonance imaging for the detection and localization of prostate cancer: combination of T2-weighted, dynamic contrast-enhanced and diffusion-weighted imaging.* BJU Int, 2011. **107**(9): p. 1411-8.
171. Othman, A.E., Falkner, F., Kessler, D.E., Martirosian, P., Weiss, J., Kruck, S., Kaufmann, S., Grimm, R., Kramer, U., Nikolaou, K., and Notohamiprodjo, M., *Comparison of different population-averaged arterial-input-functions in dynamic contrast-enhanced MRI of the prostate: Effects on pharmacokinetic parameters and their diagnostic performance.* Magn Reson Imaging, 2016. **34**(4): p. 496-501.
172. Garpebring, A., Wirestam, R., Ostlund, N., and Karlsson, M., *Effects of inflow and radiofrequency spoiling on the arterial input function in dynamic contrast-enhanced MRI: a combined phantom and simulation study.* Magn Reson Med, 2011. **65**(6): p. 1670-9.
173. Lee, S.L., Foltz, W., Driscoll, B., Fatemi, A., Menard, C., Coolens, C., and Chung, C. *Comparison of arterial input functions by magnitude and phase signal measurement in dynamic contrast enhancement MRI using a dynamic flow phantom*. in *Proceedings of the 20th Annual Meeting of ISMRM. Melbourne, Australia*. 2012.
174. Cheng, H.L., *Investigation and optimization of parameter accuracy in dynamic contrast-enhanced MRI.* J Magn Reson Imaging, 2008. **28**(3): p. 736-43.
175. Treier, R., Steingoetter, A., Fried, M., Schwizer, W., and Boesiger, P., *Optimized and combined T1 and B1 mapping technique for fast and accurate T1 quantification in contrast-enhanced abdominal MRI.* Magn Reson Med, 2007. **57**(3): p. 568-76.
176. Chung, S., Kim, D., Breton, E., and Axel, L., *Rapid B(1)(+) Mapping Using a Pre-Conditioning RF Pulse with TurboFLASH readout.* Magn Reson Med, 2010. **64**(2): p. 439-46.
177. Dinh, C.V., Steenbergen, P., Ghobadi, G., van der Poel, H., Heijmink, S.W.T.P.J., de Jong, J., Isebaert, S., Haustermans, K., Lerut, E., Oyen, R., Ou, Y., Christos, D., and van der Heide, U.A.,

Multicenter validation of prostate tumor localization using multiparametric MRI and prior knowledge. Med Phys, 2017. **44**(3): p. 949-961.
178. Di Giovanni, P., Azlan, C.A., Ahearn, T.S., Semple, S.I., Gilbert, F.J., and Redpath, T.W., *The accuracy of pharmacokinetic parameter measurement in DCE-MRI of the breast at 3 T.* Phys Med Biol, 2010. **55**(1): p. 121-32.
179. Azlan, C.A., Di Giovanni, P., Ahearn, T.S., Semple, S.I., Gilbert, F.J., and Redpath, T.W., *B1 transmission-field inhomogeneity and enhancement ratio errors in dynamic contrast-enhanced MRI (DCE-MRI) of the breast at 3T.* J Magn Reson Imaging, 2010. **31**(1): p. 234-9.
180. Sung, K., Daniel, B.L., and Hargreaves, B.A., *Transmit B1+ field inhomogeneity and T1 estimation errors in breast DCE-MRI at 3 tesla.* J Magn Reson Imaging, 2013. **38**(2): p. 454-459.
181. Park, B., Choi, B.S., Sung, Y.S., Woo, D.C., Shim, W.H., Kim, K.W., Choi, Y.S., Pae, S.J., Suh, J.Y., Cho, H., and Kim, J.K., *Influence of B1-Inhomogeneity on Pharmacokinetic Modeling of Dynamic Contrast-Enhanced MRI: A Simulation Study.* Korean J Radiol, 2017. **18**(4): p. 585-596.
182. Lutti, A., Hutton, C., Finsterbusch, J., Helms, G., and Weiskopf, N., *Optimization and validation of methods for mapping of the radiofrequency transmit field at 3T.* Magn Reson Med, 2010. **64**(1): p. 229-38.
183. Groenendaal, G., Moman, M.R., Korporaal, J.G., van Diest, P.J., van Vulpen, M., Philippens, M.E.P., and van der Heide, U.A., *Validation of functional imaging with pathology for tumor delineation in the prostate.* Radiother Oncol, 2010. **94**(2): p. 145-150.
184. Pang, Y., Turkbey, B., Bernardo, M., Kruecker, J., Kadoury, S., Merino, M.J., Wood, B.J., Pinto, P.A., and Choyke, P.L., *Intravoxel incoherent motion MR imaging for prostate cancer: An evaluation of perfusion fraction and diffusion coefficient derived from different b-value combinations.* Magn Reson Med, 2013. **69**(2): p. 553-562.
185. Chen, L., Schabel, M.C., and DiBella, E.V., *Reconstruction of dynamic contrast enhanced magnetic resonance imaging of the breast with temporal constraints.* Magn Reson Imaging, 2010. **28**(5): p. 637-45.
186. Li, J., Yu, Y., Zhang, Y., Bao, S., Wu, C., Wang, X., Li, J., Zhang, X., and Hu, J., *A clinically feasible method to estimate pharmacokinetic parameters in breast cancer.* Med Phys, 2009. **36**(8): p. 3786-94.
187. Ashton, E., Raunig, D., Ng, C., Kelcz, F., McShane, T., and Evelhoch, J., *Scan-rescan variability in perfusion assessment of tumors in MRI using both model and data-derived arterial input functions.* J Magn Reson Imaging, 2008. **28**(3): p. 791-796.
188. Hatzoglou, V., Tisnado, J., Mehta, A., Peck, K.K., Daras, M., Omuro, A.M., Beal, K., and Holodny, A.I., *Dynamic contrast-enhanced MRI perfusion for differentiating between melanoma and lung cancer brain metastases.* Cancer Med-US, 2017. **6**(4): p. 761-767.
189. Chung, M.P., Margolis, D., Mesko, S., Wang, J., Kupelian, P., and Kamrava, M., *Correlation of quantitative diffusion-weighted and dynamic contrast-enhanced MRI parameters with prognostic factors in prostate cancer.* J Med Imag Radiat On, 2014. **58**(5): p. 588-594.
190. De Naeyer, D., Verhulst, J., Ceelen, W., Segers, P., De Deene, Y., and Verdonck, P., *Flip angle optimization for dynamic contrast-enhanced MRI-studies with spoiled gradient echo pulse sequences.* Phys Med Biol, 2011. **56**(16): p. 5373-95.
191. Flouri, D., Lesnic, D., and Sourbron, S.P., *Fitting the two-compartment model in DCE-MRI by linear inversion.* Magn Reson Med, 2016. **76**(3): p. 998-1006.
192. Wang, C., Yin, F.F., and Chang, Z., *An efficient calculation method for pharmacokinetic parameters in brain permeability study using dynamic contrast-enhanced MRI.* Magn Reson Med, 2016. **75**(2): p. 739-49.
193. Yarnykh, V.L., *Optimal radiofrequency and gradient spoiling for improved accuracy of T1 and B1 measurements using fast steady-state techniques.* Magn Reson Med, 2010. **63**(6): p. 1610-26.
194. Selnaes, K.M., Heerschap, A., Jensen, L.R., Tessem, M.B., Schweder, G.J., Goa, P.E., Viset, T., Angelsen, A., and Gribbestad, I.S., *Peripheral zone prostate cancer localization by multiparametric magnetic resonance at 3 T: unbiased cancer identification by matching to histopathology.* Invest Radiol, 2012. **47**(11): p. 624-33.
195. Candes, E.J., Romberg, J., and Tao, T., *Robust uncertainty principles: exact signal reconstruction from highly incomplete frequency information.* Information Theory, IEEE Transactions on, 2006. **52**(2): p. 489-509.
196. Donoho, D.L., *Compressed sensing.* Information Theory, IEEE Transactions on, 2006. **52**(4): p. 1289-1306.
197. Block, K.T., Uecker, M., and Frahm, J., *Undersampled radial MRI with multiple coils. Iterative image reconstruction using a total variation constraint.* Magn Reson Med, 2007. **57**(6): p. 1086-98.
198. Gai, N. and Axel, L., *Correction of motion artifacts in linogram and projection reconstruction MRI using geometry and consistency constraints.* Med Phys, 1996. **23**(2): p. 251-62.
199. Winkelmann, S., Schaeffter, T., Koehler, T., Eggers, H., and Doessel, O., *An optimal radial profile order based on the Golden Ratio for time-resolved MRI.* IEEE Trans Med Imaging, 2007. **26**(1): p. 68-76.
200. Wright, K.L., Hamilton, J.I., Griswold, M.A., Gulani, V., and Seiberlich, N., *Non-Cartesian parallel imaging reconstruction.* J Magn Reson Imaging, 2014. **40**(5): p. 1022-40.

201. Feng, L., Srichai, M.B., Lim, R.P., Harrison, A., King, W., Adluru, G., Dibella, E.V., Sodickson, D.K., Otazo, R., and Kim, D., *Highly accelerated real-time cardiac cine MRI using k-t SPARSE-SENSE.* Magn Reson Med, 2013. **70**(1): p. 64-74.
202. Chan, R.W., Ramsay, E.A., Cheung, E.Y., and Plewes, D.B., *The influence of radial undersampling schemes on compressed sensing reconstruction in breast MRI.* Magn Reson Med, 2012. **67**(2): p. 363-77.
203. Rosenkrantz, A.B., Khasgiwala, A., Doshi, A.M., Ream, J.M., Taneja, S.S., and Lepor, H., *Detection of prostate cancer local recurrence following radical prostatectomy: assessment using a continuously acquired radial golden-angle compressed sensing acquisition.* Abdom Radiol (NY), 2016. **42**(1): p. 290-297.
204. Feng, L., Grimm, R., Block, K.T., Chandarana, H., Kim, S., Xu, J., Axel, L., Sodickson, D.K., and Otazo, R., *Golden-angle radial sparse parallel MRI: combination of compressed sensing, parallel imaging, and golden-angle radial sampling for fast and flexible dynamic volumetric MRI.* Magn Reson Med, 2014. **72**(3): p. 707-17.
205. Feng, L., Axel, L., Chandarana, H., Block, K.T., Sodickson, D.K., and Otazo, R., *XD-GRASP: Golden-angle radial MRI with reconstruction of extra motion-state dimensions using compressed sensing.* Magn Reson Med, 2016. **75**(2): p. 775-88.
206. Kim, S.G., Feng, L., Grimm, R., Freed, M., Block, K.T., Sodickson, D.K., Moy, L., and Otazo, R., *Influence of temporal regularization and radial undersampling factor on compressed sensing reconstruction in dynamic contrast enhanced MRI of the breast.* J Magn Reson Imaging, 2016. **43**(1): p. 261-9.
207. Hopfgartner, A.J., Tymofiyeva, O., Ehses, P., Rottner, K., Boldt, J., Richter, E.J., and Jakob, P.M., *Dynamic MRI of the TMJ under physical load.* Dentomaxillofac Radiol, 2013. **42**(9): p. 20120436.
208. Sengupta, S., Smith, D.S., Smith, A.K., Welch, E.B., and Smith, S.A., *Dynamic Imaging of the Eye, Optic Nerve, and Extraocular Muscles With Golden Angle Radial MRI.* Invest Ophthalmol Vis Sci, 2017. **58**(10): p. 4010-4018.
209. Sengupta, S., Smith, D.S., and Welch, E.B., *Continuously moving table MRI with golden angle radial sampling.* Magn Reson Med, 2015. **74**(6): p. 1690-7.
210. Lustig, M. and Pauly, J.M., *SPIRiT: Iterative Self-consistent Parallel Imaging Reconstruction from Arbitrary k-Space.* Magn Reson Med, 2010. **64**(2): p. 457-71.
211. Uecker, M., Lai, P., Murphy, M.J., Virtue, P., Elad, M., Pauly, J.M., Vasanawala, S.S., and Lustig, M., *ESPIRiT — An Eigenvalue Approach to Autocalibrating Parallel MRI: Where SENSE meets GRAPPA.* Magn Reson Med, 2014. **71**(3): p. 990-1001.
212. Griswold, M.A., Kannengiesser, S., Heidemann, R.M., Wang, J., and Jakob, P.M., *Field-of-view limitations in parallel imaging.* Magn Reson Med, 2004. **52**(5): p. 1118-26.
213. Gamper, U., Boesiger, P., and Kozerke, S., *Compressed sensing in dynamic MRI.* Magn Reson Med, 2008. **59**(2): p. 365-373.
214. Jung, H., Sung, K., Nayak, K.S., Kim, E.Y., and Ye, J.C., *k-t FOCUSS: A general compressed sensing framework for high resolution dynamic MRI.* Magn Reson Med, 2009. **61**(1): p. 103-116.
215. Jung, H., Ye, J.C., and Kim, E.Y., *Improved k-t BLAST and k-t SENSE using FOCUSS.* Phys Med Biol, 2007. **52**(11): p. 3201-26.
216. Smith, D.S., Welch, E.B., Li, X., Arlinghaus, L.R., Loveless, M.E., Koyama, T., Gore, J.C., and Yankeelov, T.E., *Quantitative effects of using compressed sensing in dynamic contrast enhanced MRI.* Phys Med Biol, 2011. **56**(15): p. 4933-46.
217. Hu, S., Lustig, M., Balakrishnan, A., Larson, P.E., Bok, R., Kurhanewicz, J., Nelson, S.J., Goga, A., Pauly, J.M., and Vigneron, D.B., *3D compressed sensing for highly accelerated hyperpolarized (13)C MRSI with in vivo applications to transgenic mouse models of cancer.* Magn Reson Med, 2010. **63**(2): p. 312-21.
218. Hu, S., Lustig, M., Chen, A.P., Crane, J., Kerr, A., Kelley, D.A., Hurd, R., Kurhanewicz, J., Nelson, S.J., Pauly, J.M., and Vigneron, D.B., *Compressed sensing for resolution enhancement of hyperpolarized 13C flyback 3D-MRSI.* J Magn Reson, 2008. **192**(2): p. 258-64.
219. Ajraoui, S., Lee, K.J., Deppe, M.H., Parnell, S.R., Parra-Robles, J., and Wild, J.M., *Compressed sensing in hyperpolarized 3He lung MRI.* Magn Reson Med, 2010. **63**(4): p. 1059-69.
220. Doneva, M., Bornert, P., Eggers, H., Stehning, C., Senegas, J., and Mertins, A., *Compressed sensing reconstruction for magnetic resonance parameter mapping.* Magn Reson Med, 2010. **64**(4): p. 1114-20.
221. Otazo, R., Kim, D., Axel, L., and Sodickson, D.K., *Combination of compressed sensing and parallel imaging for highly accelerated first-pass cardiac perfusion MRI.* Magn Reson Med, 2010. **64**(3): p. 767-76.
222. Adluru, G., Tasdizen, T., Schabel, M.C., and DiBella, E.V., *Reconstruction of 3D dynamic contrast-enhanced magnetic resonance imaging using nonlocal means.* J Magn Reson Imaging, 2010. **32**(5): p. 1217-27.
223. Wang, H., Miao, Y., Zhou, K., Yu, Y., Bao, S., He, Q., Dai, Y., Xuan, S.Y., Tarabishy, B., Ye, Y., and Hu, J., *Feasibility of high temporal resolution breast DCE-MRI using compressed sensing theory.* Med Phys, 2010. **37**(9): p. 4971-81.
224. Menzel, M.I., Tan, E.T., Khare, K., Sperl, J.I., King, K.F., Tao, X., Hardy, C.J., and Marinelli, L., *Accelerated diffusion spectrum imaging in the human brain using compressed sensing.* Magn

Reson Med, 2011. **66**(5): p. 1226-33.
225. Wu, B., Li, W., Guidon, A., and Liu, C., *Whole brain susceptibility mapping using compressed sensing.* Magn Reson Med, 2012. **67**(1): p. 137-47.
226. Ravishankar, S. and Bresler, Y., *MR image reconstruction from highly undersampled k-space data by dictionary learning.* IEEE Trans Med Imaging, 2011. **30**(5): p. 1028-41.
227. Trzasko, J.D., Bao, Z., Manduca, A., McGee, K.P., and Bernstein, M.A., *Sparsity and low-contrast object detectability.* Magn Reson Med, 2012. **67**(4): p. 1022-32.
228. Sung, K. and Hargreaves, B.A., *High-frequency subband compressed sensing MRI using quadruplet sampling.* Magn Reson Med, 2013. **70**(5): p. 1306-18.
229. Heacock, L., Gao, Y., Heller, S.L., Melsaether, A.N., Babb, J.S., Block, T.K., Otazo, R., Kim, S.G., and Moy, L., *Comparison of conventional DCE-MRI and a novel golden-angle radial multicoil compressed sensing method for the evaluation of breast lesion conspicuity.* J Magn Reson Imaging, 2017. **45**(6): p. 1746-1752.
230. Vreemann, S., Rodriguez-Ruiz, A., Nickel, D., Heacock, L., Appelman, L., van Zelst, J., Karssemeijer, N., Weiland, E., Maas, M., Moy, L., Kiefer, B., and Mann, R.M., *Compressed Sensing for Breast MRI: Resolving the Trade-Off Between Spatial and Temporal Resolution.* Investigative Radiology, 2017. **52**(10): p. 574-582.
231. Parasoglou, P., Feng, L., Xia, D., Otazo, R., and Regatte, R.R., *Rapid 3D-imaging of phosphocreatine recovery kinetics in the human lower leg muscles with compressed sensing.* Magn Reson Med, 2012. **68**(6): p. 1738-46.
232. Montefusco, L.B., Lazzaro, D., Papi, S., and Guerrini, C., *A fast compressed sensing approach to 3D MR image reconstruction.* IEEE Trans Med Imaging, 2011. **30**(5): p. 1064-75.
233. Bassett, E.C., Kholmovski, E.G., Wilson, B.D., DiBella, E.V., Dosdall, D.J., Ranjan, R., McGann, C.J., and Kim, D., *Evaluation of highly accelerated real-time cardiac cine MRI in tachycardia.* NMR Biomed, 2014. **27**(2): p. 175-82.
234. Wech, T., Pickl, W., Tran-Gia, J., Ritter, C., Beer, M., Hahn, D., and Kostler, H., *Whole-heart cine MRI in a single breath-hold--a compressed sensing accelerated 3D acquisition technique for assessment of cardiac function.* Rofo, 2014. **186**(1): p. 37-41.
235. Bahrami, N., Swisher, C.L., Von Morze, C., Vigneron, D.B., and Larson, P.E., *Kinetic and perfusion modeling of hyperpolarized (13)C pyruvate and urea in cancer with arbitrary RF flip angles.* Quant Imaging Med Surg, 2014. **4**(1): p. 24-32.
236. Ajraoui, S., Parra-Robles, J., and Wild, J.M., *Incorporation of prior knowledge in compressed sensing for faster acquisition of hyperpolarized gas images.* Magn Reson Med, 2013. **69**(2): p. 360-9.
237. Furuyama, J.K., Wilson, N.E., Burns, B.L., Nagarajan, R., Margolis, D.J., and Thomas, M.A., *Application of compressed sensing to multidimensional spectroscopic imaging in human prostate.* Magn Reson Med, 2012. **67**(6): p. 1499-505.
238. Han, S.H., Cho, F.H., Song, Y.K., Paulsen, J., Song, Y.Q., Kim, Y.R., Kim, J.K., Cho, G., and Cho, H., *Ultrafast 3D spin-echo acquisition improves Gadolinium-enhanced MRI signal contrast enhancement.* Sci Rep, 2014. **4**: p. 5061.
239. Lebel, R.M., Jones, J., Ferre, J.C., Law, M., and Nayak, K.S., *Highly accelerated dynamic contrast enhanced imaging.* Magn Reson Med, 2013.
240. Rapacchi, S., Han, F., Natsuaki, Y., Kroeker, R., Plotnik, A., Lehrman, E., Sayre, J., Laub, G., Finn, J.P., and Hu, P., *High spatial and temporal resolution dynamic contrast-enhanced magnetic resonance angiography using compressed sensing with magnitude image subtraction.* Magn Reson Med, 2014. **71**(5): p. 1771-83.
241. Zhang, T., Chowdhury, S., Lustig, M., Barth, R.A., Alley, M.T., Grafendorfer, T., Calderon, P.D., Robb, F.J.L., Pauly, J.M., and Vasanawala, S.S., *Clinical performance of contrast enhanced abdominal pediatric MRI with fast combined parallel imaging compressed sensing reconstruction.* J Magn Reson Imaging, 2014. **40**(1): p. 13-25.
242. Smith, D.S., Li, X., Gambrell, J.V., Arlinghaus, L.R., Quarles, C.C., Yankeelov, T.E., and Welch, E.B., *Robustness of quantitative compressive sensing MRI: the effect of random undersampling patterns on derived parameters for DCE- and DSC-MRI.* IEEE Trans Med Imaging, 2012. **31**(2): p. 504-11.
243. Thomas, M.A., Nagarajan, R., Huda, A., Margolis, D., Sarma, M.K., Sheng, K., Reiter, R.E., and Raman, S.S., *Multidimensional MR spectroscopic imaging of prostate cancer in vivo.* NMR Biomed, 2014. **27**(1): p. 53-66.
244. Rilling, G., Tao, Y., Marshall, I., and Davies, M.E., *Multilattice sampling strategies for region of interest dynamic MRI.* Magn Reson Med, 2013. **70**(2): p. 392-403.
245. Tao, Y., Rilling, G., Davies, M., and Marshall, I., *Carotid blood flow measurement accelerated by compressed sensing: validation in healthy volunteers.* Magn Reson Imaging, 2013. **31**(9): p. 1485-91.
246. Li, B., Dong, L., Chen, B., Ji, S., Cai, W., Wang, Y., Zhang, J., Zhang, Z., Wang, X., and Fang, J., *Turbo fast three-dimensional carotid artery black-blood MRI by combining three-dimensional MERGE sequence with compressed sensing.* Magn Reson Med, 2013. **70**(5): p. 1347-52.
247. Sharma, S.D., Hu, H.H., and Nayak, K.S., *Accelerated T2*-compensated fat fraction quantification using a joint parallel imaging and compressed sensing framework.* J Magn Reson

Imaging, 2013. **38**(5): p. 1267-75.
248. Wiens, C.N., McCurdy, C.M., Willig-Onwuachi, J.D., and McKenzie, C.A., *R2*-corrected water–fat imaging using compressed sensing and parallel imaging.* Magn Reson Med, 2014. **71**(2): p. 608-616.
249. Uecker, M., Ong, F., Tamir, J., Bahri, D., Virtue, P., Cheng, J.Y., Zhang, T., and Lustig, M., *Berkeley Advanced Reconstruction Toolbox.* Proc. Intl. Soc. Mag. Reson. Med., 2015. **23**: p. 2486.
250. Smith, D.S., Li, X., Abramson, R.G., Quarles, C.C., Yankeelov, T.E., and Welch, E.B., *Potential of compressed sensing in quantitative MR imaging of cancer.* Cancer Imaging, 2013. **13**(4): p. 633-44.
251. Dikaios, N., Arridge, S., Hamy, V., Punwani, S., and Atkinson, D., *Direct parametric reconstruction from undersampled (k, t)-space data in dynamic contrast enhanced MRI.* Med Image Anal, 2014. **18**(7): p. 989-1001.
252. Li, X., Huang, W., and Rooney, W.D., *Signal-to-noise ratio, contrast-to-noise ratio and pharmacokinetic modeling considerations in dynamic contrast-enhanced magnetic resonance imaging.* Magn Reson Imaging, 2012. **30**(9): p. 1313-22.
253. Lin, W., Guo, J., Rosen, M.A., and Song, H.K., *Respiratory motion-compensated radial dynamic contrast-enhanced (DCE)-MRI of chest and abdominal lesions.* Magn Reson Med, 2008. **60**(5): p. 1135-46.
254. Doneva, M., Bornert, P., Eggers, H., Mertins, A., Pauly, J., and Lustig, M., *Compressed sensing for chemical shift-based water-fat separation.* Magn Reson Med, 2010. **64**(6): p. 1749-59.
255. Jung, H. and Ye, J.C., *Motion estimated and compensated compressed sensing dynamic magnetic resonance imaging: What we can learn from video compression techniques.* International Journal of Imaging Systems and Technology, 2010. **20**(2): p. 81-98.
256. Fellner, C., Muller, W., Georgi, J., Taubenreuther, U., Fellner, F.A., and Kalender, W.A., *A high-resolution phantom for MRI.* Magn Reson Imaging, 2001. **19**(6): p. 899-904.
257. Sakurai, T., *A low contrast-spatial resolution phantom for MR imaging using surface coils.* Oral Radiology, 1994. **10**(1): p. 23-31.
258. Kim, H. and Morgan, D.E., *Semiautomatic Determination of Arterial Input Function in DCE-MRI of the Abdomen.* J Biomed Eng Med Imaging, 2017. **4**(2): p. 96-104.

Appendices

Appendix A: Supplementary Information on the development of the DCE-MRI Phantom Device

A 1.1: Selection of 3D Printing System and Polymer for the Production of the Measurement Chambers

Initial prototypes of the mixing chamber components were produced using several 3D-printing systems, namely a *Form1+* (Formlabs, USA), an *Ultimaker 2+* (Ultimaker, Netherlands), and an *Eden 250* (Stratasys, USA). Initial prototype mixing chambers produced using the *Form1+* and *Ultimaker 2+* systems did not have good geometric fidelity when compared with the input 3D models. The models produced using these systems also included multiple holes and occlusions in the walls (as illustrated in Figure A1.1). Prototypes produced using the *Eden 250* and *VeroClear* polymer (*FullCure-GD810*; Stratasys, USA) had very good geometric and structural fidelity, even with wall thicknesses as low as 0.3 mm. One thing of note is that during initial experiments where $MnCl_2$ was explored as a possible low-cost alternative to use in place of a Gd-based contrast agent, the *VeroClear* polymer absorbed $MnCl_2$ into the internal surface, resulting in an irreversible modification to MR signal from those areas. In light of this, these models were discarded and only Gd-based contrast agents used for all subsequent experiments (Gd-based contrast agents were not similarly absorbed by the polymer).

Figure A1.1: Photograph of prototype mixing chambers produced using (left) the *Form1+* (Formlabs, USA) system and (right) the *Eden 250* (Stratasys, USA) system.

A 1.2: Shielded Control Box and Cabling

A shielded box was constructed to allow the 25-way d-sub connection from the analog output module (*USB-DA12-8A*; ACCES, USA) to be connected to the individual pumps (*Reglo-Z*; Ismatec, Switzerland) via four 15-way d-sub connections, as shown in Figure A1.2. The box also contained four rocker switches which allowed for easy switching between manual control (i.e. with pump-rate set at the pump driver units) or voltage control (i.e. flow rates controlled via the voltage outputs from the output module), as well as a *voltage output* connection which allowed the pump-control-voltages of the system to be monitored in real-time. The wiring configuration used in the control box is shown in Figure A1.3. The analog output module was connected to the control box via a shielded 25-way female-to-female d-sub cable and the control box connected to the individual pumps via four shielded 25-way male-to-male d-sub cables.

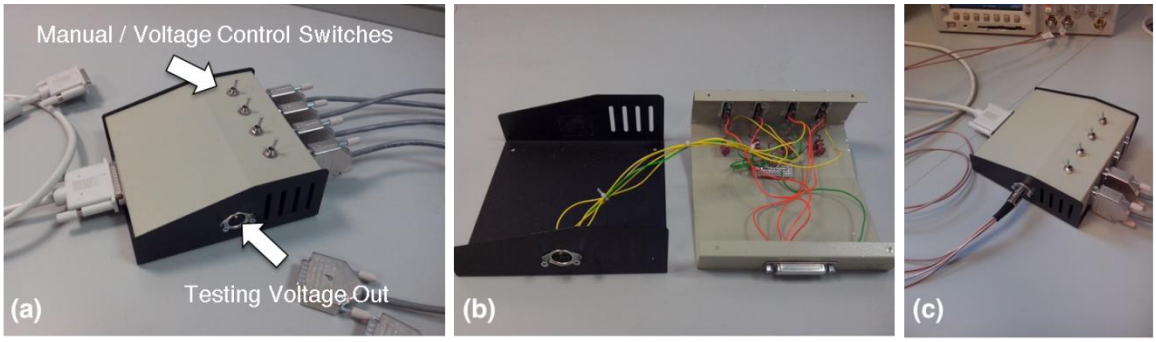

Figure A1.2: Photograph showing the shielded control box used to connect the 25 way d-sub connection from the analog output module to the four individual pumps (15 way d-sub), as well as control whether the pumps flow-rates were manually set at the driver units or controlled via the output module's output voltage, shown: (a) with control switches and voltage output connection highlighted; (b) open, showing the internal wiring; and (c) connected to an oscilloscope via a purpose-built cable for validation of the voltage outputs.

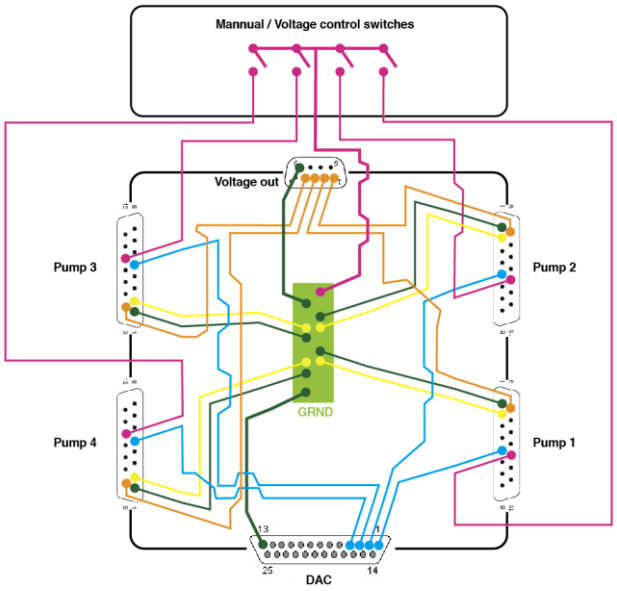

Figure A1.3: Schematic diagram showing the shielded control box wiring configuration.

A 1.3: Timing and validation of analog module outputs

Precise timing of the temporally-varying voltage signal produced using the analog output module was achieved using a software-implemented, hardware-dependant 'dwell timer' which utilised the *Windows Application Programing Interface* (API; *Windows 7 Professional;* Microsoft Corporation, USA) and *QueryPerformanceCounter* function. This method was implemented in the *Delphi* programming language (Embarcadero Technologies, USA), and allowed for high-resolution time stamps to be acquired directly from the CPU (2.7-GHz quad-core *Intel i7* (Intel Corporation, USA)), independent of (i.e. not synchronized to) any external time reference, but instead derived directly from the laptop's hardware.

The timing fidelity of the outputs produced using this method was measured and validated by setting the analog output module to produce square wave outputs at 1 Hz, 10 Hz, and 100 Hz, and measuring the frequency of the resulting voltage outputs produced using an oscilloscope (*TDS 3032b*; Tektronix, USA). The system was found to have very good timing fidelity for the output voltages, with no variation detected at 1Hz, and small frequency variations of ±0.01% and ±0.03% at 10 Hz and 100Hz respectively (all measurements made at high CPU load and with no core affinity set in order to test the worst-case scenario).

A 1.4: Phantom flow system configuration (tubing and connectors)

The final tubing arrangement and connectors used for the phantom's flow system are shown in Figure A1.4(a). This configuration was modular in design, allowing the device to be easily set-up and removed from the MRI scanner, while still keeping the system primed with fluid, as illustrated in Figure A1.4(b).

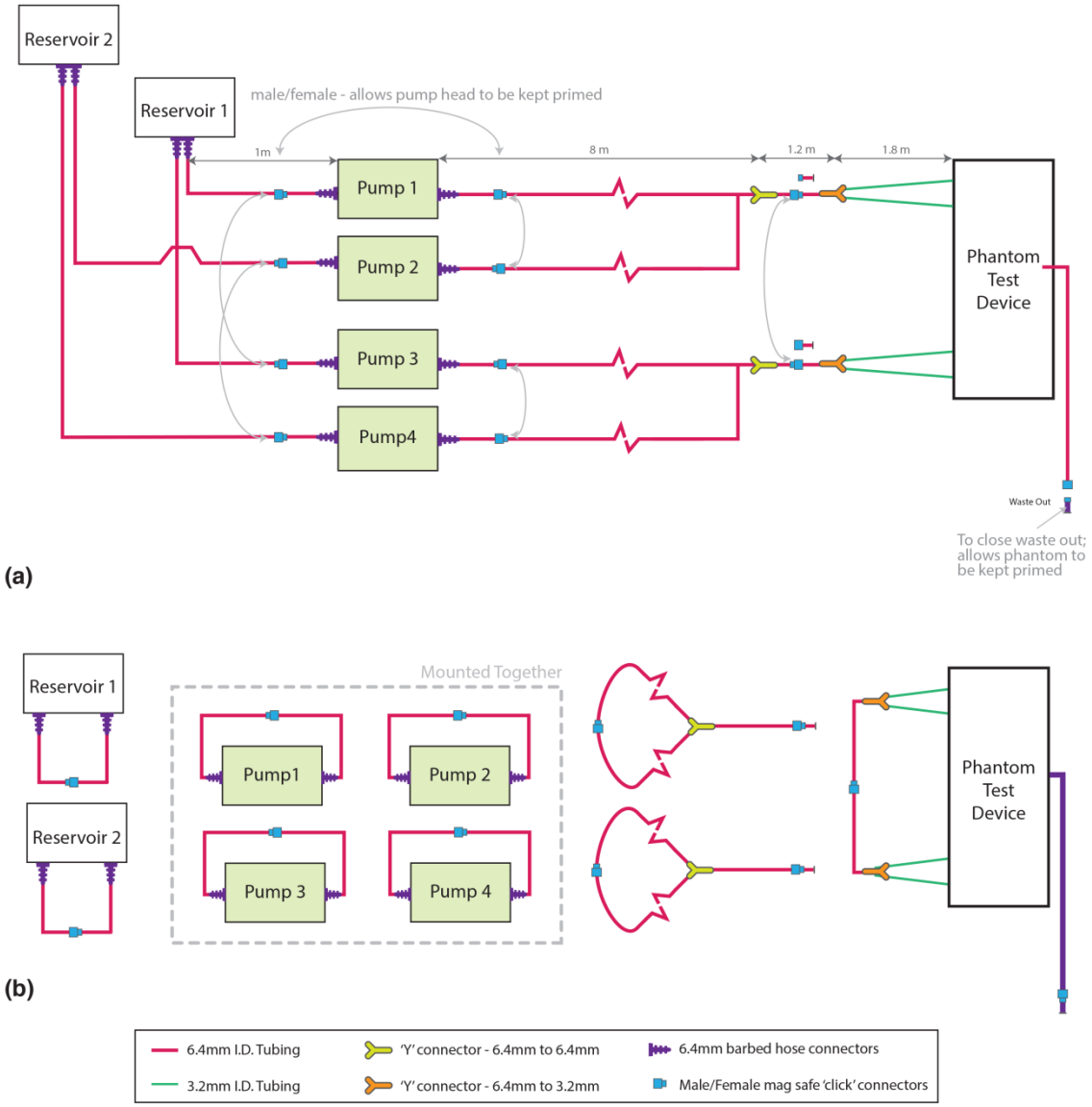

Figure A1.4: Schematic diagram showing (a) the configuration of tubing and tubing connectors used in the phantom flow system and (b) the flow system separated into its modular form.

Appendix B: Chapter 5 results: percentage errors and percentage standard deviation (S.D.) in DCE-MRI derived PK parameter values

Accuracy of LLS Tofts Model Fitting (No VFAC correction)

	Tumour						Healthy					
	Intra-session mean			Inter-session mean			Intra-session mean			Inter-session mean		
T_{res} [s]	K^{trans} %Error	v_e %Error	k_{ep} %Error	K^{trans} %Error	v_e %Error	k_{ep} %Error	K^{trans} %Error	v_e %Error	k_{ep} %Error	K^{trans} %Error	v_e %Error	k_{ep} %Error
1.2	10.5	-3.4	14.4	-0.5	-15.5	17.8	15.9	-0.8	16.8	3.2	-13.8	19.9
2.4	10.4	-3.4	14.3	-0.6	-15.5	17.6	16.1	-0.8	17.2	3.2	-13.8	20.0
3.7	10.6	-3.4	14.5	-0.3	-15.5	18.0	16.1	-0.8	17.2	3.3	-13.8	20.1
4.9	10.5	-3.4	14.4	-0.3	-15.4	18.0	16.7	-0.7	17.8	3.4	-13.7	20.1
6.1	10.9	-3.4	14.8	0.1	-15.5	18.6	17.6	-0.9	18.7	3.9	-13.8	20.7
7.3	11.8	-3.4	15.7	0.9	-15.5	19.5	18.5	-1.2	20.3	4.6	-14.0	21.9
8.6	12.2	-3.4	16.1	1.7	-15.4	20.4	19.8	-1.2	21.5	5.2	-14.0	22.5
9.8	12.5	-3.4	16.4	2.6	-15.4	21.3	21.6	-1.5	23.7	6.5	-14.2	24.4
11.0	13.0	-3.3	16.9	3.5	-15.4	22.5	23.6	-1.7	26.0	7.9	-14.3	26.2
12.2	14.0	-3.3	17.9	5.0	-15.3	24.1	25.9	-2.1	28.8	9.6	-14.6	28.6
13.5	15.4	-3.2	19.2	6.8	-15.2	26.0	27.2	-2.0	29.9	11.1	-14.8	30.6
14.7	15.4	-3.2	19.3	7.6	-15.2	27.1	29.2	-2.3	32.4	12.6	-14.9	32.6
15.9	16.0	-3.2	19.9	8.4	-15.2	28.1	31.4	-2.5	34.9	13.9	-15.1	34.4
17.1	17.5	-3.3	21.6	10.0	-15.3	30.1	33.9	-2.9	38.1	15.8	-15.4	37.1
18.4	19.6	-3.1	23.4	12.2	-15.0	32.4	36.0	-2.8	39.7	17.3	-15.3	38.8
19.6	22.6	-3.0	26.4	14.9	-14.9	35.4	37.5	-3.0	41.3	19.0	-15.5	41.0
20.8	25.4	-2.9	29.2	17.4	-14.9	38.2	38.9	-3.2	42.9	20.5	-15.7	43.1
22.0	27.5	-2.7	31.1	19.8	-14.8	40.9	39.7	-3.2	44.1	21.8	-15.9	44.8
23.3	28.9	-2.6	32.3	21.5	-14.6	42.7	40.1	-3.4	44.5	22.3	-15.9	45.6
24.5	30.2	-2.8	33.9	22.1	-14.9	43.7	40.3	-3.5	45.1	23.0	-16.1	46.6
25.7	30.3	-2.7	33.9	23.0	-14.8	44.5	39.8	-3.4	44.2	23.1	-16.1	46.8
26.9	29.1	-2.7	32.6	22.7	-14.6	44.1	39.6	-3.3	43.9	23.1	-16.2	47.1
28.2	28.3	-2.9	32.2	21.9	-14.9	43.5	39.9	-3.6	44.6	23.1	-16.2	47.0
29.4	26.4	-2.8	30.0	21.1	-14.7	42.4	39.9	-3.5	44.4	22.9	-16.2	46.7
30.6	25.8	-3.0	29.7	19.7	-15.0	41.1	40.6	-3.6	45.3	23.0	-16.2	46.9

Accuracy of NLS Tofts Model Fitting (No VFAC correction)

	Tumour						Healthy					
	Intra-session mean			Inter-session mean			Intra-session mean			Inter-session mean		
T_{res} [s]	K^{trans} %Error	v_e %Error	k_{ep} %Error	K^{trans} %Error	v_e %Error	k_{ep} %Error	K^{trans} %Error	v_e %Error	k_{ep} %Error	K^{trans} %Error	v_e %Error	k_{ep} %Error
1.2	11.4	-3.3	15.4	0.2	-15.4	18.1	18.9	-1.3	20.4	5.5	-14.2	23.1
2.4	11.5	-3.4	15.6	0.2	-15.4	18.2	19.2	-1.3	20.8	5.6	-14.2	23.3
3.7	11.4	-3.5	15.5	0.3	-15.5	18.5	19.1	-1.3	20.7	5.6	-14.2	23.3
4.9	11.1	-3.6	15.4	0.0	-15.6	18.2	19.8	-1.2	21.3	5.7	-14.1	23.3
6.1	11.0	-3.7	15.5	0.0	-15.7	18.3	20.5	-1.3	22.1	6.1	-14.1	23.8
7.3	11.6	-3.9	16.3	0.5	-15.9	19.2	21.5	-1.6	23.6	6.8	-14.4	25.0
8.6	11.9	-4.1	16.8	0.7	-16.1	19.6	22.5	-1.6	24.5	7.3	-14.3	25.4
9.8	12.0	-4.3	17.2	0.8	-16.3	20.1	24.1	-1.8	26.4	8.4	-14.4	27.0
11.0	12.4	-4.5	17.9	0.9	-16.5	20.5	25.7	-1.9	28.1	9.5	-14.5	28.4
12.2	12.7	-4.7	18.5	0.9	-16.7	20.9	27.2	-2.1	30.0	10.8	-14.7	30.2
13.5	12.4	-5.0	18.4	0.3	-16.9	20.3	27.7	-1.8	30.0	11.9	-14.7	31.5
14.7	9.8	-5.2	16.0	-1.7	-17.1	18.3	28.8	-1.9	31.3	12.8	-14.8	32.6
15.9	6.1	-5.3	12.1	-5.4	-17.2	13.9	29.8	-1.7	32.1	13.5	-14.7	33.4
17.1	1.8	-5.4	7.7	-9.1	-17.4	9.7	31.3	-1.9	33.9	14.6	-14.8	34.8
18.4	-2.8	-5.1	2.5	-13.4	-17.1	4.1	31.5	-1.3	33.3	15.1	-14.4	34.8
19.6	-7.0	-5.0	-2.1	-17.3	-16.9	-0.7	31.9	-1.1	33.4	15.8	-14.3	35.5
20.8	-11.0	-4.9	-6.3	-21.0	-16.9	-5.2	32.2	-1.0	33.5	16.2	-14.2	35.7
22.0	-14.4	-4.7	-10.1	-24.3	-16.7	-9.3	32.0	-0.6	32.9	16.4	-13.9	35.5
23.3	-17.6	-4.5	-13.7	-27.3	-16.5	-13.1	31.5	-0.3	31.9	16.0	-13.5	34.5
24.5	-19.9	-4.9	-15.8	-29.6	-17.0	-15.4	31.7	-0.6	32.5	16.3	-13.8	35.2
25.7	-22.3	-4.8	-18.3	-31.8	-16.8	-18.2	30.4	0.2	30.1	15.6	-13.2	33.5
26.9	-24.4	-4.7	-20.7	-33.8	-16.6	-20.8	28.9	1.2	27.4	14.6	-12.6	31.4
28.2	-26.4	-5.1	-22.3	-35.5	-17.1	-22.3	28.8	0.9	27.7	14.4	-12.7	31.4
29.4	-28.5	-4.8	-24.8	-37.3	-16.8	-24.9	26.8	2.5	23.8	12.8	-11.6	27.9
30.6	-30.5	-5.3	-26.6	-39.1	-17.3	-26.5	26.5	2.3	23.7	12.5	-11.7	27.7

Precision of LLS Tofts Model Fitting (No VFAC correction)

	Tumour						Healthy					
	Intra-session			Inter-session			Intra-session			Inter-session		
T_{res} [s]	K^{trans} %S.D.	v_e %S.D.	k_{ep} %S.D.	K^{trans} %S.D.	v_e %S.D.	k_{ep} %S.D.	K^{trans} %S.D.	v_e %S.D.	k_{ep} %S.D.	K^{trans} %S.D.	v_e %S.D.	k_{ep} %S.D.
1.2	0.9	1.8	2.1	12.9	13.0	4.9	0.5	2.5	2.2	13.6	15.5	2.5
2.4	1.0	1.8	2.0	13.0	13.0	5.0	0.8	2.5	2.2	13.7	15.5	2.3
3.7	1.1	1.9	2.3	12.8	13.0	4.9	0.4	2.5	2.4	13.5	15.5	2.5
4.9	0.7	1.8	1.9	12.8	13.0	5.1	0.7	2.5	2.4	13.7	15.5	2.2
6.1	1.0	1.9	2.1	12.7	12.9	5.2	1.2	2.3	1.9	13.7	15.4	2.3
7.3	1.0	1.8	2.2	12.8	13.0	5.1	1.0	2.6	2.5	13.6	15.5	2.2
8.6	0.9	1.8	2.0	12.6	13.0	5.2	1.2	2.4	2.2	13.9	15.4	1.8
9.8	1.1	1.8	1.7	12.8	13.0	5.2	1.0	2.5	2.5	13.8	15.5	2.0
11.0	1.4	1.8	2.0	12.7	13.0	5.7	1.2	2.4	2.3	13.8	15.5	2.1
12.2	1.5	1.9	1.7	13.1	12.9	5.8	1.4	2.3	2.1	14.0	15.4	1.9
13.5	1.3	1.8	1.7	13.2	13.0	6.4	1.1	2.3	1.9	13.6	15.5	2.3
14.7	1.5	1.8	1.8	13.3	13.0	7.1	1.2	2.4	2.2	13.9	15.5	2.1
15.9	1.6	1.8	1.4	13.3	12.9	7.7	1.1	2.4	1.9	14.0	15.5	2.1
17.1	2.0	1.9	1.6	13.3	13.0	7.7	1.4	2.3	1.8	14.3	15.4	2.3
18.4	2.4	1.8	1.7	13.0	12.9	8.4	1.0	2.3	1.2	14.5	15.5	2.4
19.6	2.1	1.9	1.6	13.1	12.9	8.1	1.1	2.3	1.0	14.6	15.5	2.7
20.8	2.0	1.9	1.5	13.2	12.9	8.2	1.5	2.2	0.9	14.9	15.5	2.6
22.0	1.8	1.8	1.7	13.0	13.0	8.3	1.8	2.2	1.4	15.2	15.5	2.8
23.3	1.8	1.8	1.6	13.3	12.9	8.5	1.8	2.2	1.0	15.0	15.5	2.4
24.5	2.0	1.8	1.9	13.5	13.0	7.8	2.5	2.0	1.7	15.4	15.3	3.0
25.7	2.1	1.8	2.2	13.6	13.0	8.4	2.3	2.2	1.8	15.1	15.5	2.9
26.9	1.8	1.7	2.2	13.6	12.9	9.5	2.5	2.1	1.8	14.7	15.6	3.0
28.2	1.9	1.8	2.1	14.1	13.0	8.9	2.3	2.1	1.7	15.2	15.4	2.8
29.4	1.8	1.7	2.2	13.9	13.0	10.0	2.2	2.2	1.5	15.1	15.6	3.0
30.6	2.1	1.8	2.3	14.1	13.0	9.3	2.3	2.0	1.5	15.2	15.4	3.0

Precision of NLS Tofts Model Fitting (No VFAC correction)

	Tumour						Healthy					
	Intra-session			Inter-session			Intra-session			Inter-session		
T_{res} [s]	K^{trans} %S.D.	v_e %S.D.	k_{ep} %S.D.	K^{trans} %S.D.	v_e %S.D.	k_{ep} %S.D.	K^{trans} %S.D.	v_e %S.D.	k_{ep} %S.D.	K^{trans} %S.D.	v_e %S.D.	k_{ep} %S.D.
1.2	7.6	1.8	9.1	17.9	13.1	8.9	0.7	2.4	1.9	13.9	15.4	2.2
2.4	8.0	1.8	9.4	18.3	13.1	9.2	1.0	2.4	1.9	14.0	15.4	2.0
3.7	7.9	1.9	9.5	17.9	13.1	9.1	0.6	2.5	2.0	13.9	15.4	2.1
4.9	8.2	1.8	9.6	18.3	13.1	9.3	0.8	2.5	2.0	14.0	15.4	1.9
6.1	7.9	1.9	9.4	18.1	13.0	9.1	1.2	2.2	1.6	14.0	15.3	2.0
7.3	8.2	1.9	9.8	18.2	13.1	9.4	1.0	2.5	2.2	13.9	15.5	1.9
8.6	8.4	2.0	10.1	18.5	13.0	9.7	1.2	2.3	1.9	14.2	15.3	1.7
9.8	8.5	2.0	10.1	18.6	13.0	9.8	0.9	2.4	2.1	14.1	15.5	2.1
11.0	8.5	2.1	10.3	18.5	13.0	10.0	1.1	2.3	1.9	14.1	15.5	2.1
12.2	8.3	2.2	10.2	18.6	12.9	9.9	1.3	2.3	1.7	14.2	15.4	2.0
13.5	8.2	2.2	10.1	18.7	12.9	9.9	1.1	2.3	1.6	13.8	15.5	2.3
14.7	7.9	2.2	9.9	18.3	13.0	9.5	1.0	2.4	1.9	14.0	15.5	2.0
15.9	7.3	2.2	9.3	18.1	12.9	9.1	1.0	2.4	1.8	13.9	15.6	2.1
17.1	6.7	2.3	8.8	17.7	13.0	8.5	1.1	2.3	1.8	14.1	15.5	2.0
18.4	5.9	2.2	7.8	17.1	12.9	7.6	1.0	2.3	1.7	13.9	15.6	2.2
19.6	5.6	2.2	7.6	17.0	12.8	7.3	0.8	2.4	1.8	13.8	15.7	2.3
20.8	5.0	2.2	6.9	16.5	12.9	6.7	0.9	2.4	1.8	13.9	15.7	2.2
22.0	4.8	2.2	6.6	16.4	13.0	6.5	0.8	2.5	1.8	13.9	15.7	2.2
23.3	4.5	2.2	6.4	16.3	12.9	6.3	0.8	2.5	1.8	13.7	15.8	2.4
24.5	4.3	2.2	6.1	16.1	13.0	6.1	1.0	2.3	1.5	14.0	15.5	2.0
25.7	4.1	2.2	5.9	16.0	13.0	6.0	0.6	2.5	1.9	13.9	15.7	2.4
26.9	4.0	2.2	5.8	16.0	12.9	6.0	0.8	2.4	1.6	13.7	15.8	2.6
28.2	3.9	2.2	5.8	15.9	13.0	5.9	0.7	2.4	1.7	14.0	15.6	2.3
29.4	3.8	2.2	5.6	16.0	12.9	5.8	0.7	2.5	1.9	13.9	15.9	2.8
30.6	3.8	2.3	5.7	15.9	13.0	5.7	0.9	2.3	1.5	14.0	15.7	2.5

Accuracy of LLS Tofts Model Fitting (with VFAC correction)

	Tumour						Healthy					
	Intra-session mean			Inter-session mean			Intra-session mean			Inter-session mean		
T_{res} [s]	K^{trans} %Error	v_e %Error	k_{ep} %Error	K^{trans} %Error	v_e %Error	k_{ep} %Error	K^{trans} %Error	v_e %Error	k_{ep} %Error	K^{trans} %Error	v_e %Error	k_{ep} %Error
1.2	2.3	4.1	-1.7	-0.8	-2.1	1.4	3.3	6.9	-3.3	-2.7	-1.2	-1.4
2.4	2.4	4.1	-1.7	-0.9	-2.1	1.4	3.4	6.9	-3.1	-2.6	-1.2	-1.2
3.7	2.4	4.1	-1.6	-0.6	-2.1	1.6	3.4	6.9	-3.2	-2.7	-1.0	-1.6
4.9	2.4	4.2	-1.7	-0.5	-2.0	1.7	3.8	7.1	-2.9	-2.5	-1.1	-1.3
6.1	2.6	4.1	-1.4	-0.2	-2.1	2.0	4.6	6.9	-2.1	-2.3	-1.0	-1.2
7.3	3.6	4.2	-0.5	0.7	-2.1	2.9	5.3	6.4	-0.8	-1.5	-1.5	0.1
8.6	4.0	4.2	-0.2	1.3	-2.0	3.5	6.5	6.5	0.2	-1.0	-1.4	0.5
9.8	4.4	4.2	0.2	2.2	-1.9	4.3	8.1	6.0	2.2	0.2	-1.8	2.2
11.0	5.4	4.3	1.1	3.5	-1.9	5.7	9.9	5.8	4.2	1.5	-1.9	3.5
12.2	6.6	4.3	2.2	4.9	-1.8	7.0	12.0	5.2	6.7	3.1	-2.3	5.5
13.5	7.7	4.4	3.1	7.1	-1.6	9.0	13.2	5.4	7.5	4.6	-2.4	7.2
14.7	7.4	4.4	3.0	8.1	-1.7	10.2	15.1	4.9	10.0	6.1	-2.7	9.2
15.9	7.9	4.3	3.4	9.1	-1.6	11.1	17.4	4.7	12.4	7.6	-3.0	11.0
17.1	9.3	4.3	4.8	10.5	-1.9	12.8	20.4	3.8	16.3	10.0	-3.7	14.3
18.4	11.4	4.6	6.5	13.4	-1.4	15.2	22.4	4.2	17.5	11.7	-3.4	15.6
19.6	14.7	4.8	9.4	16.4	-1.2	18.1	24.3	3.9	19.6	13.7	-3.9	18.4
20.8	18.1	4.9	12.5	19.3	-1.1	20.9	26.0	3.6	21.4	15.7	-4.2	20.9
22.0	20.8	5.2	14.8	22.4	-0.9	23.8	27.1	3.4	22.8	17.4	-4.4	23.0
23.3	22.6	5.4	16.3	24.6	-0.7	25.8	28.0	3.3	23.5	18.3	-4.4	23.9
24.5	24.4	5.2	18.2	24.9	-1.0	26.5	28.8	2.7	25.1	19.5	-5.0	25.8
25.7	24.6	5.3	18.4	26.4	-0.9	27.7	28.3	3.1	24.1	19.8	-4.9	26.0
26.9	23.8	5.4	17.5	26.7	-0.6	27.9	27.9	3.3	23.3	19.7	-4.9	25.9
28.2	23.3	5.0	17.4	25.6	-1.1	27.3	28.6	2.7	24.8	20.1	-5.2	26.7
29.4	21.5	5.2	15.5	25.6	-0.8	27.0	28.1	3.1	23.8	19.4	-4.9	25.5
30.6	21.0	4.8	15.4	23.9	-1.2	25.8	29.2	2.7	25.3	20.0	-5.2	26.6

Accuracy of NLS Tofts Model Fitting (with VFAC correction)

	Tumour						Healthy					
	Intra-session mean			Inter-session mean			Intra-session mean			Inter-session mean		
T_{res} [s]	K^{trans} %Error	v_e %Error	k_{ep} %Error	K^{trans} %Error	v_e %Error	k_{ep} %Error	K^{trans} %Error	v_e %Error	k_{ep} %Error	K^{trans} %Error	v_e %Error	k_{ep} %Error
1.2	1.3	4.4	-2.9	-1.3	-1.8	0.6	6.0	6.2	-0.1	0.1	-2.1	2.3
2.4	1.5	4.4	-2.7	-1.2	-1.8	0.6	6.3	6.1	0.2	0.2	-2.1	2.4
3.7	1.3	4.3	-2.8	-1.2	-1.8	0.7	6.2	6.1	0.1	0.2	-2.0	2.3
4.9	1.1	4.3	-2.9	-1.3	-1.9	0.7	6.6	6.3	0.4	0.1	-1.9	2.1
6.1	1.1	4.1	-2.8	-1.4	-2.0	0.7	7.2	6.2	1.0	0.6	-1.9	2.6
7.3	1.7	4.0	-2.1	-1.0	-2.1	1.2	8.1	5.7	2.4	1.3	-2.3	3.7
8.6	1.9	3.9	-1.8	-0.9	-2.3	1.5	9.1	5.9	3.1	1.6	-2.1	3.8
9.8	1.9	3.7	-1.6	-0.5	-2.4	2.0	10.6	5.5	4.9	2.7	-2.4	5.3
11.0	2.8	3.6	-0.7	-0.2	-2.6	2.5	12.1	5.4	6.4	3.8	-2.5	6.5
12.2	3.7	3.5	0.3	0.4	-2.8	3.3	13.6	5.1	8.2	5.2	-2.8	8.2
13.5	4.5	3.4	1.2	0.8	-2.8	3.7	14.0	5.6	8.0	6.1	-2.7	9.1
14.7	3.2	3.1	0.2	0.1	-3.0	3.2	15.3	5.4	9.4	7.1	-2.8	10.3
15.9	0.9	3.0	-2.0	-2.4	-3.1	0.8	16.4	5.6	10.2	7.9	-2.6	10.9
17.1	-2.5	3.0	-5.2	-5.4	-3.4	-2.0	18.3	5.1	12.6	9.4	-3.0	12.9
18.4	-6.5	3.3	-9.4	-9.5	-2.9	-6.7	18.5	6.2	11.6	9.9	-2.2	12.5
19.6	-10.2	3.6	-13.2	-12.9	-2.8	-10.4	19.1	6.4	12.0	10.8	-2.2	13.4
20.8	-13.7	3.8	-16.9	-16.5	-2.6	-14.1	19.5	6.5	12.2	11.4	-2.0	13.8
22.0	-16.5	4.1	-19.7	-19.5	-2.5	-17.4	19.4	7.0	11.6	11.8	-1.6	13.8
23.3	-19.1	4.2	-22.3	-22.2	-2.3	-20.3	19.0	7.6	10.6	11.5	-1.0	12.7
24.5	-21.1	3.8	-23.9	-24.5	-2.9	-22.2	19.6	6.7	12.1	12.3	-1.8	14.4
25.7	-23.0	3.8	-25.8	-26.6	-2.7	-24.5	18.4	8.1	9.6	11.5	-0.8	12.5
26.9	-24.9	4.0	-27.7	-28.6	-2.4	-26.8	17.0	9.6	6.7	10.4	0.3	10.2
28.2	-26.6	3.4	-29.0	-30.3	-3.1	-28.0	17.3	8.8	7.9	10.7	-0.3	11.1
29.4	-28.6	3.8	-31.2	-32.2	-2.6	-30.4	15.3	11.2	3.7	8.9	1.7	7.3
30.6	-30.4	3.3	-32.6	-34.0	-3.3	-31.7	15.3	10.6	4.3	9.0	1.2	7.8

Precision of LLS Tofts Model Fitting (with VFAC correction)

	Tumour						Healthy					
	Intra-session			Inter-session			Intra-session			Inter-session		
T_{res} [s]	K^{trans} %S.D.	v_e %S.D.	k_{ep} %S.D.	K^{trans} %S.D.	v_e %S.D.	k_{ep} %S.D.	K^{trans} %S.D.	v_e %S.D.	k_{ep} %S.D.	K^{trans} %S.D.	v_e %S.D.	k_{ep} %S.D.
1.2	0.8	2.1	1.7	2.3	4.8	2.8	0.8	2.9	2.1	6.2	7.6	1.9
2.4	0.8	2.1	1.7	2.2	4.8	3.0	1.2	2.9	2.1	6.2	7.5	1.7
3.7	0.8	2.2	2.0	2.3	4.8	2.9	0.7	3.0	2.3	6.2	7.5	1.7
4.9	0.9	2.1	1.9	2.2	4.8	3.2	1.0	3.0	2.3	6.2	7.6	1.6
6.1	1.0	2.2	2.0	2.0	4.8	3.3	1.3	2.6	1.7	6.5	7.3	1.6
7.3	0.8	2.1	2.1	2.1	4.9	3.2	1.3	3.0	2.4	6.4	7.5	1.4
8.6	0.7	2.1	1.9	1.8	4.8	3.5	1.5	2.8	2.1	6.6	7.4	1.1
9.8	0.7	2.1	1.5	1.8	4.8	3.3	1.3	2.9	2.3	6.6	7.6	1.5
11.0	1.2	2.1	1.5	1.5	4.8	3.8	1.5	2.7	2.2	6.8	7.5	1.4
12.2	1.7	2.2	1.0	2.1	4.8	3.7	1.7	2.7	2.0	7.1	7.3	1.3
13.5	1.6	2.2	1.0	2.2	4.8	4.6	1.5	2.7	1.8	6.6	7.5	1.5
14.7	1.8	2.2	1.2	2.9	4.8	5.6	1.6	2.8	2.2	6.9	7.5	1.3
15.9	2.1	2.2	0.8	3.1	4.7	6.3	1.6	2.8	2.1	6.9	7.5	1.4
17.1	2.5	2.2	1.4	3.6	4.8	6.4	1.8	2.7	2.1	7.2	7.4	1.8
18.4	3.0	2.2	1.7	4.0	4.7	7.3	1.3	2.7	1.7	7.2	7.5	1.9
19.6	2.7	2.2	1.7	3.9	4.7	6.9	1.2	2.8	1.6	7.1	7.7	2.2
20.8	2.6	2.2	1.4	3.8	4.7	6.8	1.3	2.7	1.0	7.1	7.7	2.1
22.0	2.2	2.1	1.4	3.4	4.8	6.8	1.6	2.7	1.3	7.2	7.7	2.3
23.3	2.1	2.1	1.0	3.4	4.7	6.9	1.6	2.6	0.7	7.1	7.7	1.9
24.5	2.1	2.1	0.9	3.6	4.9	6.2	2.4	2.4	1.4	7.5	7.5	2.6
25.7	1.9	2.1	1.0	3.2	4.8	6.6	2.3	2.5	1.7	7.3	7.6	2.6
26.9	1.8	2.1	0.7	3.6	4.7	7.8	2.7	2.4	1.9	7.2	7.7	2.8
28.2	2.0	2.1	0.7	3.8	4.8	7.2	2.6	2.5	1.9	7.5	7.5	2.7
29.4	1.8	2.1	0.8	4.2	4.7	8.4	2.5	2.5	1.7	7.6	7.7	2.8
30.6	2.1	2.1	1.1	4.2	4.7	7.7	2.6	2.3	1.7	7.6	7.5	2.8

Precision of NLS Tofts Model Fitting (with VFAC correction)

	Tumour						Healthy					
	Intra-session			Inter-session			Intra-session			Inter-session		
T_{res} [s]	K^{trans} %S.D.	v_e %S.D.	k_{ep} %S.D.	K^{trans} %S.D.	v_e %S.D.	k_{ep} %S.D.	K^{trans} %S.D.	v_e %S.D.	k_{ep} %S.D.	K^{trans} %S.D.	v_e %S.D.	k_{ep} %S.D.
1.2	5.1	2.1	6.7	6.7	4.8	6.3	1.2	2.8	1.9	6.2	7.6	2.0
2.4	5.5	2.1	7.0	7.2	4.8	6.6	1.5	2.8	1.9	6.3	7.6	1.9
3.7	5.3	2.1	6.9	6.9	4.7	6.2	1.1	2.9	2.1	6.3	7.6	2.1
4.9	5.7	2.1	7.2	7.2	4.8	6.6	1.3	2.9	2.1	6.3	7.6	1.8
6.1	5.3	2.1	6.9	6.9	4.8	6.3	1.6	2.5	1.5	6.5	7.4	2.2
7.3	5.6	2.1	7.3	7.3	4.8	6.4	1.4	2.9	2.2	6.5	7.6	2.0
8.6	5.9	2.2	7.5	7.6	4.8	6.7	1.6	2.7	1.9	6.7	7.5	1.6
9.8	6.0	2.1	7.5	7.5	4.8	6.5	1.3	2.8	2.0	6.7	7.7	2.1
11.0	6.0	2.2	7.7	7.9	4.8	6.7	1.5	2.7	1.9	6.8	7.6	2.2
12.2	5.9	2.3	7.7	7.9	4.9	6.6	1.7	2.6	1.7	7.0	7.4	2.3
13.5	6.0	2.2	7.7	8.2	4.8	7.0	1.5	2.6	1.5	6.5	7.6	2.3
14.7	6.0	2.3	7.8	7.9	4.9	7.1	1.5	2.8	1.9	6.7	7.7	2.0
15.9	5.6	2.3	7.4	7.6	4.9	7.5	1.5	2.8	1.7	6.7	7.7	2.0
17.1	5.2	2.3	7.0	7.3	5.1	7.6	1.6	2.7	1.8	6.9	7.7	2.1
18.4	4.5	2.3	6.2	6.8	5.1	7.2	1.4	2.7	1.6	6.7	7.8	2.2
19.6	4.4	2.3	6.0	6.5	5.2	6.9	1.3	2.8	1.8	6.5	7.9	2.3
20.8	3.7	2.3	5.3	5.8	5.3	6.1	1.3	2.8	1.7	6.5	8.0	2.1
22.0	3.4	2.2	5.0	5.8	5.2	5.6	1.3	2.9	1.9	6.4	8.0	2.1
23.3	3.3	2.3	4.9	5.8	5.2	5.3	1.3	2.9	1.7	6.3	8.0	2.2
24.5	3.1	2.3	4.6	6.0	5.2	4.8	1.5	2.6	1.4	6.5	7.7	2.0
25.7	3.0	2.2	4.5	6.2	5.2	4.7	1.1	2.8	1.8	6.3	7.9	2.2
26.9	3.0	2.3	4.6	6.3	5.1	4.8	1.4	2.7	1.5	6.1	8.0	2.4
28.2	2.9	2.3	4.5	6.4	5.1	4.5	1.2	2.8	1.6	6.3	7.9	2.2
29.4	3.0	2.3	4.6	6.4	5.1	4.8	1.2	3.0	1.8	6.2	8.2	2.6
30.6	2.9	2.3	4.5	6.3	5.2	4.6	1.3	2.7	1.4	6.3	8.0	2.4

Appendix C: Chapter 6 results: percentage errors and percentage standard deviation (S.D.) in DCE-MRI derived PK parameter values

	PK Modelling Accuracy											
	Tumour						Healthy					
	Intra-session mean			Inter-session mean			Intra-session mean			Inter-session mean		
RSD	K^{trans}	v_e	k_{ep}	K^{trans}	v_e	k_{ep}	K^{trans}	v_e	k_{ep}	K^{trans}	v_e	k_{ep}
[%]	%Error	%Error	%Error	%Error	%Error	%Error	%Error	%Error	%Error	%Error	%Error	%Error
	CbC						CbC					
4.68	-	-	-	-	-	-	-	-	-	-	-	-
6.25	-	-	-	-	-	-	-	-	-	-	-	-
12.5	-35.3	-16.2	-19.6	-49.6	-41.1	-24.8	-14.3	-38.1	39.8	-20.3	-43.1	40.2
25.0	-9.3	-19.6	13.0	-13.1	-17.1	4.6	-3.5	-18.4	18.0	-5.3	-19.4	17.6
50.0	-1.8	-4.0	2.5	-0.5	-1.0	0.7	14.0	3.4	8.2	14.3	7.3	6.4
75.0	-1.2	-4.5	3.6	-1.7	-5.7	4.4	3.5	1.6	2.1	0.9	-0.8	2.0
100.0	-1.7	-2.5	0.9	-0.4	-1.8	1.5	0.8	0.4	2.7	0.2	2.0	-1.7
	PI						PI					
4.68	-32.9	-31.3	-1.9	-29.9	-30.4	-5.2	-25.9	-34.0	14.3	-32.2	-40.7	13.0
6.25	-3.6	4.7	-7.5	3.1	9.5	-5.4	17.5	9.4	6.0	13.4	5.9	6.5
12.5	-20.1	-10.4	-10.3	-8.1	-5.4	-2.6	0.1	2.0	-3.1	-4.5	-4.8	-0.1
25.0	-6.6	-4.4	-1.9	-3.8	-2.3	-0.8	-0.5	-1.6	0.1	-3.1	-2.8	-1.2
50.0	-2.5	-1.8	-0.5	0.1	1.3	-1.1	3.6	2.7	1.3	0.5	-1.2	2.0
75.0	-1.1	-1.2	0.0	-1.4	-2.1	0.2	4.5	5.4	-4.5	-2.3	-0.3	-1.8
100.0	0.9	1.6	-0.6	0.7	0.8	0.1	3.6	4.7	-3.0	0.9	3.2	-1.9
	PICS						PICS					
4.68	-12.1	-1.7	-11.6	-4.9	0.4	-3.2	-3.4	-5.7	9.7	2.5	-6.6	8.4
6.25	-9.4	-2.1	-8.5	-1.6	-0.5	-1.4	5.8	-6.5	10.0	-4.4	-9.7	8.3
12.5	-8.1	-3.9	-4.3	-5.4	-6.1	1.1	1.8	-5.2	4.1	-4.5	-7.6	5.0
25.0	-5.1	-4.3	-0.5	-3.0	0.8	-3.6	-2.0	-5.4	3.5	-1.9	-5.3	2.5
50.0	-4.3	-4.7	0.5	-0.8	-1.0	0.4	-0.6	-2.6	1.2	-1.7	-4.4	3.0
75.0	-1.4	-2.8	1.6	-2.4	-4.0	1.2	4.1	5.1	-2.9	1.1	1.6	-0.3
100.0	-1.2	-2.1	1.0	-0.1	-1.5	1.5	-1.2	2.2	-2.2	1.8	0.5	1.4

PK Modelling Precision

	Tumour						Healthy					
	Intra-session			Inter-session			Intra-session			Inter-session		
RSD	K^{trans}	v_e	k_{ep}	K^{trans}	v_e	k_{ep}	K^{trans}	v_e	k_{ep}	K^{trans}	v_e	k_{ep}
[%]	**%S.D.**	**%S.D.**	**%S.D.**	**%S.D.**	**%S.D.**	**%S.D.**	**%S.D.**	**%S.D.**	**%S.D.**	**%S.D.**	**%S.D.**	**%S.D.**
			CbC						**CbC**			
4.68	-	-	-	-	-	-	-	-	-	-	-	-
6.25	-	-	-	-	-	-	-	-	-	-	-	-
12.5	45.7	66.2	50.7	67.3	24.2	60.8	7.0	10.1	4.1	7.3	11.7	4.8
25.0	6.7	2.8	8.7	9.1	7.6	4.9	1.5	3.0	2.6	2.9	2.0	3.7
50.0	1.8	3.9	3.9	1.6	4.6	4.2	1.8	4.0	2.1	9.4	5.8	4.6
75.0	4.7	2.9	3.8	4.8	5.9	5.0	4.1	1.6	5.0	6.2	5.2	8.2
100.0	4.5	4.0	4.2	3.9	3.8	3.7	11.0	7.2	6.4	9.3	5.8	5.8
			PI						**PI**			
4.68	15.0	13.8	8.0	12.9	16.0	15.6	9.6	4.3	4.9	21.0	16.8	5.7
6.25	8.0	4.0	7.1	10.9	13.1	5.5	9.9	6.8	4.0	4.9	3.5	4.4
12.5	5.2	3.1	5.6	5.7	7.4	4.2	8.4	4.6	5.1	9.6	6.7	5.1
25.0	2.9	5.2	5.7	3.7	10.4	7.4	4.8	3.5	2.0	3.1	4.1	3.6
50.0	3.5	4.7	5.3	2.6	4.8	3.4	4.6	4.7	1.5	4.8	5.2	3.6
75.0	5.7	2.6	4.3	5.1	4.6	3.9	3.7	5.2	3.1	8.1	6.0	5.9
100.0	4.2	2.6	3.3	4.3	4.2	3.6	2.1	3.8	2.4	6.3	2.4	5.9
			PICS						**PICS**			
4.68	2.5	5.0	3.2	6.7	7.3	3.7	1.1	10.9	5.2	6.8	6.9	2.0
6.25	4.0	5.4	6.1	3.4	5.9	6.8	4.0	6.7	3.3	5.8	3.4	5.1
12.5	2.0	4.4	3.6	3.9	7.4	4.2	6.6	5.5	3.1	2.0	3.7	3.9
25.0	1.2	3.9	4.5	3.1	5.7	3.0	1.7	1.7	1.4	3.2	1.9	3.9
50.0	2.1	3.7	2.7	1.8	5.2	3.4	3.5	2.9	2.0	2.2	2.8	1.4
75.0	3.3	2.9	3.2	3.8	4.4	3.4	3.6	6.1	2.9	3.1	4.8	2.1
100.0	3.6	3.2	2.7	3.0	4.2	3.7	3.3	1.8	3.7	1.4	2.6	1.7